



TECHNISCHE UNIVERSITÄT
BERGAKADEMIE FREIBERG

Die Ressourcenuniversität. Seit 1765.

Viscosity of Slags

Von der Fakultät für Maschinenbau, Verfahrens- und Energietechnik
der Technischen Universität Bergakademie Freiberg

genehmigte

Dissertation

zur Erlangung des akademischen Grades

Doktor-Ingenieur
(Dr.-Ing.)

vorgelegt von **Dipl.-Ing. Arne Bronsch**

geboren am 28.05.1983 in Schlema

Gutachter: Prof. Dr.-Ing. B. Meyer, TU Bergakademie Freiberg
Prof. Dr.-Ing. H. Hessenkemper, TU Bergakademie Freiberg

Tag der Verleihung: Freiberg, den 13. Juli 2017

V e r s i c h e r u n g

Hiermit versichere ich, dass ich die vorliegende Arbeit ohne unzulässige Hilfe Dritter und ohne Benutzung anderer als der angegebenen Hilfsmittel angefertigt habe; die aus fremden Quellen direkt oder indirekt übernommenen Gedanken sind als solche kenntlich gemacht.

Bei der Auswahl und Auswertung des Materials sowie bei der Herstellung des Manuskripts habe ich Unterstützungsleistungen von folgenden Personen erhalten:

- Bernd Meyer
- Stefan Guhl

Weitere Personen waren an der Abfassung der vorliegenden Arbeit nicht beteiligt. Die Hilfe eines Promotionsberaters habe ich nicht in Anspruch genommen. Weitere Personen haben von mir keine geldwerten Leistungen für Arbeiten erhalten, die nicht als solche kenntlich gemacht worden sind.

Die Arbeit wurde bisher weder im Inland noch im Ausland in gleicher oder ähnlicher Form einer anderen Prüfungsbehörde vorgelegt.

Freiberg, 13. Juli 2017

Dipl.-Ing. Arne Bronsch

Danksagung

Die vorliegende Arbeit entstand über einen Zeitraum von 7 Jahren während meiner Zeit als wissenschaftlicher Mitarbeiter an der Technischen Universität Bergakademie Freiberg am Institut für Energieverfahrenstechnik und Chemieingenieurwesen, Professur für Energieverfahrenstechnik und thermische Rückstandsbehandlung, unter Herrn Prof. Dr.-Ing. B. Meyer. Ihm möchte ich meinen ganzen Dank für das entgegengebrachte Vertrauen, dem Ausbau der Labortechnik und meiner Finanzierung über das Projekt VIRTUHCON bzw. aus freien Institutsmitteln aussprechen.

Weiterhin gilt mein Dank meinem Forschungsgruppenleiter Herrn Dr.-Ing. S. Guhl für die anregenden Diskussionen zur Lösung von Problemen im Bereich Schlackeviskosität und den angrenzenden Gebieten, im Besonderen zu den Themen DTA und dem Bau des Quenchofens.

Besonderer Dank gilt meinen langjährigen Arbeitskollegen der Abteilung Mineralstoffsysteme. Mit ihnen verbrachte ich dienstlich wie auch bei privaten Gelegenheiten eine schöne Zeit. Namentlich sei hier Herr D. Schwitalla aufgeführt, der mich auch fachlich sehr unterstützte. Nicht vergessen möchte ich ebenfalls Herrn Prof. Dr. P. Masset und Herrn Dr. Schmetterer für ihre Geduld am Anfang meiner Arbeit.

Im Weiteren bedanke ich mich bei allen anderen wissenschaftlichen Mitarbeitern, Technikern und Laborangestellten für die anregenden Diskussionen, schnellen Analysen und kompetent durchgeführten Arbeiten. Stellvertretend seien hier Hr. Dr. rer. nat. Schreiner, Hr. Baltrusch, Hr. Lohse, Fr. Neubert und Hr. Wagner aufgeführt.

Abschließend möchte ich mich aus ganzem Herzen bei meiner Frau Martina für ihre unentwegte Zusprache, Nachsicht und Unterstützung und bei meinen Eltern bedanken.

Freiberg, März 2017

Arne Bronsch

List of Contents

List of Tables.....	vi
List of Figures	viii
Symbols and Abbreviations	xviii
1. Introduction and Aim.....	1
2. General Overview of Slag	2
2.1 Viscosity.....	2
2.1.1 Viscosity Introduction	2
2.1.2 Flow behavior of fluids	3
2.2 Slag Definition and Phase Diagrams	4
2.3 Solid Slag Structure	5
2.4 Liquid Slag Structure.....	10
2.5 Basicity and B/A-ratio.....	11
2.6 Slag Components.....	13
2.6.1 Silicon dioxide	13
2.6.2 Aluminum oxide	13
2.6.3 Calcium oxide	15
2.6.4 Iron oxide	16
2.6.5 Magnesium Oxide	18
2.6.6 Potassium Oxide.....	19
2.6.7 Sodium Oxide	20
2.6.8 Titanium Oxide.....	21
2.6.9 Phosphorous.....	22
2.6.10 Sulfur.....	22
2.7 Summary of Last Chapters.....	23
3. Slag Viscosity Toolbox.....	25
3.1 Slag Viscosity Predictor.....	25
3.2 Slag Viscosity Database.....	26
3.3 Prediction Quality of Viscosity Models.....	27
4. Classic Slag Viscosity Modelling.....	30

4.1	Selected Classic Viscosity Models	31
4.1.1	S ²	32
4.1.2	Watt-Fereday	32
4.1.3	Bomkamp.....	32
4.1.4	Shaw.....	32
4.1.5	Lakatos	33
4.1.6	Urbain	33
4.1.7	Riboud	33
4.1.8	Streeter.....	34
4.1.9	Kalmanovitch-Frank	34
4.1.10	BBHLW	34
4.1.11	Duchesne	34
4.1.12	ANNliq	35
4.2	Need of Improvement in Viscosity Literature	35
4.3	Summary of Last Chapters.....	36
5.	Advanced Slag Viscosity Modelling	37
5.1	Crystallization.....	37
5.1.1	Nucleation.....	38
5.1.2	Crystallization Rate	39
5.1.3	Crystallization Measurement Methods	39
5.2	Slag Properties Changes During Crystallization	40
5.2.1	Slag Density.....	40
5.2.2	Solid Volume Fraction	46
5.2.3	Estimation of Slag Composition During Cooling	46
5.3	Viscosity Depending on Particles and Shear Rate.....	47
5.3.1	Einstein-Roscoe Equation	48
5.3.2	Improved Modelling Approach by Modified Einstein-Roscoe	49
5.4	Summary of Last Chapters.....	50
6.	Experimental Procedures	52
6.1	Viscosity Measurements	52

6.1.1	Estimating Parameter Ranges of Viscosity Measurements	53
6.1.2	Viscosity Measurement Procedure	54
6.2	Thermal Analysis of Slags	55
6.2.1	Experimental Conditions of DTA	55
6.3	Phase Determination	55
6.3.1	Quench Experiment Processing	56
6.3.2	Phase Determination on XRD Results	56
6.4	Summary of Last Chapters	57
7.	Results and Discussion	58
7.1	Selected Slag Samples	58
7.1.1	Slag Sample Composition Before Viscosity Measurements	58
7.1.2	Slag Sample Composition After Viscosity Measurements	59
7.2	General Results of Viscosity Measurements	60
7.2.1	Viscosity under Air Atmosphere	63
7.2.2	Viscosity under Reducing Atmospheres	65
7.2.3	Viscosity under Constant Partial Oxygen Pressure	66
7.2.4	Summary of Last Chapter	68
7.3	Mineral Formation	69
7.3.1	General Results on Primarily Mineral Formation	69
7.3.2	Influences on Primarily Mineral Formation	70
7.3.3	Mineral Formation over Wide Temperature Ranges	71
7.3.4	Summary of Last Chapter	77
7.4	Results Obtained by DTA	78
7.4.1	Comparing Results obtained by DTA and Quenching	80
7.4.2	Summary of Last Chapter	82
7.5	Shear Rate Influence on Slag Viscosity	82
7.5.1	Shear Rate Influence under Oxidizing Atmospheres	83
7.5.2	Shear Rate Influence under Reducing Atmospheres	87
7.5.3	Shear Rate Influence under Constant Atmospheres	91
7.5.4	Summary of chapter	92

7.6	Atmospheric Influence on Viscosity	93
7.6.1	Summary of Last Chapter	95
7.7	Cooling Rate Influence on Slag Viscosity	95
7.7.1	Summary of Last Chapter	97
8.	Advanced Viscosity Modelling Approach	99
8.1	Prediction Quality of Classical Viscosity Models.....	99
8.1.1	Selecting the Best Viscosity Model for Newtonian Flow	99
8.1.2	Summary of Last Chapter	103
8.2	Predicting Liquidus Temperature.....	103
8.2.1	Comparing Liquidus Calculations and Quenching Experiments	103
8.2.2	Comparing DTA Results and Liquidus Calculations	105
8.2.3	Summary of Last Chapter	107
8.3	Predicting Liquid Slag Composition.....	108
8.3.1	Results of Slag Composition Calculations at Oxidizing Conditions ...	108
8.3.2	Results of Slag Composition Calculations at Reducing Conditions...	110
8.3.3	Summary of Last Chapter	111
8.4	Modelling Approach	112
8.4.1	Development of Datasets for Advanced Viscosity Modeling.....	113
8.4.2	Summary of Last Chapter	116
8.5	Results of Advanced Slag Viscosity Modelling Approach	116
8.5.1	Summary of Last Chapter	121
9.	Summary.....	123
10.	Appendix: Information on Classic Viscosity Modelling.....	126
10.1	Backgrounds of Applied Viscosity Models.....	126
10.2	Viscosity Model of the BCURA (S^2)	129
10.3	Watt-Fereday.....	130
10.4	Bomkamp	130
10.5	Shaw	131
10.6	Lakatos Model	132
10.7	Urbain Model	133

10.8	Riboud Model	134
10.9	Streeter Model	136
10.10	Kalmanovitch-Frank Model	137
10.11	BBHLW Model	137
10.12	Duchesne Model	139
10.13	ANNliq Model	141
11.	Appendix: Settings of Equilibrium Calculations	143
12.	Appendix: Parameters of Einstein-Roscoe Equation	153
13.	Appendix: Ash and Slag Sample Preparation	155
14.	Appendix: Experimental Procedures: Viscometer	159
14.1	General Viscometer Description	159
14.2	Temperature Calibration	160
14.3	Viscometer Calibration	160
14.4	Accuracy and Reproducibility of HT-Viscosity Measurements	161
14.5	Influence of Inductive Heating	163
14.6	Influence of Measurement System Materials	164
15.	Appendix: Experimental Procedures: Quenching Furnace	167
16.	Appendix: Slag Sample Parameters and Composition	168
17.	Appendix: Slag Viscosity Measurements Results	175
18.	Appendix: Viscosities at Different Cooling Rates	182
19.	Appendix: Slag Viscosity Modelling: AALE Calculations	187
20.	Appendix: Advanced Viscosity Modelling: a-factors	193
21.	Appendix: Slag Mineral Phase Investigations and Modelling	197
22.	Appendix: Results of DTA Measurements on Slags	207
23.	Appendix: Advanced Slag Viscosity Modelling Approach	211
	References	228

List of Tables

Table 1: Viscosity of selected fluids [4].	3
Table 2: Selected network formers, network modifiers and amphoteric [10] [17].	9
Table 3: Selected calculation properties for SVP within FactSage 6.4.	26
Table 4: Properties of SVDB in November 2015.	26
Table 5: Examples on calculated errors to illustrate performance functions.	29
Table 6: Selection of viscosity modelling methods.	30
Table 7: Selection of viscosity models.	31
Table 8: Comparison of mentioned parameters to the number of references.	35
Table 9: Referenced partial molar volumes for calculations of slag molar volume by Lange and Carmichael [121].	43
Table 10: Referenced partial molar volumes for calculations of slag molar volume by Mills and Rhine 1989 [120].	43
Table 11: Slag and mineral properties to calculate slag densities in this work.	44
Table 12: Values of a-factors taken from several references.	49
Table 13: Parameter ranges of viscosity measurements.	54
Table 14: Parameters for phase determination by XRD analysis.	57
Table 15: Flow properties of slags for a cooling rate of -2 K/min in the viscosity range up to 100 Pa s for oxidizing atmospheres.	62
Table 16: Flow properties of slags for a cooling rate of -2 K/min in the viscosity range up to 100 Pa s for reducing atmospheres.	63
Table 17: Flow properties of slags for a cooling rate of -2 K/min in the viscosity range up to 100 Pa s for constant partial oxygen pressures.	63
Table 18: Number of a-factor violations in view of models.	114
Table 19: Number of a-factor violations in view of slags.	115
Table 20: Slag groups by modelling results.	120
Table 21: Selected Artificial Neuronal Network structures [163].	128
Table 22: Compositional ranges covered by S^2 development [35].	129
Table 23: Compositional ranges covered by Watt-Fereday model [165].	130
Table 24: Factors for the Shaw model referenced by [90] and [35].	132
Table 25: Compositional ranges for Lakatos model development [68].	133
Table 26: Separation of network formers, modifiers and amphoteric by [91,100].	133
Table 27: Content ranges for the development of Riboud model.	135
Table 28: Compositional range of slags for Streeter model development [95].	136
Table 29: Compositional range of slags for BBHLW model development [92].	138
Table 30: Development input data and parameter ranges of Duchesne model [93].	139
Table 31: Weights to first hidden layer within ANN Duchesne model [93].	140

Table 32: Weights for output nodes of Duchesne model [93].	141
Table 33: Input data and parameter ranges used to develop the ANNliq model [83].	141
Table 34: Weights to first hidden layer within ANNliq model [83].	142
Table 35: Weights for output nodes for ANNliq model [83].	142
Table 36: Solution species selected for phase calculations by SVP.	143
Table 37: Compound species of FactSage selected for phase calculations.	143
Table 38: Details of used density data to estimate density model performance.	148
Table 39: Recommended densities of minerals found in crystallized slags.	149
Table 40: Values of α and n factors of Einstein-Roscoe equation taken from several references.	153
Table 41: Increase of molybdenum within a coal ash after high temperature measurements.	165
Table 42: Selected crucible and bob materials.	166
Table 43: Parameters of quenching furnace.	167
Table 44: Slag composition, weight basis, before viscosity measurements.	168
Table 45: Slag composition, molar basis, before viscosity measurements.	170
Table 46: Slag composition, weight basis, after viscosity measurements.	172
Table 47: AALE calculated on viscosity predictions and measurements in the ranges $\eta=0-25$ Pa s, $a=-2$ K/min, all shear rates, B/A on mass, air.	187
Table 48: AALE calculated on viscosity predictions and measurements in the ranges $\eta \leq 25$ Pa s, $a=-2$ K/min, all shear rates, B/A on mass, reducing atmospheres.	189
Table 49: AALE calculated on viscosity predictions and measurements in the ranges $\eta \leq 25$ Pa s, $a=-2$ K/min, all shear rates, B/A on mass, nitrogen gas is oxidizing.	190
Table 50: AALE calculated on viscosity predictions and measurements in the ranges $\eta \leq 25$ Pa s, $a=-2$ K/min, all shear rates, B/A on mass, nitrogen gas is reducing.	190
Table 51: Minimum and maximum a -factors of extensively investigated samples, oxidizing conditions, all shear rates, all solid volume fractions.	193
Table 52: Minimum and maximum a -factors from extensively investigated samples, reducing conditions, all shear rates, all solid volume fractions.	194
Table 53: Minerals, abbreviations and chemical formulas.	197

List of Figures

Figure 1: Two-Plates-Model	2
Figure 2: Shear rate depending a) flow curves and b) viscosity curves.	3
Figure 3: Different particles in a) orientation in resting state and b) oriented under shear.	4
Figure 4: Particles are a) orientated in rest and b) entangled under shear.	4
Figure 5: Schematic of a eutectic binary phase diagram of two metal oxides [6].	5
Figure 6: SiO_4 -Tetrahedron with bond angle and bond length [10].	6
Figure 7: Bonds within the SiO_4 complex a) polar, b) covalent, c) double bond [10].	6
Figure 8: $[\text{SiO}_4]$ -tetrahedron connections a) in solid quartz and b) in molten quartz [12,13].	7
Figure 9: Atomic force microscope images of a silica glass [15].	7
Figure 10: Weakened glass structure by introduction of Na_2O as network modifier [12,13].	8
Figure 11: Schematic representation of tetrahedra formed by Si, O and a network modifier [34].	10
Figure 12: T-B/A-relationship of viscosities of 25 Pa s [37].	13
Figure 13: T-B/A-relationship of viscosities of 25 Pa s (own measurements).	13
Figure 14: Viscosity decreasing effect of alumina addition to silica, wt.-ratios [52].	14
Figure 15: Influence of Al_2O_3 to SiO_2 -CaO- Al_2O_3 melts at temperatures of a) 1500 °C and b) 1400 °C.	15
Figure 16: Viscosity vs. temperature for a binary melt of SiO_2 -CaO [56].	15
Figure 17: Viscosity vs. temperature for SiO_2 - Al_2O_3 -MgO-CaO systems with a) MgO=2 wt.-% and b) MgO=5 wt.-% [57].	16
Figure 18: Fe-ratio over temperature for different SiO_2 -CaO- Fe_2O_3 melts [49].	17
Figure 19: Fe-ratio of two Na_2O - SiO_2 - Fe_2O_3 melts as function of partial oxygen pressure [58].	17
Figure 20: Viscosity dependence on Fe^{3+} -distribution [49].	18
Figure 21: Viscosity as function of Fe-ratio for several temperatures [49]	18
Figure 22: Viscosity influence of of MgO for a) binary SiO_2 -MgO melts and b) quaternary SiO_2 - Al_2O_3 -CaO-MgO melts [52,69,70].	19
Figure 23: Viscosity decrease by increase of K_2O for binary SiO_2 - K_2O melts [69]	20
Figure 24: Viscosity decrease by increase of K_2O for ternary SiO_2 - Fe_2O_3 - K_2O [71].	20
Figure 25: Viscosity influence by Na_2O for binary SiO_2 - Na_2O melts [69].	21
Figure 26: Viscosity influence by Na_2O for ternary melts made from Al_2O_3 - SiO_2 - Na_2O [72].	21
Figure 27: Influence of TiO_2 on viscosity at a) 1500 °C and b) 1400 °C [55].	22

Figure 28: Influence of P_2O_5 on the viscosity of a) CaO- P_2O_5 mixture [75] and b) Na_2O - P_2O_5 mixture [76].	22
Figure 29: Viscosity of imaginary slag and modelling to describe performance functions.	29
Figure 30: Schematic of nucleation in view of Gibbs energy ΔG [36].	38
Figure 31: Rate distribution of nucleus formation and crystal growth [116].	39
Figure 32: Molar Volume V_m of a binary slag with a) linear volume function and b) a non-linear volume function [34].	42
Figure 33: Comparison of measured and calculated densities by a) slag bulk composition, Fe-free model by Lange and b) Fe-bearing model by Lange, model by Mills and model used in this work.	45
Figure 34: Schematic of collided particles forming a collision duoblet, size ratio 2:1 [134].	49
Figure 35: Flow chart of improved viscosity modelling.	50
Figure 36: Schematic description of sample preparation and measurements for slag investigations.	52
Figure 37: Samples listed by B/A-ratio for a) all samples, b) oxidizing conditions, c) reducing conditions and d) measured under nitrogen.	58
Figure 38: Mass-based composition of samples before viscosity measurements.	59
Figure 39: Mole-based composition of samples before viscosity measurements.	59
Figure 40: Slag composition after viscosity measurement.	60
Figure 41: Viscosities related to temperature and B/A-ratio under oxidizing atmospheres, $a=-2$ K/min, $\gamma=50$ 1/s.	64
Figure 42: Temperature differences starting at 5 Pa s for selected samples under oxidizing atmospheres, $a=-2$ K/min, $\gamma=50$ 1/s.	65
Figure 43: Viscosities related to temperature and B/A-ratio under reducing atmospheres, $a=-2$ K/min, $\gamma=50$ 1/s.	66
Figure 44: Temperature differences starting at 10 Pa s for selected samples under reducing conditions, $a=-2$ K/min, $\gamma=50$ 1/s.	66
Figure 45: Viscosities related to temperature and B/A-ratio under technical nitrogen atmospheres, $a=-2$ K/min, $\gamma=25$ 1/s.	67
Figure 46: a) Contents and b) ratios of SiO_2 , Al_2O_3 and CaO of slags measured under nitrogen gas.	67
Figure 47: Temperature differences starting at 5 Pa s under technical nitrogen atmospheres, $a=-2$ K/min, $\gamma=50$ 1/s.	67
Figure 48: Primarily detected minerals found by quenching experiments at oxidizing atmospheres.	70

Figure 49: Primarily detected minerals found by quenching experiments at reducing atmosphere.	70
Figure 50: Number of detected mineral phases including all temperature points.	73
Figure 51: Number of minerals in respect to amount of metal ions.	73
Figure 52: Number of Al-containing minerals with respect to atmosphere.	74
Figure 53: Number of Ca-containing minerals with respect to atmosphere.	74
Figure 54: Number of Mg-containing minerals with respect to atmosphere.	75
Figure 55: Number of Fe-containing minerals with respect to atmosphere.	75
Figure 56: Average DTA onset temperatures of exothermal events under a) oxidizing and b) reducing conditions.	79
Figure 57: Temperature differences of DTA events obtained at oxidizing and reducing conditions.	80
Figure 58: Comparison of onset temperatures obtained by DTA and crystallization temperature ranges obtained by quenching.	82
Figure 59: Temperatures, interpolated solid volume fractions and mineral names at equal viscosities as function of shear rates under oxidizing atmospheres. .	84
Figure 60: Temperature differences of viscosities measured at shear rates of 12.5 1/s and above, air atmosphere.	85
Figure 61: Temperature differences of viscosities measured at shear rates of 25 1/s and above, air atmosphere.	86
Figure 62: Temperature differences of viscosities measured at shear rates of 50 1/s and above, air atmosphere.	87
Figure 63: Temperatures, interpolated solid volume fractions and mineral names of equal viscosities as function of shear rates under reducing atmospheres. .	88
Figure 64: Temperature differences of viscosities measured at shear rates of 12.5 1/s and above, reducing conditions.	89
Figure 65: Temperature differences for viscosities measured at shear rates of 25 1/s and above under reducing conditions.	90
Figure 66: Temperature differences of viscosities measured at shear rates of 25 1/s and above, reducing conditions.	90
Figure 67: Temperatures of equal viscosities as function of shear rates under constant partial oxygen pressures.	91
Figure 68: Temperature differences of viscosities measured at shear rates of 12.5 1/s and above, constant partial oxygen pressures.	92
Figure 69: Temperature differences of viscosities measured at shear rates of 25 1/s and above, constant partial oxygen pressures.	92

Figure 70: Temperatures of selected viscosities under oxidizing and reducing conditions at a shear rate of 50 1/s.....	94
Figure 71: Temperature differences of selected viscosities for oxidizing and reducing conditions and changed shear rates.....	95
Figure 72: Temperatures to obtain a defined viscosity for different cooling rates at a constant shear rate.....	97
Figure 73: AALE of classic viscosity models, ≤ 25 Pa s, cooling rate -2 K/min, all shear rates.....	99
Figure 74: AALE obtained from classic viscosity models from a) S2 to Urbain and from b) Riboud to ANNliq, $\eta \leq 25$ Pa s, all shear rates, all slags, oxidizing conditions.....	101
Figure 75: Δ AALE of slags measured under reducing conditions and calculated on oxidizing and reducing parameters.....	102
Figure 76: Δ AALE obtained from classical viscosity models a) S2 to Urbain and b) Riboud to ANNliq, $\eta \leq 25$ Pa s, all shear rates, nitrogen atmospheres.....	102
Figure 77: Differences of liquidus temperatures calculated by SlagH and SlagA solution species.....	104
Figure 78: Liquidus temperatures obtained by slag quenching and by calculations with SVP.....	105
Figure 79: Calculated liquidus temperatures of selected slags.....	106
Figure 80: Temperature differences of calculated liquidus temperatures and onset temperatures obtained by DTA under a) oxidizing and b) reducing conditions.....	107
Figure 81: Recommended viscosity modelling approach.....	113
Figure 82: Devolution of fitted a-factors for S2 model under a) oxidizing and b) reducing conditions.....	114
Figure 83: a-factors with different slopes of a) single slag (S42) and b) different slags (Bomkamp model).....	116
Figure 84: AALE of slags with interpolated SVF=0.....	117
Figure 85: AALEs of best classic and advanced viscosity modelling under oxidizing atmosphere, SVF>0 and all shear rates.....	118
Figure 86: AALEs of best classic and advanced viscosity modelling under reducing atmosphere, SVF>0 and all shear rates.....	118
Figure 87: AALEs of best classic and advanced viscosity modelling under nitrogen atmosphere, SVF>0 and all shear rates, assuming a) oxidizing and b) reducing conditions.....	118
Figure 88: Scheme of a MLP basic topology of an ANN [163].....	128

Figure 89: Ashing furnace chamber.	155
Figure 90: High-temperature furnace a) of Carbolite and b) TOMMI plus.	156
Figure 91: Damages caused by slag boil over within a high temperature furnace.	156
Figure 92: Reetz vertical tube furnace 1650 to adjust oxidation state.	157
Figure 93: Influence of temperature a) to partial oxygen pressure of different CO:CO ₂ ratios and b) on the Fe ₂ O ₃ /FeO mass ratio at 70 vol.-% CO and 60 vol.-% CO ₂ . Input is pure Fe ₂ O ₃ , liquidus temperature is 1375.3 °C.	158
Figure 94: HT-Viscometer a) from outside with closed door and b) open measurement chamber.	159
Figure 95: a) Dimensions of crucible and spindle, b) crucible with poor insulation and c) crucible with enhanced insulation at high temperatures.	160
Figure 96: Reproducibility of silicon oil viscosity calibration for shear rate $\dot{\gamma}=75$ 1/s. .	162
Figure 97: Calibration of measuring system with standard glass DGG1 with different shear rates. Cooling rate is -2 K/min.	162
Figure 98: Reproducibility of high temperature viscosity measurements of DGG1 at a shear rate of a) $\dot{\gamma}=25$ 1/s and b) $\dot{\gamma}=50$ 1/s	163
Figure 99: a) Quench furnace installed at the laboratory and b) schematic representation.	167
Figure 100: Slag viscosity measurements on slags S1 to S6 at a cooling rate of -2 K/min.	175
Figure 101: Slag viscosity measurements on slags S7 to S12 at a cooling rate of -2 K/min.	176
Figure 102: Slag viscosity measurements on slags S13 to S18 at a cooling rate of -2 K/min.	177
Figure 103: Slag viscosity measurements on slags S19 to S24 at a cooling rate of -2 K/min.	178
Figure 104: Slag viscosity measurements on slags S25 to S30 at a cooling rate of -2 K/min.	179
Figure 105: Slag viscosity measurements on slags S31 to S36 at a cooling rate of -2 K/min.	180
Figure 106: Slag viscosity measurements on slags S37 to S42 at a cooling rate of -2 K/min.	181
Figure 107: Slag S6 measured at different cooling rates.	182
Figure 108: Slag S7 measured at different cooling rates.	183
Figure 109: Slag S29 measured at different cooling rates.	183
Figure 110: Slag S30 measured at different cooling rates.	184
Figure 111: Slag S39 measured at different cooling rates.	185

Figure 112: Slag S39 measured at different cooling rates.....	186
Figure 113: AALE as function of B/A-ratio obtained from classical viscosity models a) S2 to Urbain and b) Riboud to ANNliq, $\eta \leq 25$ Pa s, all shear rates, oxidizing conditions.	191
Figure 114: AALE as function of B/A-ratio obtained from classical viscosity models a) S2 to Urbain and b) Riboud to ANNliq, $\eta \leq 25$ Pa s, all shear rates, reducing conditions.	191
Figure 115: AALE obtained from classical viscosity models a) S2 to Urbain and b) Riboud to ANNliq, $\eta \leq 25$ Pa s, all shear rates, nitrogen atmosphere assumed to be oxidizing.	192
Figure 116: AALE obtained from classical viscosity models a) S2 to Urbain and b) Riboud to ANNliq, $\eta \leq 25$ Pa s, all shear rates, nitrogen atmosphere assumed to be reducing.	192
Figure 117: Fitted a-factors of extensively investigated slags, all shear rates, all solid volume fractions, S2 to Urbain. Left hand: oxidizing conditions, right hand: reducing conditions.....	195
Figure 118: Fitted a-factors of extensively investigated slags, all shear rates, all solid volume fractions, Riboud to ANNliq. Left hand: oxidizing conditions, right hand: reducing conditions.	196
Figure 119: Phase analysis for samples under oxidizing conditions, S4 to S20.	198
Figure 120: Phase analysis for samples under oxidizing conditions, S29 to S42.	199
Figure 121: Phase analysis of samples prepared under reducing conditions, slags S7 to S39.	200
Figure 122: Phase analysis of samples prepared under reducing conditions, S41.	201
Figure 123: Liquid slag composition obtained by quenching experiments and calculations at oxidizing conditions, S4 to S14.....	202
Figure 124: Liquid slag composition obtained by quenching experiments and calculations at oxidizing conditions, S16 to S32.....	203
Figure 125: Liquid slag composition obtained by quenching experiments and calculations at oxidizing conditions, S36 to S42.....	204
Figure 126: Liquid slag composition obtained by quenching experiments and calculations at reducing conditions, S7 to S31.....	205
Figure 127: Liquid slag composition obtained by quenching experiments and calculations at reducing conditions, S35 to S41.....	206
Figure 128: DTA curves of slag S6, oxidizing atmospheres.	207
Figure 129: DTA curves of slag S7, reducing atmospheres.	207
Figure 130: DTA curves of slag S13, oxidizing atmospheres, including repetitions. ..	207

Figure 131: DTA curves of slag S13, reducing atmospheres.	207
Figure 132: DTA curves of slag S14, oxidizing atmospheres, including repetitions. ...	207
Figure 133: DTA curves of slag S16, oxidizing atmospheres, agreement to viscosity measurements.....	208
Figure 134: DTA curves of slag S16, reducing atmospheres.	208
Figure 135: DTA curves of slag S19, reducing atmospheres.	208
Figure 136: DTA curves of slag S20, oxidizing atmospheres, including repetitions. ...	208
Figure 137: DTA curves of slag S29, oxidizing atmospheres.	208
Figure 138: DTA curves of slag S30, reducing atmospheres.	209
Figure 139: DTA curves of slag S31, reducing atmospheres.	209
Figure 140: DTA curves of slag S32, oxidizing atmospheres.	209
Figure 141: DTA curves of slag S35, reducing atmospheres.	209
Figure 142: DTA curves of slag S36, oxidizing atmospheres, including repetitions. ...	209
Figure 143: DTA curves of slag S39, reducing atmospheres.	210
Figure 144: DTA curves of slag S40, oxidizing atmospheres.	210
Figure 145: DTA curves of slag S41, reducing atmospheres.	210
Figure 146: DTA curves of slag S42, oxidizing atmospheres, including repetitions. ...	210
Figure 147: Slag S1, nitrogen atmosphere, classic modelling assuming oxidizing and reducing conditions.....	211
Figure 148: Slag S2, oxidizing atmosphere, AALE by $\eta \leq 25$ Pa s and $\eta \leq 100$ Pa s....	211
Figure 149: Slag S3, oxidizing atmosphere.....	211
Figure 150: Slag S4, oxidizing atmosphere, classic modelling, AALE by $\eta \leq 25$ Pa s and $\eta \leq 100$ Pa s.	211
Figure 151: Slag S5, reducing atmosphere, classic modelling, additional oxidizing atmosphere.	211
Figure 152: Slag S6, oxidizing atmosphere, classic modelling.	212
Figure 153: Slag S7, reducing atmosphere, classic modelling, AALE by $\eta \leq 25$ Pa s and $\eta \leq 100$ Pa s.	212
Figure 154: Slag S8, oxidizing atmosphere, classic modelling.	212
Figure 155: Slag S8, oxidizing atmosphere, advanced modelling.	212
Figure 156: Slag S9, oxidizing atmospheres, classic modelling, AALE by $\eta \leq 25$ Pa s and $\eta \leq 100$ Pa s.	212
Figure 157: Slag S10, oxidizing atmospheres, classic modelling.	213
Figure 158: Slag S10, oxidizing atmospheres, advanced modelling, best classic model S2 by AALE.	213
Figure 159: Slag S10, oxidizing atmospheres, advanced modelling, best advanced model Watt-Fereday by AALE.	213

Figure 160: Slag S11, reducing atmospheres, classic modelling.....	213
Figure 161: Slag S12, nitrogen atmospheres, oxidizing atmosphere for classic modelling.	213
Figure 162: Slag S12, nitrogen atmospheres, oxidizing conditions and Streeter model for advanced modelling.....	214
Figure 163: Slag S12, nitrogen atmospheres, reducing conditions, classic viscosity modelling.	214
Figure 164: Slag S13, oxidizing atmospheres, classic modelling.	214
Figure 165: Slag S13, oxidizing atmospheres, advanced modelling by Bomkamp model.....	214
Figure 166: Slag S13, oxidizing atmospheres, advanced modelling by S2 model.	214
Figure 167: Slag S14, oxidizing atmospheres, classic modelling.	215
Figure 168: Slag S14, oxidizing atmospheres, advanced modelling, best classic model.	215
Figure 169: Slag S14, oxidizing atmospheres, advanced modelling, best advanced model.....	215
Figure 170: Slag S15, oxidizing atmospheres, classic viscosity modelling.	215
Figure 171: Slag S16, oxidizing atmosphere, classic viscosity modelling.	215
Figure 172: Slag S17, oxidizing conditions, classic and advanced modelling close to each other.	216
Figure 173: Slag S18, oxidizing atmospheres, classic modelling.	216
Figure 174: Slag S18, oxidizing atmosphere, advanced modelling of best classic model.....	216
Figure 175: Slag S19, reducing atmosphere, classic modelling.	216
Figure 176: Slag S20, oxidizing atmosphere, classic modelling.	216
Figure 177: Slag S21, oxidizing atmosphere, classic modelling.	217
Figure 178: Slag S21, oxidizing atmosphere, advanced modelling.	217
Figure 179: Slag S22, reducing atmosphere, classic modelling.	217
Figure 180: Slag S23, oxidizing atmosphere, classic modelling.	217
Figure 181: Slag S23, oxidizing atmosphere, advanced modelling.	217
Figure 182: Slag S24, nitrogen atmospheres, oxidizing conditions assumed for classic modelling.	218
Figure 183: Slag S24, nitrogen atmospheres, oxidizing conditions assumed for advanced modelling.....	218
Figure 184: Slag S24, nitrogen atmospheres, reducing conditions assumed for classic modelling.	218
Figure 185: Slag S25, reducing conditions, classic modelling.	218

Figure 186: Slag S25, reducing conditions, advanced modelling.	218
Figure 187: Slag S26, oxidizing atmosphere, classic modelling, best AALE of ≤ 25 Pa s (Duchesne) and ≤ 100 Pa s (S2).....	219
Figure 188: Slag S26, oxidizing atmosphere, advanced modelling, best AALE of ≤ 100 Pa s.	219
Figure 189: Slag S26, oxidizing atmosphere, advanced modelling, best AALE ≤ 25 Pa s (Duchesne).....	219
Figure 190: Slag S27, nitrogen atmosphere, classic modelling of oxidizing and reducing conditions.	219
Figure 191: Slag S28, nitrogen atmosphere, classic modelling assuming oxidizing and reducing conditions.....	219
Figure 192: Slag S28, nitrogen atmosphere, advanced modelling assuming oxidizing conditions.	220
Figure 193: Slag S29, oxygen atmosphere, classic modelling.....	220
Figure 194: Slag S29, oxygen atmosphere, advanced modelling.....	220
Figure 195: Slag S30, reducing atmosphere, classic modelling.	220
Figure 196: Slag S31, reducing atmosphere, classic modelling.	220
Figure 197: Slag S31, reducing atmosphere, advanced modelling.....	221
Figure 198: Slag S32, oxidizing atmosphere, classic modelling.	221
Figure 199: Slag S32, oxidizing atmosphere, advanced modelling by best classic AALE (ANNliq).....	221
Figure 200: Slag S32, oxidizing atmosphere, advanced modelling by best fitting model (Urbain).	221
Figure 201: Slag S33, nitrogen atmosphere, classic modelling assuming oxidizing conditions, best AALE (Duchesne) and best advanced model (Watt-Fereday).	221
Figure 202: Slag S33, nitrogen atmosphere, advanced modelling assuming oxidizing conditions by best advanced AALE (Watt-Fereday).	222
Figure 203: Slag S33, nitrogen atmosphere, classic modelling assuming reducing conditions.	222
Figure 204: Slag S34, nitrogen atmospheres, classic modelling assuming oxidizing conditions.	222
Figure 205: Slag S34, nitrogen atmospheres, advanced modelling assuming oxidizing conditions.	222
Figure 206: Slag S34, nitrogen atmospheres, classic modelling assuming reducing conditions.	222

Figure 207: Slag S35, reducing atmosphere, classic modelling by best classic model (ANNliq) and best advanced model (Streeter).....	223
Figure 208: Slag S35, reducing atmosphere, advanced modelling by best advanced model.....	223
Figure 209: Slag S36, oxidizing atmosphere, classic modelling by best classic model (Bomkamp) and best advanced model (Duchesne).	223
Figure 210: Slag S36, oxidizing atmosphere, advanced modelling by best advanced model.....	223
Figure 211: Slag S37, nitrogen atmosphere, classic modelling assuming oxidizing conditions.	223
Figure 212: Slag S37, nitrogen atmosphere, advanced modelling assuming oxidizing conditions.	224
Figure 213: Slag S37, nitrogen atmosphere, classic modelling assuming reducing conditions.	224
Figure 214: Slag S37, nitrogen atmosphere, advanced modelling assuming reducing conditions.	224
Figure 215: Slag S38, nitrogen atmosphere, classic modelling assuming oxidizing conditions, best model of AALE ≤ 25 Pa s (Bomkamp) and of AALE \leq Pa s (S2).	224
Figure 216: Slag S38, nitrogen atmosphere, advanced modelling assuming oxidizing conditions, best model of AALE ≤ 25 Pa s.	224
Figure 217: Slag S38, nitrogen atmosphere, advanced modelling assuming oxidizing conditions, best model of AALE ≤ 100 Pa s.	225
Figure 218: Slag S38, nitrogen atmosphere, classic modelling assuming reducing conditions, selected model is best for further advanced modelling.	225
Figure 219: Slag S38, nitrogen atmosphere, advanced modelling assuming reducing conditions, selected model is best for advanced.	225
Figure 220: Slag S39, reducing atmosphere, classic modelling.	225
Figure 221: Slag S39, reducing atmosphere, advanced modelling.....	225
Figure 222: Slag S40, oxidizing atmosphere, classic modelling.	226
Figure 223: Slag S40, oxidizing atmosphere, advanced modelling.	226
Figure 224: Slag S41, reducing atmosphere, classic modelling.	226
Figure 225: Slag S41, reducing atmosphere, advanced modelling.....	226
Figure 226: Slag S42, oxidizing atmosphere, classic modelling.	226
Figure 227: Slag S42, oxidizing atmosphere, advanced modelling.	227

Symbols and Abbreviations

Roman Symbols

Symbol	Description	Unit
\bar{T}_{norm}	Duchesne model: linearized temperature	K
\bar{V}_{slag}	molar volume of slag	m ³ /mol
\bar{X}_i	Duchesne model: normalized molar components of $i=\text{SiO}_2, \text{Al}_2\text{O}_3, \text{Fe}_2\text{O}_3, \text{CaO}, \text{MgO}, \text{Na}_2\text{O}, \text{K}_2\text{O}, \text{MnO}$	-
$\bar{\bar{X}}_i$	Duchesne model: linearized individual slag component	-
A_2O_3	Urbain model: is mole fraction of amphoteric	-
B_i	Urbain model: numerical value, $i=0-3$	-
E^*	Shaw model: activation energy	kcal/mol
E_A	activation energy of flow	kJ/mol
E_η	VFT model: activation energy to start viscous flow	J/mol
F	field strength	1/m; 1/10 ⁻¹⁰ m
F', F'', F'''	Streeter model: factors depending on silica content	-
G_C	free enthalpy of crystal	J/mol
G_S	free enthalpy of slag	J/mol
$Input_{note}(j)$	Duchesne model: Input data to hidden layer nodes	-
M_{slag}	molar mass of slag	kg/mol
$Output_{note}(j)$	Duchesne model: Calculated data from hidden layer	-
R_C	inner radius of crucible	m
R_G	universal gas constant, 8.314·10 ⁻³	kJ/mol K
R_S	radius of bob immersed into slag	m
T_0	VFT model: additional constant	K
T_{DTA}	temperature of a property obtained by DTA measurement	K
T_S	BBHLW model: temperature shift of constant viscosity	K
T_{calc}	calculated temperature of a property	K
T_{norm}	Duchesne model: normalized temperature	K
\bar{V}	molar volume	m ³ /mol
$V_{mineral}$	volume of mineral species	kg/m ³
V_{slag}	volume of slag	kg/m ³
V_{solid}	volume of solid(s)	kg/m ³
X_i	mole fraction of component i	-
X_{norm}	Duchesne model: normalize molar slag composition	-
c_1	Arrhenius relation: first material constant	Pa s
c_2	Arrhenius relation: second material constant	K
c_T	Shaw model: first coordinate of point of intersection	1/T
c_η	Shaw model: second coordinate of point of intersection	Pa s
s_i^0	Shaw model: component-depending factor	-
$w_H(i, j)$	Duchesne model: signal weights i going to node j	-

x_i	mass fraction of component i	-
$\pm\Delta T$	deviation of measured temperature	K
Δ	Streeter model: additional term of final viscosity equation	Pa s
h	distance	m
k	Boltzmann constant, $1.381 \cdot 10^{-23}$	J/K
ΔG	Gibbs energy of crystallization	J/mol
ΔT	temperature difference	K
A	area	m ²
A	VFT, Lakatos, Urbain, Kalmanovitch-Frank: constant	Pa s
A	BBHLW model: weighted molar ratio	-
a	distance of metal ions to oxygen ions	m;
B	models of VFT, Lakatos, Urbain: constant	Pa s/K
F	force	N
M	molar mass	kg/kmol
MO	Urbain model: mole fraction of network modifiers	-
N	number of data points	-
<i>Output</i>	Duchesne model: normalized viscosity output	Pa s
S	BCURA (S ²) model: silica ratio	-
T	temperature	K
V	volume	m ³
a	Einstein-Roscoe equation: a-factor	-
b	Streeter model linear factor	-
c	Watt-Fereday model: constant	Pa s
<i>equiv. Fe₂O₃</i>	equivalent iron oxide, all Fe is Fe ³⁺	-
f	solid volume fraction (SVF)	-
m	mass	kg
m	Watt-Fereday model: constant	Pa s/°C
m	Streeter model: factor depending on silica content	-
n	number of moles, n-factor of Einstein-Roscoe equation	-
n	revolutions per minute	1/min
s	Shaw model: characteristic slope of slag mixture	Pa s T
t	Watt-Fereday model: temperature	°C
v	velocity	m/s
Z		

Greek Symbols

Symbol	Description	Unit
$\dot{\gamma}_S$	shear rate of non-standard viscometer system	1/s
$\dot{\gamma}$	shear rate	1/s
ε_0	Weymann model: height of potential barrier between equilibrium positions	-
$\bar{\eta}$	Shaw model: viscosity of metal oxide mixture	Pa s
η_0	viscosity of pure liquid, suspending liquid	Pa s
η_0	Shaw model: hypothetical viscosity	Pa s
η_i	Shaw model: viscosity of component i	Pa s
η_m	measured viscosity	Pa s
η_{mix}	viscosity of liquid-solid suspension	Pa s
η_p	predicted viscosity	Pa s
η_r	relative viscosity	-
ρ_0	density of pure substance	kg/m ³
Δ	Streeter model: additional term of final viscosity equation	Pa s
α	Urbain model: fraction of network modifiers and amphoteric	-
α	Kalmanovitch-Frank model: factor to describe composition	-
η	dynamic viscosity	Pa s
$\dot{\gamma}_S$	shear rate of non-standard viscometer system	1/s
$\eta(T)$	viscosity is function of temperature T	Pa s
π	Pi	-
ρ	density	kg/m ³
τ	shear stress	Pa
κ	Weymann model: transition probability	-

Abbreviations

Abbreviation	Explanation
AAE	average absolute error
AALe	average absolute logarithmic error
AARE	average absolute relative error
AE	absolute error
ALe	absolute logarithmic error
ANN	ANNliq viscosity model
ARE	absolute relative error
BBHLW	Viscosity model of Browning, Bryant, Hurst, Lucas and Wall
Bom	Bomkamp viscosity model
CCP	cubic close packing
Duc	Duchesne viscosity model
F.I.O.	For information only
FS	FactSage TM
HCP	hexagonal close packing
HT	High temperature
KF	Kalmanovitch-Frank viscosity model
Lak	Lakatos viscosity model
LRO	long range order
n.d.	not determined
RCP	random close packing
RDFs	radial distribution function
Ref.	reference
Rib	Riboud viscosity model
S2	BCURA (S ²) viscosity model
Sha	Shaw viscosity model
SRO	short range order
Str	Streeter viscosity model
SVDB	slag viscosity data base
SVF	solid volume fraction
SVP	slag viscosity predictor
Urb	Urbain viscosity model
WF	Watt-Fereday viscosity model
XRD	X-ray diffraction
XRF	X-ray florescence

1. Introduction and Aim

The purpose of this work is to characterize the flow behavior of molten mineral matter occurring in gasification processes. The exact knowledge of slag flow behavior is necessary to ensure a safe, reliable and efficient gasification process with liquid slag outlet, e.g. entrained flow gasification and the British Gas-Lurgi process. Dynamic viscosity is considered the most important property to describe the flow behavior.

Numerous viscosity models are available to predict the slag dynamic viscosity. These models are mainly empirical within narrow ranges in composition and temperatures of slags. A Newtonian flow behavior is usually assumed. Slag in technical processes can deviate from these narrow development ranges. Moreover, partial crystallization can occur, causing non-Newtonian flow behavior. Under these circumstances, classic viscosity models fail to accurately predict slag viscosity.

Comprehensive viscosity measurements were carried out. Additionally, a selection of slags was investigated by quenching experiments, XRD phase analysis and DTA measurements. From these results, an estimation of the cooling behavior was established. The Einstein-Roscoe-equation was modified to include the found results. Finally, a viscosity modelling approach is given to improve the prediction performance of classical viscosity models.

2. General Overview of Slag

The following sections give a short introduction on slag, the parameters describing it and the flow behavior. Also, slag components and their influence on melt behavior will be discussed. Information was mainly taken from glass technology references due to the similarities between slag and glass melts.

2.1 Viscosity

Viscosity is the measurement of the resistance of a fluid towards a motion. Also, it is the tendency of a fluid to dissipate energy due to internal fluid friction [1,2]. First mathematical descriptions of viscosity were done by Newton at the end of the 17th century [3]. A short introduction is given below.

2.1.1 Viscosity Introduction

Fundamental rheological parameters are described by the Two-Plates-Model, Figure 1. The upper plate with the area A is set in motion by the force F and the velocity v results. The lower fixed plate is stationary, $v=0$. Between these plates, there is the distance h , and a fluid is sheared in this shear gap. Two important shear conditions have to be fulfilled:

1. Adhesion of samples without any wall-slip effect to both sides.
2. Laminar flow conditions and no turbulence.

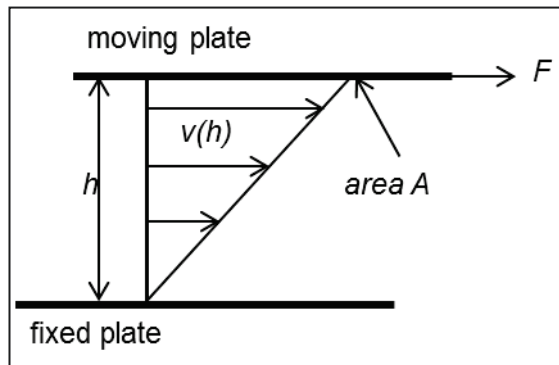


Figure 1: Two-Plates-Model

Dynamic (or shear) viscosity η is given by Eq. (1), where shear stress τ is in Pa and shear rate $\dot{\gamma}$ is in 1/s (reciprocal seconds), Eq. (2) and (3). The unit of dynamic viscosity η is Pa s. A fluid between two parallel plates of $A=1 \text{ m}^2$ at a distance $h=1 \text{ m}$, that requires a moving force of $F=1 \text{ N}$ to achieve a relative velocity of $v=1 \text{ m/s}$, has a dynamic viscosity of 1 Pa s .

$$\eta = \frac{\tau}{\dot{\gamma}} \quad (1)$$

$$\tau = \frac{F}{A} \quad (2)$$

$$\dot{\gamma} = \frac{v}{h} \quad (3)$$

To improve reading quality, the single word viscosity stands for dynamic (shear) viscosity in this work. Viscosity data of several materials are given in Table 1 for instance [4].

Table 1: Viscosity of selected fluids [4].

Material	Viscosity in Pa s
Gases / air at 20 °C	$10 \cdot 10^{-6}$ to $20 \cdot 10^{-6}$ / $18 \cdot 10^{-6}$
Water at 20 / 90 °C	$1 \cdot 10^{-3}$ / $0.315 \cdot 10^{-3}$
Mercury	$1.55 \cdot 10^{-3}$
Wine, fruit juices	$2 \cdot 10^{-3}$ to $5 \cdot 10^{-3}$
Milk	$2 \cdot 10^{-3}$ to $10 \cdot 10^{-3}$
Olive oils	0.1
Glycerine	1.48
Honey, syrups	10
Bitumen at 80 / 60 / 40 / 20 / 0 °C	200 / $1 \cdot 10^3$ / $20 \cdot 10^3$ / $500 \cdot 10^3$ / $1 \cdot 10^6$

2.1.2 Flow behavior of fluids

Figure 2 a) and b) give an overview on change in flow and viscosity when the shear rate varies.

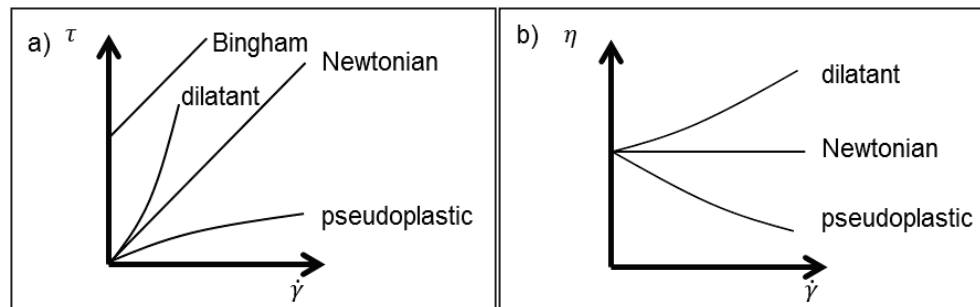


Figure 2: Shear rate depending a) flow curves and b) viscosity curves.

An ideal viscous or Newtonian fluid is characterized by a constant slope within the τ - $\dot{\gamma}$ -plot, which means a constant curve with zero slope in the η - $\dot{\gamma}$ -plot. Few substances are Newtonian within standard applications and measurement ranges, e.g. water, gasses, silicone oils [4].

Bingham-fluids need a certain amount of force before viscous flow starts. This is indicated by a shear stress $\tau > 0$ in the flow curve plot. The force necessary to start flow defines the yield point. Their flow behavior can also be Newtonian, dilatant and pseudoplastic.

Pseudoplastic (shear-thinning) fluids show a decreasing slope within the τ - $\dot{\gamma}$ -plot and viscosity is decreasing. Examples of fluids having a shear-thinning behavior are polymer solutions, most coatings, glues, shampoos, emulsions and suspensions with needle-

shaped particles. The shear-thinning behavior of suspensions is explained by the micro structure of these materials. In resting state, particles are suspended randomly. When a force (shear) is given to the fluid, the particles start to orientate in shear direction. This effect of orientation increases with increasing shear rate. In result, viscosity decreases, Figure 3. Suspensions with agglomerated particles also show a shear-thinning behavior when the shear forces disintegrate agglomerates. Then, the dispersion liquid is no longer bound and free to flow.

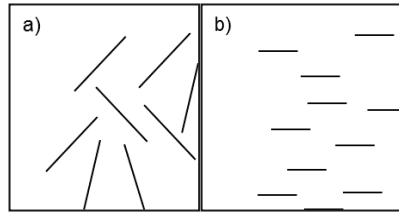


Figure 3: Different particles in a) orientation in resting state and b) oriented under shear.

Dilatant (shear-thickening) flow behavior is indicated by an increasing curve slope within the τ - $\dot{\gamma}$ -plot. Accordingly, viscosity is increasing with increasing shear rate. Examples of shear-thickening fluids are dispersions with a high concentration of solid matter, ceramic suspensions, starch dispersions, paper coatings, polymers and natural rubber [4]. Reasons of shear-thickening behavior of fluids are listed:

- Particles exist in oriented layers at low shear rates while at high shear rates the repulsive forces between particles lead to an increase in chaotic, viscosity increasing, structures [5].
- Particles agglomerate under shear due to the development of short range hydrodynamic lubrication forces overcoming repulsive forces between particles [5].
- Long, branched molecules as found in polymers start to entangle under shear stress, Figure 4.
- Particles start to rotate or interact stronger, resulting an increasing flow [4].

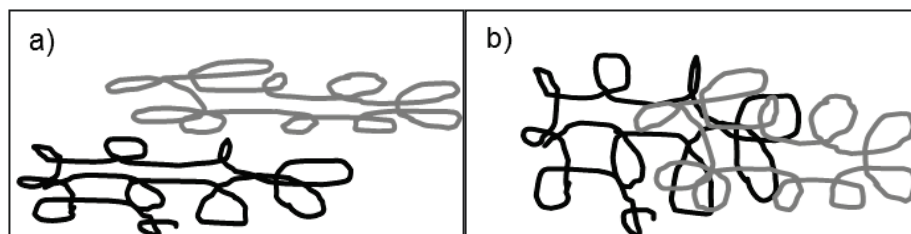


Figure 4: Particles are a) orientated in rest and b) entangled under shear.

2.2 Slag Definition and Phase Diagrams

Slags are the remains of minerals (metal oxides, sulfates, carbonates etc.) generated at high temperature processes as byproduct, e.g. fuel ashes in gasification, or as main product, e.g. the melt in glass production. Within this work, melts are multi-component

oxide systems and they will exhibit a specific cooling behavior. A selection of possible phase conditions during cooling is given on the basis of a binary system, Figure 5.

1. Slag is completely molten at T_{start} above liquidus temperature T_{liq}
2. Cooling below T_{liq} introduces crystallization if several points are met, e.g. an adequate cooling rate and a crystal nucleus. A mixture of solid mineral (B_{sol}) and liquid slag (X_{liq}) is formed. The composition of the remaining liquid slag X_{liq} changes when the growing mineral consumes slag compounds. Under ideal conditions, the composition of slag will change following the liquidus line.
3. Further cooling causes solidification at the eutectic point, $X_{\text{liq}}=0$. In special cases, when a eutectic slag composition is available, the transition between liquid and solid state without the formation of a solid-liquid mixture is observable.

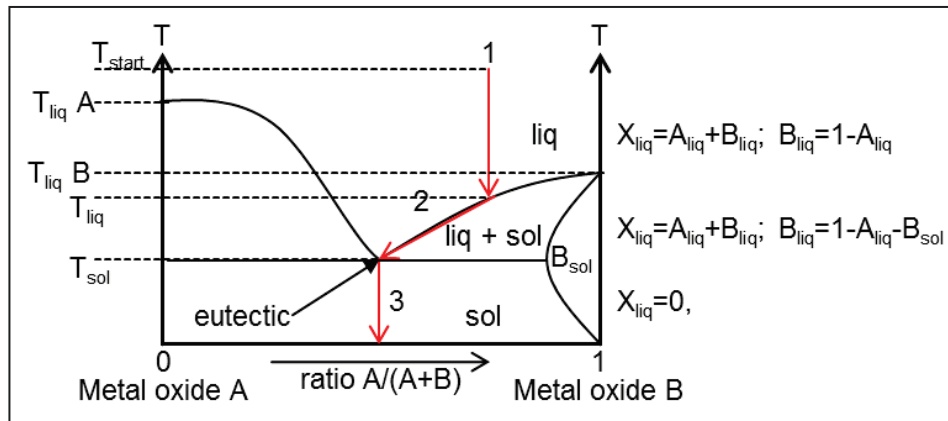


Figure 5: Schematic of a eutectic binary phase diagram of two metal oxides [6].

Industrial processes often show non-ideal behavior. The above described ideal behavior can significantly differ with changing process parameters such as cooling rate, starting temperature or available initial nucleus. The slag can solidify as a glass without any formation of minerals, or as a glass-mineral mixture, as a single mineral, or a mixture of minerals. An introduction to the crystallization behavior of slags is given in chapter 5.1.

2.3 Solid Slag Structure

The structure of solidified slags is connected to structures of glasses. Several structural models were developed in the last decades especially for silicates. An overview of solid slag structure and structure models is given to understand the structure of a molten slag.

Tammann defined glasses as highly undercooled or supercooled liquids. Later investigations on glasses with X-ray diffraction confirmed this assumption [7–10]. Goldschmidt developed first empirical rules for glass-formation. There, glass formation depends on the size ratios of ions. A radius ratio between cation and anion, $r_{\text{cation}}:r_{\text{anion}}$, of 0.2 to 0.4 seems to be necessary to form a glass [11].

Postulated in 1932 by Zachariasen and experimentally confirmed in 1933 by Warren, the glass network theorem was developed [12,13]. Other names are glass network hypothesis or continuous random network model. There, the $[\text{SiO}_4]$ -tetrahedron is a vital structural unit.

The basic element for a wide range of structure models is the $[\text{SiO}_4^{4-}]$ -tetrahedron or silicate tetrahedron for silicate melts. A silicon atom within the center is surrounded by four oxygen atoms, Figure 6. The characteristic shape of the tetrahedron is based on the electron configuration of silicon within the combination of oxygen atoms. A detailed description based on quantum mechanics and orbital theory is given in [10]. In appearance of oxygen, the SiO_4 -tetrahedron can occur in several forms, Figure 7. Investigations on the electron density distribution within quartz indicated the occurrence of mixed bonds [14].

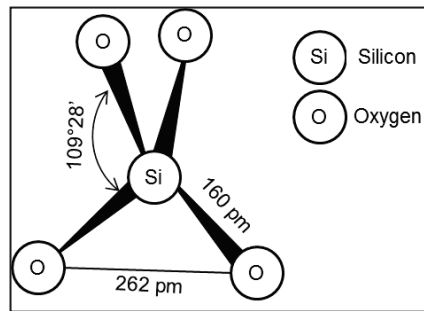


Figure 6: SiO_4 -Tetrahedron with bond angle and bond length [10].

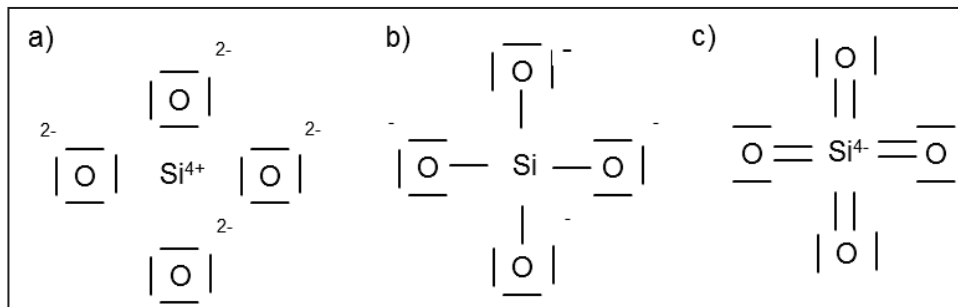
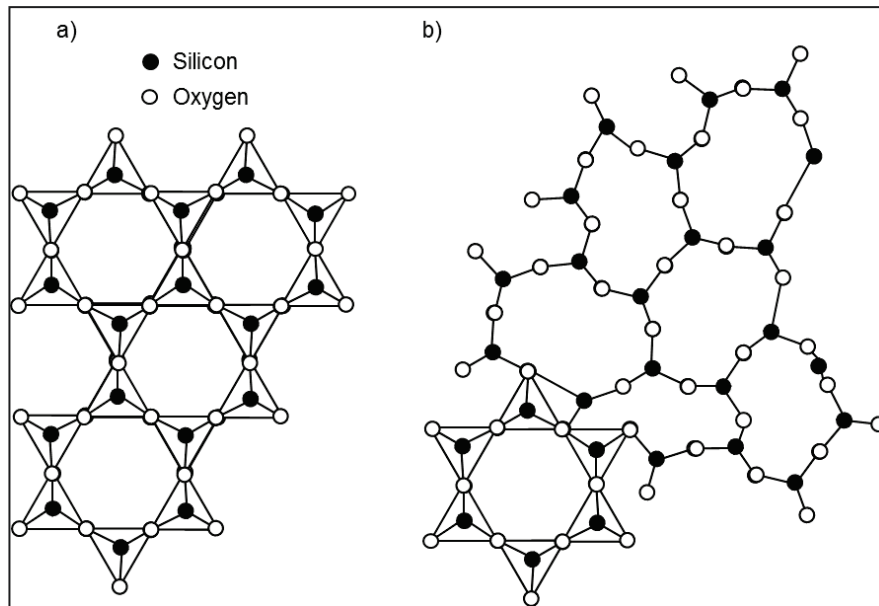


Figure 7: Bonds within the SiO_4 complex a) polar, b) covalent, c) double bond [10].

Contrary to the regular symmetrical appearance of tetrahedra within a crystal, the tetrahedra within a glass are occurring in an irregular way, Figure 8. During cooling, the network of tetrahedra is formed by polymerization. The established regular structure is named crystalline or crystal while the irregular structure is defined as amorphous, glassy, random network or glass. The length scale between structure units of the same orientation within a crystal is long and therefore it is named “long range order” (LRO). In contrast to a crystal, the distance between structure units of the same orientation is short within a glass. This is defined as “short range order” (SRO).



The fourth oxygen of $[\text{SiO}_4]$ -tetrahedra is above or below the plane of projection.
Figure 8: $[\text{SiO}_4]$ -tetrahedron connections a) in solid quartz and b) in molten quartz [12,13].

Atomic force microscope images of a silica glass obtained under an ultra-high-vacuum are giving evidence of the discussed structures, Figure 9. Several features can be seen: interatomic distances, groupings of atoms and network holes (dark areas). Possible O–O bonds are depicted by solid lines, A and C. Si–O bonds are indicated by dashed lines, B. The right-hand bar indicates the high of structures [15].

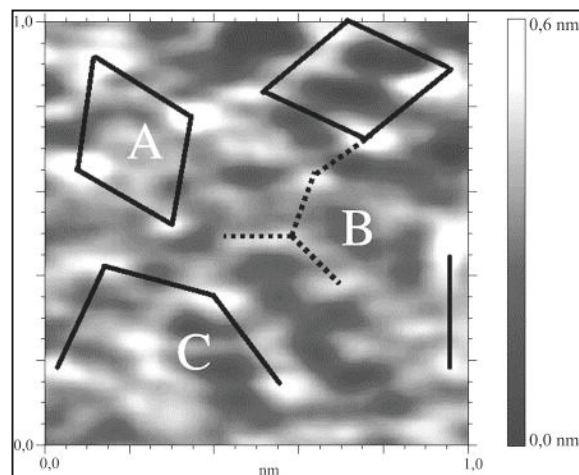


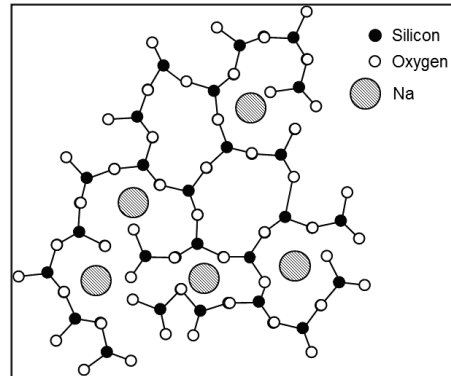
Figure 9: Atomic force microscope images of a silica glass [15].

Zachariasen formulated the rules for glass formation which are as follows.

In a glass forming oxide of the formula A_mO_n ,

1. One oxygen atom may be linked to no more than two A atoms.
2. The number of oxygen atoms surrounding A atoms must be small.
3. The oxygen polyhedral share only corners with each other, neither edges nor faces.
4. At least three corners in each polyhedron must be shared.

The formed crystalline or glassy structures can be opened by introducing other large cations in form of metal oxides. The added oxygen occupies the vacant corner of the opened tetrahedron while the large cation enters the hole, thus modifying and weakening the network, Figure 10. A statistical, random and uniform distribution is assumed.



The fourth oxygen is above or below plane of projection.

Figure 10: Weakened glass structure by introduction of Na_2O as network modifier [12,13].

Zachariasen defined three groups of cations that are affecting the structure and therefore the properties of glasses. This categorization is fundamental for further work on slags. Due to the importance in glass science, geological physics, metallurgy etc., there is an enormous amount of investigations on the three categories. These three categories are:

1. network formers, which building up glassy or crystalline networks and tetrahedra,
2. network modifiers or conditional glass formers or intermediates, which are breaking up the oxygen bridges between tetrahedra to facilitate the integration of metal ions and
3. amphoteric, which show a forming or a modifying behavior depending on the glass composition [10,16]

In this work, the nomenclature will be network formers, modifiers and amphoteric. A selection of components related to slags is given in Table 2. The work of [17] indicated the coordination number as “known or assumed”. Boron occurs twice in the network former category. It takes an oxygen coordination number of 3 in pure B_2O_3 glass, while it takes the coordination number 4 in borate glasses as mixture with silica. Aluminum in Al_2O_3 crystal is reported with a coordination number of 6. In certain combinations, such as $\text{CaO}_{12}(\text{Al}_2\text{O}_3)_7$, the coordination number is 4. Network formers mostly show a coordination number of 3 or 4, while network modifiers have an oxygen coordination number of 6 or more. Amphoteric are ranging from 4 to 6.

Dietzel [18] introduced the field strength F as an attribute to classify into network formers, network modifiers and amphoteric. The field strength is defined as ratio of metal ion valency Z and the cubic distance to the oxygen ion a^2 calculated in Å, Eq. (4).

$$F = \frac{Z}{a^2} \quad (4)$$

Network formers are in the range $1.4 < Z/a^2 < 2.0$. Network modifiers and amphoteric are reported in the range $0.1 < Z/a^2 < 0.4$ and $0.5 < Z/a^2 < 1.0$, respectively. Amphoteric have values between network formers and network modifiers. Within a multicomponent glass or slag, amphoteric can strengthen the tetrahedra network, coordination number is 4, or brighten it, coordination number 6 to 8. Aluminum Al is defined as network former and as amphoteric. Also, lead Pb and magnesium Mg are reported as network modifiers or amphoteric.

Table 2: Selected network formers, network modifiers and amphoteric [10] [17].

M in MO _x	Valence	Oxygen Coordination No.	Z/a^2	Ref.
Network former				
B	3	3	1.34	[11,17,18]
B	3	4		[11,17]
Si	4	4	1.57	[11,17,18]
Al	3	4		[17]
P	5	4	2.1	[11,17,18]
V	5	4		[17]
Network modifier				
Pb	4	6	0.27	[17]
Pb	2	4		[17]
Pb	2	8		[18]
Mg	2	6	0.33	[17]
Ca	2	8		[17,18]
Na	1	6		[17,18]
K	1	9	0.13	[17]
K	1	8		[18]

Continuation of Table 2

M in MO _x	Valence	Oxygen Coordination No. Amphoteric	Z/a^2	Ref.
Ti	4	6	1.04	[17,18]
Pb	2	2		[17]
Al	3	6	0.84	[17,18]
Al	3	4	0.96	[18]
Mg	2	6	0.45	[18]
Mg	2	4	0.53	[18]
Fe	3	6	0.76	[18]
Fe	3	4	0.85	[18]

Also, other structure theories were additionally developed. The crystallite theory was firstly mentioned by Lebedew in 1921 and later, 1930 and 1936, supported by X-ray analysis. There, a statistical distribution of metal ions (network modifiers) within the glass is supposed, while an upper order of cation arrangements is assumed by the crystallite theory. The structure of glass is considered as a batch of microcrystals [19–21].

Bernal and co-workers developed the random close packing model, RCP, to explain the glass structure of compounds with less or no covalent directional bonds [22,22]. Non-directional bonding appears within ionic, metallic or van-der-Waals substances.

Additional structure conceptions are referenced elsewhere [23–25,25–32].

2.4 Liquid Slag Structure

Silicate melts show an ionic behavior [33]. As pointed out in chapter 2.2, silicate melts are built up of SiO₄⁴⁻ tetrahedra which joined to form chains or rings by bridging or bonding oxygen (BO). Several cations tend to break these structures, such as Na⁺, Ca²⁺, Mg²⁺, Fe²⁺. These are network modifiers. Non-bridging oxygen (NBO) is formed with ions of O⁻ and free O²⁻, Figure 11.

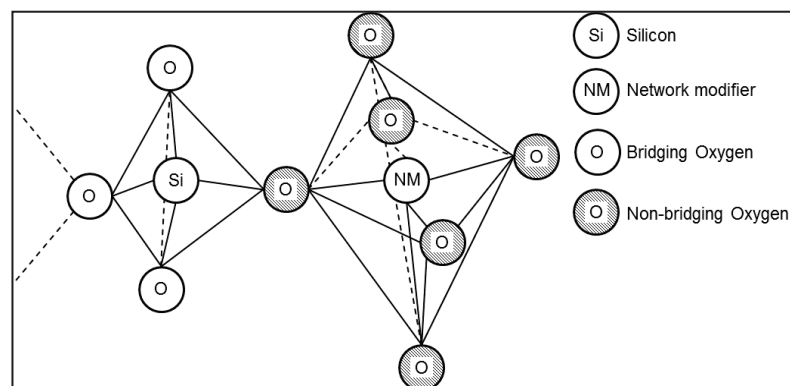


Figure 11: Schematic representation of tetrahedra formed by Si, O and a network modifier [34].

The silicate melts containing various 3-dimensionally, interconnected anion units such as SiO_2 , $\text{Si}_2\text{O}_5^{2-}$, $\text{Si}_2\text{O}_6^{4-}$, $\text{Si}_2\text{O}_7^{2-}$, SiO_4^{4-} which coexists in the melt. Other cations such as Ti^{4+} , P^{5+} , Al^{3+} and Fe^{3+} also form tetrahedra and can be incorporated into the silica network as TiO_4^{4-} , PO_3^{3-} , AlO_4^{5-} and FeO_4^{5-} anion units. Electrical charge-balance has to be established by cations like Ca^{2+} or Na^+ to form fourfold negative tetrahedra. In case of AlO_4^{5-} anion unit, the result will be NaAlO_4^{4-} or $\text{AlO}_4^{4-}\text{-Ca-AlO}_4^{4-}$ [34].

The rapid increase of viscosity during the cooling depends on the formation of disordered, infinite networks. Small ionic units with low coordination numbers, such as the $[\text{SiO}_4]$ -tetrahedron (coordination number of 4) or the $[\text{BO}_3]$ -triangle (coordination number of 3), start polymerization [10].

2.5 Basicity and B/A-ratio

The ratio between network modifying and network forming ions is one of the most utilized and discussed numbers to describe the properties of slags and glass melts. There are 12 references within the slag Atlas [34] and three references within the reviewing work of Vargas et al. [35] cited for different equations of the B/A-ratio.

As introduced, the concentration or activity of oxygen ions is essential for the structure and polymerization of slags. A view to aqueous solutions facilitates comparisons. There, the concentration of H^+ -ions is the measure for acidity and represented by the pH-value. A similar measure can be applied for oxide melts where the basicity represents the amount of O^{2-} -ions. The pO-value can be measured by electrochemical techniques [36].

To sum up the behavior of melt components, the Brønsted definition for acids is modified. An acidic melt component accepts electrons while a basic melt component donates electrons [33]. Basic components are named “alkaline” in some references [37]. This nomenclature is not recommended to prevent confusion, because network modifiers are not only alkaline earths.

A selection of formulations with references to calculate the B/A-ratio is given in Eq. (5) to Eq. (12). The amount of components can be introduced as fractions on mass or mole basis, indicated by x or X , respectively.

Ref.

$$\frac{B}{A} = \frac{\text{Base}}{\text{Acid}} = \frac{\text{network modifiers}}{\text{network formers}} \quad (5)$$

$$[38,39] \quad \frac{B}{A} = \frac{x_{\text{CaO}}}{x_{\text{SiO}_2}} \quad (6)$$

$$[40] \quad \frac{B}{A} = \frac{X_{\text{MeO}}}{X_{\text{SiO}_2} + 2 \cdot X_{\text{P}_2\text{O}_5} + 1/2 \cdot X_{\text{Al}_2\text{O}_3} + 1/2 \cdot X_{\text{Fe}_2\text{O}_3}} \quad (7)$$

$$[41] \quad \frac{B}{A} = \frac{x_{\text{CaO}} + x_{\text{Fe}_2\text{O}_3} + x_{\text{FeO}} + x_{\text{K}_2\text{O}} + x_{\text{MgO}} + x_{\text{Na}_2\text{O}}}{x_{\text{Al}_2\text{O}_3} + x_{\text{SiO}_2} + x_{\text{TiO}_2}} \quad (8)$$

$$[35,42] \quad \frac{B}{A} = \frac{X_{Na2O} + X_{K2O} + X_{CaO} + X_{MgO} + X_{FeO}}{X_{SiO2} + X_{Al2O3} + X_{Fe2O3} + X_{TiO2}} \quad (9)$$

$$[43]\} \quad \frac{B}{A} = \frac{X_{Na2O} + X_{K2O} + X_{CaO} + X_{MgO} + X_{Fe2O3}}{X_{SiO2} + X_{Al2O3} + X_{TiO2}} \quad (10)$$

$$[37] \quad \frac{B}{A} = \frac{CaO + MgO + Fe_2O_3 + Na_2O + K_2O}{SiO_2 + Al_2O_3 + TiO_2} \quad (11)^*$$

*The authors do not indicate “mass” or “molar” within the given equation.

$$\text{This work} \quad \frac{B}{A} = \frac{x_{CaO} + x_{Fe2O3} + x_{FeO} + x_{K2O} + x_{MgO} + x_{Na2O}}{x_{Al2O3} + x_{SiO2} + x_{TiO2} + x_{P2O5}} \quad (12)$$

The definition of amphoteric as basic or acidic component has to be carefully chosen. Amphoteric behaves as network former or as network modifier depending on the glass composition. Al_2O_3 in binary mixture with SiO_2 or in high amounts within a multicomponent-system is reported to be a network modifier while in a ternary or higher system it is referenced as network former together with SiO_2 . A similar behavior is known about Fe^{3+} in (IV) coordination as network former and in (VI) coordination as network modifier. The coordination number depends on charge balancing provided by bulk composition [33]. Chapter 2.6 is discussing the influence of slag components in detail.

The T-B/A-relationship for a viscosity of 25 Pa s is given in Figure 12. Above this viscosity value slag becomes difficult to remove from an entrained gasifier [44]. The B/A-ratio was calculated by Eq. (11). A critical review cannot be given due to the absence of additional data like detailed composition or the atmospheric conditions during the measurements. A ratio of $B/A < 0.5$ indicates an increase of temperature to receive $\eta = 25$ Pa s. The intermediate range $0.5 < B/A < 1.5$ requires lowest temperatures while an increase of temperature is reported for $B/A > 1.5$ to achieve 25 Pa s. As pointed out in the beginning of the chapter, a high B/A-ratio includes an excess supply of basic, network breaking and changing compounds. The silica tetrahedra are disconnected, the viscosity decreases. On the other side, for low B/A-ratios and high amounts of acidic, network forming compounds, the viscosity will increase due to the formation of interconnections.

Similar observations were done by own measurements within a series of artificial and natural slag systems, Figure 13. All measurements were carried out under air with a shear rate of $\dot{\gamma} = 25$ 1/s in the Bähr-HT-Viscometer. The B/A-ratio was not increased by a certain method. Instead, the slags were sorted by their composition-dependent B/A, chapter 7.1. An introduction to own viscosity measurements is given in chapter 6.1.

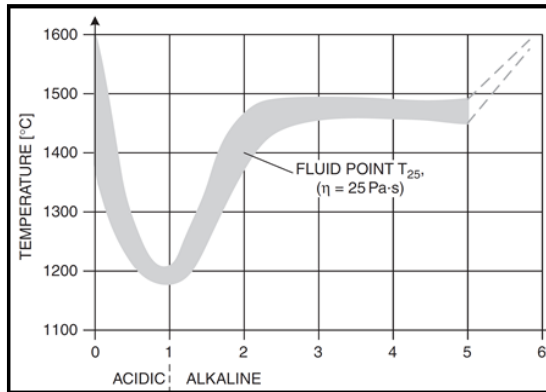


Figure 12: T-B/A-relationship of viscosities of 25 Pa s [37].

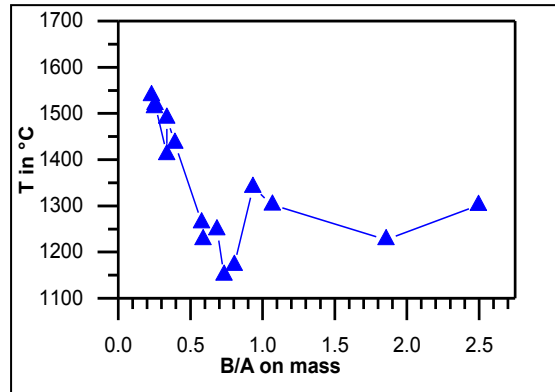


Figure 13: T-B/A-relationship of viscosities of 25 Pa s (own measurements).

2.6 Slag Components

Ashes, geological melts, glasses etc. are consisting of metal oxides in a wide variation of component quantity and mass ranges [16,37,45,46]. As pointed out in chapter 2.3, components are influencing the structure and therefore the properties of slags. A summary and short overview of metal oxides is given in the following sections.

2.6.1 Silicon dioxide

Silicon dioxide, also named silicon oxide, SiO_2 , or just silicate plays the most important role in slag viscosity prediction. As major constituent of natural coal ash slags and glasses, its participation is well investigated. Numerous viscosity models are depending on silicate, chapter 4.1.

The chemical and structural behavior of SiO_2 was introduced in detailed by chapters 2.3 and 2.4. As network former, it is increasing viscosity with increasing amount in a slag system. Some slag systems are poor in silicate, i.e. ashes of Rhenish lignite.

2.6.2 Aluminum oxide

Aluminum oxide or alumina are synonyms of Al_2O_3 . Known as an amphoteric, it is mainly used as network former within a multicomponent slag system. Depending on mass fraction, high concentrations of Al^{3+} are reported to modify a network and lower the viscosity. The formation of a five- or sixfold coordination is assumed.

Low concentrations of Al^{3+} are defined as network former, viscosity is increasing. Al^{3+} forms a fourfold coordination in addition with silicon Si^{4+} . The charge difference between Al^{3+} and Si^{4+} has to be balanced by an additional network modifier such as Na^+ or K^+ to form the NaAl^{4+} ion. A higher charged network modifying cation has to be sited between two Al^{3+} ions.

The distribution of Al-O-Al, Al-O-Si and Si-O-Si bonds within a melt depends on the field strength of added network modifiers. Low-field strength cations (low Z/a^2), such as

K^+ , tend to form Al-O-Si bonds whereas high-field strength cations (high Z/a^2) from network modifiers series, such as Mg^{2+} or Ca^{2+} , prefer to form another type of bonds [47].

Phase separation, the formation of two immiscible liquid slag phases, has to be taken into account for slag investigations. Al-rich and Si-rich liquid phases were found for binary SiO_2 - Al_2O_3 -systems [48]. A significant influence on viscosity properties cannot be excluded.

Al_2O_3 has not the same polymerization effect than Fe_2O_3 when a pure SiO_2 -CaO-melt was doped with 5 and 10 wt.-% [49].

Viscosity maxima were found for melts with Al/M molar ratios ($X_{Al_2O_3}/(X_{M_2O}+X_{MO})$) around Al/M=1. All Al^{3+} -ions are in tetrahedral coordination, i.e. the slag structure is best connected [50,51].

Binary silicate melts exhibit a network modifying behavior of Al_2O_3 , Figure 14. With increasing alumina content, the viscosity decreases. Doubling the alumina content is decreasing the viscosity by 15 times, A/S=1.70. A continuing addition of alumina is still causing a viscosity decrease, but not in the former magnitude effect, A/S=3.96. Viscosity data was obtained by rotational technique [52].

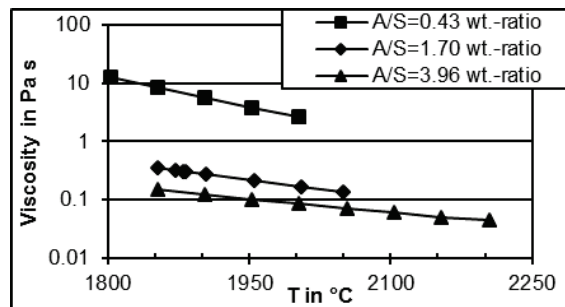


Figure 14: Viscosity decreasing effect of alumina addition to silica, wt.-ratios [52].

More complex ternary melts are influenced by two parameters, Al_2O_3 ratio and temperature. High temperatures are indicating a depolymerized network. When the network is also attacked by network modifiers, i.e. calcia CaO, alumina acts as network former. Viscosity increases by increasing alumina content, Figure 15 a) at C/S=1. There, the amount of network modifying CaO is reduced, the network forming power of alumina is less, see Figure 15 a) at C/S=0.4. A significant decrease in viscosity was reported for C/S=0.14 and Al_2O_3 =20 wt.-%. The network modifying nature of Al_2O_3 is dominant due to the high amount of silica.

Lower temperatures inhibit the influence of alumina at high C/S wt.-ratios. The network is opened by network modifiers, but not by the temperature effect at C/S=1, Figure 15 b).

The influence of alumina is significantly changing the polymerization of the network for a higher amount of silica, lower C/S-ratio. In opposite to the elevated temperature

case, alumina is increasing viscosity, Figure 15 b) at $C/S=0.5$. Data was obtained from [53–55].

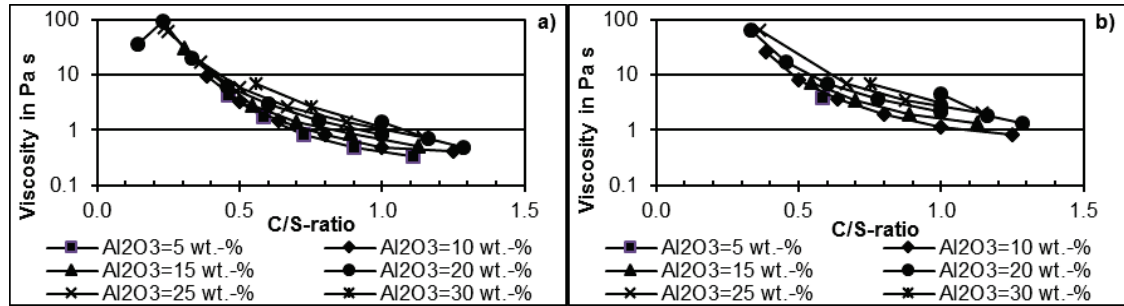


Figure 15: Influence of Al_2O_3 to SiO_2 -CaO- Al_2O_3 melts at temperatures of a) 1500 °C and b) 1400 °C.

2.6.3 Calcium oxide

Calcium oxide, CaO, calcia or in older references burnt lime, is an alkaline earth and defined as network modifier. CaO is donating oxygen and therefore opens the silicate network which lowers the viscosity. Eightfold coordination is referenced, Table 2.

A binary slag of SiO_2 -CaO was measured by Bockris 1954 within a molybdenum crucible and spindle by a rotational viscometer [56]. An increasing CaO content lowers viscosity. Significant viscosity decreases were found for C/S wt.-ratios between 0.41 and 0.72. Higher amounts of CaO were less influencing the melt viscosities, Figure 16. As long the silicate network is not too much depolymerized, the network modifying behavior is still effective.

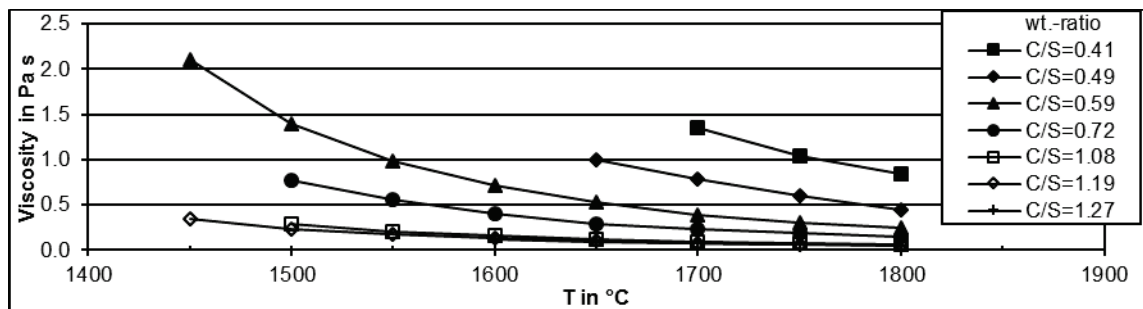


Figure 16: Viscosity vs. temperature for a binary melt of SiO_2 -CaO [56].

Higher melt systems are more complex due to the interplay of network formers and modifiers. The network breaking behavior of CaO is still present, but is less predictable. Shankar measured the viscosities of different SiO_2 - Al_2O_3 -MgO-CaO melts by a rotational viscometer, using molybdenum crucible and spindle and argon purging gas, Figure 17. In both experimental series, viscosity was significantly changed when the CaO content was raised for 9 or 6 wt.-%, respectively [57]. It is assumed, that the high amount of SiO_2 and Al_2O_3 are providing charge balance up to a given maximum of CaO content. Above this maximum, the silicate network is suddenly opened.

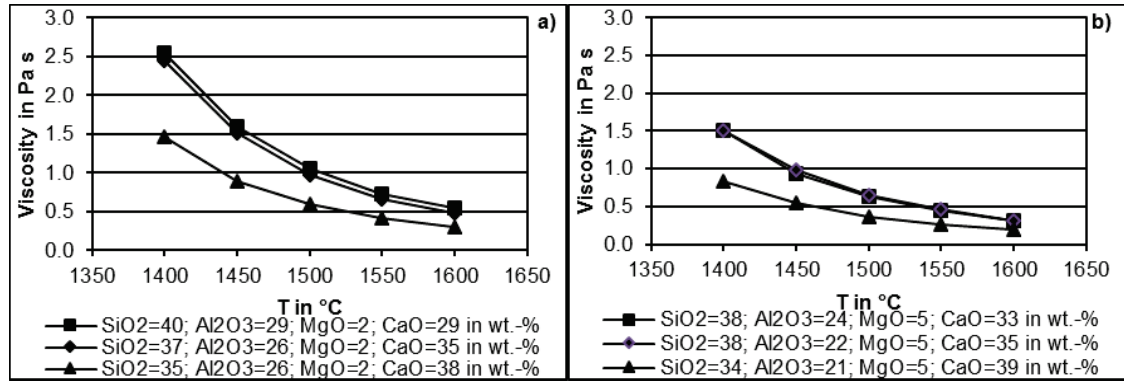


Figure 17: Viscosity vs. temperature for $\text{SiO}_2\text{-Al}_2\text{O}_3\text{-MgO-CaO}$ systems with a) $\text{MgO}=2$ wt.-% and b) $\text{MgO}=5$ wt.-% [57].

2.6.4 Iron oxide

The behavior of iron oxide in silicate melts is described to be “complicated” [33]. Iron oxide can occur as ferric or ferrous ion, Fe^{3+} and Fe^{2+} , respectively. The coordination number and therefore the integration into the silicate network can occur in three variations for slags,

- tetrahedrally for Fe^{3+} in (IV) coordination,
- non-tetrahedrally for Fe^{3+} in (VI) coordination [58]
- octahedrally for Fe^{2+}

as found by [59]. Critical discussions about other coordination numbers especially for Fe^{2+} were done [58], but will not be discussed in detail.

Furthermore, the presence of free oxygen provided by iron oxide can be described as follows, Eq. (13) to (15). In acid slags iron oxide additions decrease the viscosity more than in basic slags due to the fact, that longer chains can be more easily broken than short chains. So, the same addition of iron oxide in basic slags will result in a smaller decrease of viscosity. Additionally, threefold iron in the ferrite anion state is not able to provide oxygen to break up silicate chains in basic slags [60].



Two parameters are influencing the ratio between Fe^{3+} and Fe^{2+} . These are temperature and partial oxygen pressure. The equilibrium between Fe^{3+} and all available iron over temperature was investigated for four melts by [49], Figure 18. Preparation of the $\text{SiO}_2\text{-CaO-Fe}_2\text{O}_3$ systems was carried out under air atmosphere. The $\text{Fe}^{3+}/\sum \text{Fe}$ -ratio was calculated on data obtained by Mössbauer spectroscopy.

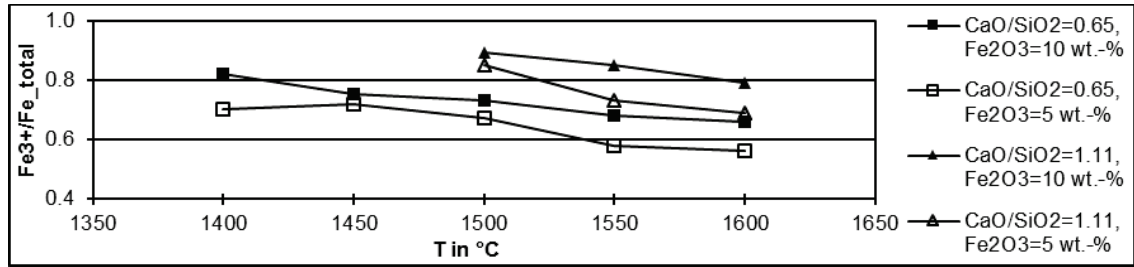


Figure 18: Fe-ratio over temperature for different SiO_2 -CaO- Fe_2O_3 melts [49].

The relationship between the partial oxygen pressure $p\text{O}_2$ and the $\text{Fe}^{3+}/\sum \text{Fe}$ -ratio is exemplary given in Figure 19. Two melts from the Na_2O - SiO_2 - Fe_2O_3 system were prepared under an atmosphere of $\text{CO}:\text{CO}_2$ gas mixture. The $\text{Fe}^{3+}/\sum \text{Fe}$ -ratio was determined by Mössbauer spectroscopy [58].

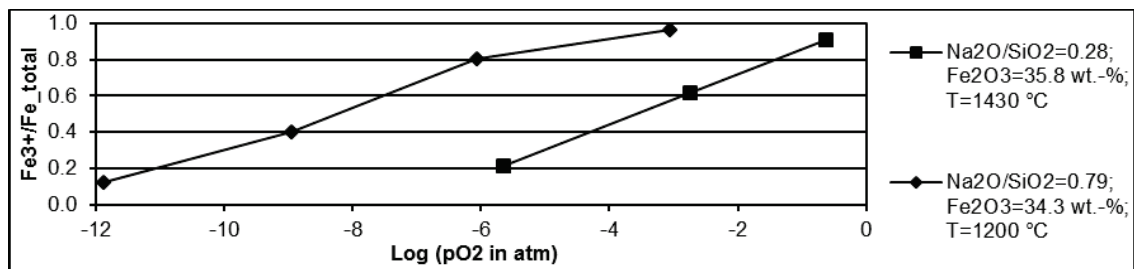


Figure 19: Fe-ratio of two Na_2O - SiO_2 - Fe_2O_3 melts as function of partial oxygen pressure [58].

No dependence between viscosity and Fe-oxidation state was found by [45] within magmatic melts. There, the Fe_2O_3 -content was less than 5 wt.-%.

In contrast, Urbain 1982 [52] found an increase of viscosity, when Fe^{2+} was oxidized to Fe^{3+} . In this case, a systematic investigation on SiO_2 -FeO up to SiO_2 -CaO-FeO- Fe_2O_3 slags was carried out. The maximum amount of FeO was almost 80 wt.-% for simple compositions and up to 20 wt.-% of FeO and 12 wt.-% for Fe_2O_3 for multicomponent slag systems.

Seki and Oeters 1984 [60] researched the system CaO-FeO- Fe_2O_3 - SiO_2 . The viscosity of slags with low iron contents was more influenced by the B/A-ratio than slags with high iron contents. As expected, the viscosity decreases with increasing B/A-ratio. For systems with a high amount of iron, the influence of the B/A-ratio was less significant. In return, an increase of Fe^{2+} was decreasing viscosity. A change in slag structure was defined introducing the molar ratio $X_{\text{Fe}_2\text{O}_3}/(X_{\text{FeO}} + X_{\text{CaO}})$. For a value of <0.5 , Fe^{3+} is supposed to exist as Fe^{3+} -cation for acidic slags and as ferrite anion in basic slags. For values of >0.5 , both free Fe^{3+} and Fe^{2+} anions existed simultaneous. The amount of FeO and Fe_2O_3 varied in the range 4 to 32 wt.-% and 7 to 54 wt.-%, respectively.

Mysen et al. 1985 [49] investigated the viscosity of slags by rotational viscometry. Structure identification was done by Mössbauer spectroscopic analysis on quenched samples. A variation of 5 and 10 wt.-% Fe_2O_3 was applied to melt systems of SiO_2 -CaO.

While the C/S-ratio from 0.65 to 1.11 increased by increasing the CaO-content, viscosity decreased as result, Figure 20.

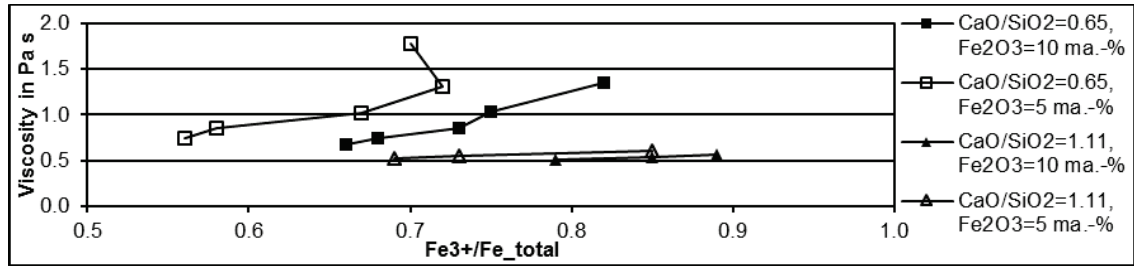


Figure 20: Viscosity dependence on Fe^{3+} -distribution [49].

The viscosity of the pure SiO_2 -CaO-mixtures was increased when Fe^{3+} was added and the network forming behavior of Fe_2O_3 was pointed out. When more tetrahedrally Fe_2O_3 was added, the viscosity decreased, Figure 21. This indicated the amphoteric behavior of Fe^{3+} for these compositional ranges.

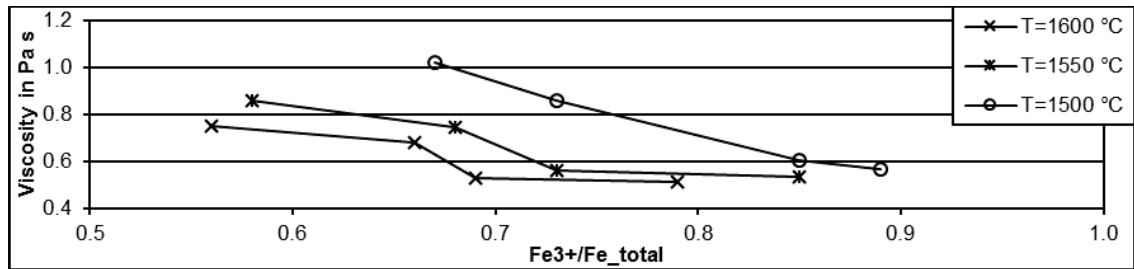


Figure 21: Viscosity as function of Fe-ratio for several temperatures [49]

Dingwell and Virgo 1987 [58] measured the viscosities of two melts in the Na_2O -FeO- Fe_2O_3 - SiO_3 system under different oxidation states achieved by CO/CO_2 gas mixtures. Quenched samples were taken to perform Mössbauer spectra analysis. Fe^{2+} was indicated as network modifier while Fe^{3+} is a network former for high partial oxygen pressures and a network modifier for low partial oxygen pressures. Fe^{3+} was also found in (VI) coordination.

The works of Hurst et al. [61–63] and Song et al. [64] were extensive and showed the complexity to adjust and indicate the $\text{Fe}^{3+}/\text{Fe}^{2+}$ -ratio. Both authors measured viscosity under low partial oxygen pressures p_{O_2} . While Hurst was applying a sacrifice crucible made from graphite, Song is using pure H_2 or CO atmospheres to avoid the formation of Fe^{3+} . A minimum partial oxygen pressure p_{O_2} of around $1 \cdot 10^{-17}$ atm was calculated by FactSage 6.4 within the applied temperature range. The formation of metallic iron was computed. No evidence of metallic Fe was reported in the cited literature.

2.6.5 Magnesium Oxide

Magnesium oxide, magnesia, or MgO , is defined as network modifier, Table 2. It is reducing slag viscosity less than CaO. MgO tends to decrease its coordination from six to four at higher temperatures. This ends in a viscosity increase around 1650-1700 °C

for binary SiO_2 -MgO melts around 45 wt.-% MgO. Below and above this temperature, the η -T-curve behaves normal [65].

MgO is expected to form MgO_4^{6-} tetrahedra or can be housed in interstices as octahedral coordination in binary melts due to the small Mg^{2+} ions [66,67]. Ternary melts are influenced in another way. MgO is stepwise changed from MgO_6^{10-} octahedra to MgO_4^{6-} tetrahedra when Al_2O_3 is added and MgO is removed from melts with 50 mole-% of SiO_2 [50]. More complex melts offered are influenced by changes in MgO content at above 1350 °C [68].

A general network modifying behavior was found by [69] and [52] for binary SiO_2 -MgO melts. Figure 22 a) indicates the decrease of viscosity for increasing MgO content. The same viscosity reducing behavior was observed by [70] for quaternary SiO_2 - Al_2O_3 -CaO-MgO melts, Figure 22 b). All data were recorded by rotational viscometry.

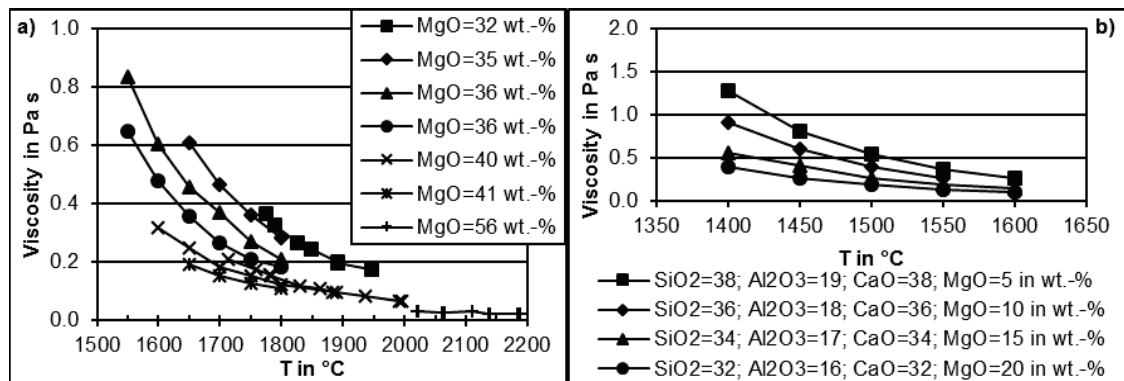


Figure 22: Viscosity influence of of MgO for a) binary SiO_2 -MgO melts and b) quaternary SiO_2 - Al_2O_3 -CaO-MgO melts [52,69,70].

2.6.6 Potassium Oxide

Potassium oxide, K_2O , is referenced as network modifier, Table 2. In general, K_2O plays a minor role in slag viscosity research. Within all examined slag samples of this work, K_2O has a maximum of 6.3 wt.-%, Table 44.

A detailed investigation on the influence of K_2O can be found for the melt system SiO_2 - K_2O , Figure 23. The content of potassium oxide was increased and viscosity decreased [69]. The influence of K_2O on viscosity is non-proportional. At 1600 °C, the increase in K_2O by a factor of around 2.5 results in a decrease of viscosity with a factor of around 4.4. Increasing K_2O by a factor of 4 leads to a decrease in viscosity around a factor of 20. A similar behavior is found over all temperature ranges.

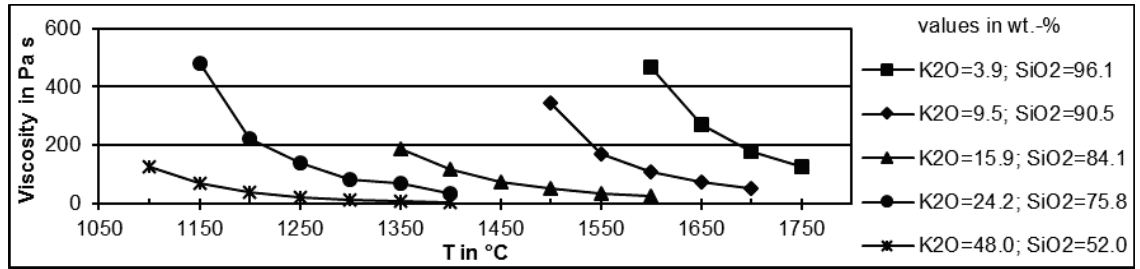


Figure 23: Viscosity decrease by increase of K_2O for binary SiO_2 - K_2O melts [69]

The network modifying behavior of K_2O can be also found for ternary systems, Figure 24. Measurements were carried out under air atmosphere. Therefore, the major part of iron oxide is in Fe^{3+} state. Network forming behavior is expected. When K_2O is increased in steps of circa 5 wt.-%, viscosity decreases within steps of one magnitude [71].

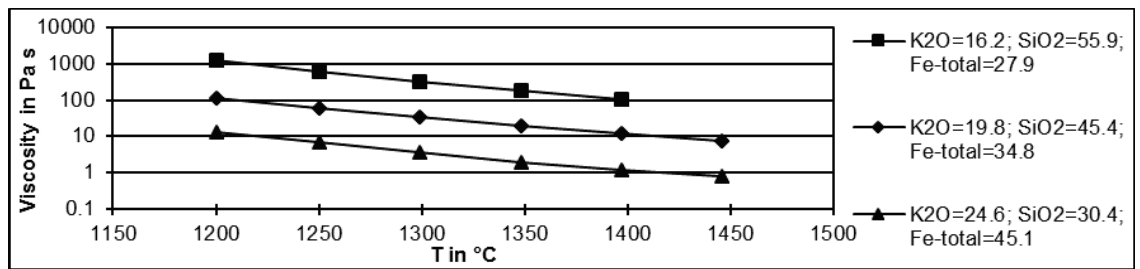


Figure 24: Viscosity decrease by increase of K_2O for ternary SiO_2 - Fe_2O_3 - K_2O [71]

Multi-component slag systems are containing a variation of other network modifiers. Hence, the influence of these network modifiers on K_2O and therefore the influence of K_2O to slag viscosity is not clear definable.

2.6.7 Sodium Oxide

Sodium oxide, Na_2O , is a network modifier, Table 2. In industrial slags, Na_2O is a minor component. The amount of Na_2O was found to be maximum 4.6 wt.-% within examined slag samples of this work, Table 44.

Na_2O has a dramatic influence on viscosity of binary melt systems, Figure 25. Increasing the amount of Na_2O at 1350 °C by 5 wt.-% in total results in decreasing of viscosity by 3.5 times. This effect is constant over wide temperatures within the Na_2O amounts of 20 wt.-%. Above 20 wt.-%, the network breaking behavior of sodium oxide is inhibited due to the absence of a polymerized network.

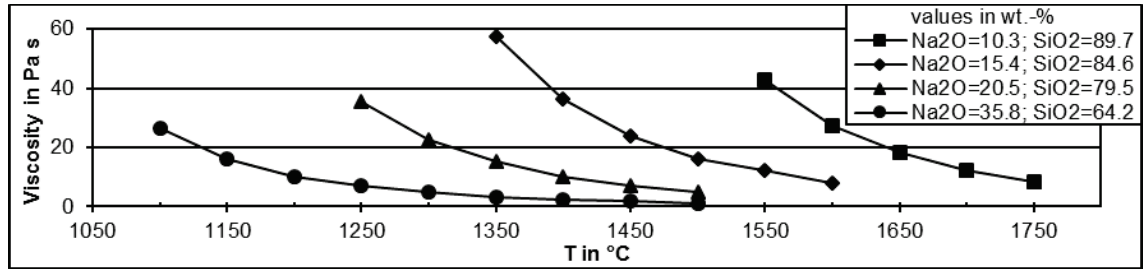


Figure 25: Viscosity influence by Na_2O for binary SiO_2 - Na_2O melts [69].

The network modifying behavior can also be found for ternary system, Figure 26. Despite the fact that the reported data was achieved with a rotational viscometer using an alumina measuring system, the trend in viscosity decrease can be recognized [72]. The change in the $\text{Al}_2\text{O}_3/\text{SiO}_2$ -ratio is not taken into account due to both components are estimated to be network formers within the given slag composition.

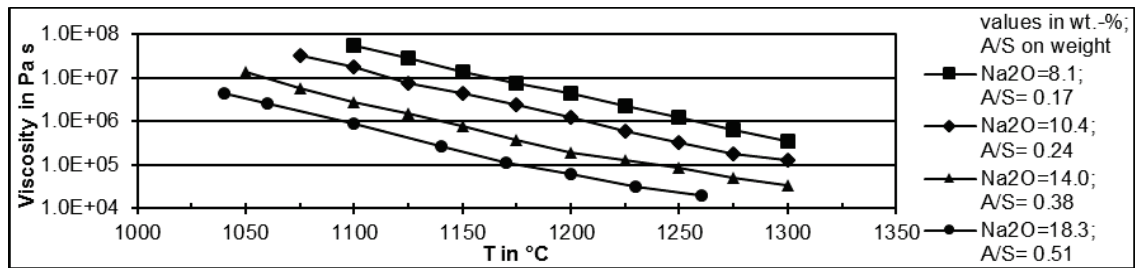


Figure 26: Viscosity influence by Na_2O for ternary melts made from Al_2O_3 - SiO_2 - Na_2O [72].

Detailed investigations on Na_2O are not available for multi-component slag systems. There, sodium oxide is acting together with other network modifiers. A clear differentiation cannot be done on viscosity decreasing effects.

2.6.8 Titanium Oxide

Titanium oxide, TiO_2 , is considered to behave like SiO_2 . Ti^{4+} ions are fitting into the Si^{4+} network and polymerize the melt. An increase of viscosity is observed. This defines TiO_2 as network former [33]. In glass technology, TiO_2 plays an amphoteric role [17,18].

For low contents of TiO_2 , an octahedral coordination was found. When TiO_2 concentration increases, the coordination number decreases. A sudden change in viscosity was found for SiO_2 - Na_2O - TiO_2 melts above 10 mol-% of TiO_2 content. Well polymerized networks received a viscosity increase by increasing the TiO_2 content at temperatures below 600 °C. Less polymerized networks received a viscosity decrease at temperatures above 600 °C. When the TiO_2 concentration of 10 mol-% was exceeded, the increase of viscosity for low temperatures was stopped [73].

Measurements on melts made from SiO_2 - CaO and SiO_2 - Al_2O_3 - CaO under nitrogen atmosphere show a constant influence of TiO_2 in the mass fraction range $\text{TiO}_2 \geq 0.1$. In general, an increase of TiO_2 is decreasing viscosity for several C/S-ratios based on mass, Figure 27. Viscosity is most decreased in the mass fraction range $0.1 < \text{TiO}_2 < 0.25$,

while at higher TiO_2 concentrations the network is too much broken to be significantly influenced.

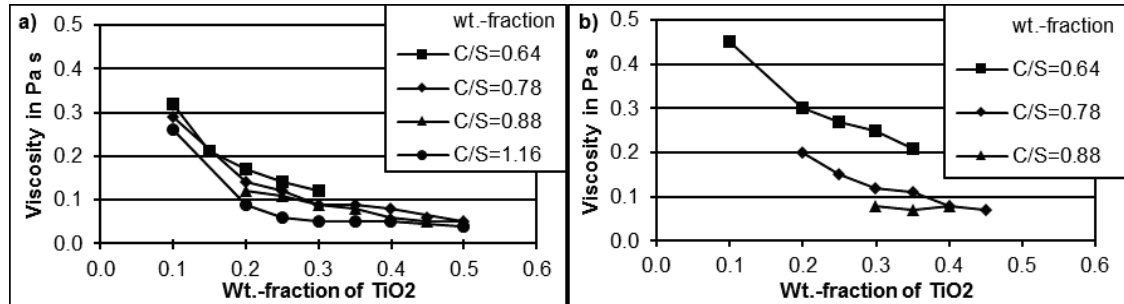


Figure 27: Influence of TiO_2 on viscosity at a) 1500 °C and b) 1400 °C [55].

The influence of TiO_2 for the investigated systems in this work should be negligible due to the small detected mass ratios.

2.6.9 Phosphorous

Phosphorous, P, is a minor component in coal ashes, but can be enriched up to 4.7 wt.-% as found in samples of this work, Table 44. Less investigations are available on the influence of P_2O_5 . Due to the fact P_2O_5 is a network former; an increasing amount of P_2O_5 should increase viscosity [74]. Figure 28 supports this theory. A binary CaO - P_2O_5 system was stepwise enriched with P_2O_5 and viscosity increased also [75]. A similar trend was found by investigations on Na_2O - P_2O_5 mixtures [76]. Additionally, P seems to strength the network at low temperatures in a surpassing way. At elevated temperatures, the network is scattered in such a dimension that the network forming property of P_2O_5 does fail.

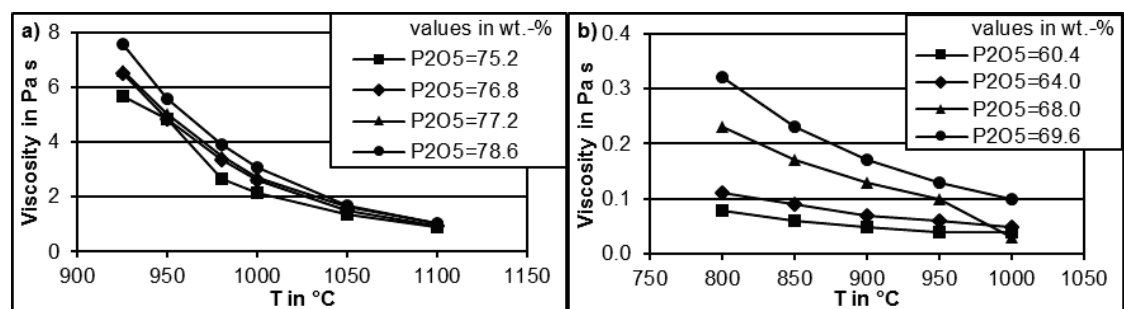


Figure 28: Influence of P_2O_5 on the viscosity of a) CaO - P_2O_5 mixture [75] and b) Na_2O - P_2O_5 mixture [76].

2.6.10 Sulfur

Coal ashes contain sulfur S up to 25 wt.-% related to other oxides. Sources of sulfur within the ash are minerals e.g. anhydrite CaSO_4 and its hydrates and Jarosite $(\text{M}^+)\text{Fe}_3(\text{SO}_4)_2(\text{OH})_6$ [77,78]. In presence of sulfur oxide SO_3 , carbonates such as limestone CaCO_3 , magnesite MgCO_3 and siderite FeCO_3 are transformed to anhydrite CaSO_4 , magnesium sulfate MgSO_4 and ferrous sulfate FeSO_4 . Carbon monoxide CO_2 is

by the way released. Sulfur oxide requires sufficient oxygen to be formed from sulfides [79]. Alkali metal and alkaline earth metals sulfates are decomposed above about 980 °C, little or no SO₃ is found in most slags that have been heated to much higher temperatures [80].

Sulfur occurs in form of an anion in slag [81]. The solubility of sulfur depends on temperature, pressure, bulk composition, and the fugacity of oxygen and sulfur. Two main valence states are referenced for sulfur in basaltic magmas, these are sulfide S²⁻ and sulfate SO₄²⁻. The higher the temperature, the lower is the solubility of free sulfur [82]. Binary Al₂O₃-CaO slags are reported to fix between 1 and 2.5 wt.-%. Ternary Al₂O₃-CaO-SiO₂ slags offers sulfur capacities in the range of 1·10⁻²-1·10⁻⁴ mass-% at 1500 °C and 1·10⁻¹-1·10⁻⁴ mass-% at 1650 °C. By approximation, the solubility of S decreases with the number of slag components and increases with the ratio of CaO, FeO or MnO [34].

The effect of sulfur on slag viscosity is rarely given in literature due to the low amount of stored sulfur in slags. It is supposed, that low amounts of S do not vary slag viscosity in a significant level. Examined slags of this work contain up to 0.2 wt.-% of SO₃ after measurements, Table 46.

2.7 Summary of Last Chapters

- Dynamic viscosity can be Newtonian or non-Newtonian when shear rates are changed. Numerous non-Newtonian flow behaviors are known.
- A separation into dilatant (shear-thickening) and pseudo-plastic (shear-thinning) non-Newtonian flow behavior is assumed to be sufficient within this work.
- Slags are mixtures of molten (mostly) metal oxides. Sulfur and Phosphorus are not non-metals, but have also to be mentioned. Several phase changes (liquid, solid-liquid, solid) can occur during cooling procedure.
- The structure of slags is defined as a three-dimensional network of (mostly) metal cations and oxygen anions. The most important structure in literature is the [SiO₄]-tetrahedron.
- The structure of slags deviates from the structure of a crystal by the distance between reoccurring network sections. A chaotic structure with a “short range order” (SRO) is assumed for slags. On the other hand, crystals consist of organized structures with a “Long range order” (LRO).
- Two variables influence the viscosity of slags. First, Elevated temperatures are weakening the slag network and viscosity decreases. Second, the interactions of metal and non-metal oxides within slag composition.
- Network formers are strengthening the network and therefore an increase of viscosity is to be supposed.

- Network modifiers weakening the network and a decrease of viscosity is expected.
- Amphoteric oxides exhibit forming or modifying properties in dependence to the gross slag composition.
- The base-acid-ratio (B/A-ratio) is consulted to describe the relation of network formers, network modifiers and amphoteric oxides.
- Within the number of slag components, the characteristic influence of each component decreases.

3. Slag Viscosity Toolbox

A part of this thesis was to create and continuously extend a slag viscosity database and a modelling tool: Together, it is the slag viscosity modelling tool box. It consists of two parts:

- The slag viscosity predictor (SVP) and
- the slag viscosity data base (SVDB)

First publicized in 2012, the toolbox was continuously extended [83]. The viscosity data collection was used to validate viscosity predictions on experimentally obtained values. Additionally, it is used to compare calculated mass and volume fractions of partly-liquid slags from experimental validated phase formations.

3.1 Slag Viscosity Predictor

The slag viscosity predictor (SVP) is a Microsoft® Excel file using Microsoft® Visual Basics for Application (VBA). Viscosities can be predicted on temperature and composition defined by mass or mole fraction of metal oxides. 12 viscosity models are included in their unmodified versions. An introduction to these models is given in chapter 4.1.

If FactSage 6.4 [84] is available, predictions on phase formation, slag composition and solid volume fractions (SVF) can be carried out. The SVF is the volume fraction of minerals in comparison to the total volume of minerals and slag, chapter 5.2.2. The found SVF can be later applied to improve viscosity predictions. Table 3 includes adjustments of the FactSage calculations.

An important step is the selection of the solution species database to apply slag composition predictions. Several opportunities are available in dependency of the bulk slag composition. Two databases were chosen for further investigations:

- SlagA database was developed to cover slag compositions made from metal oxides. It is the more common database. A sulfur content below 10 wt.-% is covered while Fluorine is not.
- SlagH database was later selected to calculate properties of possible liquid slag mixtures containing CaF_2 as found in blast furnaces or aluminum production.

A comparison and critical discussion between these two databases is given in chapter 8.2 with respect to liquidus temperature calculation. Results of slag phase composition modelling will be compared in chapter 8.3. Detailed information of selected phases and solutions are given in the appendix, Table 36 to Table 37.

Table 3: Selected calculation properties for SVP within FactSage 6.4.

Property		Value
Software version		FactSage 6.4
Databases		FactPS, FToxid, FTmisc,
Solution species for slag		SlagH
Compound species	gas (real)	73
	pure liquids	42
	pure solids	250
Total species		511
Total solutions		27
Total phases		320
Included oxides		SiO ₂ , Al ₂ O ₃ , Fe ₂ O ₃ , FeO, CaO, MgO, Na ₂ O, K ₂ O, MnO, TiO ₂ , CaF ₂

Depending on phase prediction by thermochemical equilibrium software FactSage, the opportunity to calculate the solid-liquid interactions on slag is given. If the formation of minerals is predicted, the influence on the slag flow behavior can be calculated by the Einstein-Roscoe equation. Read chapter 5 for details of the Einstein-Roscoe equation.

3.2 Slag Viscosity Database

The slag viscosity database (SVDB) contains the results and parameters of viscosity measurements of numerous references and own measurements. Properties of SVDB are listed in Table 4.

Table 4: Properties of SVDB in November 2015.

Property		Value, name		
Number of references		81		
Number of own samples		55		
Number of oxide systems		1066		
Number of own measurements		192		
Number of considered atmospheres		13		
Temperature range in °C		531.6 – 2482		
Viscosity range in log (Pa s)		-2.7 – 14.35		
Partial oxygen pressure in atm		1.4·10 ⁻²⁵ – 0.21		
Tabled oxides and ranges		Min in wt.-%	Max in wt.-%	Occurrence
	SiO ₂	0	100	30164
	Al ₂ O ₃	0	100	28825
	Fe ₂ O ₃	0	85.1	25183
	FeO	0	83.5	1116
	Fe	0	1	137
	CaO	0	60.0	29318
	MgO	0	55.6	26524
	Na ₂ O	0	49.4	24308
	K ₂ O	0	48.0	23332

MnO	0	72.2	2390
Continuation of Table 4			
Property	Value, name	Property	Value, name
TiO ₂	0	50.0	22100
B ₂ O ₃	0	13.5	19
P ₂ O ₅	0	83.1	14740
NiO	0	1.2	307
ZrO ₂	0	2.2	243
CaF ₂	0	29.9	329
SO ₃	0	11.2	17943
Cr ₂ O ₃	0	60.0	170
V ₂ O ₅	0	10.0	85
Total datapoints		30364	

The SVDB consists of a Microsoft® Excel file. Melt compositions are tabled in fractions of moles and mass. Viscosity and temperature information were extracted from tables or plots provided by references or taken from own experiments.

Information are given about the crucible and spindle material, the applied atmospheres, viscosity measurement techniques, shear rate, source format, calculated amount of liquid or solid slag amount and references. The value “unknown” defines absence of information on a parameter like atmosphere, measurement system or measurement technique. Some measurement techniques do not require any crucible or spindle. Therefore, the value “N/A” is set.

Next to parameters taken from references, also viscosity predictions and phase calculations are available. This information was achieved by application of the slag viscosity predictor (SVP).

By application of a pre-built mask and Microsoft® Visual Basic for Applications (VBA), requests on the SVDB can be carried out. The opportunity is given to define a request on all listed properties in the section above. The performance function of the average absolute logarithmic error (AALE) is printed at the end of the request. An introduction to the AALE is given in chapter 3.3.

3.3 Prediction Quality of Viscosity Models

Predicted viscosities have to be compared with measured data to evaluate the model quality. This comparison is realized by performance functions. These functions must be adjusted on the existing datasets of measured and predicted viscosity-temperature-relationships. Therefore, it is important to separate into data sets consisting of

- a single data point or
- more than one data point and so a range of viscosity-temperature measurements.

In case of a single value for predictions and measurements, the absolute error (AE), absolute relative error (ARE) and absolute logarithmic error (ALE) can be used, Eq. (16) to (18). Predicted values are represented by η_p and measured values are represented by η_m , respectively.

$$AE = |\eta_p - \eta_m| \quad (16)$$

$$ARE = \left| \frac{\eta_p - \eta_m}{\eta_m} \right| \quad (17)$$

$$ALE = |\log_{10} \eta_p - \log_{10} \eta_m| \quad (18)$$

The AE indicates the total difference of predictions and measurements, while the ARE delivers the normalized deviation. The magnitude of deviation or difference at all is neglected by the ALE.

To validate the model performance over n data points, an averaging has to be applied on the suggested functions, Eq. (19) to (21). AAE, AARE and AALE are average absolute error, average absolute relative error and average absolute logarithmic error. Index i is predicted or measured value at i^{th} position.

$$AAE = \frac{1}{N} \sum_{i=1}^N |\eta_{pi} - \eta_{mi}| \quad (19)$$

$$AARE = \frac{1}{N} \sum_{i=1}^N \frac{|\eta_{pi} - \eta_{mi}|}{\eta_{mi}} \quad (20)$$

$$AALE = \frac{1}{N} \sum_{i=1}^N |\log_{10} \eta_{pi} - \log_{10} \eta_{mi}| \quad (21)$$

Table 5 contains examples on calculated errors to illustrate the performance functions. The viscosity of an imaginary slag was measured within a temperature range of 1000-1300 °C. Four data points were recorded. Two viscosity models, M1 and M2, were selected to predict the viscosity. An error of +60 % for model M1 and -50 % for M2 is pressed in this example. The performance functions AE and ARE show a disadvantage for Model M1 due to higher values in comparison to model M2. By logarithmic calculus, the discussed facts are obliterating. The ALE gives a smaller value for model M1 than for model M2.

To cover the whole range of data points, an averaging has to be done on the performance functions. Now, small differences have a low weight versus large

differences and AAE will be misinterpreted. A solution is the application of AARE. In this case, the error will become normalized for small and large differences. Unfortunately, it creates a difference in positive or negative errors although the average errors are similar. To overcome these disadvantages, the AALE has to be introduced. The smaller AALE is the less are deviations of predictions and measurements. Best agreement is found for $AALE=0$. Consequently, the best model is M1 over all records.

Table 5: Examples on calculated errors to illustrate performance functions.

	i	-	1	2	3	4
	T	°C	1000	1100	1200	1300
Model	M1	Pa s	160	80	16	8
	M2		50	25	5	2.5
Measurement	-	Pa s	100	50	10	5
Error	M1	-	+60 %			
	M2		-50 %			
AE	M1	Pa s	60	30	6	3
	M2		50	25	5	2.5
ARE	M1	-	0.6	0.6	0.6	0.6
	M2	-	0.5	0.5	0.5	0.5
ALE	M1	-	0.204	0.204	0.204	0.204
	M2	-	0.301	0.301	0.301	0.301
AAE	M1	Pa s	24.8			
	M2		20.6			
AARE	M1	-	0.60			
	M2	-	0.50			
AALE	M1	-	0.204			
	M2	-	0.301			

A depiction of the above discussed points is given in Figure 29. By a subjective point of view, the model M1 with an error of +60 % is in disadvantage of model M2, error - 50 %. Of course, the best model over the entire record is M1.

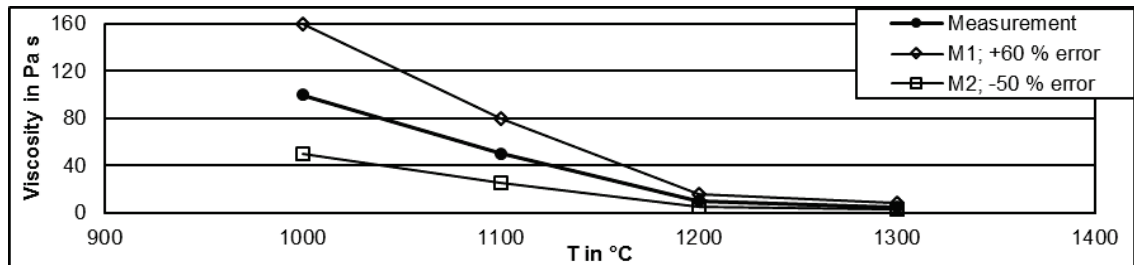


Figure 29: Viscosity of imaginary slag and modelling to describe performance functions.

The AALE will be used to compare and validate viscosity predictions with measurements for a range of temperature-viscosity datasets.

4. Classic Slag Viscosity Modelling

Modelling is the most rapid way to receive viscosity of a slag. Depending on slag bulk composition and temperature, viscosity can be estimated. It is a precondition that the chosen viscosity model is valid on the applied slag composition and temperature range. Time consuming and expensive measurements are not necessary. Technical processes can be quickly adapted to changed parameters, e.g. slag composition.

Numerous viscosity models were developed since the middle of the 20th century. In general, four kinds of viscosity models are available. A selection is given in Table 6.

Table 6: Selection of viscosity modelling methods.

Basic principle	Example	Remarks
Thermo-dynamics	Adam-Gibbs-M. [85]	<ul style="list-style-type: none"> ○ motion occurs on internal cooperative rearrangement of molecules ○ one molecule disturbs movement of many molecules at a decreasing temperature ○ viscosity is described by configurational entropy ΔS and temperature T
	Free-Volume [86]	<ul style="list-style-type: none"> ○ fluid's molecules are transported by "jumping" from one void to another void, when void's free volume v_f is same as molecule volume v_m ○ the probability P of the molecule's movement depends on communal entropy S_c
	Avramov-Milchev-M. [87,88]	<ul style="list-style-type: none"> ○ determining temperature dependence of average jump frequencies of molecules ○ distribution function of barriers for jumping molecules depends on entropy S ○ viscosity is function of S
Physics	Molecular Dynamics Simulation (MDS) [89]	<ul style="list-style-type: none"> ○ simulating movement of ions, including kinetic, potential and interatomic potentials [16] ○ MDS applied to predict slag structure at elevated temperatures ○ slag structure provides information about viscosity (Q^n-values)
	Monte Carlo Simulation	<ul style="list-style-type: none"> ○ simulating random movement of particles ○ accepting movement, when Boltzmann factor confirms an increase of energy by move ○ radial distribution function of atoms, taken from e.g. ion scattering measurements, is background for structure and therefore viscosity

Continuation of Table 6

Basic principle	Example	Remarks
Semi-empirical, semi-physical	Shaw [90]	○ background are basic viscosity models
	Urbain [91]	○ such as Arrhenius equation, Vogel-Fulcher-Tammann, Weymann equation
	Lakatos [68]	○ Viscosity-temperature-relationship is described by use of factors
	BBHLW [92]	○ factors depending on slag composition and were developed on experimental data sets of melts [35]
Artificial Neural Network	ANNliq, Duchesne [83]	○ influences of viscosity (temperature, fraction component i , component $i+1$) are parameterized
		○ model is “trained” on database of viscosity measurements containing a sufficient number of data points
		○ viscosity is calculated by weighted parameters developed by trained model [93]

4.1 Selected Classic Viscosity Models

A part of this work is the application of twelve viscosity models. The selection was done on 10 semi-empirical and 2 Artificial Neural Network models. The models of S2, Watt-Fereday, Bomkamp, Shaw, Lakatos, Urbain, Riboud, Streeter and Kalmanovitch-Frank are collected within the review of [35]. This work is often cited in slag viscosity literature. The models of BBHLW, Duchesne and ANNliq were selected in a collaborative paper [83].

See appendix chapter 10 for detailed descriptions of the physical and mathematical backgrounds. The models will be abbreviated in figures and tables due to absence of space. These abbreviations are given in Table 7.

Table 7: Selection of viscosity models.

Model name	Abbreviation
S ² (BCURA)	S2
Watt-Fereday	WF
Bomkamp	Bom
Shaw	Sha
Lakatos	Lak
Urbain	Urb
Riboud	Rib
Streeter	Str
Kalmanovitch-Frank	KF
BBHLW	BBHLW
Duchesne	Duc
ANNliq	ANN

4.1.1 S²

Developed by the British Coal Utilization Research Association (BCURA) in early 1960s, the BCURA or S² model is based on an Arrhenius form of viscosity equation [94]. The correlation was developed on 62 ash samples. Completely molten slags and Newtonian flow behavior are assumed.

The model is reported to underestimate viscosity for low-rank coals. Also, the model should be applied on slag analysis and not on ash/coal analysis due to the risk of significant losses of components during heating [95]. As shown in Eq. (50), major components are SiO₂, Fe₂O₃, CaO and MgO. A recalculation to 100 % has to be performed after exposing remaining components. This neglecting of components and the inflexible handling with Fe oxidation states can lead to massive deviations in prediction quality.

4.1.2 Watt-Fereday

Depending on former work of Reid and Cohen [1], the Watt-Fereday model was developed in the 1960s. The viscosity-temperature relations of 113 mixtures of British coal ashes were the fundament. Completely molten slags are assumed. Although viscosity measurements were obtained under “forming gas” (90 vol.-% nitrogen and 10 % hydrogen gas) the oxidation states of iron were omitted. Major ash components as SiO₂, Al₂O₃, Fe₂O₃, CaO and MgO are included for viscosity modelling. Minor components of British coal ashes, such as Na₂O, K₂O, Mn₃O₄ and TiO₂ can be neglected due to their low proportions. This involves a recalculation to 100 wt.-% of the major components.

4.1.3 Bomkamp

The Bomkamp model, published in 1976, is a modification of the Watt-Fereday model to take MgO into account for viscosity prediction [96,97].

Computed viscosities were higher than the measured one for slags of Western Canadian coals [41]. Good prediction quality with an average deviation less than 30 % to experimental data was found for slags covering $42 \leq \text{SiO}_2 \text{ wt.-%} \leq 55$ and $\text{Na}_2\text{O wt.-%} \leq 5$ and $\text{SiO}_2 \text{ wt.-%} \leq 34$, respectively [98].

4.1.4 Shaw

The Shaw model bases on the previous data compilations and calculations of Bottinga and Weill published in 1972 [45]. Slag and melt systems with two to six components were chosen from 25 references with a final number of 2440 data points.

The performance of the Shaw model for $\eta > 1 \cdot 10^7$ Pa s suffers from underestimation. Furthermore, no influence of thermal history, e.g. evaporation of components, is covered [35].

4.1.5 Lakatos

The Lakatos model was published in 1972. Viscosity measurements performed on 30 soda-lime glasses covered a viscosity range of 10 – $1 \cdot 10^{12}$ Pa s. The number of oxides within a glass system varied between three and six. Lakatos applied the Vogel-Fulcher-Tammann (VFT) equation to calculate viscosity. The prediction quality of the model is described as good by Lakatos. Standard deviations were in the range of 4.4 – 2.3 °C for viscosity ranges from 30 – $3 \cdot 10^{11}$ Pa s when viscosity was fixed and therefore the temperature at this viscosity was calculated. Higher deviations as found for measurements of samples not belonging to the development assembly were explained by insufficient finings. Discrepancies found in comparison to older data occur on errors in measurement techniques [68].

The applicability of the Lakatos model is assumed to be good for high-silica, high-alkali or alkaline slags. Due to the small compositional variations in soda-limes glasses and therefore a small development range, viscosity prediction quality will fail for slags with varying compositions.

4.1.6 Urbain

The Urbain model was published in 1981 as a further development from an earlier work [91,99]. Aim was the quick and cheap estimation of viscosities of molten aluminosilicate melts in industrial applications. Finally, the model was extended on 54 binary and ternary oxides, silicates and aluminosilicates [100]. The ternary systems were in the form SiO_2 – Al_2O_3 – MO and SiO_2 – Al_2O_3 – M_2O . MO and MO_2 represent bi- and monovalent oxides.

The Urbain model is described with a well accuracy by numerous authors [101–104]. It was popular to be modified by multiple authors.

4.1.7 Riboud

The Riboud model was introduced in 1981 [105]. Intention was the viscosity prediction of continuous casting slags to determine several processing parameters, e.g. material transport, thermal insulation and steel transport by flowing. Over 40 melts were taken into account for model development, 23 synthetic and 22 industrial slags.

The prediction quality was found to differ around 1.2 % for blast furnace slags under air estimation. Deviations of around 7 magnitudes were discovered for applications with high silica, calcia and sodium contents as found for glass forming processes [83].

4.1.8 Streeter

The Streeter model was published in 1984 by the Bituminous Coal Research, Inc., (BCR) to cover viscosity predictions for low-rank-coal slags. Data on slag rheology was necessary to operate slagging fixed-bed gasifier at Grand Forks Energy Technology Center (GFETC), Grand Forks, North Dakota; and BI-GAS entrained-bed slagging gasifier at Homer City, Pennsylvania [106,107]. To found viscosity data, 17 slags (9 lignites, 7 sub-bituminous and 1 bituminous low rank coals) were investigated. The performance of the Streeter model is referenced as not sufficient good for high-silica, low CaO and MgO and low B/A-ratio coal ashes. A disagreement of several magnitudes is reported [104].

4.1.9 Kalmanovitch-Frank

The Kalmanovitch-Frank model was first described in 1988 [108]. An improvement of the original Urbain model to experimental data taken from Machin [53,54,109] was done. Measurement data of British coal ash slags, Illinois #6 and Pittsburgh #8 coal ash slags agree well with viscosity predictions. In general, a better viscosity prediction quality was not found when compared to the original Urbain model. Furthermore, the Kalmanovitch-Frank model shows weak points for low temperatures, causing $\eta > 1000 \text{ Pa s}$ [35].

Due to the separation of FeO and Fe₂O₃, reducing atmospheric conditions are introduced. This should generate an advantage over models without separating iron oxidation states.

4.1.10 BBHLW

The BBHLW model is named after the developers Browning, Bryant, Hurst, Lucas and Wall. Released in 2003, the model targeted to introduce reducing atmospheric conditions taken from 117 samples of fluxed and unfluxed coal ashes and synthetic slags.

The BBHLW model shows a significant better prediction quality than the Kalmanovitch-Frank, S² and Watt-Fereday models. Viscosities of coal ash slags were calculated most accurate, while for synthetic slag systems above 1000 Pa s discrepancies are reported. Insufficient input data for model development is mentioned as reason [92]. In a comparison with twelve viscosity models, the BBHLW model is listed within the four best viscosity prediction methods for industrial applications covering entrained flow gasification, glass production and blast furnace [83].

4.1.11 Duchesne

The Duchesne model was published in 2010 and belongs to the group of Artificial Neural Network models [93]. The author pointed out an advantage over the models of Urbain, Riboud, Kalmanovitch-Frank and BBHLW [93]. It has to be mentioned, that the

Duchesne model was trained on the same data which were later used for validation. The application of temperatures and slags out of the training parameters can result in deviations.

4.1.12 ANNliq

The ANNliq model was published in 2012 and belongs also to the group of Artificial Neural Network models [110]. In general, it is a re-training of the Duchesne model, section 4.1.11. Duchesne et al. 2013 carried out case studies, including glass forming, entrained flow gasification and blast furnace conditions. The ANNliq was compared with the prediction results of eleven semi-physical models and one Artificial Neural Network model. Best agreement to measured values was found for the glass formation case study for temperatures resulting in $\eta < 10$ Pa s. There, the deviation was ± 1.4 fold (AALE=0.153) to the given measurement. Deviations of circa 8 magnitudes (AALE=7.752) are reported for glass forming processes and $\eta > 1 \cdot 10^8$ Pa s. Expecting entrained flow gasifier conditions, the model is partly well predicting viscosity. An error of $0.311 < \text{AALE} < 2.332$ is referenced. From the given investigations, it can be recommended, that the ANNliq is not suitable for predicting processes with $\eta > 1000$ Pa s.

4.2 Need of Improvement in Viscosity Literature

Viscosity data and measurement parameters were collected within the slag viscosity data base, chapter 3.2. Due to the character of experiments at high temperatures, viscosity measurements underlie several influences. Although this fact is known, numerous authors are not discussing in detail these problems. Furthermore, some references are not describing important details of experiments, Table 8.

Table 8: Comparison of mentioned parameters to the number of references.

Parameter	Indications / total references
atmosphere	38/75
crucible or bob material	47/75
measurement technique	68/75
shear rate	18/75

Also, lag of information is found for other kinds of parameters. Authors apply a reducing atmosphere by adding graphite crucibles to the viscometer furnace. No information is given about the temperature at this position to estimate the partial oxygen pressure p_{O_2} . Other authors mention p_{O_2} but do not cite the detection technique [61]. Some investigations on the influence of the Fe^{3+}/Fe^{2+} ratio are referenced, but no effort was done to determine the Fe^{3+}/Fe^{2+} ratio [111]. The contamination of slag sample is accepted by the use of measuring systems made of alumina. The change of viscosity by

contamination is known, but not discussed nor taken into account for further investigations or evaluations [112].

The problems numerated above are limiting the confidence in literature. All work on viscosity has to be critically examined when the results have to be used. To obtain most trustable experimental data, own viscosity measurements have to be carried out.

4.3 Summary of Last Chapters

- Viscosity modelling of slags is undertaken since decades.
- Developers covered the viscosity of artificial slags, magmatic melts and melts from technical applications.
- A dozen classic models were selected to calculate the temperature-composition depending viscosity of slags.
- All selected models are developed on experimental data sets. The quality of viscosity measurements in terms of reproducibility, atmosphere, experimental setup etc. is not verified for all references.
- It is necessary to perform own measurements to obtain proper viscosity records.

5. Advanced Slag Viscosity Modelling

A prediction error has to be taken into account for slag viscosity modelling due to several reasons. On the one hand, the applied viscosity model is not in accordance to the used slag composition. On the other hand, a number of circumstances, e.g. measurement system materials, atmospheres, temperature, etc. affect the flow behavior of slags. See also chapter 4.2 for more detailed information. How much these circumstances influenced viscosity model development in the past cannot be estimated today.

One of the most important influences on slag flow behavior is the formation of particles by crystallization. There, two main phenomena overlap at the same time.

1. Change of slag composition and
2. switching from Newtonian to non-Newtonian flow behavior.

Furthermore, the influence of crystals to heat transfer within the melt has to be considered [113].

When crystallization and related circumstances are investigated, the found information has to be included to viscosity modelling.

5.1 Crystallization

Crystallization is the reverse process of melting. When a single substance is cooled down from liquid state, crystallization should initiate at the same temperature as fusion. A multi-component system will similar behave, read chapter 2.2.

If no crystallization is developed during cooling, the result is called “glassy state” or “glass”. Basic work about crystallization was done by Tammann [8]. In view of glasses, crystallization is defined as “devitrification”. Within this work, the term crystallization describes the formation of mineral particles in all kinds of investigated slags. Two important parameters represent crystallization [36]:

1. Nucleation, the formation of crystal seeds, and
2. crystallization velocity, the rate of forming and growing of crystals.

Crystallization of melts occurs in three modes [114]:

1. Polymorphic crystallization, in which the glass transforms into a crystal of same composition.
2. Primary crystallization, in which glass and crystal have different compositions.
3. Eutectic crystallization, which is a cooperative transformation to two phases while maintaining the mean composition.

5.1.1 Nucleation

Nucleation is the formation of crystallization centers, the nucleus. Without any center, no mineral will be formed. The classical nucleation theory implies the onset of crystallization as a function of

- cooling rate and
- solidification behavior of the melt [113].

Nucleation is also separated into

- homogenous nucleus formation, where nuclei are formed from the melt by a function of probability; and
- heterogeneous nucleus formation, where nuclei are introduced to the melt by nucleation agents.

The homogenous nucleus formation will be described below. In a homogenous melt, nucleation is a function of statistics. The lower the temperature, the better is heat transfer by conduction and therefore the driving force of nucleation is higher. If the temperature is too low, e.g. below solidus temperature T_s , nucleation is not occurring within short length of time.

In a thermodynamic description by Turnbull in 1950, the nucleation driving force is the difference in Gibbs energy ΔG given in Eq. (22), where G_C is free enthalpy of the crystal and G_S is free enthalpy of the remaining slag [115].

$$\Delta G = G_C - G_S \quad (22)$$

A maximum in ΔG means a maximum in nucleus formation. The nucleus radius at this point is defined as critical nucleus radius r_{cr} . According to the laws of thermodynamics, all processes are supported into the direction of smaller ΔG -values. An agglomeration of molecules is stable for $r > r_{critical}$, due to ΔG decreases by further nucleus growth. Agglomerates in the regime $r < r_{cr}$ will collapse due to smaller ΔG -values. Unused agglomerates are called embryos.

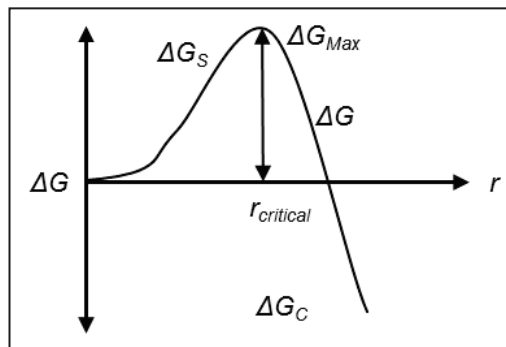


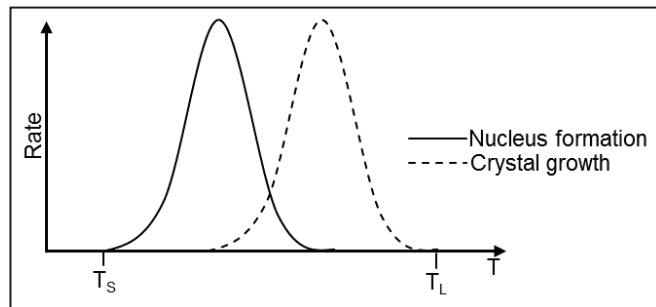
Figure 30: Schematic of nucleation in view of Gibbs energy ΔG [36].

5.1.2 Crystallization Rate

Basic work on crystallization was done by Tammann in the begin of the 20th century [7,8]. A concept similar to nucleation was developed. The rate of crystallization is small for

- high temperatures due to the removal of crystallization heat and
- low temperatures, resulting in high viscosities and therefore a decrease in material transport to the formed particle.

An optimal crystallization rate C is detected for a medium temperature. This temperature varies from optimum nucleation temperature. Consequently, crystallization is influenced by two overlapping parameters: nucleation and crystallization rate, Figure 31. The maximum of crystallization rate will be at a higher temperature as the maximum of nucleation.



T_S – solidus temperature and T_L – liquidus temperature

Figure 31: Rate distribution of nucleus formation and crystal growth [116].

5.1.3 Crystallization Measurement Methods

As defined in the sections above, crystallization consists of two parts:

1. Nucleation and
2. Crystal growth.

The measurement method of crystallization is limited. Nucleation appears in the nanometer dimension. As long the nucleus is not starting to grow and form a crystal, its detection will be hard by visual methods.

Crystal growth measurement is more achievable. A selection of methods is described below:

1. Quenching: A sample is annealed at a given temperature and afterwards quickly cooled down to “freeze” the condition of the sample. Investigations can be done by optical microscopy, e.g. counting the number and measuring the dimensions of crystals. The quenching method is complex due to the furnace and the sample suspension system. Heating and cooling rates to adjust the sample properties are limited to the furnace, while quenching is abrupt within the quench bath.

Water and oil are the best heat transfer media at room temperature [117]. Also, quenched samples can be examined by X-ray diffraction (XRD), chapter 6.3.2.

2. Hot-stage microscopy: A microscope with a heated sample stage takes permanently pictures of a melt. The method is sufficient enough for small samples and moderately cooling rates [36].
3. Hot thermocouple microscopy: Two methods are available. First method is the single hot thermocouple technique (SHTT). There, the sample is pointed on the pearl of a single thermocouple and viewed by a microscope. An alternating or pulsed electric voltage is heating the TC. Between the pulsed heating cycles, the temperature at the tip is indicated by the measured thermoelectric voltage. The second method is double hot thermocouple technique (DHTT). In this case, the sample can be pointed between two thermocouples. Both thermocouples can be alternately used as heater or temperature indicator [113,118].
4. Differential thermal analysis (DTA) and differential scanning calorimetry (DSC): Detecting the heat of phase changes (melting/solidification/solid phase changes) is a quick method to observe the thermal behavior of a sample.

5.2 Slag Properties Changes During Crystallization

When crystallization occurs, slag composition will permanently change by time and temperature. Separated minerals consume slag components. Changes of liquid slag composition result in a change of viscosity of the remaining slag. Furthermore, formed minerals are found to change the flow behavior from Newtonian to non-Newtonian. The knowledge of actual slag composition is mandatory to validate the observations of slag viscosity measurements.

5.2.1 Slag Density

In general, the density of a pure substance ρ_0 is defined by Eq. (23), where m represents mass in kg or g, V is volume in m^3 or cm^3 , M is molar mass in kg/kmol or g/mol, \bar{V} is molar volume in m^3/kmol or cm^3/mol and n is number of molecules in moles.

$$\rho_0 = \frac{m}{V} = \frac{M}{\bar{V}} = \frac{m}{n \cdot \bar{V}} \quad (23)$$

Several techniques are available to estimate slag density [34]:

- Picnometry, where a known volume of slag is weighed within a reservoir.
- Buoyancy or Archimedean method, where the weight of a body is measured before and after immersing into the melt.
- Volumetric or dilatometry, where slag volume is compared between low and high pressure within a pressure-resistant chamber.

- Manometer-based, where the change of slag height in comparison to applied pressure within a manometer is recorded.
- Maximum bubble pressure method, where a capillary is immersed within the melt and the pressure difference of a purging gas between initial and final immersion depth is known.
- Sessile droplet method, where the phase boundary angle of a slag drop on a substrate is consulted to calculate volume of the melt sample.

The used device materials have to be heat and slag resistant. Furthermore, the handling of complex devices at elevated temperatures is limited. The most recommended applications are Archimedean, maximum bubble pressure and sessile drop method.

Modelling of slag or glass density is primarily done on empirical observations. The density will be related to

- temperature and
- composition.

Therefore, several opportunities to estimate the density ρ are available, Eq. (24) and (25), where ρ_0 is a basic density, ρ_i is density factor for each slag component and x_i is mass fraction of the component from bulk composition. Factors have to be tabled for the desired temperature range for calculation. Densities within liquid state can be up to 20 % lower than in solid state at room temperature as found for glasses [36,119].

$$\rho = \sum_{n=1}^i \rho_i \cdot x_i \quad (24)$$

$$\rho = \rho_0 + \sum_{n=1}^i \rho_i \cdot x_i \quad (25)$$

An additional way to estimate slag composition is the introduction of the molar slag volume. There, the change of the molar volume of a mixture made from component 1 and 2 is considered. Depending on the physical properties of metallic ions, the volume of a defined slag part will change, Figure 32. Eq. (23) has to be modified to overcome a multi-component slag system.

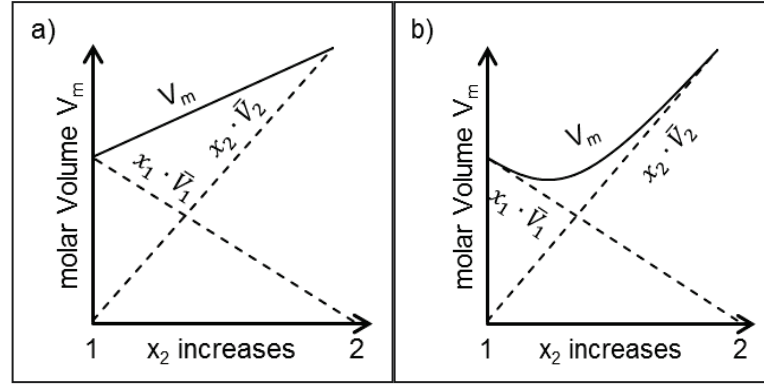


Figure 32: Molar Volume V_m of a binary slag with a) linear volume function and b) a non-linear volume function [34].

The modification results in Eq. (26) where M_i is molar mass, X_i is molar fraction, \bar{V}_i is partial molar fraction and index i of component i . Complex calculations methods for \bar{V}_i in view of composition and temperature were developed.

Mills and Rhine extended the basic equation with respect to the slag structure depending on SiO_2 and Al_2O_3 content. \bar{V}_i of SiO_2 and Al_2O_3 is therefore not constant, Eq. (27) and Eq. (28), respectively. Density of slag as a function of temperature $\rho(T)$ is finally calculated by Eq. (29), where T is temperature in K [120].

Lange and Carmichael observed the partial molar volume of 11 slag components within 64 mixtures. They found no significant change of \bar{V}_i within the examined temperature range of 1300-1600 °C for all slag components. The overall slag molar volume is given in Eq. (30). Eq. (31) describes \bar{V}_i for iron containing melts, where $\bar{V}_{i,1773\text{ K}}$ is the partial molar volume found for the component i at 1500°C, $\frac{d\bar{V}_i}{dT}$ is the slope of \bar{V}_i plotted over temperature T [121].

$$\rho = \frac{\sum_{n=1}^i (M_i \cdot X_i)}{\sum_{n=1}^i (\bar{V}_i \cdot X_i)} = \frac{M_{slag}}{\bar{V}_{slag}} \quad (26)$$

$$\bar{V}_{\text{SiO}_2} = 19.55 + 7.966 \cdot X_{\text{SiO}_2} \quad (27)$$

$$\bar{V}_{\text{Al}_2\text{O}_3} = 28.31 + 32 \cdot X_{\text{Al}_2\text{O}_3} - 31.45 \cdot X_{\text{Al}_2\text{O}_3}^2 \quad (28)$$

$$\rho = \frac{\sum_{n=1}^i (M_i \cdot X_i)}{[\sum_{n=1}^i (\bar{V}_i \cdot X_i)] \cdot (1 + 0.0001 \cdot (T - 1773))} \quad (29)$$

$$\bar{V}_{slag}(T) = [X_{\text{Na}_2\text{O}} \cdot X_{\text{TiO}_2} \cdot \bar{V}_{\text{Na}_2\text{O-TiO}_2,1773\text{ K}}] + \sum_{n=1}^i X_i \cdot \bar{V}_i(T) \quad (30)$$

$$\bar{V}_i(T) = \bar{V}_{i,1773\text{ K}} + \frac{d\bar{V}_i}{dT} \cdot (T - 1773) \quad (31)$$

Published partial molar volumes \bar{V}_i are given in Table 9 and Table 10. As pointed out by the developers, the density model of Lange and Carmichael has a deviation of 0.2-0.5 % comparing calculations and measurements [121]. Experimental uncertainties are not taken into account. A later review of their work and improving density functions for iron-free melts resulted in a much higher deviation range 0.25-5.7 % [122]. Mills et al. estimated a modelling error of ± 2 -3 % depending on experimental uncertainties. The cited values are recommendations to modelers [34,120].

Table 9: Referenced partial molar volumes for calculations of slag molar volume by Lange and Carmichael [121].

T in K	iron-free		iron-bearing				Standard Deviation cm ³ /mol
	\bar{V}_i	$\frac{d\bar{V}_i}{dT} \cdot 10^{-3}$	\bar{V}_i				
	cm ³ /mol	cm ³ /mol·K	cm ³ /mol				
	1773	1773	1573	1673	1773	1873	0.01
SiO ₂	26.88	-0.33	26.92	26.90	26.91	26.90	0.31
Al ₂ O ₃	37.52	0.74	36.80	37.11	37.37	37.63	0.81
TiO ₂	23.98	8.76	22.43	23.16	23.89	24.60	0.94
Fe ₂ O ₃	n.d.	n.d.	41.44	42.13	42.97	43.94	0.33
FeO	n.d.	n.d.	13.35	13.65	13.97	14.23	0.28
MgO	11.85	2.45	11.24	11.45	11.73	11.98	0.33
CaO	16.84	4.22	16.27	16.57	16.85	17.15	0.83
Na ₂ O	29.53	7.90	28.02	28.78	29.51	30.26	1.34
K ₂ O	47.10	12.68	44.61	45.84	47.01	48.22	0.63
Li ₂ O	17.42	5.82	16.19	16.85	17.36	17.90	0.13
Na ₂ O-TiO ₂	20.10	n.d.	20.33	20.28	20.21	19.99	0.01

n.d. – not determined [121].

Table 10: Referenced partial molar volumes for calculations of slag molar volume by Mills and Rhine 1989 [120].

T in K	\bar{V}_i
	cm ³ /mol
	1773
SiO ₂	19.55+7.966· x_{SiO_2}
Al ₂ O ₃	28.31+32· $x_{Al_2O_3}$ -31.45· $x_{Al_2O_3}^2$
TiO ₂	24.0
Fe ₂ O ₃	38.4
FeO	15.8
MgO	16.1
CaO	20.7
Na ₂ O	33.0
K ₂ O	51.8*
MnO	15.6

Continuation of Table 10

	\bar{V}_i cm ³ /mol
P ₂ O ₅	65.7
CaF ₂	31.3

* - value was taken from [34].

Within this work, values of partial molar volumes are taken from Table 11. These are averages of referenced \bar{V}_i taken from [121]. The temperature dependence is less significant. Between 1300-1600 °C, the difference is around 10 % for TiO₂ and Li₂O. Those oxides are minor within a slag. Values of major components, as SiO₂, Al₂O₃ and CaO, ranges within 0.1-6.5 %. A temperature-depending calculation of \bar{V}_i was neglected for this reason. SiO₂ and Al₂O₃ are also set to be constant due to great improvement in comparison to calculation procedures recommended by [120]. Furthermore, the slag specie Na₂O-TiO₂ is replaced.

The advantage of this procedure is the quick change of values within calculation methods, e.g. within the source code of the Slag Viscosity Predictor (SVP), chapter 3.1. The SVP in connection with thermochemical equilibrium software FactSage permits the calculation of liquid slag composition. Additionally, the number of slag species is increased. Calculation of \bar{V}_i of not cited slag species are indicated by * in Table 11. Density data were taken from FactSage 6.4 and the program "View Data".

Table 11: Slag and mineral properties to calculate slag densities in this work.

Slag specie -	M_i -	Phase at RT -	ρ_i		\bar{V}_i liquid cm ³ /mol	this work
	g/mol		at RT	liquid g/cm ³		
SiO ₂	60.08	Tridymite	2.27	2.34	26.53	26.90
Al ₂ O ₃	101.96	Sapphire	3.97	3.99	25.68	37.29
Fe ₂ O ₃	159.69	Hematite	5.28	5.28	30.26	42.52
FeO	71.84	Wustite	5.87	5.87	12.25	13.80
CaO	56.08	Lime	3.35	3.35	16.76	16.74
MgO	40.30	Periclase	3.58	3.58	11.25	11.65
Na ₂ O	61.98	solid-a	2.27	2.27	27.30	29.22
K ₂ O	94.20	solid	2.32	2.32	40.60	46.56
MnO*	70.94	solid	5.45	5.45	13.02	13.02
TiO ₂	79.87	Anatase	3.84	4.25	20.80	23.61
CaF ₂	78.07	alpha	3.18	3.06	24.55	25.51
Ti ₂ O ₃ *	143.73	solid	4.60	4.60	31.25	31.25
NaF	41.99	solid	2.56	2.57	16.42	16.34
KF	58.10	solid	2.48	2.45	23.43	23.69

Continuation of Table 11

Slag specie	M_i -	Phase at RT	ρ_i		\bar{V}_i		this work
			at RT g/cm ³	liquid cm ³ /mol	at RT liquid	liquid	
MgF ₂	62.30	solid	3.08	3.01	20.23	20.67	20.67
FeF ₂ *	93.84	solid	4.09	4.09	22.94	22.94	22.94
MnF ₂ *	92.93	solid	3.98	3.98	23.35	23.35	23.35
Mn ₂ O ₃ *	157.87	Braunite	4.50	4.50	35.08	35.08	35.08

RT – room temperature

Calculations were validated on circa 210 measured density data points. Details and references are given in Table 38, appendix. Results are represented in Figure 33 a) and b).

Density calculations with densities of pure solid or liquid components are failing. An average error of 22 % and 23 % was found. The model of Lange and Carmichael for Fe-free melts has also less agreement to measured values. The average error is 34 %, Figure 33 a). The reason of deviations is not known exactly and is supposed to depend on not suitable partial molar volumes. The differences of \bar{V}_i between pure substances and within a mixture are significant.

The model of Lange and Carmichael featuring Fe shows great improvement of density calculation. An average error of 4.4 % is found. Introducing the model of Mills and Rhine is resulting in an average error of 3.7 %. For this work, a simpler model with constant \bar{V}_i is applied. The average error is 4.3 % and therefore in the range between Lange model and Mills model, Figure 33 b).

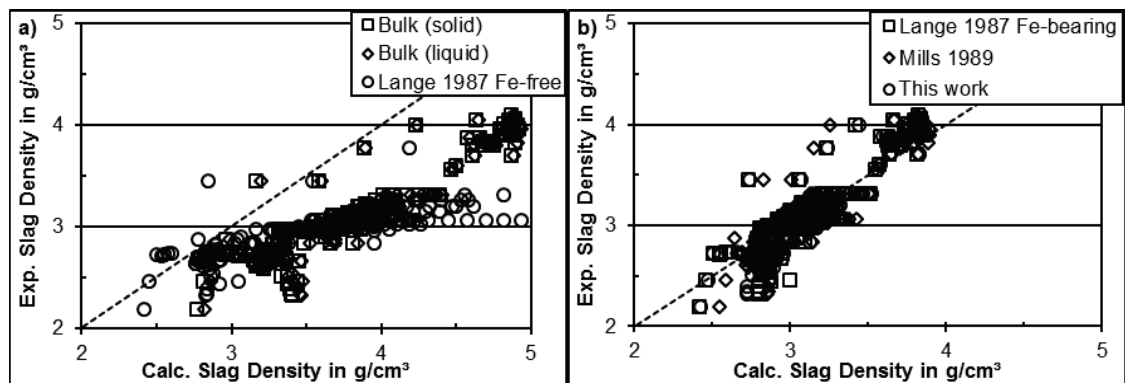


Figure 33: Comparison of measured and calculated densities by a) slag bulk composition, Fe-free model by Lange and b) Fe-bearing model by Lange, model by Mills and model used in this work.

Density measurements on slag sample S40 were performed by Mr. Daniel Schwitalla, TU Freiberg [123]. An average density of $\rho_{exp}=2990 \text{ kg/m}^3$ was observed by maximum

bubble pressure method. The model featured within this work is in agreement, $\rho_{thesis}=3005 \text{ kg/m}^3$.

The models of Lange or Mills are more detailed and more related to the physical background. The calculation method of density recommended within this work is simpler and shows the same agreement.

5.2.2 Solid Volume Fraction

Solid volume fraction f is calculated by Eq. (32). It is the volume relationship between minerals and remaining slag. The knowledge about the formed mineral is mandatory to estimate the remaining slag composition. Slag volume V_{slag} is obtained by transposing Eq. (26). Mineral volume $V_{mineral}$ is calculated by transposing Eq. (23).

$$f = \frac{V_{solid}}{V_{slag} + V_{solid}} = \frac{\sum_{n=1}^i V_{mineral,i}}{V_{slag} + \sum_{n=1}^i V_{mineral,i}} \quad (32)$$

Applied mineral densities are given in Table 39, appendix. These values were used within this work. In absence of temperature-related density function, the density at room temperature has to be selected. A significant deviation is not expected due to less differences in mineral density over wide temperature ranges.

5.2.3 Estimation of Slag Composition During Cooling

Most common methods to estimate the slag composition at elevated temperatures are:

- Thermochemical equilibrium calculations by e.g. FactSage, chapter 3.1.
- Experimental investigations by e.g. slag quenching and XRD analysis afterwards, chapter 6.3.

The precise calculation of slag compositions by thermochemical equilibrium is sophisticated due to the crystallization kinetics. Therefore, validation has to be done on experimental data.

Slag samples were quenched at high temperatures. Later, phase classification was achieved by XRD analysis. The experimental process is explicit described in chapter 6.3. Following calculation steps were done to estimate slag composition for a defined temperature point.

1. Obtain mass fractions of amorphous and mineral phases by XRD (Rietveld method) for at least two temperature points.
2. Do linear interpolation to estimate mineral mass fraction within the slag for all viscosity-temperature records.

3. Subtract SiO_2 , Al_2O_3 , CaO etc. of slag components by mass fractions SiO_2 , Al_2O_3 , CaO etc. of mineral phases.
4. Consider inaccuracy of phase determination. Therefore, check remaining mass fraction of slag components x_i . The maximum mass fraction of a mineral phase depends on the maximum available amount of each single slag component.
5. For $x_i < 0$, set the component to 0.
6. For $x_i \geq 0$, formed minerals are in accordance with available slag component mass fractions.
7. Calculate molar fraction of remaining slag.
8. Calculate molar volume of remaining slag.
9. Calculate the density of slag in respect to temperature.
10. Calculate the volume of slag in respect to temperature.
11. Calculate density of each mineral in respect to temperature.
12. Calculate the volume of each mineral in respect to temperature.
13. Calculate mass fractions and volume fractions of slag and mineral phases, respectively.

5.3 Viscosity Depending on Particles and Shear Rate

The formation of mineral particles due to crystallization has to be taken into account for the investigated slag systems. Consequently, the flow behavior can change to non-Newtonian when shear rate is varied. A number of models describe the non-Newtonian flow behavior of a fluid. For a condensed information read [4,6,35].

This work applies the Einstein-Roscoe equation due to its physical background and particle-depending viscosity calculation. It was also used in the original or a modified form in the works of [83,112,124–126] to describe the non-Newtonian flow within the liquid-solid temperature range of slags. Several advantages of the Einstein-Roscoe equation are:

- Predictions are valid for elevated solid volume fractions,
- less empirical than the simple power law models [6] or the Vand model with its constants c and d [127–129],
- the diameter of the suspended particles is not mandatory as in the Sherman model [130] and
- the number of boundary conditions (initial viscosity, initial uniform temperature, shear rate plateau) is less in comparison to the Shaw model [131] or the Quemada model [130].

The listed points are not a critic of the referenced works. Of course, other equations can be used for predicting the non-Newtonian flow.

5.3.1 Einstein-Roscoe Equation

The Einstein-Roscoe equation is based on primary works of Einstein 1906 and 1911 [132,133]. Einstein developed an approach to estimate the molecular dimensions of liquids for further work on diffusion. Roscoe seized the work of Einstein and applied the found results to solid particles within a liquid [134]. There, the dimension shifted from molecular to microscopic suspension systems. The basic assumption is given in Eq. (33), where η_r represents the relative viscosity, η_{mix} is the viscosity of the mixture of particles and suspending liquid, η_0 is the viscosity of the pure liquid and f is volume concentration of spheres. No respect to size distribution of suspended spheres is given.

$$\eta_r = \frac{\eta_{mix}}{\eta_0} = 1 + 2.5 \cdot f \quad (33)$$

Roscoe classified the occurrence of particles within a suspending liquid into three cases:

1. spheres of very differ sizes,
2. spheres of equal sizes and high concentration, and
3. spheres of equal sizes and low concentration

Introducing these particles to the original Einstein equation and the infinitesimal small increase of viscosity for an infinitesimal increase of f , differential Eq. (34) is established.

$$\frac{d\eta}{df} = \frac{2.5 \cdot \eta}{1 - f} \quad (34)$$

The differential solution of Eq. (34) concludes in Eq. (35). Factor a includes influences to viscosity due the size distribution of the suspended particles. Parameter n is -2.5 in respect of the principle work of Einstein.

$$\eta_{mix} = \eta_0 \cdot (1 - a \cdot f)^n \quad (35)$$

Parameter a was discussed on several solid volume fractions and particle size distributions. This factor also describes the interaction of particles within the suspending liquid. A certain amount of liquid is “frozen” between colliding spheres due to surface tension. As result, additional aggregates are formed, called spheroids, Figure 34. The size ratio of these spheroids is varying and depends, e.g. on particle concentration, surface tension referred to liquid and particle, shear rate etc. Due to the formation of “frozen” liquid, the effective particle volume increases and therefore the concentration also does increase.

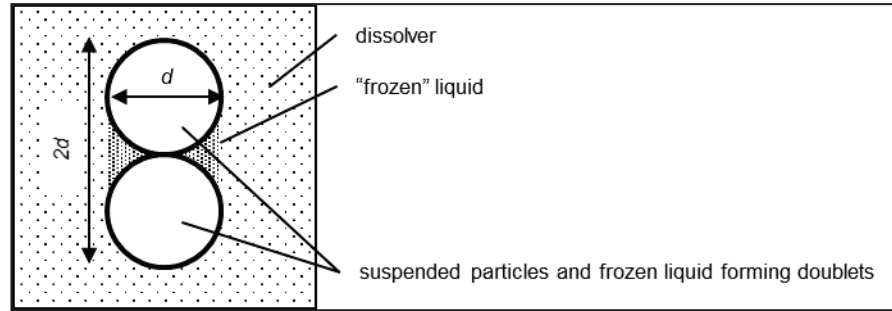


Figure 34: Schematic of collided particles forming a collision duoblet, size ratio 2:1 [134].

Parameter n describes the slope within the η_r - f -plot taken from the original work of Einstein. Depending on the analytical background, changing n is questionable. Some authors were applying changes to n , but without physical declarations. In view of minimize the modelling effort; parameter n should be set as constant. Most common values of a and n are given in Table 12. A more detailed literature survey is in Table 40, appendix.

Table 12: Values of a-factors taken from several references.

a-factor	Conditions / Remarks	Size ratio	Distributions	Reference
1.00	○ spheres of very diverse sizes	1.71:1	25 vol.-% < 3.4 μm	[135]
	○ valid for all concentrations $0.05 < f < 0.45$	2.74:1	25 vol.-% > 6.0 μm	
	○ water-based mixture		25 vol.-% < 150 μm 25 vol.-% > 190 μm	[136]
1.35	○ spheres of equal sizes	n.d.	n.d.	[129,134]
	○ high and medium concentrations			
	○ invalid for $f \geq \frac{1}{1.35} \geq 0.7401$ (close-packing)			
	○ water-based mixture			

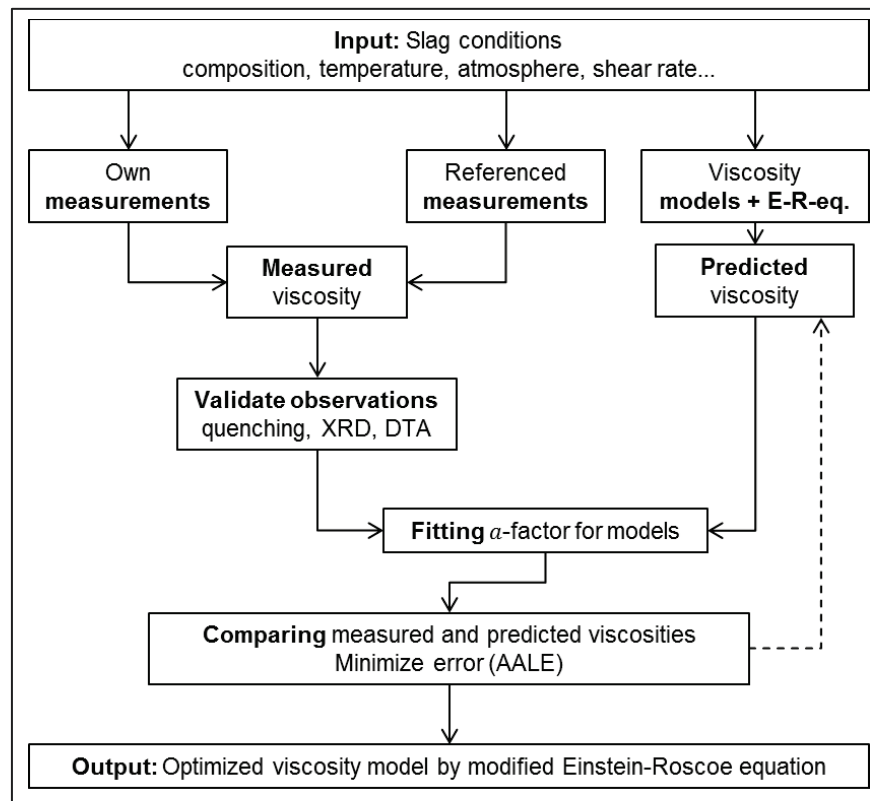
n.d. – not determined

5.3.2 Improved Modelling Approach by Modified Einstein-Roscoe

The Einstein-Roscoe equation is an opportunity to introduce the changes on flow behavior due to solid particles, chapter 5.1. As found by a number of references, the a-factor can be variable for different slag compositions, particle shapes and solid volume fractions f .

An approach to improve slag viscosity models is suggested, Figure 35. Viscosity of slag and the associated experimental parameters have to be recorded or at least found in literature. Prediction of viscosity is done parallel. Results of viscosity measurements, e.g. change from Newtonian to non-Newtonian flow behavior, have to be validated by phases analysis or DTA. Alternatively, mineral phase prediction can be done by

thermochemical equilibrium calculations. Providing the solid volume fraction f to the Einstein-Roscoe equation, a -factor fitting can be carried out. The quality of enhanced modelling is controlled by minimizing the average absolute logarithmic error AALE. When AALE achieves 0, a -factor fitting stops. Finally, viscosity prediction improves. The original viscosity model is not changed, but the result is enhanced by application of processing conditions.



AALE – Average absolute logarithmic error

E-R-eq. – Einstein-Roscoe equation

Figure 35: Flow chart of improved viscosity modelling.

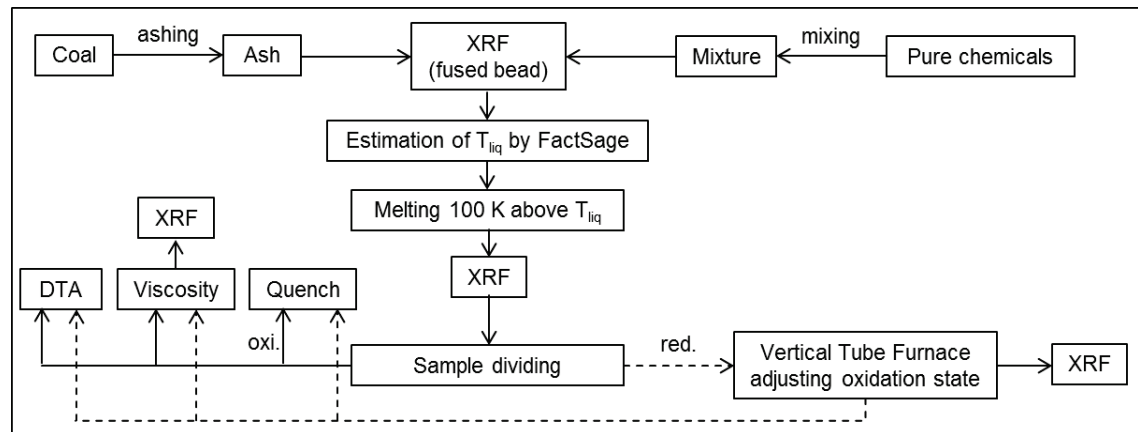
5.4 Summary of Last Chapters

- Several effects during the cooling of slag have to be taken into account.
- These circumstances could change the prediction performance of classic viscosity models. It is necessary to introduce the expected changes to viscosity modelling.
- Crystallization can be covered by computation or experiments. Thermochemical equilibrium software is available and was introduced in chapter 3.1. To overcome the complex process of crystallization, practical measurements on examined slags are suggested. Sample quenching and further XRD analysis for phase determination is carried out in this work.

- Slag density is calculated by a model applying partial molar volumes of slag components. The necessary values are collected from different references. A comparison to cited densities agrees well.
- The solid volume fraction (SVF) of slags is calculated by a simple model. Therefore, the slag density and the composition of formed minerals must be available. Several mineral densities are cited and included to the model.
- The slag composition is stepwise calculated on results of XRD phase analysis obtained by sample quenching and given temperature points.
- The Einstein-Roscoe equation was chosen to include the shear rate and particle depending flow behavior of a slag when mineral formation is experimentally verified. The a-factor of the E-R equation is fitted on viscosity measurements for each classic viscosity model as long the best agreement between recorded data and computed viscosity is found.

6. Experimental Procedures

Experimental investigations on slags are linked to several steps. Sample preparation and miscellaneous measurements have to be carried out to interpret data obtained by rotational viscometry. The following sections are giving an overview of applied measurement and preparations techniques. A flow sheet of sample handling is given in Figure 36.



oxi – oxidizing (air) atmosphere; red. – reducing atmospheric conditions by CO/CO₂

Figure 36: Schematic description of sample preparation and measurements for slag investigations.

The sample preparation and measuring methods are condensed described in the following section. A detailed overview with facility description is given in the appendix, chapters 13 to 15.

1. Ashing of coal for 36 h according to DIN 51719. In case of artificial slag samples, no ashing was necessary. Afterwards, ultimate analysis of ash or powder and X-ray fluorescence (XRF) of melted bead were carried out.
2. Slagging under air atmosphere in a crucible of Pt95-Rh5. Temperatures of 50-100 K above calculated liquidus temperature were applied to provide a completely molten, glassy and homogenous sample. Some ashes exhibit a swelling behavior during heating procedure. There were no relations found to slag composition nor heating rates. A heating rate of + 2 K/min is recommended. The slag was milled afterwards. XRF analysis on melt bead were obtained.
3. Slagging was repeated under reducing conditions when viscosity measurements under reducing conditions were planned. Therefore, a vertical tube furnace with atmospheric control of CO and CO₂ was in use. The temperature was also set to 50-100 K above calculated liquidus temperature.

6.1 Viscosity Measurements

Slag viscosity was determined by high temperature viscosity measurements in a Searle-type rotational viscometer manufactured by Bähr Thermoanalyse GmbH

(Hüllhorst, Germany). Crucible and spindle deviated from standard measurements systems. For non-standard viscometer measurement system, the shear rate $\dot{\gamma}_S$ has to be calculated by Eq. (36). R_C is the inner radius of the crucible, R_S is the radius of the bob, both in m, and n is the number of revolutions per minute of the spindle [4].

$$\dot{\gamma}_S = \frac{2 \cdot R_C^2}{R_C^2 - R_S^2} \cdot \frac{2 \cdot \pi \cdot n}{60} \quad (36)$$

Sample heating takes place by an inductive furnace. The crucible is axial placed within a water-cooled copper inductive coil. The crucible acts as susceptor and heats up the sample inside. Several challenges to provide repeatable experiments were successfully completed.

- An adequate insulation of the crucible to obtain an isothermal temperature profile by high-temperature resistance ceramic fiber-based insulation.
- Temperature calibration before each measurement series by an external B-type thermocouple.
- Viscometer calibration due to the non-standard measurement system. Silicon oils were applied at room temperatures. Standard glasses were selected at temperatures up to 1450 °C.
- Installing of a gas supply system for CO and CO₂.
- Estimating the influence of crucible material and inductive heating system to viscosity measurements. No significant error sources were found in literature.

Details of the mentioned points are in chapter 14, appendix.

6.1.1 Estimating Parameter Ranges of Viscosity Measurements

Viscosity measurements can be performed in wide temperature ranges and magnitudes of viscosity. To minimize the experimental expenditure, the range of parameters has to be limited. Additionally, parameters must be in vicinity of technical processes, Table 13. Finally, a compromise between measurement device options, gasification processes and examination of results has to be found, chapter 6.1.2.

Table 13: Parameter ranges of viscosity measurements.

Parameter	Remarks	Value/Range	Reference
Temperature	<ul style="list-style-type: none"> depends on gasification process and place in reactor (at burner, at gas outlet, in moving coal bed) 	>1200-1800 °C	[37]
Partial oxygen pressure	<ul style="list-style-type: none"> function of gas composition and place in reaction zone (oxygen nozzle, burner, coal particle, moving coal bed) 	1-1·10 ⁻¹⁵ atm	
Viscosity	<ul style="list-style-type: none"> depends on process entrained flow gasifier British Gas-Lurgi 	5-25 Pa s, 1-67 Pa s <10 Pa s	[44,137] [138,139]
Shear rate	<ul style="list-style-type: none"> not mentioned in literature for technical processes most viscosity measurements in literature were performed without consideration of shear rate estimation of shear rate on slag flow velocity and slag layer dimensions 	1-100 1/s	[137]

6.1.2 Viscosity Measurement Procedure

Viscosity measurements were carried out in non-isothermal procedure. Slag was measured from a high starting temperature with a standard cooling rate of $\alpha = -2$ K/min. Other cooling rates were also applied for further investigations. Abort criterions were achieving of a maximum viscosity of 100-200 Pa s or a maximum torque of 50 mNm.

The shear rate range was selected by several points. First, the shear rate within a technical process depends on the slag layer thickness and the flow rate, Table 13. Second, the viscometer head must be sufficient sensitive for shear rate detection at selected viscosities. So, the shear rate was selected to be in the range 12.5-75 1/s.

Starting temperature of all measurements was 50-100 K above estimated liquidus temperature. Holding time on constant temperature was set to 15 min. On the one hand, the sample has to be protected before volatilization. On the other hand, residence time of slag is less than one hour within the gasifier. During holding time, the immersed bob rotated to support steady state.

Atmospheres were selected as follows. Oxidizing conditions were applied by measuring viscosity in air. Reducing conditions were supplied by Brooks mass flow controllers with gas flows in the range of 600-700 ml/min of CO and 400-300 ml/min for CO₂, respectively. The aim was to establish atmospheres with 60-70 vol.-% of CO and 30-40 vol.-% of CO₂.

6.2 Thermal Analysis of Slags

Differential thermal analysis (DTA) was chosen to determine thermal events during slag cooling. Primary, the beginning or onset of mineral formation within the slag was desired.

Application of DTA on glass and slag samples was done by several authors to detect crystallization by sample heating [140–144] [145] and sample cooling [146–149].

An exothermal heat flow indicates the formation of crystals while melting of minerals is given by endothermal heat flows.

6.2.1 Experimental Conditions of DTA

A Netzsch STA 409 C was selected for this work. Evaluation of DTA curves was done by the software Netzsch Proteus®. The temperature was calibrated against indium, tin, zinc, aluminum, silver, gold und nickel.

In general, all samples were given to a DTA crucible made from Iridium. Slag powder as filled into the sample crucible with around 200 mg to improve heat transport during the measurement. Experiments under oxidizing conditions were provided by artificial air with a volume flow of 170 ml/min. Reducing conditions were established by purging the sample chamber with a mixture of CO and CO₂ gas. The used gas ratio ranged between 400-700 ml/min CO and 600-300 ml/min CO₂ (60-70 vol.-% of CO and 30-40 vol.-% of CO₂) and will be given in detail later. Scanning electron microscopy was done on some crucibles after DTA measurements to image the developed surface.

The temperature program was defined as follows.

- Heating up to 50-100 K above estimated liquidus temperature to support full melting with a heating rate of $a=20$ K/min,
- dwell time of 5-15 min to establish complete melting and remove of gas bubbles,
- cooling to 850 °C with each cooling rate, and
- repeating the experiment with the next cooling rate.

The selected cooling rates were $a=-1$, -2 , -10 , -20 and -60 K/min. It was supposed to cover a wide range of possible cooling rates as they occur in industrial processes. To prevent the apparatus before high thermal stress, the cooling rate was set to a minimum of $a=-1$ K/min. The upper cooling rate was $a=-60$ K/min and was limited by the Netzsch device.

6.3 Phase Determination

The determination of mineral phases within slag is necessary to re-calculate the slag composition for the investigated temperature point. Information has to be given about:

1. The amount of mineral phase in comparison to the remaining slag and

2. the composition (name) of the separated mineral phase.

Test series with selected slags were realized. These included sample quenching at desired temperatures with defined temperature programs and X-ray diffraction for phase analysis.

6.3.1 Quench Experiment Processing

Quenching is a method, where a slag sample is rapidly chilled from high to low temperature. The aim is to “freeze” the conditions at the interesting temperature. Together with subsequent analysis, information can be attained about:

- slag structure [42,150]
- $\text{Fe}^{3+}/\text{Fe}^{2+}/\text{Fe}_{\text{total}}$ ratios [121,151]
- mass fraction of slag and mineral [124,152]
- mineral phase name [153]

Approximately 2 grams of powdered sample were filled in a Pt-Au crucible. This amount of powder is sufficient to receive enough sample mass for afterwards analysis. Also, the rapid sample cooling is improved by small amounts. After placing the crucible within the isothermal temperature zone of the quench furnace, gas supply is switched on if necessary. To avoid the formation of explosive atmospheres, the alumina tube is purged for a sufficient long time with nitrogen to degrade the oxygen amount inside the alumina tube. In the next step, the purging gas CO/CO₂ was switched on.

The furnace is heated up with 10 K/min at low temperatures. Due to natural convection around the furnace, the heating rate is successively decreased. At higher temperatures, heating rates are around 1 K/min. All quenches started 50-100 K above liquidus temperature. A dwell time of 15 min was applied to let the sample equilibrate. The first quench was done at highest temperature by releasing the suspension wire. The crucible hits the water surface after <0.4 s of free fall and is immediately quenched within a water pool. Details of the quenching furnace are given in chapter 15, appendix.

All other experiments differ from the releasing temperatures. After reaching the highest temperature and holding the sample for 15 min, a cooling rate of -2 K/min was used for cooling down to the desired releasing temperature. There, the crucible suspension was released without any dwell times. After the experiment, the furnace was purged again with nitrogen in case of reducing atmospheres. When the furnace was sufficient cold, the crucible was taken from the quench pool.

6.3.2 Phase Determination on XRD Results

The quenched samples were removed from the Pt crucible and prepared in a McCone Micronizing Mill with cylindric grinding elements made of ZrO₂ to preserve the crystalline

structure. Rietveld refinement was applied for analysis. Amorphous phases were determined as residues of liquid slag portions “frozen” during the quenching, Eq. (37). This phase is clarified as “liquid slag” in the further investigations. Table 14 gives an overview of details applied to XRD analysis.

$$x_{amorph} = x_{slag} = 100 - x_{mineral} \quad (37)$$

Table 14: Parameters for phase determination by XRD analysis.

Device	D8 Discover with FlipStick sample changer
Tube	Co
Detector	Vantec-1
Slit	12 mm long, 15 mm wide
Rotation	none
Measurement time	2.5 h/sample
Measurement angle	10-90° (2 Θ)
Phase determination	Bruker EVA, Bruker TOPAS

The necessary minimum size for the detection of mineral particles has to be taken into account. References recommend a particle size distribution of 1-10 μm for ideal phase estimation. When particles are $<0.2 \mu\text{m}$, reflexes of X-rays become too stretched. A clear examination of the diffractogram can be hampered [154]. Similar size ranges are also reported by providers of analysis software [155].

6.4 Summary of Last Chapters

- The dynamic viscosity of molten slag samples was obtained by a rotational Searl-type viscometer with inductive heating and a non-standard measurement system made of Pt-Rh.
- Calibration of the non-standard measurement system and the temperature indication were required.
- A limitation in ranges of viscosity, temperature, gas composition and shear rates must be done due to the wide variations of these properties in technical processes.
- DTA was chosen to support the expected results of viscosity measurements in the upcoming chapters.
- A furnace was developed to generate quenched slags for further XRD phase analysis. These results will be used to explain the found results of viscosity measurements and DTA. Furthermore, a recalculation of temperature-depending slag composition is necessary for future modelling.

7. Results and Discussion

7.1 Selected Slag Samples

The viscosity of 42 slag samples was measured under air atmosphere, nitrogen or reducing conditions, Figure 37 a) to d). The mass-dependent B/A-ratio was achieved for sample classification. Unless otherwise noted, Eq. (12) was in use. The major part of samples is acidic and below $B/A=1$.

10 pairs of slag were measured at oxidizing and reducing conditions. The influence on viscosity of changing partial oxygen pressure is given in chapter 7.6.

A number of 18 samples was selected to perform extensive investigations by DTA, quenching and XRD phase analysis. These slags are named “extensively investigated” in the following chapters. They are also marked by filled symbols in Figure 37 a) to c).

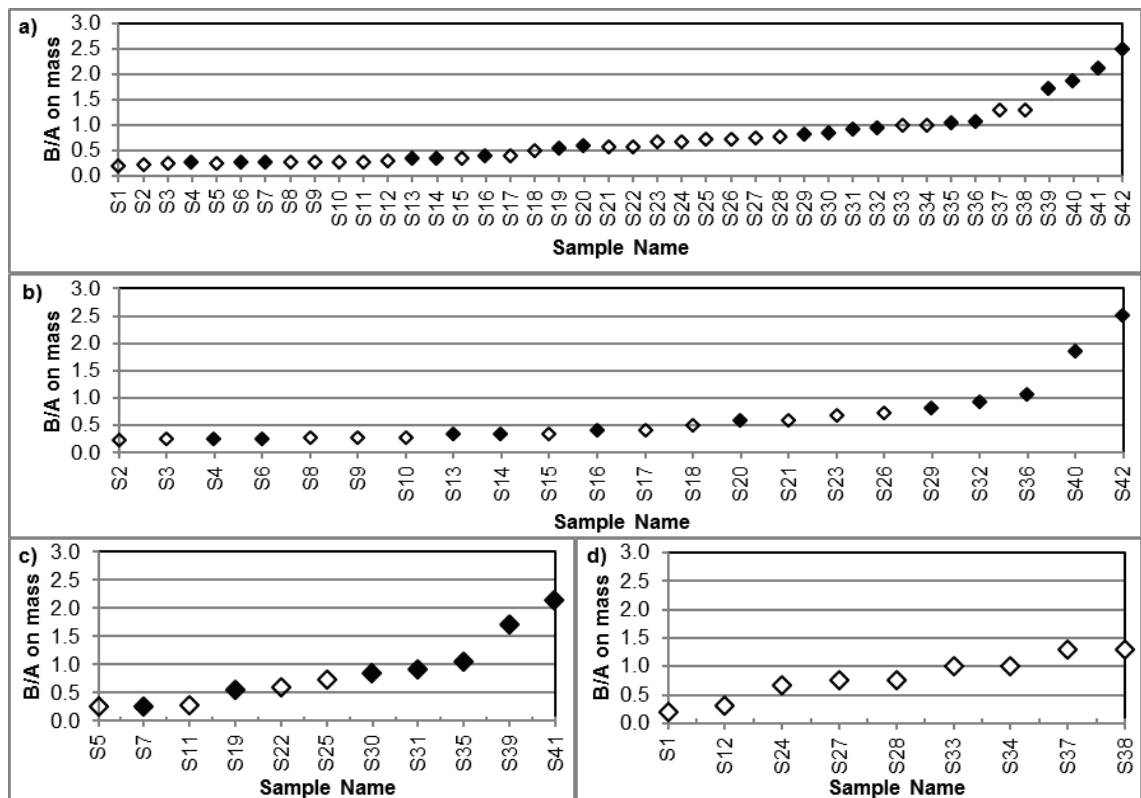


Figure 37: Samples listed by B/A-ratio for a) all samples, b) oxidizing conditions, c) reducing conditions and d) measured under nitrogen.

7.1.1 Slag Sample Composition Before Viscosity Measurements

The mass-based composition of slag samples is visualized by Figure 38. For integrity, a mole-based composition is given in Figure 39. Additionally, the composition is given by numbers in Table 44 and Table 45 in the appendix. There is no general advantage to prefer mass or moles for the investigated slags. In view of practicality, following evaluations are mass-based.

A huge variation in major components can be found for all samples. For example, SiO_2 ranges from 18-78 wt.-% for samples S2 and S4, while Al_2O_3 varies from 1.2-62 wt.-%

%. CaO is a minor component for sample S1 by 3 wt.-%, while CaO is 40.3 wt.-% within sample S23.

Additional network modifiers such as MgO, Na₂O, K₂O and P₂O₅ appear mostly as minor components. Exceptions are as follows. MgO is detected with over 10 wt.-% for samples as S24, S35 and S36. Also, K₂O can be found with more than 5 wt.-% in sample S27 and S37. P₂O₅ can be found with up to 4.8 wt.-% in sample S11, but is below 1 wt.-% for mostly all samples.

Other minor components are TiO₂ and sulfur, calculated as SO₃. TiO₂ can also vary up to 1.2 %, but is mostly around 0.5-1 wt.-%. The amounts of sulfur are commonly below 0.1 wt.-%, but there are also exceptions such as S15, S17 and S28 with more than 1 wt.-% of SO₃.

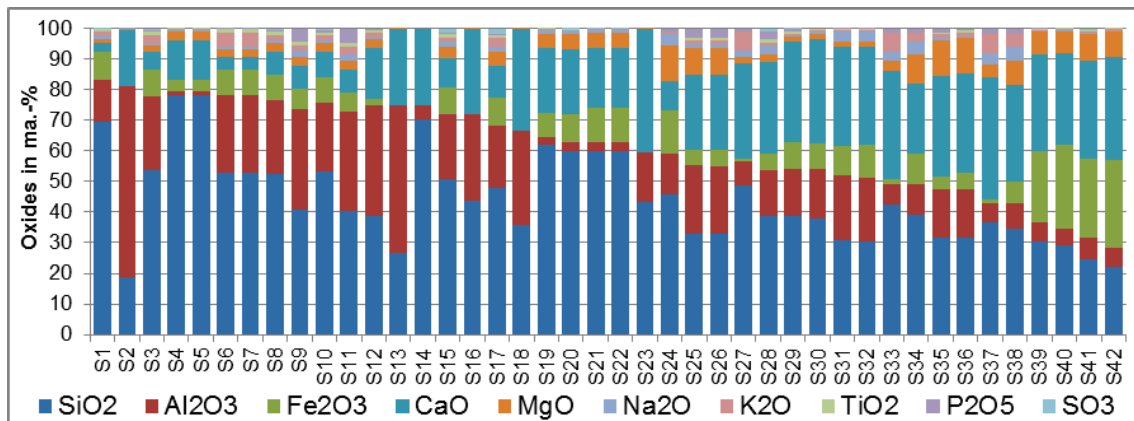


Figure 38: Mass-based composition of samples before viscosity measurements.

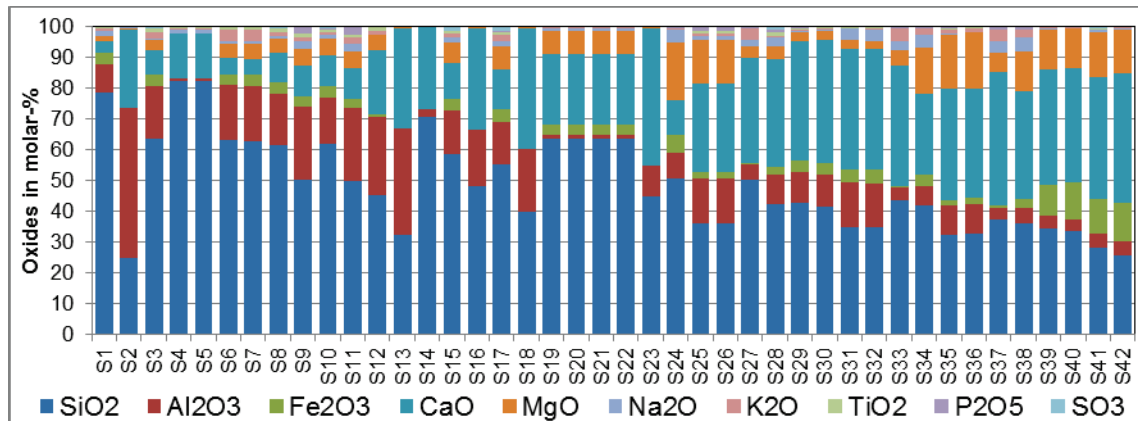


Figure 39: Mole-based composition of samples before viscosity measurements.

7.1.2 Slag Sample Composition After Viscosity Measurements

Removal of the slag from the crucible after viscosity measurement turned out to be difficult. After each test series, the slag was manually heated up to a temperature point to ensure stickiness by an elevated viscosity. A part of the sample remained at the measurement system's bob when it was lifted out of the crucible. After cooling, the bob was cleaned by physical force. The obtained slag pieces were milled and send to XRF analysis.

Figure 40 represents the composition of the specimen removed by the above outlined method. Equation (38) was applied to calculate the composition difference Δx_i where $x_{i,before}$ is the amount of the slag component within the initial composition and $x_{i,after}$ is the amount of the corresponding slag component within the extracted specimen.

$$\Delta x_i = x_{i,before} - x_{i,after} \quad (38)$$

Slag samples S1, S5, S14, S19 and S41 were skipped due to an unsuccessful removal. The found composition has to be used with care. Deviations from initial composition before measurements can result of

- depletion of slag components due to evaporation, K_2O , Na_2O , SO_3 etc. or
- partly crystallization and sinking of denser minerals within the crucible during removal of slag what leads to an inhomogeneous slag composition at the bob.

Two oxides were found to increase in a great measure. These are SiO_2 (27 slags) and TiO_2 (20 slags). The evaporation behavior of silicon oxide and TiO_2 are generally known to be low.

Sulfur SO_3 (22 slags) and P_2O_5 (19 slags) show also an increase, but were not included to the count due to average changes within approximately below 0.2 wt.-%. This is below the accuracy of the XRF analysis.

Examples of decreasing oxides are CaO (25 slags), Al_2O_3 , Fe_2O_3 and MgO (each 24 slags), Na_2O (21 slags) and K_2O (20 slags). A decreasing content implies a loss of components within the specimen stuck on the bob. This can be traced back on the enrichment of other oxides as pointed out above. CaO , Al_2O_3 , Fe_2O_3 and MgO are not volatile. Consequently, they form minerals, sinking to the bottom of the crucible. Na_2O and K_2O highly volatile and evaporate during the measurement.

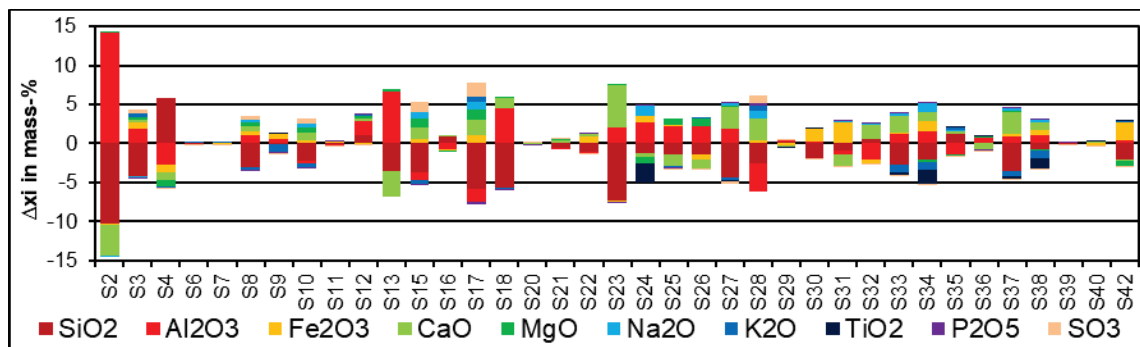


Figure 40: Slag composition after viscosity measurement.

7.2 General Results of Viscosity Measurements

Viscosity measurements on 42 slag samples were carried out with a variation in shear rates, atmospheres and cooling rates. Extensive evaluation follows in the upcoming chapters after introducing mineral formation and DTA results. Viscosities of all slag

samples and shear rate information are given within Figure 100 to Figure 106 in the appendix.

A condensed summary of observations in the viscosity range up to 100 Pa s for a cooling rate of -2 K/min is given in Table 15 to Table 17 for measurements under oxidizing, reducing and constant atmospheres. A brief description of the recorded viscosities follows. Several slags are changing the flow behavior within the investigated temperature range. This is indicated by two or more entries in the tables below. In cases where no transitions were found between Newtonian and non-Newtonian flow, the onset temperatures/viscosities are marked with "<" or ">". Some records started at temperatures in a region of non-Newtonian flow due to the limited torque sensitivity of the viscometer. However, the heating program started at temperatures above the calculated liquidus and a completely molten slag has to be supposed. Slags with only one viscosity measurement are marked with "n/a". No conclusion of flow behavior can be given without at least two different shear rates. These are slags S9 and S18 which were not measured with different shear rates.

The results are heterogeneous. Only Newtonian flow was found for samples S7, S17, S20 and S23.

The majority, 32 samples, is non-Newtonian from the beginning of the measurement or becomes non-Newtonian within the examined viscosity range. Without giving attention to the flow development during cooling, 23 samples are pseudo-plastic and 5 samples are dilatant.

A change in flow behavior from dilatant to pseudo-plastic was found for samples S4, S30, S35 and S40. Sample S8 starts from a dilatant flow and becomes Newtonian at lower temperatures. Turning from Newtonian to a pseudo-plastic flow can be found for 17 samples. Only 2 samples, S26 and S29, turn from a Newtonian to a dilatant behavior.

Estimations of the flow behavior can be carefully deduced by the basicity. In oxidizing conditions, the temperature for starting non-Newtonian flow has a minimum of circa 1175 °C at a B/A of around 0.8. The onset temperature increases for a basicity above or below B/A=0.8. Where B/A<0.8 forces higher onset temperatures than B/A>0.8. Similar observations are found for reducing and constant atmospheric conditions.

A rough correlation between the onset of shear-depending flow as function of viscosity can be derived from B/A-ratio. The onset viscosity of non-Newtonian flow decreases for increasing B/A-ratios. A non-Newtonian flow is expected even at low viscosities for slags with an elevated B/A-ratio. Exceptions of this correlation are the slags S4, S13, S16, S26 and S27. A good relationship is therefore found at reducing conditions. No critical temperature or viscosity exists for a wide range of slags. Non-Newtonian flow can occur within a wide range of temperature or viscosity.

Table 15: Flow properties of slags for a cooling rate of -2 K/min in the viscosity range up to 100 Pa s for oxidizing atmospheres.

Sample	B/A	Flow behavior	T _{onset} or T-range	η_{onset} or η -range
-	on mass	-	°C	Pa s
S2	0.230	pseudo-plastic	>1528	<66
S3	0.252	pseudo-plastic	>1566	<19
S4	0.255	dilatant	1576	15.5
		pseudo-plastic	1505	77
S6	0.256	pseudo-plastic	1435	74
S8	0.274	dilatant	>1450	<35
		Newtonian	<1450	>35
S9	0.280	n/a	n/a	n/a
S10	0.285	pseudo-plastic	1370	66
S13	0.337	pseudo-plastic	1495	6
S14	0.337	pseudo-plastic	1480	32
S15	0.346	pseudo-plastic	1353	52
S16	0.392	pseudo-plastic	1472	5
S17	0.412	Newtonian	-	-
S18	0.499	n/a	n/a	n/a
S20	0.578	Newtonian	-	-
S21	0.589	Newtonian	-	-
S23	0.684	Newtonian	-	-
S26	0.734	dilatant	1200	8
S29	0.805	dilatant	1176	22.5
S32	0.932	pseudo-plastic	1382	>9.4
S36	1.069	pseudo-plastic	1310	14.5
S40	1.857	dilatant	>1224	<35
		pseudo-plastic	<1224	>35
S42	2.497	pseudo-plastic	>1360	<13

Table 16: Flow properties of slags for a cooling rate of -2 K/min in the viscosity range up to 100 Pa s for reducing atmospheres.

Sample	B/A on mass	Flow behavior	T _{onset} or T-range °C	η _{onset} or η-range Pa s
-	-	-	-	-
S5	0.255	pseudo-plastic	1580	24.3
S7	0.256	Newtonian	-	-
S11	0.287	pseudo-plastic	1331	28
S19	0.546	pseudo-plastic	1166	20
S25	0.726	dilatant	>1284	<4
S30	0.833	Newtonian	>1180	<12
		dilatant	1130-1180	73-11
		pseudo-plastic	<1130	>75
S31	0.903	pseudo-plastic	1348	4.5
S35	1.046	Newtonian	>1260	<4
		dilatant	1230-1260	21-4
		pseudo-plastic	<1230	>21
S39	1.705	pseudo-plastic	<1260	<7
S41	2.126	pseudo-plastic	>1216	<13

Table 17: Flow properties of slags for a cooling rate of -2 K/min in the viscosity range up to 100 Pa s for constant partial oxygen pressures.

Sample	B/A on mass	Flow behavior	T _{onset} or T-range °C	η _{onset} or η-range Pa s
-	-	-	-	-
S1	0.192	pseudo-plastic	>1600	<62
S12	0.309	pseudo-plastic	>1470	<18
S25	0.726	pseudo-plastic	1227	20
S27	0.749	pseudo-plastic	1373	6
S28	0.764	dilatant	>1255	<13
S33	1.000	dilatant	>1210	<7
S34	1.000	pseudo-plastic	1241	3.7
S37	1.297	pseudo-plastic	1410	6.8
S38	1.300	Newtonian	-	-

7.2.1 Viscosity under Air Atmosphere

Results of viscosity measurements under oxidizing conditions are given in Figure 41. The temperature difference starting from 5 Pa s is depicted in Figure 42. Not all samples are supporting viscosity data for the chosen parameters.

Slags show a dramatic decrease in temperature to provide a certain viscosity within the B/A-range 0.23 to 0.75, namely 1656 °C to 1234 °C for a viscosity of 5 Pa s. Additionally, viscosity is changing less over wide temperature steps. For example, sample S2 has a temperature change of 43 K from 5-10 Pa s. This indicates a glassy flow behavior on the one hand and an elevated viscosity on the other hand due to the high amount of network modifiers.

An exceptional behavior is found for samples S13 and S14. Both samples are artificial slags made from mixtures of Al_2O_3 -CaO- SiO_2 powders. Sample S14 has a higher B/A-ratio than S13, but a higher temperature for similar viscosities is recorded. As reason, the high silica content of around 70 wt.-% in S14 is mentioned. Sample S13 has a silica content of 26 wt.-%, but is rich in Al_2O_3 . Within these simple artificial ternary systems, the possible network modifying behavior of Al_2O_3 is well distinct. The CaO content is equal for both artificial slags and therefore supposed to influence viscosity in the same way.

Attention should be given to generalize the observations within the B/A-range from 0.23 to 0.75. Although minimum temperatures are found within this B/A-range, the temperature differences are at maximum. Samples S20 and S21 showing temperature differences of almost 200 K from 5 to 100 Pa s.

The temperature to support a specific viscosity increases rapidly by increasing the B/A-ratio in the range 0.75-0.93. The temperature difference between viscosity changes becomes smaller. This indicates a crystalline cooling behavior. For example, sample S32 has a temperature difference of 20 K from 5-10 Pa s.

The temperature to reach a certain viscosity is decreasing for increasing B/A-ratios between 0.93 and 1.87. Dramatic viscosity differences are found for small temperature steps. Sample S40 exhibit a temperature difference of around 2 K from 5-10 Pa s. Above B/A=1.87, the temperature for a specific viscosity is increasing again. Results of the last two plotted samples S40 and S42 have to be carefully examined. These samples contain over 27 wt.-% of Fe_2O_3 . The influence of formed minerals has to be included. A correlation between viscosity and mineral formation is given in chapter 7.5.

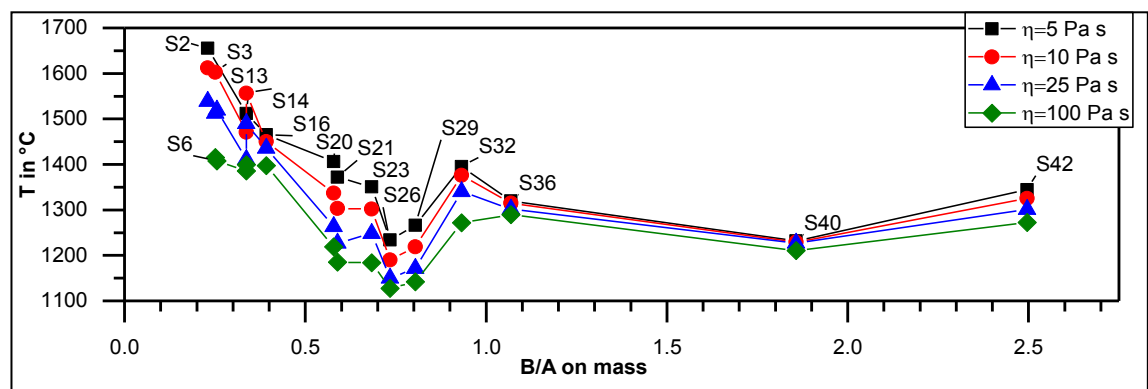


Figure 41: Viscosities related to temperature and B/A-ratio under oxidizing atmospheres, $a=-2$ K/min, $\dot{\gamma}=50$ 1/s.

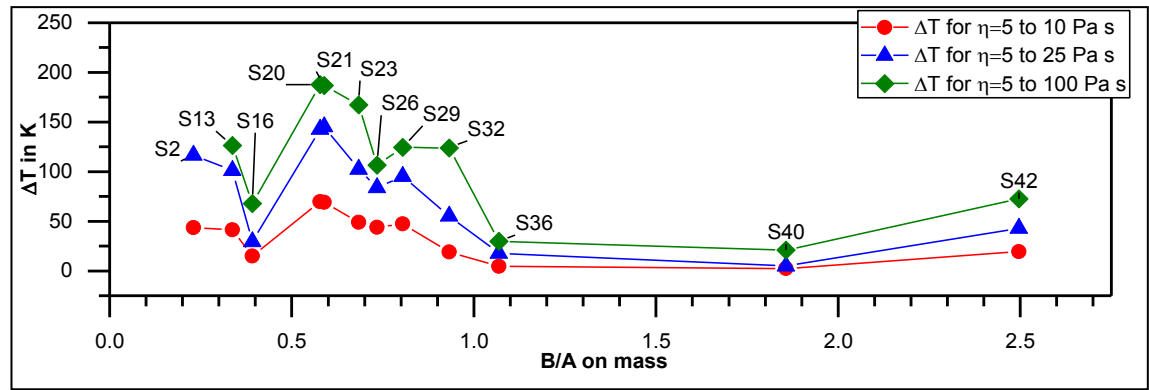


Figure 42: Temperature differences starting at 5 Pa s for selected samples under oxidizing atmospheres, $\alpha=2$ K/min, $\gamma=50$ 1/s.

7.2.2 Viscosity under Reducing Atmospheres

Results of slag viscosity measurements obtained under reducing conditions are given in Figure 43. Temperature differences from 10 Pa s to 25 and 10 Pa s to 100 Pa s are given in Figure 44. Data points of 5 Pa s were not recorded for all slags. Therefore, a limited number of viscosity measurements is given.

Similar to oxidizing atmospheres, a rapid temperature decrease is found for B/A-ratios between 0.25-0.83 to provide a desired viscosity. More than 1700 °C are necessary to provide a viscosity of 5 Pa s at B/A=0.25 due to the network forming behavior of SiO₂ and Al₂O₃. In contrast, a temperature of 1229 °C is sufficient to form a viscosity of 5 Pa s at B/A=0.83.

A significant influence on the viscosity-temperature behavior can be found for samples S5 and S7. B/A-ratios are close to each other, 0.256 and 0.257. A difference of around 90 K was found for providing a viscosity of 10 Pa s. Sample S5 is silica-rich with an SiO₂ amount of 78 wt.-%, while the dominant network modifier is CaO with 13 wt.-%. Sample S7 has an intermediate silica content of 53 wt.-% and an alumina content of 25.8 wt.-%. The network modifying power comes in this case from the elevated amounts of Fe₂O₃ and K₂O, 8.1 wt.-% and 4.5 wt.-%. At reducing conditions, Fe³⁺ is converted to Fe²⁺ and becomes definitely network modifying. Viscosity minimizing occurs.

The temperature has to be increased to provide a certain viscosity in the narrow range of B/A=0.83-0.90. For B/A-ratios>0.90, the temperature continuously decreases to obtain a specific viscosity. This behavior is contributed to the high amount of Fe²⁺, what is minimizing viscosity of the remaining liquid slag. Samples S39 and S41 contain over 23 wt.-% of FeO. Mineral formation is estimated and will be discussed within chapter 7.5.2.

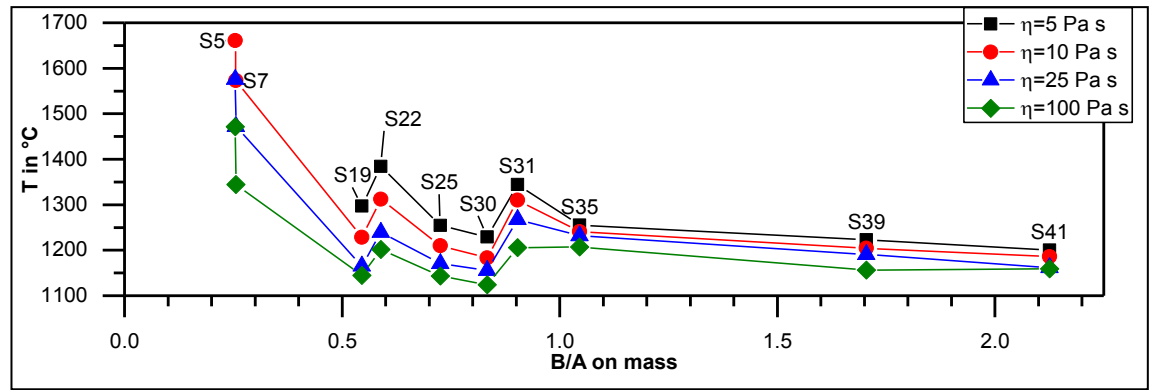


Figure 43: Viscosities related to temperature and B/A-ratio under reducing atmospheres, $\alpha = -2$ K/min, $\dot{\gamma} = 50$ 1/s.

The devolution of the temperature difference as function of B/A-ratio differs to results found at oxidizing atmospheres. In general, the temperature difference at reducing atmospheres is decreasing with increasing B/A-ratio. A maximum of around 225 K in temperature difference was recorded for S7, while S35 exhibit a difference of 34 K from 10 to 100 Pa s. The formation of particles was found to be responsible for a rapid viscosity increase within small temperature differences, chapter 7.5.2.

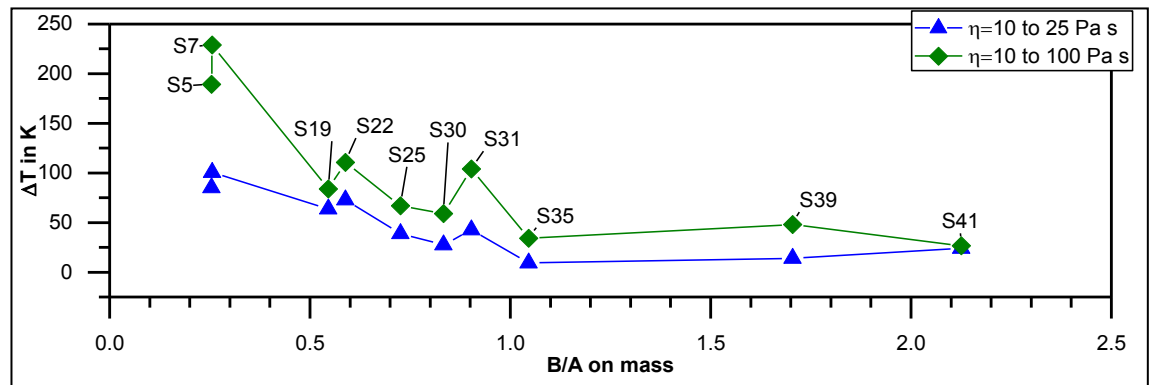


Figure 44: Temperature differences starting at 10 Pa s for selected samples under reducing conditions, $\alpha = -2$ K/min, $\dot{\gamma} = 50$ 1/s.

7.2.3 Viscosity under Constant Partial Oxygen Pressure

Results of viscosity measurements done under technical nitrogen atmosphere are given in Figure 45. The aim of applying technical nitrogen gas was to establish a constant partial oxygen pressure pO_2 of around $2 \cdot 10^{-6}$ atm for all temperatures.

A decreasing temperature results in an increasing viscosity. The obtained dataset shows a well-developed w-like curve. This is differing from results of oxidizing and reducing conditions. There, the curve shape is more u-, v- or l-like.

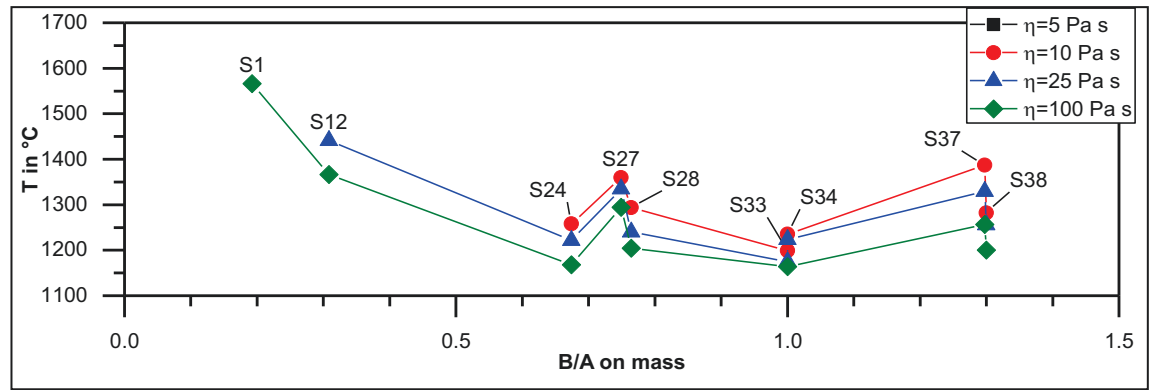


Figure 45: Viscosities related to temperature and B/A-ratio under technical nitrogen atmospheres, $\alpha=-2$ K/min, $\dot{\gamma}=25$ 1/s.

The fluctuating curve progression is related to the fluctuating ratio of $(\text{CaO}+\text{MgO})/(\text{SiO}_2+\text{Al}_2\text{O}_3)$, Figure 46. Under the assumption of CaO and MgO are network modifier, the temperature has to decrease to keep a specific constant viscosity for an increasing content of CaO and MgO, respectively. This agrees with recorded viscosity data except for S37 and S38, $B/A > 1.25$. The formation of minerals is expected, but not proven by viscosity measurements.

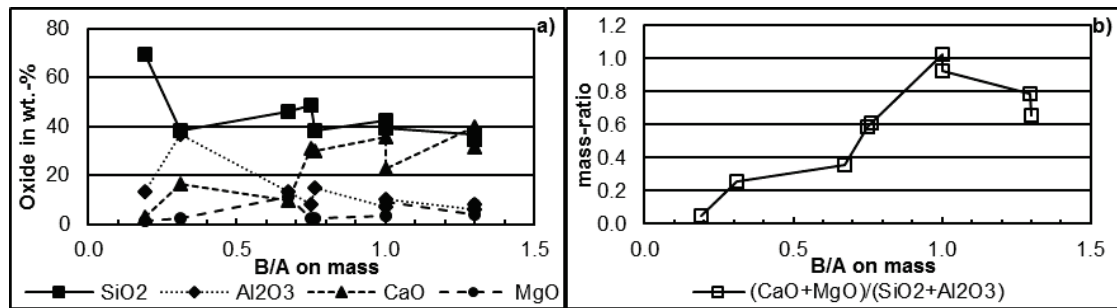


Figure 46: a) Contents and b) ratios of SiO_2 , Al_2O_3 and CaO of slags measured under nitrogen gas.

The temperature difference between minimum viscosity of 5 Pa s and elevated viscosities of 10, 25 and 100 Pa s is given in Figure 47. Against observations found for oxidizing and reducing conditions, the temperature difference increases significantly for B/A-ratios above 1.0. Differences up to 150 K are detected between 5 to 100 Pa s at B/A-ratios around 1.3. Samples S37 and S38 exhibit an almost Newtonian flow behavior.

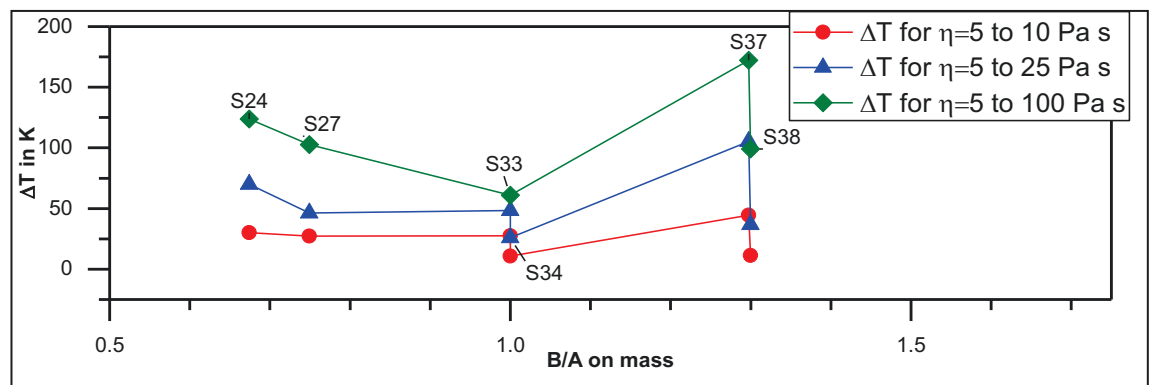


Figure 47: Temperature differences starting at 5 Pa s under technical nitrogen atmospheres, $\alpha=-2$ K/min, $\dot{\gamma}=50$ 1/s.

7.2.4 Summary of Last Chapter

Following points about the temperature-viscosity behavior of samples can be estimated from B/A-ratios:

- Oxidizing and reducing conditions are offering a similar curve course of the viscosity-temperature relationship depending on B/A-ratio.
- A minimum in viscosity was found for B/A-ratios around 0.75 for oxidizing and reducing conditions. The lower the B/A-ratio, the higher was the temperature to provide equal viscosities.
- Similar viscosity values were achieved for wide compositional differences above B/A-ratios of 1.0 and equal temperatures.
- Measurements at $pO_2=2 \cdot 10^{-6}$ atm offered m-like curve devolution. An elevated amount of CaO and MgO seems to be the reason for the observed behavior. Crystallization is assumed at B/A-ratios over 1.2 for this sample series.

Temperature differences at equal viscosities are describing following slag properties:

- Wide temperature differences denote glassy flow behavior, while small differences indicate crystalline flow behavior.

Observations at oxidizing conditions are as follows:

- B/A-ratios from 0.23 to 1.0 strongly differ in temperature differences of equal viscosities.
- B/A-ratios above 1.0 show similar trends in viscosity-temperature relationships.

Observations at reducing conditions:

- Temperature differences between viscosity steps decreases with increasing B/A-ratio.

Observations at constant partial oxygen pressure:

- Temperature differences significantly increases for B/A-ratios above 1.0. The fluctuating ratio of $(CaO+MgO)/(SiO_2+Al_2O_3)$ is similar to the viscosity trend.
- A glassy slag flow was found for elevated B/A-ratios. This is not in accordance with findings of oxidizing or reducing atmospheric conditions. A direct influence of atmospheres could not be proved. Also, the influence of CaO and MgO must be taken into account. Partial crystallization is assumed, but is not proven by the Newtonian flow behavior of S37 and S38.

7.3 Mineral Formation

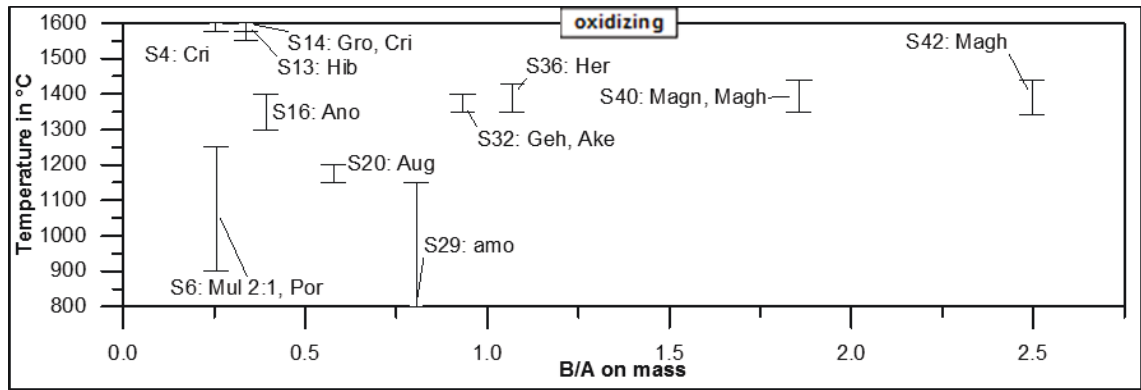
7.3.1 General Results on Primarily Mineral Formation

Selected slag samples were quenched and mineral formation was analyzed by XRD. The temperature ranges of primarily detected minerals are given in Figure 48 and Figure 49 for oxidizing and reducing conditions, respectively. The formation of primarily minerals is given within temperature steps. Only minerals are listed which are more or equal than 1 wt.-%. Phases below 1 wt.-% are summed up as "Residual oxides".

Three groups of samples established. The first group exhibit minerals at highest quenching temperatures. This indicates an incompletely molten slag due to the limited quench furnace temperature. These are samples S4, S13 and S14. Found mineral species were Cristobalite SiO_2 , Hibonite $\text{CaAl}_{12}\text{O}_{19}$ and Grossular $\text{Ca}_3\text{Al}_2(\text{SiO}_4)_3$. The existence of Cristobalite and Hibonite is in agreement with their high liquidus temperatures, 1722.7 °C and 1832.8 °C, respectively. Whereas pure Grossular seems not be stable at temperatures above 800 °C [84]. The presence of Grossular is therefore a kinetic and mass transfer related issue. Grossular could decompose to other minerals and finally melt completely after a dwell time of more than 15 min. Slags S13 and S14 have elevated amounts of calcia, around 25 wt.-%. This prevents the dissolution of calcia-rich minerals. A similar behavior is found for S4 with an elevated amount of silica, 78 wt.-%. Therefore, silica-rich minerals are inhibited to melt. Completely molten slags are supposed when holding time or final temperature would be increased.

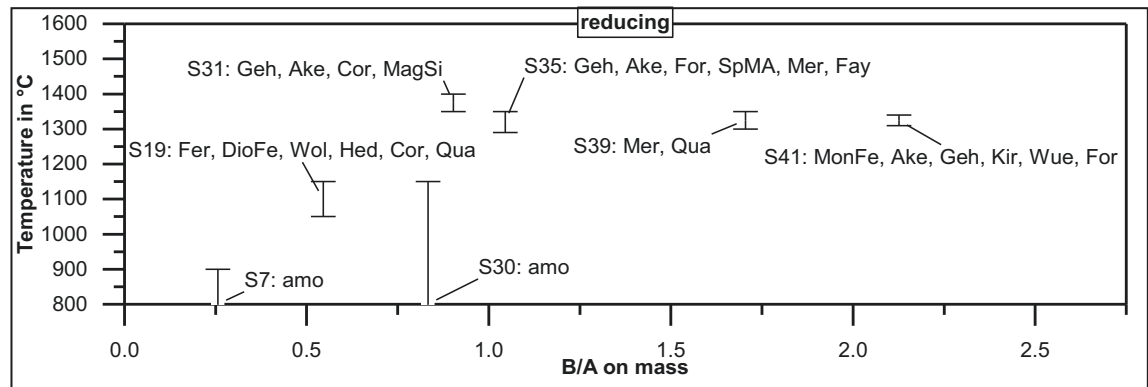
The second group of slags is amorphous at all investigated temperature ranges. These are samples S7, S29 and S30. There is no clear evidence within the composition to explain the observed behavior. The influence of the B/A-ratio can be excluded due to the wide range from B/A=0.25 to B/A=0.80.

The third group of slags is forming minerals within the observed temperature ranges. Some samples form more than one primary mineral. No statement can be done which is the first formed mineral when several mineral phases are found at one quenching point. Samples S35 and S36 are also included to the third group of slags while solid phases are found at 1430 °C. XRD analyses verify the Spinels MgAl_2O_4 and Hercynite $\text{Fe}^{2+}\text{Al}_2\text{O}_4$, respectively. Calculated liquidus temperatures are around 1381 °C. Nevertheless, samples S35 and S36 were defined to be completely molten due to an insufficient dwell time.



Abbreviations of mineral names are in Table 53, appendix.

Figure 48: Primarily detected minerals found by quenching experiments at oxidizing atmospheres.



Abbreviations of mineral names are in Table 53, appendix.

Figure 49: Primarily detected minerals found by quenching experiments at reducing atmosphere.

7.3.2 Influences on Primarily Mineral Formation

Minerals found at samples S4, S13 and S14 are not considered within the discussion below. Sample S4 was not quenched under reducing conditions due to the high liquidus temperature while samples S13 and S14 are free on iron oxide.

Atmospheres are influencing the number of minerals. At oxidizing conditions, not more than two primarily minerals are formed for each slag when crystallization occurs. Under reducing conditions, the number of primarily minerals increases per slag. Not less than two minerals were detected when primarily crystallization starts. The influence of a decreased viscosity at reducing atmospheres is not proofed. As found in chapters 7.2 and 7.6, a significant lowering of viscosity was recorded for sample S7 and a CO-CO₂ gas mixture. The corresponding sample S6 (oxidizing conditions) exhibited a higher viscosity. A lower viscosity should enhance the mass transfer of slag components to the growing mineral. Regardless, S7 was found to be amorphous although an improved crystallization behavior was to be supposed. A similar behavior is given for the slag pair S29/S30.

Five slag components are found in detected minerals. These are SiO₂, Al₂O₃, CaO, MgO and Fe₂O₃. Silica and calcia are the most consumed oxides within the whole B/A-

ratio. A silica content of more than 30 wt.-% is needed to form silicon-containing minerals.

Calcium can be consumed from minerals even at amounts of 4 wt.-%, S6. It is excluded from mineral formation especially at B/A-ratios above 1.0, elevated amounts of iron oxide and oxidizing conditions. Under reducing atmospheres, calcium is used in mineral formation without any restrictions to the entire slag composition.

Alumina is absent from mineral formation for amounts of less than 15 wt.-%. A restriction due to side effects of other components cannot be excluded, but the data set is insufficient for a clear statement.

Magnesia is only consumed within 7 slags. There is no clear evidence on a limiting content where it is used for mineral formation. For example, slag S32 has 1.3 wt.-% of MgO and Akermanite $\text{Ca}_2\text{MgSi}_2\text{O}_7$ was detected. However, sample S36 has an MgO amount of 11.9 wt.-%, but no magnesia-containing mineral was found. Reducing conditions and a B/A-ratio above 0.5 are enhancing the consumption of MgO.

An Fe_2O_3 concentration of more than 5.5 wt.-% prefers the formation of iron containing minerals, but the absence of Fe-containing minerals was even found for Fe_2O_3 contents of more than 23 wt.-%, S39. Ferric oxide, Fe^{3+} , was found only in minerals formed at oxidizing conditions. Ferrous oxide, Fe^{2+} , was found in minerals formed at both oxidizing and reducing atmospheres, together with Fe^{3+} . The existence of Fe^{2+} at oxidizing conditions can be explained as follows.

- Fe^{2+} does not partly appear within minerals formed at oxidizing conditions. The charge exchange by other substances, e.g. Al_2O_3 in slag S6 has to be taken into account. Also, slags with CaO amounts over 20 wt.-% are providing the formation of ferrous-containing minerals, as found in S20, S36, and S40.
- Fe^{2+} and Fe^{3+} are forming a thermochemical equilibrium even under oxidizing conditions. The higher the temperature, the higher the amount of Fe^{2+} within the liquid part of the slag. If Fe^{2+} is integrated into minerals, a change in oxidation state is inhibited by kinetics.

Iron-containing minerals seem to be more formed by an increasing B/A-ratio. This effect is related to the growing amount of iron oxide within samples of elevated B/A-ratios, Figure 38.

7.3.3 Mineral Formation over Wide Temperature Ranges

Selected slags were quenched at different temperatures to determine the phase distribution. Phases obtained under oxidizing conditions are given in Figure 119 and Figure 120, see appendix. Results of reducing conditions are given in Figure 121 and Figure 122, see appendix.

The amorphous part of a sample was defined to be glassy slag. Minerals only listed when the detected amount was above 1 %. Below this limit, minerals listed as “Residual oxides” and their related metal ion part. Some slags were quenched above or below temperatures where viscosity data was not recorded. These are cases to estimate the liquidus temperature. The discussion of mineral formation will be done also for temperature ranges above the 100 Pa s limit.

Aim of quenching was not to compare all slags with each other. Reasons of this investigation were first to compare results taken from DTA and viscosity measurements. Second, this was the origin to evaluate results for further phase modelling.

An overview of all counted mineral phases is given in Figure 50. Incompletely molten slags are S4, S13, S14, S35 and S36. Slag S4 was not further investigated due to the high melting point. Slags S35 and S36 were defined to be completely molten due to the lesser amounts of minerals. Slags S13 and S14 are artificial and consists of alumina, calcia and silica. The high-melting mineral Hibonite $\text{CaAl}_{12}\text{O}_{19}$ is the initial solid phase found in S13. Hibonite grows to approximately 20 wt.-% at 1360 °C and decreases at lower temperatures to 7 wt.-%. S13 is completely solid at 1250 °C. Main phases are Gehlenite $\text{Ca}_2\text{Al}_2\text{SiO}_7$, Anorthite $\text{CaAl}_2\text{Si}_2\text{O}_8$ and pure alumina Al_2O_3 . Slag S14 shows Grossularia $\text{CaAl}_2(\text{SiO}_3)_3$ and Cristobalite SiO_2 as initial minerals with a total of 5 wt.-%. Grossularia is not found at temperatures below 1500 °C and Cristobalite becomes the main mineral phase, followed by Quartz SiO_2 . The occurrence of Quartz at this temperature is exceptional. High-temperature Quartz is formed at 867 °C. Reason of the occurrence can be an inadequate cooling rate during quenching and consequently the development of Quartz from a silica-rich part of the melt. The formation of Quartz from a meta-stable phase is not taken into account [156,157]. The present minerals can be the seeds for heterogeneous crystallization. Starting the cooling of the same slag from a completely molten state can end in an entire different mineral formation.

Molten slags with occurring crystallization are S6, S7, S16, S19, S20, S31, S32, S39, S40, S41 and S42. Slags S35 and S36 are additionally defined to be in molten state. The number of formed mineral phases depends on the quantity of slag components and the quenching temperature. Artificial slag S16 made from a mixture of SiO_2 - Al_2O_3 - CaO is forming 75 wt.-% of Anorthite $\text{CaAl}_2\text{Si}_2\text{O}_8$ at 1300 °C. The residual phase is slag. Natural slags show another behavior. The number of minerals varies from two to nine, natural slags S32 and S35 at temperatures around 1300 °C. No natural slag was completely crystallized. The amorphous part ranged from 85 wt.-% at 900 °C to 5 wt.-% at 1250 °C for S6 and S35. The number of discovered minerals agrees with observations from chapter 7.2. Lowest viscosities and Newtonian flow behavior were found for slags in a B/A-range around 0.50-0.75.

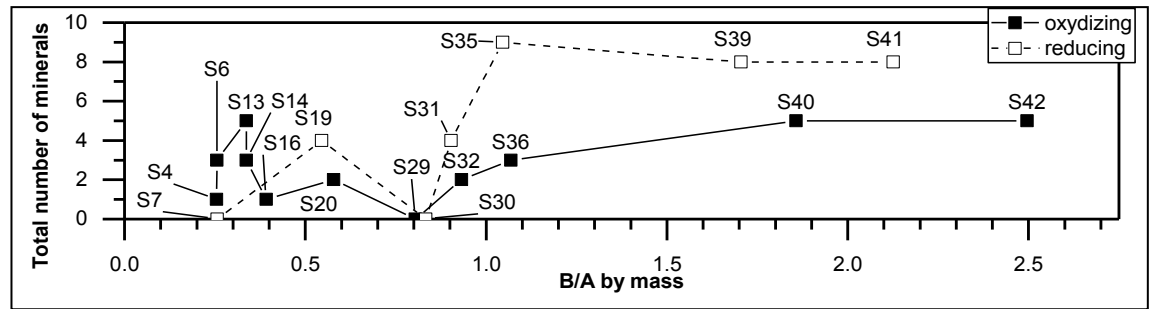


Figure 50: Number of detected mineral phases including all temperature points.

The found minerals vary within the B/A-ratio. While for S6, $B/A=0.256$, mostly alumino-silicates are developed, the mineral complexity increases with increasing B/A, Figure 51. Excluding artificial slag S14, the artificial slags S13 and S16 form mostly calcia- alumino-silicates like Anorthite $\text{CaAl}_2\text{Si}_2\text{O}_8$ and Gehlenite $\text{Ca}_2\text{Al}_2\text{SiO}_7$. B/A-ratios are below 0.40. Calcia-alumino-silicates are the major phases above a B/A-range of 0.833. Especially for reducing conditions, the number of minerals has a significant maximum above a B/A-ratio of 1.04, S39. Major phases above $B/A=1.70$ are Akermanite $\text{Ca}_2\text{MgSi}_2\text{O}_7$, Monticellite- Fe^{++} $\text{CaFe}_{0.12}\text{Mg}_{0.88}\text{SiO}_4$, Magnetite $\text{Fe}^{++}\text{Fe}^{+++}_2\text{O}_4$ and Spinel $\text{MgAl}_{0.79}\text{Fe}^{+++}_{1.21}\text{O}_4$ around a temperature of 1200 °C.

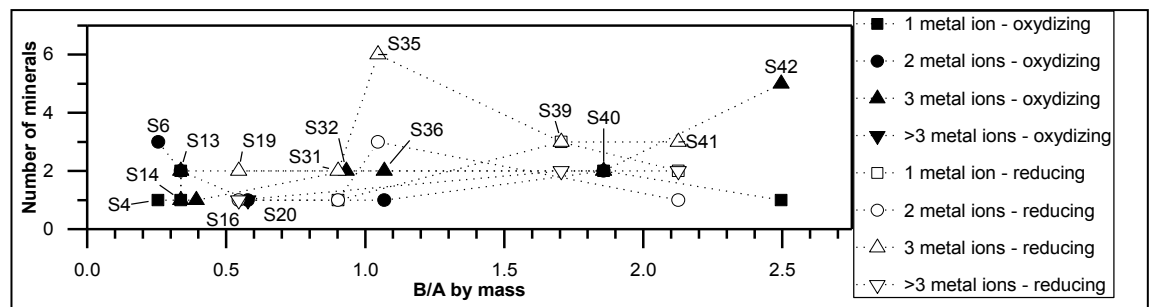


Figure 51: Number of minerals in respect to amount of metal ions.

The consumption of Al^{3+} by the number of minerals for oxidizing and reducing conditions is given in Figure 52. Again, this evaluation is not done on a single temperature. Results are taken from wide temperature ranges. Oxidizing conditions seems to force the formation of Al^{3+} containing minerals at B/A-ratios below 0.5. This result is partly valid. Slags S13, S14 and S16 offers high amounts of Al_2O_3 . This supports the integration of aluminum containing minerals. No measurements were carried out for these slags at reducing conditions. However, no comparison between oxidizing and reducing atmospheres can be done on these slags. Slag S6 was repeated also under reducing conditions, see results of S7. There, slag was amorphous for all temperature steps. Although the Al_2O_3 content falls short of 10 wt.-%, high B/A-ratios lead to an increased amount of minerals consuming Al^{3+} .

Reducing conditions result in a significantly high number of aluminum consuming minerals at B/A-ratios around 1.0. The power of integration seems to lose efficiency for

B/A-ratios above 1.8. Slag pair S42/S41 was made from same coal ash, but show small deviations in their composition. This leads to different B/A-ratios. The loss of component integration cannot be exactly determined on the B/A-ratio.

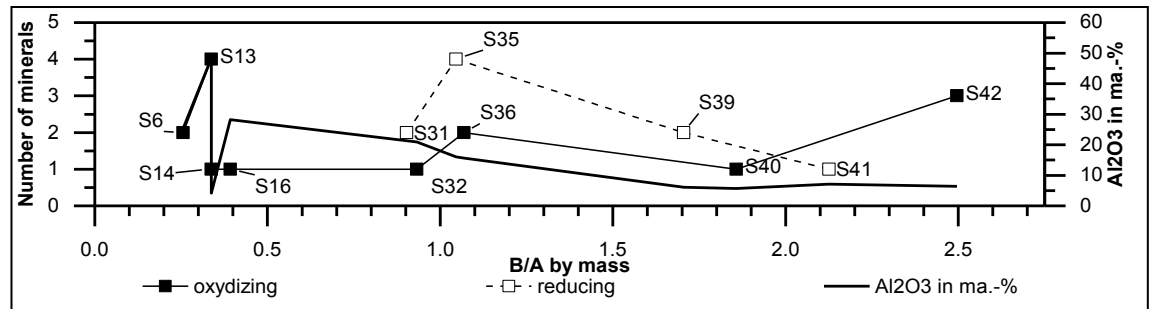


Figure 52: Number of Al-containing minerals with respect to atmosphere.

The number of Ca^{+} -containing minerals with respect to the B/A-ratio is given in Figure 53. No minerals with Ca^{+} were found for B/A-ratios below 0.3. Slags S13, S14 and S16 exhibit the formation of Ca-containing slags. These slags are artificial and only consist of the system Al_2O_3 -CaO-SiO₂. Results maybe not comparable to natural slags. Except for slag pair S32/S31, reducing conditions forces the consumption of Ca^{+} by minerals. Ca^{+} is known as a good network modifying mobile ion due to the large field strength in comparison to the ion diameter. Reducing atmospheres lowers the viscosities. The lower viscosity is improving the transport of Ca^{+} -ions. The elevated amount of CaO, up to 30 wt.-%, has also to be considered for mineral formation.

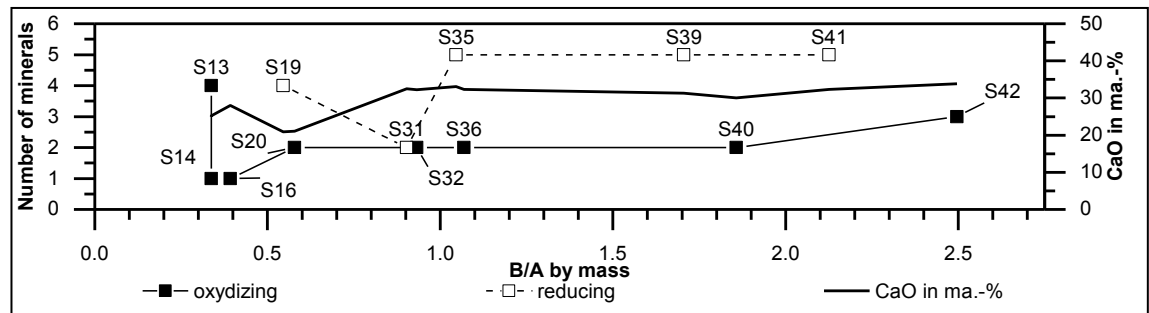


Figure 53: Number of Ca-containing minerals with respect to atmosphere.

The number of Mg^{+} -consuming minerals over the B/A-ratio is given in Figure 54 for oxidizing and reducing atmospheres. No Mg^{+} -containing mineral was detected at B/A-ratios below 0.5. Although, MgO is present in samples below this B/A-ratio. Oxidizing and reducing conditions generate the similar number of minerals within B/A-ratios of 0.5 to 1.0. Above B/A=1.0, reducing conditions are forcing a significant higher number of Mg^{+} -minerals. Like results exhibit from Ca^{+} -minerals, Mg^{+} is an ion with an elevated field strength. The limitation of Mg-mineral formation is the amount of MgO.

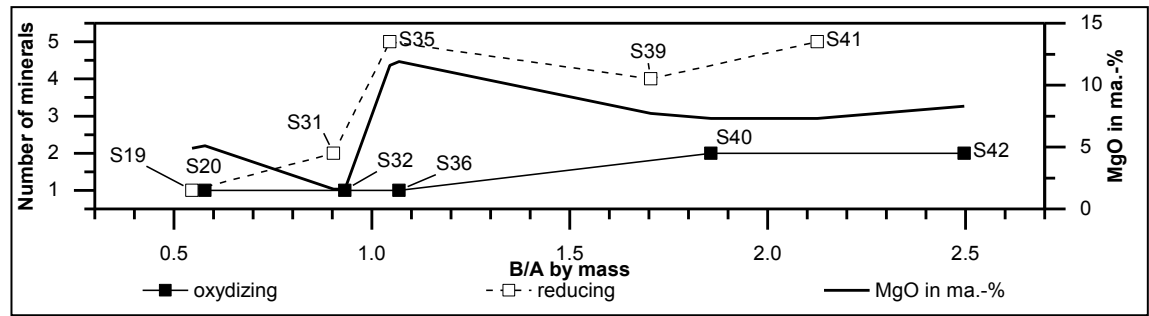


Figure 54: Number of Mg-containing minerals with respect to atmosphere.

The integration of Fe^{2+} and Fe^{3+} to minerals was observed over wide B/A-ratios, Figure 55. Ferric iron Fe^{3+} was found only for oxidizing conditions. Especially at high Fe_2O_3 -contents, the found minerals are Maghemite $\text{Fe}^{+++}_2\text{O}_3$, Brownmillerite $\text{Ca}_2(\text{Al}, \text{Fe}^{+++})_2\text{O}_5$ and the Spinel $\text{MgAl}_{0.79}\text{Fe}^{+++}_{1.21}\text{O}_4$. Two slags, S6 and S40, also generate minerals with ferrous iron Fe^{2+} at oxidizing conditions. There, the main mineral is Magnetite $\text{Fe}^{++}\text{Fe}^{+++}_2\text{O}_4$.

At reducing conditions, only minerals containing ferrous iron Fe^{2+} are formed. Major minerals are Monticellite-Fe $\text{CaFe}^{++}_{0.12}\text{Mg}_{0.88}\text{SiO}_4$, Ferrobustamite $(\text{CaFe}^{++})(\text{SiO}_3)_2$ and Hedenbergite $\text{CaFe}^{++}\text{Si}_2\text{O}_6$.

An elevated iron content does not force the formation of Fe-consuming minerals. S35 contains 4 wt.-% of Fe_2O_3 and Fayalite $\text{Fe}^{2+}_2\text{SiO}_4$ was detected. S31 and S32 are containing circa 10 wt.-% of Fe_2O_3 , but no iron was found within minerals.

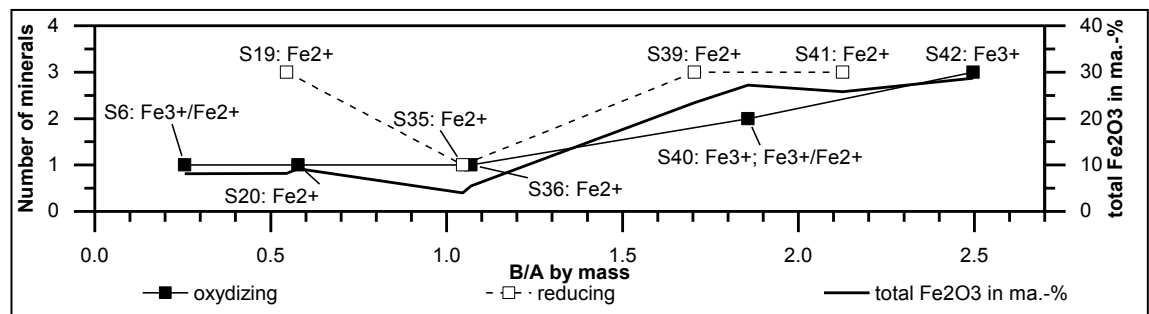


Figure 55: Number of Fe-containing minerals with respect to atmosphere.

Finally, mineral formation is discussed on pairs of similar B/A-ratios, but changed atmospheric conditions. The slag pair S6/S7 differs less. Phases of aluminosilicates of around 10 wt.-% are detected in S6 under air at 900 °C. S7 is amorphous in reducing conditions. The found viscosity at 900 °C is in the order of several magnitudes and does not play a role in mass transfer.

Slag pair S20/S19 differs also in the temperature of initial crystallization. First minerals, mostly Fe^{2+} and Fe^{3+} Pyroxene, found at 1150 °C in S20 under oxidizing conditions. S19 was quenched at a lower temperature of 1050 °C. There, main minerals are Ferrobustamite $(\text{CaFe}^{2+})(\text{SiO}_3)_2$ with circa 30 wt.-% and Fe^{2+} -containing Diopside $\text{Ca}(\text{Mg}_{0.75}\text{Fe}_{0.25})\text{Si}_2\text{O}_6$ of around 7 wt.-%.

Slag pair S32/S31 agrees well in view of phase names. Gehlenite $\text{Ca}_2\text{Al}_2\text{SiO}_7$ is the major phase. Akermanite $\text{Ca}_2\text{MgSi}_2\text{O}_7$ is the second mineral found at 1350 °C under oxidizing conditions. Under reducing conditions, Corundum Al_2O_3 and Magnesium Silicate Mg_2SiO_4 are additionally formed. The amount of liquid slag is doubled at 1300 °C for oxidizing conditions than for reducing ones. The slag amount keeps constant around 20 wt.-% from 1300 to 1200 °C at reducing conditions. There are no significant changes in the mass distribution of minerals.

Slag pair S36/S35 agrees well in view of residual slag at similar temperatures. On the other hand, the formed minerals are not comparable. The main mineral phases under oxidizing conditions, S36, are Akermanite $\text{Ca}_2\text{MgSi}_2\text{O}_7$ and the Spinel Hercynite $\text{Fe}^{2+}\text{Al}_2\text{O}_4$ with up to 70 wt.-% and 13 wt.-%, respectively. Gehlenite $\text{Ca}_2\text{Al}_2\text{SiO}_7$ becomes a major phase under reducing conditions with maximum 49 wt.-%, S35. Akermanite is represented by circa 18 wt.-%. Another considerable mineral phase is Monticellite CaMgSiO_4 , formed between 1290 °C to 1250 °C. As found for other slags under reducing conditions, the number of mineral phases with less than 5 wt.-% is up to six. The consumption of Fe^{2+} is especially observed for oxidizing conditions which is not in agreement with other results. The only mineral containing Fe^{2+} under reducing conditions is Fayalite $\text{Fe}^{++}_2\text{SiO}_4$. This mineral appears at 1290 °C and disappears at lower temperatures.

Slag pair S40/S39 differs in the temperature of initial crystallization. S40 primarily exhibit Fe-containing minerals at 1350 °C under oxidizing conditions. These are Magnetite $\text{Fe}^{2+}\text{Fe}^{3+}_2\text{O}_4$ and Maghemite $\text{Fe}^{3+}_2\text{O}_3$. The amount of these two minerals steadily grows up to 30 wt.-% and 10 wt.-% for Magnetite and Maghemite, respectively. At 1200 °C, the number of mineral phases escalates. Akermanite $\text{Ca}_2\text{MgSi}_2\text{O}_7$ appears and becomes major part around 45 wt.-%. Magnetite is reduced to 17 wt.-% which is half as the temperature point before. Gehlenite $\text{Ca}_2\text{Al}_2\text{SiO}_7$ and Magnesium Silicate Mg_2SiO_4 are below 15 wt.-% in total. Maghemite almost disappears. Slag S39 primarily shows minerals at 1300 °C under reducing atmospheres. These are Merwinite $\text{Ca}_3\text{MgSi}_2\text{O}_8$ and Quartz SiO_2 , 20 wt.-% and 5 wt.-%. Quartz is resolved from slag at lower temperatures and Monticellite $\text{CaFe}_{0.12}\text{Mg}_{0.88}\text{SiO}_4$ is found to be around 29 wt.-%. This mineral develops up to 56 wt.-% at 1200 °C. Merwinite is also consumed down to 5 wt.-%. Gehlenite $\text{Ca}_2\text{Al}_2\text{SiO}_7$ and Wuestite Fe^{2+}O are minor phases with less than 8 wt.-% in summary. The amount of remaining slag is similar in both atmospheres with 20 wt.-%.

Slag pair S42/41 shows agreements in crystallization onset. Only small amounts of Maghemite $\text{Fe}^{+++}_2\text{O}_3$ were detected at 1350 °C under oxidizing conditions in S42. The Maghemite content grows not appreciable from 2.5 wt.-% to 5 wt.-% in the temperature range 1350 °C to 1330 °C. No Maghemite is found at 1300 °C. In return, Merwinite

$\text{Ca}_3\text{MgSi}_2\text{O}_8$ was formed up to 15 wt.-%. An elevated number of minerals is discovered at 1200 °C. S41 started crystallization between 1340-1340 °C at a reducing atmosphere. The initial mineral phase Merwinite $\text{Ca}_3\text{MgSi}_2\text{O}_8$ raises up to 30 wt.-%. In agreement to S42, Merwinite disappears within the temperature range to the final quench at 1180 °C. There, Monticellite $\text{CaFe}_{0.12}\text{Mg}_{0.88}\text{SiO}_4$ becomes the major phase with 40 wt.-%, followed by Akermanite $\text{Ca}_2\text{MgSi}_2\text{O}_7$ with 16 wt.-% and Gehlenite $\text{Ca}_2\text{Al}_2\text{SiO}_7$ with 11 wt.-%. Kirschsteinite $\text{Ca}(\text{Fe}^{2+}_{0.69}\text{Mg}_{0.31})\text{SiO}_4$, Wuestite Fe^{2+}O and Forsterite Mg_2SiO_4 are minor minerals with a summary of 12 wt.-%. Slag S41 has a higher amount of melt as S42 at similar temperatures.

7.3.4 Summary of Last Chapter

Three groups of slags were found from the viewpoint of crystallization:

- Incompletely molten slags due to inadequate heating power of the quench furnace or dwell.
- Completely amorphous slags over all quench temperatures or at least within the viscosity range up to 100 Pa s. This effect is found for slags with B/A-ratio below 0.80.
- Slags, which were amorphous at highest temperatures and developed mineral phases within the investigated temperature steps.

The influence of oxidizing and reducing atmospheres on crystallization is summed up as follows:

- Oxidizing conditions mostly formed one mineral phase. Reducing conditions force slags to develop more mineral species.
- Primarily formed minerals are containing silica, alumina, calcia, magnesia and iron oxide. The consumption of the slag components is effected by properties such as B/A-ratio, atmosphere and component ratios.
- For primary crystallization, iron was found as Fe^{3+} only at oxidizing conditions whereas Fe^{2+} can occur in both atmospheres. Side effects like charge exchange by other slag components and the thermochemical equilibrium of $\text{Fe}^{2+}/\text{Fe}^{3+}$ are pointed out. Fe^{2+} -containing minerals are detected at temperatures below 1150 °C also for oxidizing conditions and B/A-ratios below 0.80.
- Artificial slags made from three components generate less mineral phases when the quenching process starts from molten state. Incompletely molten artificial slags form more than three mineral phases. Undissolved minerals are suspected to be a crystallization nucleus.
- The presence of minerals around 1 wt.-% at the beginning of the quenching process seems not to influence crystallization in a significant kind. No difference

in crystallization behavior could be established in case of slag pair S36/S35. Again, these slags were defined molten for further investigations.

- A mineral can be a major phase at elevated temperatures but becomes minor at lower temperatures due to decomposition or dissolution into the remaining slag. Examples are Hibonite CaAl_2O_9 in S13, Magnetite $\text{Fe}^{2+}\text{Fe}^{3+}_2\text{O}_4$ in S40 and Merwinite $\text{Ca}_3\text{MgSi}_2\text{O}_8$ in S39. The kind of atmosphere does not influence this observation.
- Minerals can disappear. Grossularite $\text{Ca}_3\text{Al}_2(\text{SiO}_4)_3$ is an initial mineral in S14 at 1575 °C with 3 wt.-%. It is not again detected below 1500 °C. Merwinite $\text{Ca}_3\text{MgSi}_2\text{O}_8$ was detected around 1300 °C but it is completely disappeared at lower quenching temperatures, S41 and S42. In case of S41, a transformation of Merwinite to Monticellite $\text{CaFe}^{++}_{0.12}\text{Mg}_{0.88}\text{SiO}_4$ is possible. Both minerals are nesosilicates. Fe^{2+} is present at low temperatures and reducing conditions due to the minimized partial oxygen pressure. Under oxidizing atmospheres, the formation of Akermanite $\text{Ca}_2\text{MgSi}_2\text{O}_7$ and Gehlenite $\text{Ca}_2\text{Al}_2\text{SiO}_7$ from Merwinite is not validated by the relationship of minerals. Akermanite and Gehlenite belong to the group of sorosilicates.

7.4 Results Obtained by DTA

DTA measurements were carried out on extensively investigated samples, Figure 128 to Figure 146. Exothermic events denote the formation of minerals due to crystallization. The onset of crystallisation was extracted from recorded data by the appropriate software delivered with the DTA device, Netzsch Proteus®. Some samples were measured with repeated cooling rates to obtain information about the behavior of multi-heated samples and the crystallisation procedure. There, the onset temperatures were determined by average onset temperatures of individual runs.

A few samples exhibit more than one exothermic peak during cooling, e.g. S13 at -1 K/min, S36 at -20 K/min and all slags after S39 for almost all cooling rates. The formation of several mineral species is to be supposed. XRD measurements are supporting this assumption, chapter 7.3. Due to the less appearance of a multi-peak DTA curve, the following discussion is done on the first exothermic peak.

The extracted onset temperatures are represented in Figure 56 a) for oxidizing atmospheres and in Figure 56 b) for reducing conditions. In general, an increase of cooling rate is decreasing the onset temperature of exothermic events for both atmospheres. Not all samples exhibit exothermic events for all cooling rates. Supercooling is assumed when a critical cooling rate is exceeded.

Increasing the B/A-ratio is effecting two properties. First, all cooling rates result in exothermal events. Second, the temperature difference between different cooling rates

becomes less. Sample S20 has a difference of 250 K over all onset temperatures, whereas all samples after S35 exhibit temperature differences less than 100 K. The observed effects are an evidence of improved mineral formation at elevated B/A-ratios. Furthermore, supercooling is suppressed.

A v-shaped curve was found for oxidizing atmospheres. The minimum onset temperatures are in the B/A-ratio range of 0.50-0.75. The DTA-curve obtained under reducing conditions is in v-like shape. Artificial slags S13 and S14 were again measured under reducing conditions. S13-red exhibit an exothermic signal around 1193 °C only at a cooling rate of $a=-2$ K/min. Other exothermal signals were not found. S14-red was glassy for the entire cooling rate range. Due to the lack of viscosity measurements and XRD phase analysis on artificial slags under reducing conditions, no effort was given to follow this idea. The minimum temperature was found around B/A=0.5.

Samples S6 and S7 show no exothermal effects for cooling rates less or equal -2 K/min while at cooling rates above -2 K/min DTA signals are recorded. For S6, undercooling is not the reason at low cooling rates. Minerals were detected by XRD analysis for quenching at a cooling rate of -2 K/min. For S7, the onset of glass transformation is to be supposed for exothermic peaks at cooling rates above -2 K/min. Viscosity is assumed to be too low for mass transfer to support mineral formation.

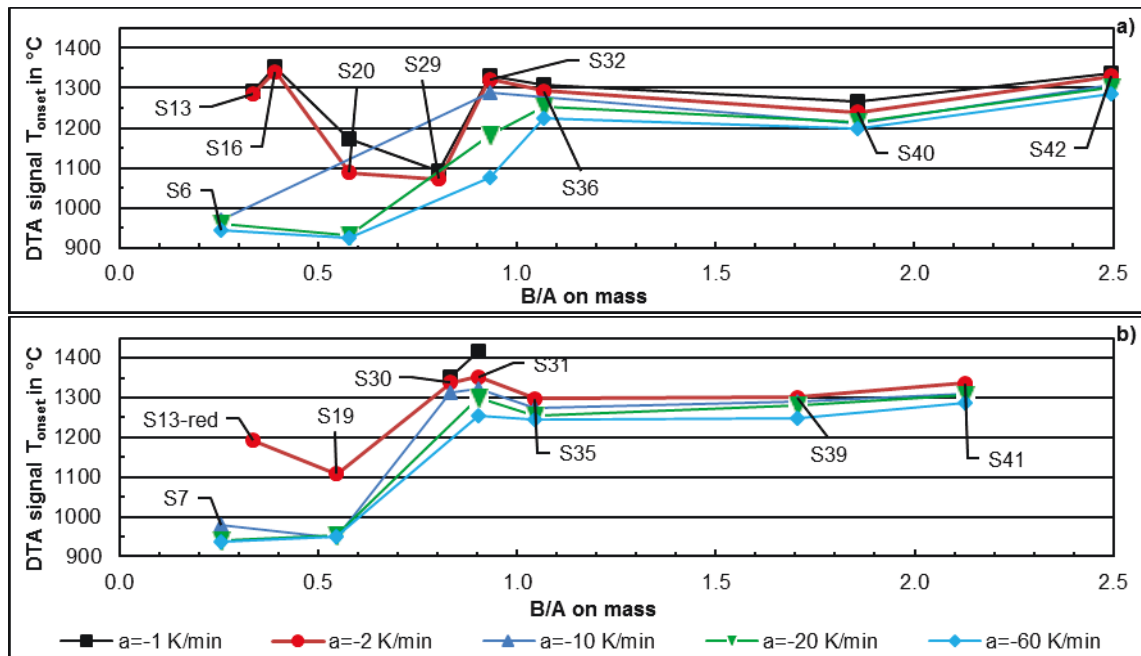


Figure 56: Average DTA onset temperatures of exothermal events under a) oxidizing and b) reducing conditions

Temperature differences ΔT in K of exothermal events obtained by DTA were calculated by equation Eq. (39). DTA_{air} and DTA_{red} are onset temperatures of oxidizing and reducing conditions in °C. A positive difference indicates an elevated onset of

supposed crystallization at oxidizing conditions while a negative value means higher temperatures under reducing conditions.

$$\Delta T = DTA_{air} - DTA_{red} \quad (39)$$

Two slags exhibit a significant difference of onset temperatures. The onset of S13 under air was circa 100 K higher than at reducing conditions. As introduced, S13 is an artificial slag. Either the simple composition of S13 is influencing the onset of crystallization or this kind of sample is influenced in a specific way by changed surface tensions of CO/CO₂-atmospheres. A XRD analysis of quenched artificial slag samples was not performed under reducing conditions. Again, investigations on artificial systems under reducing conditions were suspended. Sample S30 starts exothermic events at reducing conditions almost 300 K above S29 in air atmosphere. These samples were also found to exhibit a dilatant flow behavior, especially at oxidizing conditions. Relationships between flow behavior and cooling behavior due to structural reasons should not be excluded. Due to the found amorphous behavior by XRD analysis, the validity of DTA results must be controversially discussed.

Slags S32 and S31 are the only pair, where temperature differences were obtained at varying cooling rates. Different primary minerals were detected by XRD under oxidizing and reducing atmospheres. This seems to influence onset temperatures. Similar properties are found for slag pair S40/S39. Various minerals are formed under different atmospheres. There, the onset of exothermic events starts at circa 100 K more under oxidizing conditions.

The onset temperatures obtained by DTA at different atmospheres are in agreement for other slags.

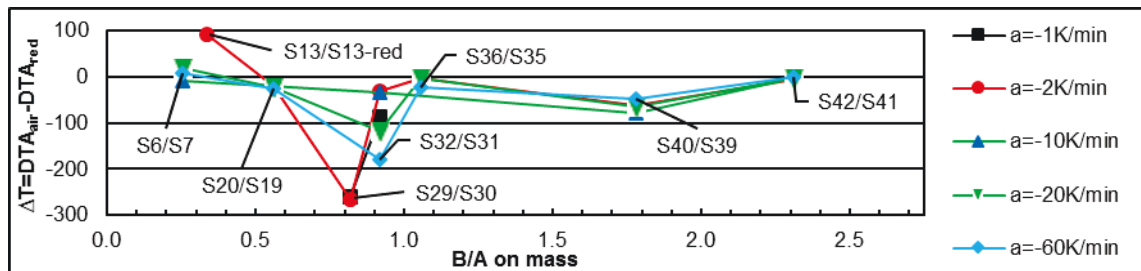


Figure 57: Temperature differences of DTA events obtained at oxidizing and reducing conditions.

7.4.1 Comparing Results obtained by DTA and Quenching

DTA measurements are more advantageous than quench experiments or viscosity measurements. The sample amount is less, smaller DTA crucibles are cheaper and a DTA device requires less monitoring during operation. Therefore, DTA results are selected to estimate the behavior of a slag in view of crystallization at different cooling

rates. A comparison with liquidus temperature ranges obtained by sample quenching is given in Figure 58.

In general, four groups of slags were found:

- First group: DTA signals and temperature range of initial mineral formation are in agreement. These are slags S16, S19, S29, S35, S39, S41 and S42.
- Second group: DTA signals are below the temperatures of initial crystallization. These are slags S13, S20, S32, S36 and S40.
- Third group: DTA signals are above the temperatures of initial crystallization, only represented by slag S30.
- Fourth group: No DTA signal was observed. These are slags S6, S7 and S14.

Sample S6 exhibit no DTA signals for cooling rates below or equal -2 K/min. Cooling rates above -2 K/min result in exothermal events. On the other hand, Fe-containing minerals in the range of 10 ma-% were detected by XRD analysis of S6 at 900 °C and a cooling rate of -2 K/min. Crystallization seems to be supported within the quench crucible, e.g. by impurities or cracks at the crucible's inner wall.

XRD analysis of quenched slag S7 indicated no mineral formation even at a temperature of 900 °C. This is in accordance with DTA measurements at -2 K/min. The recorded DTA signal at cooling rates above -2 K/min seems to be an evidence of glass transformation. Furthermore, the viscosity is expected to be in the range of several magnitudes. Material transport of slag components to a mineral is inhibited.

Sample S13 was quenched at 1550 °C and around 10 wt.-% Hibonite $\text{CaAl}_{12}\text{O}_{19}$ was detected by XRD. Reason of the elevated amount of Hibonite is an insufficient holding time of the sample before quenching. DTA measurements started at 1600 °C and a complete molten sample is expected. Therefore, DTA results seems to be more valid than results obtained by XRD.

Sample S14 was also found to contain minerals at elevated temperatures. DTA measurements exhibit no exothermal signal at all cooling rates. For that reason, S14 seems not to be completely molten at maximum quenching temperatures due to a limitation of the quench furnace. DTA measurements started above liquidus temperature.

Samples S32, S36 and S40 exhibit DTA signals at lower temperatures as determined by quenching. An inhibition of crystallisation is to be supposed within the DTA crucible, e.g. by a smooth surface. The quenching crucible is more rough and provides thereby more crystallization seeds.

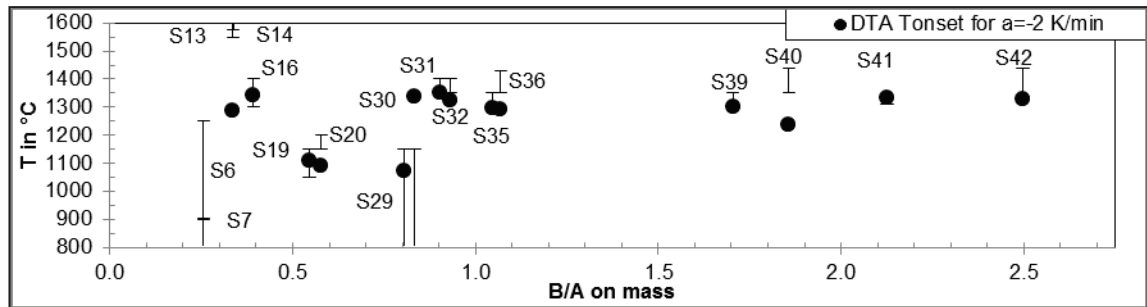


Figure 58: Comparison of onset temperatures obtained by DTA and crystallization temperature ranges obtained by quenching.

7.4.2 Summary of Last Chapter

- Cooling rate and B/A-ratio are influencing the cooling behavior of completely molten slags
- Natural slags with B/A-ratios below 0.50 are supposed to undercool due to the high amount of network formers. Artificial slags S13, S14 and S16 exhibit crystallization evidences by XRD or DTA analysis. The B/A-ratio is below 0.50. CaO was found to be responsible for crystallization, e.g. by forcing the formation of calcia containing minerals.
- Temperature differences of exothermic events recorded at reducing and oxidizing atmospheres are almost similar. Disagreement was found for artificial slag S13. There, the change in surface tension within the system crucible-slag-atmosphere or the slag itself can be the reason. Also, slags of $0.80 < B/A < 0.93$ start a exothermic event at lower temperatures under oxidizing condnions. There, the flow behavior is dilatant or different primary minerals were detected. A variation in primary minerals can also influence DTA events.
- The found DTA onset temperatures can be used in the further part of the work to estimate the beginning of a thermochemical event, e.g. crystallization and slag compositional changes afterwards.

7.5 Shear Rate Influence on Slag Viscosity

The influence on viscosity by changing the shear rate is given for oxidizing and for reducing conditions. Viscosity measurements were obtained at a cooling rate of -2 K/min. To support the found viscosity data, the amount of mineral material is calculated on extensively investigated samples as given in chapter 7.3. For the sake of completeness, the shear rate influence of samples measured under nitrogen gas atmosphere is given in Figure 67. An analysis of mineral volume fractions is not available.

Viscosities of 5, 10, 25 and 100 Pa s were selected and plotted on the left-hand side by their temperature-basicity-relationship. On the right-hand side, there are the volume fractions of minerals (SVF) over basicity related to the temperatures of the left-hand side.

A Newtonian flow behavior is depicted by overlapping data points in the temperature-basicity-plot. For a pseudo-plastic (shear-thinning) flow behavior, the data point of a low shear rate is at higher temperature than the data point of the increased shear rate. Dilatant (shear-thickening) flow behaviors are represented in the other way. An increase in shear rate leads to an elevated temperature for equal viscosities.

7.5.1 Shear Rate Influence under Oxidizing Atmospheres

Results of measurements under oxidizing atmospheres and varying shear rates are given in Figure 59. Slags with a Newtonian flow behavior are depicted by overlapping data points for different shear rates, e.g. S16 and S20 at $\eta=5$ Pa s or S6 and S29 at $\eta=100$ Pa s. They are also proofed to be completely molten by quenching experiments.

Another group of slags shows a Newtonian flow behavior, but an elevated amount of minerals. For example, S32 at $\eta=5$ Pa s, where SVF ranges between 0.05-0.10. Only Anorthite $\text{CaAl}_2\text{Si}_2\text{O}_8$ was found. At higher viscosities, according to lower temperatures, these slags turn into a non-Newtonian behavior. Slag S32 has a SVF of 0.45-0.65 at $\eta=25$ Pa s within a temperature range of 1360-1313 °C. Various minerals such as Anorthite $\text{CaAl}_2\text{Si}_2\text{O}_8$, Gehlenite $\text{Ca}_2\text{Al}_2\text{SiO}_7$ and Akermanite $\text{Ca}_2\text{MgSi}_2\text{O}_7$ are formed.

Other slags without phase analysis are selected additionally for completeness, e.g. S2, S3, S11, S26 etc. These slags are all in the basicity range $B/A < 0.80$. The slight dilatant behavior of S26 at viscosities around 10 Pa s must be mentioned. The reason cannot be defined clearly. Also slag S25 with the similar composition shows dilatant flow behavior under reducing conditions, Figure 63. Both samples have an P_2O_5 amount of 3 wt.-%. No influence of P_2O_5 to the flow behavior with respect to the molecular structure is reported in literature. But, a relationship of P_2O_5 to dilatant flow behavior cannot be excluded.

Artificial slags of low B/A-ratios are changing in flow behavior at a low SVF, e.g. S13 $\eta=10$ Pa s with SVF=0.075 and S16 $\eta=100$ Pa s with SVF=0.1. These slags are based on the system Al_2O_3 -CaO-SiO₂. Natural slags are showing a Newtonian behavior over a wide viscosity/temperature range. The particle influence becomes more unclear, the more the B/A-ratio increases. Comparing samples S32, S36, S40 and S42 offers an unsteady relationship between flow behavior and SVF, e.g. the level of SVF is not in correlation with the change in flow behavior.

The abbreviation of minerals is as follows: Akermanite - Ake - $\text{Ca}_2\text{MgSi}_2\text{O}_7$; Anorthite - Ano - $\text{CaAl}_2\text{Si}_2\text{O}_8$; Cristobalite (h) - Cri - SiO₂; Gehlenite - Geh - $\text{Ca}_2\text{Al}_2\text{SiO}_7$; Grossularia - Gro - $\text{Ca}_3\text{Al}_2(\text{SiO}_4)_3$; Hibonite - Hib - $\text{CaAl}_{12}\text{O}_{19}$; Kirschsteinite - Kir - $\text{CaFe}^{++}(\text{SiO}_4)$; Maghemite $\gamma\text{-Fe}_2\text{O}_3$ - Mag - $\text{Fe}^{3+}_2\text{O}_3$; Magnesioferrite - Maf - $\text{MgFe}^{+++}_2\text{O}_4$; Magnetite - Mat - $\text{Fe}^{++}\text{Fe}^{+++}_2\text{O}_4$; Merwinite - Mer - $\text{Ca}_3\text{Mg}(\text{SiO}_4)_2$; Monticellite - Mon - CaMgSiO_4 ;

Quartz (h) - Qua - SiO_2 ; Spinel - MgS - MgAl_2O_4 ; Spinel-hercynite - Her - $\text{Fe}^{++}\text{Al}_2\text{O}_4$; Srebrodolskite - Sre - $\text{Ca}_2\text{Fe}^{+++}_2\text{O}_5$

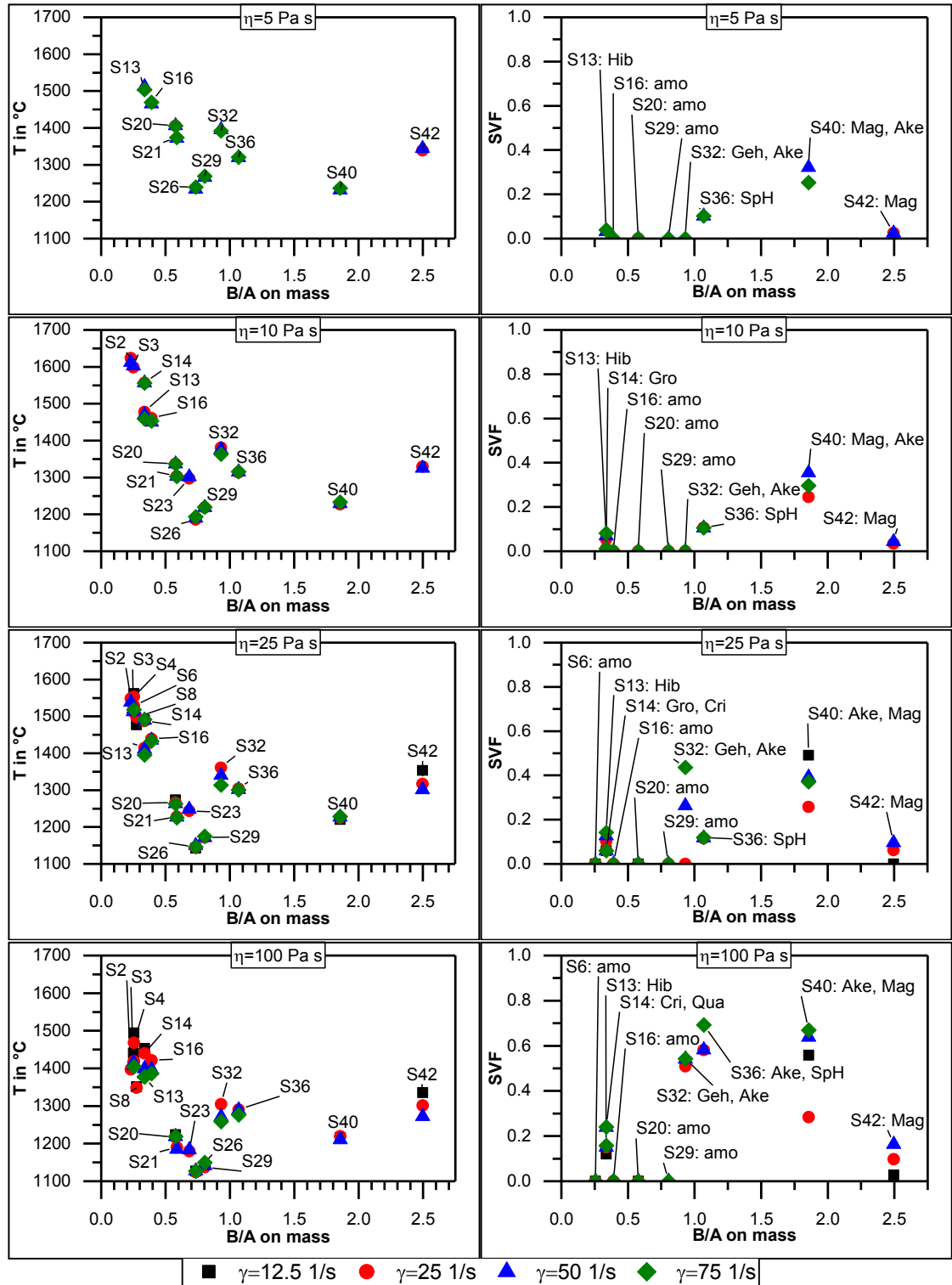


Figure 59: Temperatures, interpolated solid volume fractions and mineral names at equal viscosities as function of shear rates under oxidizing atmospheres.

The temperature difference at equal viscosities and changed shear rates is given in the section below, Figure 60. This depiction was chosen to support the results of the section above. The temperature difference was calculated by Eq. (40), where viscosities $\eta_1 = \eta_2$ and shear rates $\dot{\gamma}_1 < \dot{\gamma}_2$.

$$\Delta T = T(\eta_1)_{\dot{\gamma}_1} - T(\eta_2)_{\dot{\gamma}_2} \quad (40)$$

A negative temperature difference represents dilatant (shear-thickening) flow behavior while a positive temperature difference indicates pseudo-plastic (shear-thinning) flow behavior. In respect of temperature and viscosity accuracy, samples with temperature differences in the narrow range of ± 10 K are not influenced by changed shear rates. This does not indicate a Newtonian flow behavior at all. Moreover, it shows the changes in flow behavior between two or more shear rates. Additionally, the results from the section above are supported.

Maximum temperature differences can be found for wide varying shear rates, Figure 60. There, slags S14 and S42 shows differences of around +80 K and +60 K at 100 Pa s. This is in relationship with the estimated SVF of up to 20 vol.-%. The flow behavior was defined to be pseudo-plastic for the chosen temperatures. Slag S8 has a temperature difference of around -20 K/min at 25 Pa s. This indicates a dilatant flow behavior due to structural background. No mineral fraction is to be supposed at the given temperature and B/A-ratio. At higher viscosities, the flow behavior becomes Newtonian for S8.

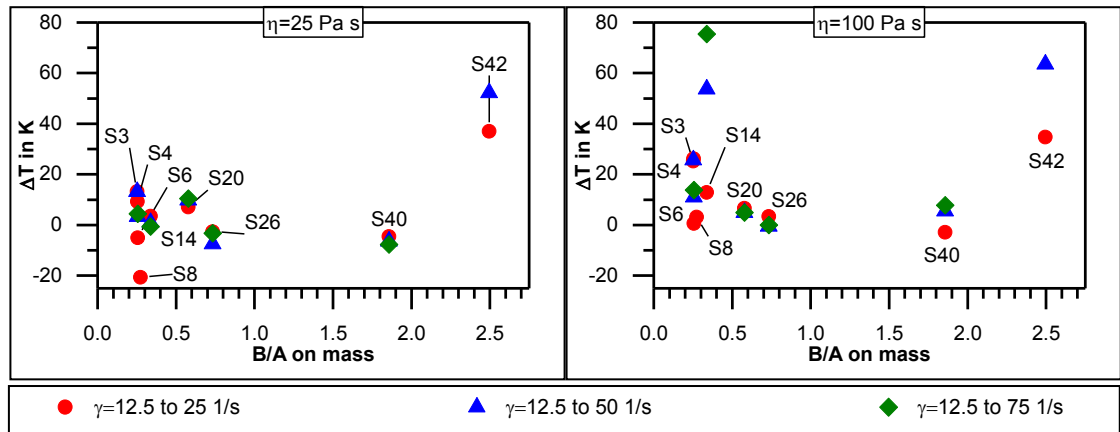


Figure 60: Temperature differences of viscosities measured at shear rates of 12.5 1/s and above, air atmosphere.

With an increasing shear rate, the temperature differences decrease, Figure 61. The maximum difference for pseudo-plastic slags is around +60 K, S14 at 100 Pa s. An example of dilatant slags is well depicted by S29 at 100 Pa s. There, structural reasons were mentioned due to the absence of mineral phases.

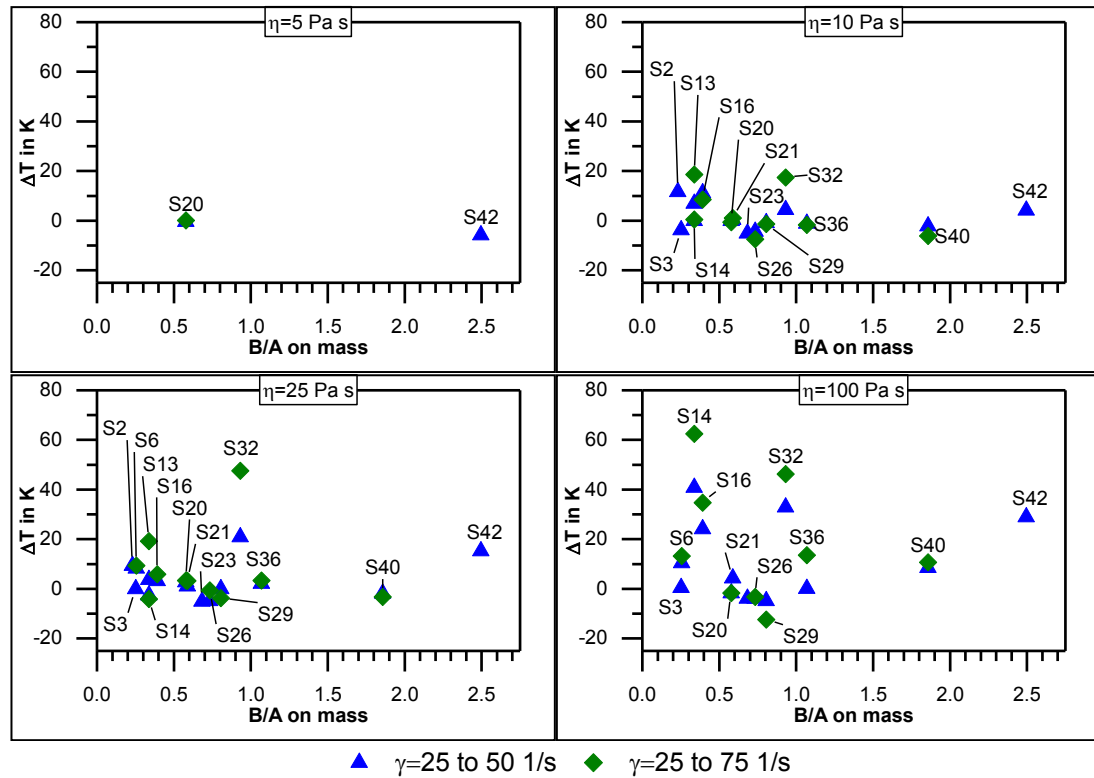


Figure 61: Temperature differences of viscosities measured at shear rates of 25 1/s and above, air atmosphere.

Almost all slags seem to be Newtonian for changes between highest shear rates, Figure 62. This means, there are only small deviations in viscosity values within the discussed shear rate steps. This does not indicate a Newtonian flow in general. Slags S13 and S40 were definite to be pseudo-plastic, but this is hardly visible by the given plot.

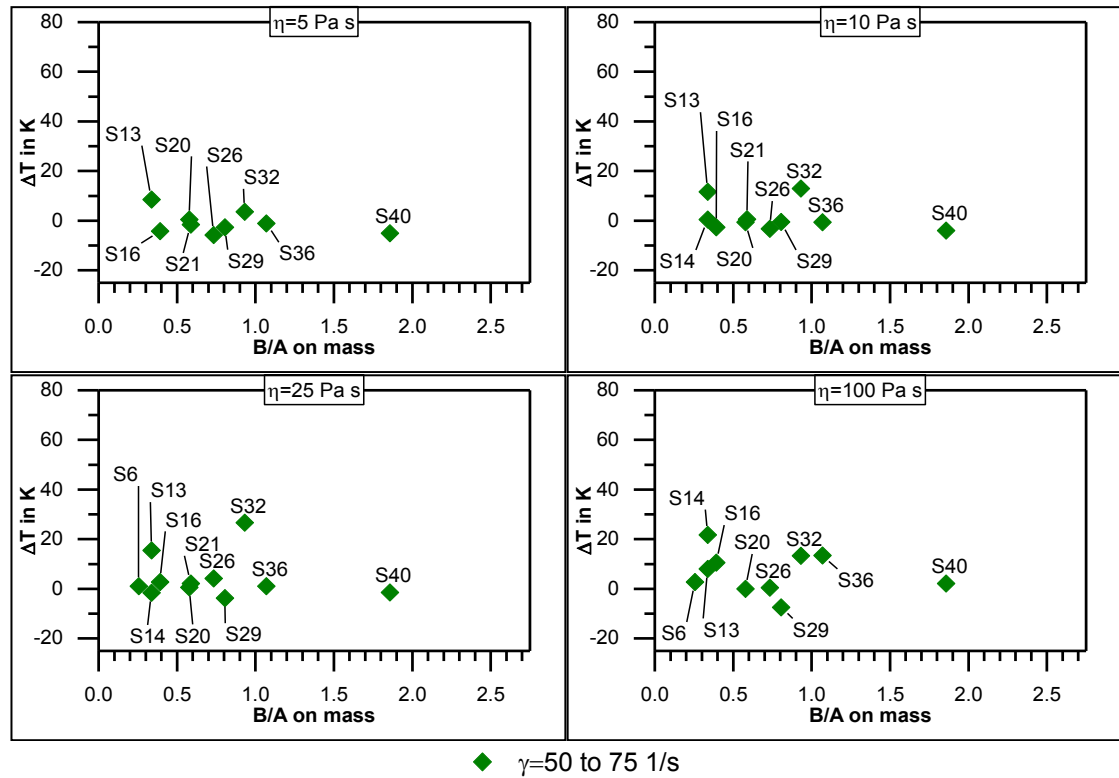


Figure 62: Temperature differences of viscosities measured at shear rates of 50 1/s and above, air atmosphere.

7.5.2 Shear Rate Influence under Reducing Atmospheres

Results of measurements under reducing atmospheres are given in Figure 63. An almost shear-independent flow behavior was found for slags with a basicity of $B/A < 0.9$. No mineral matter was detected by XRD analysis of quenched slags S7, S19 and S30. Other slags within this B/A -range are also expected to be amorphous at least to a viscosity below 25 Pa s.

The dilatant behavior of sample S25 at viscosities around 10 Pa s and above has to be mentioned. A structural background for the found flow behavior cannot be excluded, because the formation of minerals is not expected within the temperature range. The composition is similar to sample S26. Both slags show a P_2O_5 content of 3 wt.-%. This content is above the average of all samples.

The influence of particles is more developed as under oxidizing conditions for slags with a $B/A > 0.9$. At low viscosities, slags with suspended particles differ by changing the shear rate, e.g. S31 and S39 at $\eta = 5$ Pa s. The main reason for the observation is the high amount of particles at temperatures supporting $\eta = 5$ Pa s.

Observations show a dilatant flow behavior of sample S35 for viscosities around 10 Pa s and above. In this case, the SVF is around 0.7. Primary formed mineral is Gehlenite $Ca_2Al_2SiO_7$, followed by Magnesioferrite $MgFe_2O_4$, Akermanite $Ca_2MgSi_2O_7$ and Spinel $MgAl_2O_4$. No other slag owns similar high mineral amounts within a viscosity of 10 Pa s. The flow behavior of S35 changes from dilatant to pseudo-plastic when

viscosity is increased. The SVF remains on a constant level and mineral species do not change. Sample S35 shows the dramatic influence of SVF on flow behavior for minimum temperature changes.

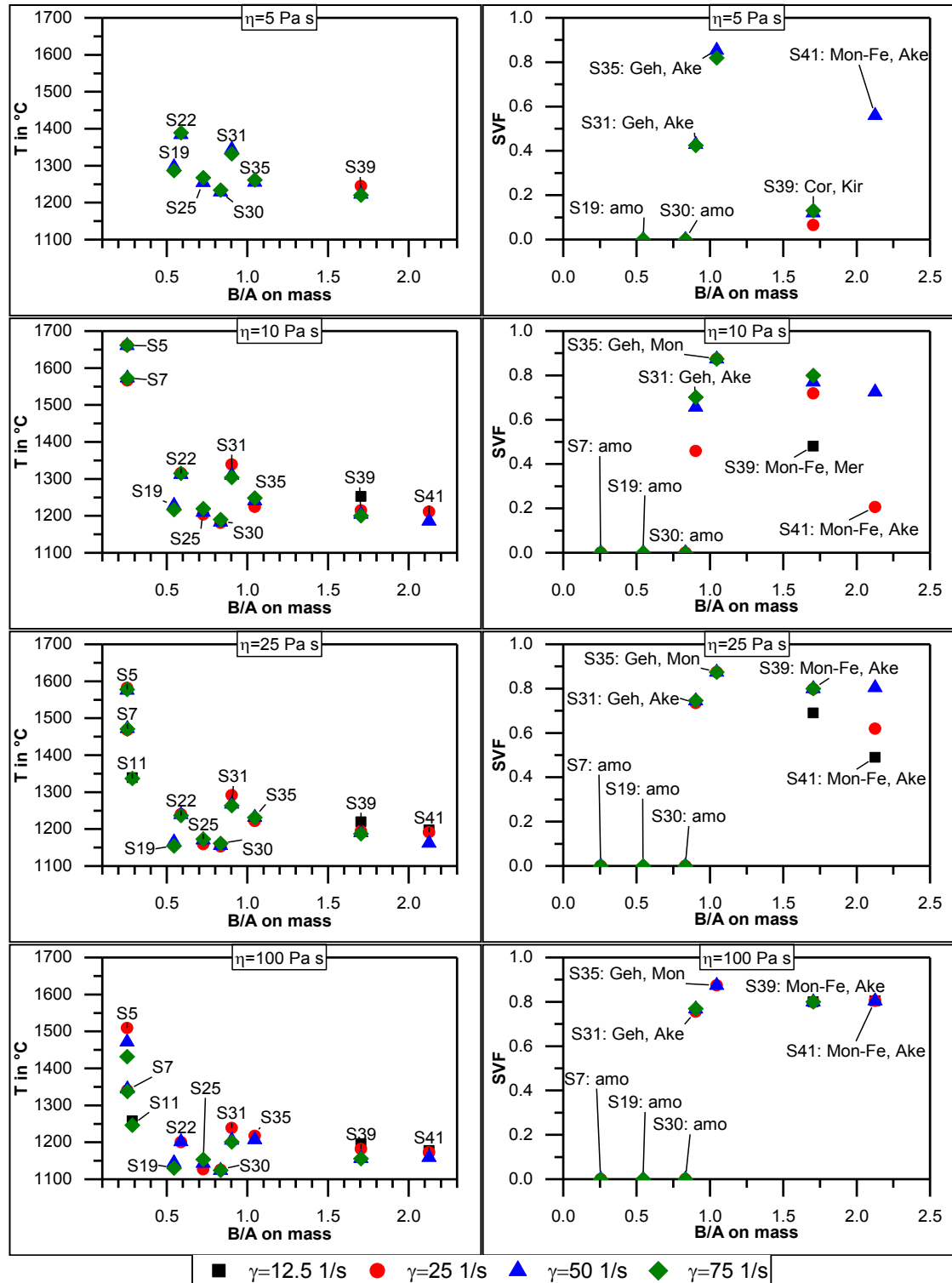


Figure 63: Temperatures, interpolated solid volume fractions and mineral names of equal viscosities as function of shear rates under reducing atmospheres.

The abbreviation of minerals is as follows:

Akermanite - Ake - $\text{Ca}_2\text{MgSi}_2\text{O}_7$; Anorthite - Ano - $\text{CaAl}_2\text{Si}_2\text{O}_8$; Cristobalite (h) - Cri - SiO_2 ; Gehlenite - Geh - $\text{Ca}_2\text{Al}_2\text{SiO}_7$; Grossularia - Gro - $\text{Ca}_3\text{Al}_2(\text{SiO}_4)_3$; Hibonite - Hib -

CaAl₁₂O₁₉; Kirschsteinite - Kir - CaFe⁺⁺(SiO₄); Maghemite γ -Fe₂O₃ - Mag - Fe³⁺₂O₃; Magnesioferrite - Maf - MgFe⁺⁺⁺₂O₄; Magnetite - Mat - Fe⁺⁺Fe⁺⁺⁺₂O₄; Merwinite - Mer - Ca₃Mg(SiO₄)₂; Monticellite - Mon - CaMgSiO₄; Quartz (h) - Qua - SiO₂; Spinel - MgS - MgAl₂O₄; Spinel-hercynite - Her - Fe⁺⁺Al₂O₄; Srebrodolskite - Sre - Ca₂Fe⁺⁺⁺₂O₅

Temperature differences of equal viscosities and varied shear rates are given in the pictures below. The difference was calculated on Eq. (40). A negative temperature difference means a shear-thickening flow behavior while a positive temperature difference indicates shear-thinning flow behavior.

The amount of data points is less for viscosity measurements within shear rates of 12.5 1/s and above, Figure 64. No slag show a dilatant flow behavior. Only slags S11 and S41 seems to be pseudo-plastic for comparisons of low and high shear rates.

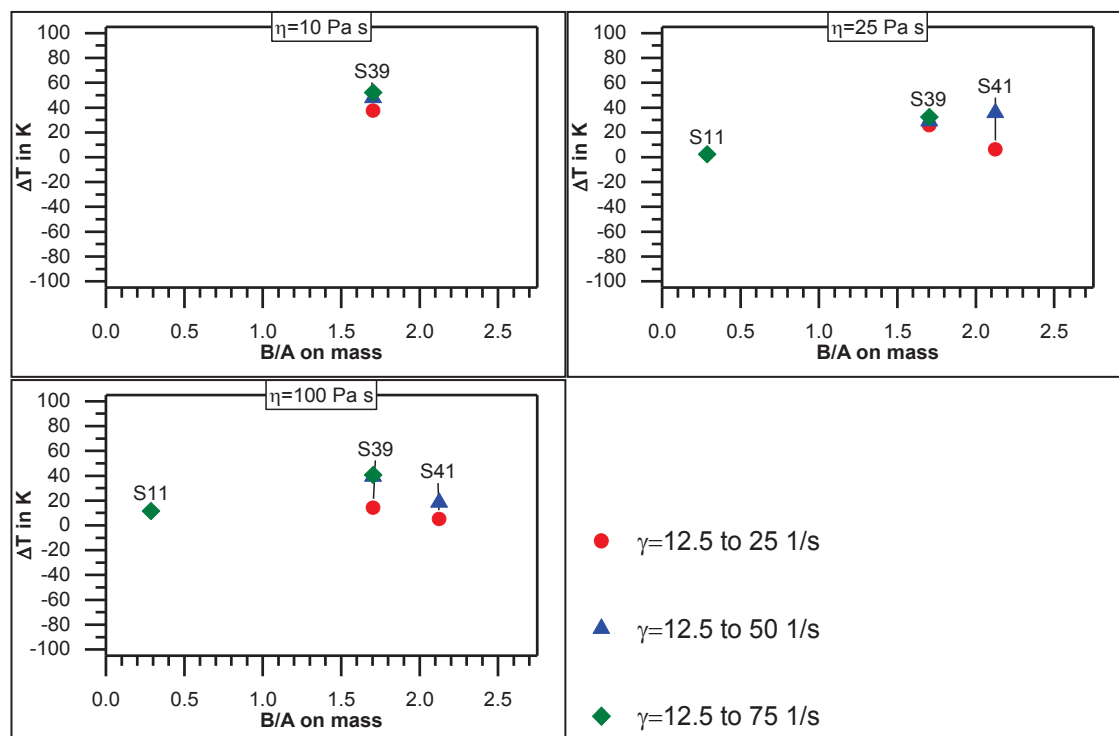


Figure 64: Temperature differences of viscosities measured at shear rates of 12.5 1/s and above, reducing conditions.

Temperature differences of shear rates between 25 and 75 1/s are depicted in Figure 65. The dilatant flow behavior of slags S25, S30 and S35 are recognized by a negative temperature difference. Also, the change from a dilatant to a pseudo-plastic flow is found for S35. While at a viscosity of 10 Pa s the temperature difference is around -20 K, the deviation becomes +10 K at 100 Pa s.

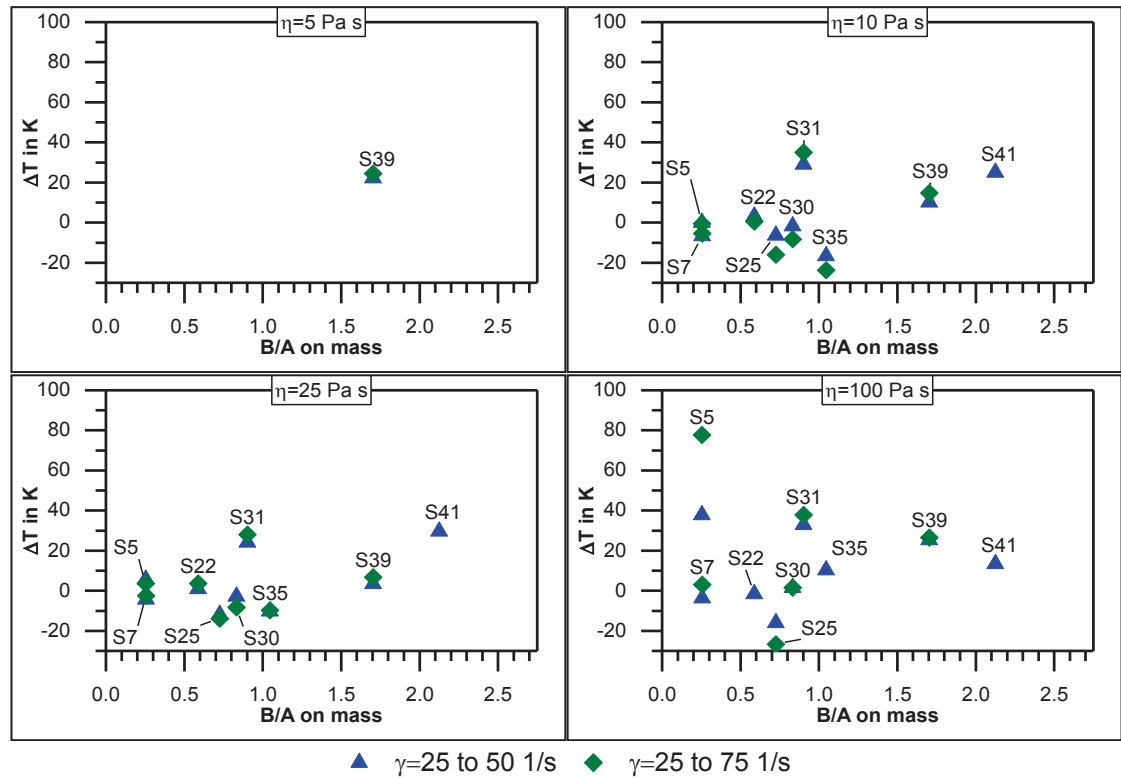


Figure 65: Temperature differences for viscosities measured at shear rates of 25 1/s and above under reducing conditions.

Like results obtained from oxidizing conditions, the viscosity difference becomes less for changes between high shear rates. Only slags S5, S19 and S25 remained as non-Newtonian.

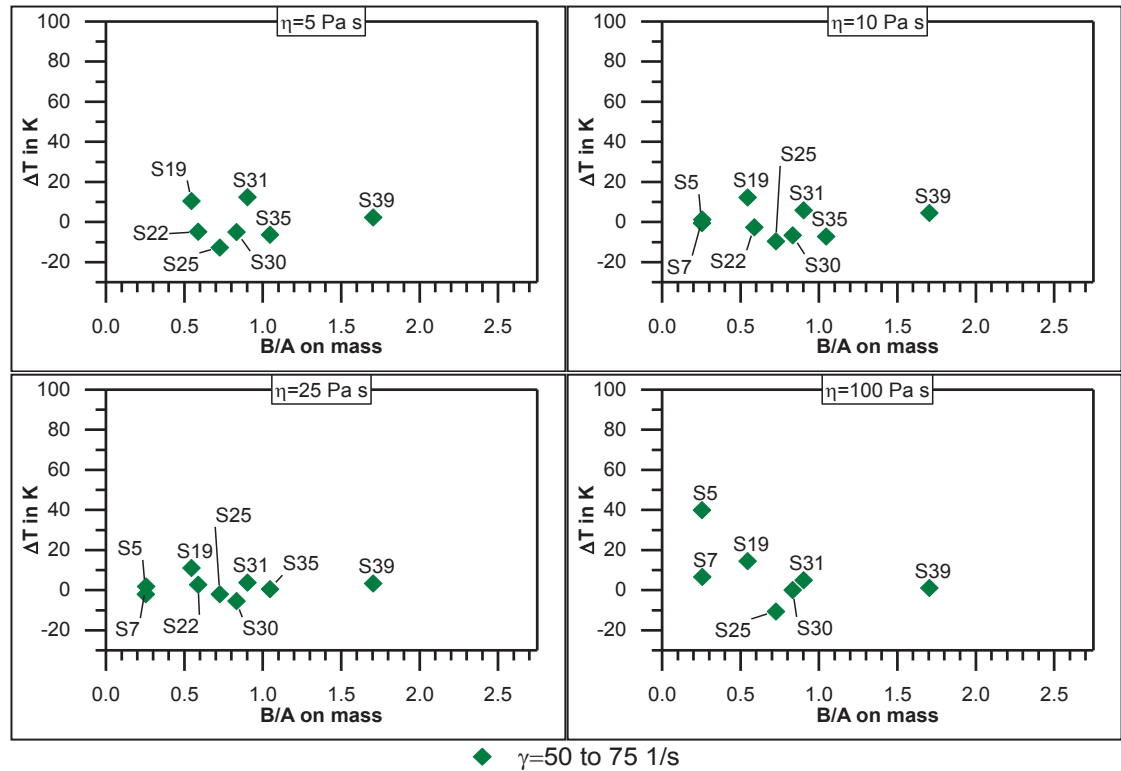


Figure 66: Temperature differences of viscosities measured at shear rates of 25 1/s and above, reducing conditions.

7.5.3 Shear Rate Influence under Constant Atmospheres

Viscosity measurements were carried out under technical nitrogen to offer an atmosphere with a constant partial oxygen pressure of $p_{O_2}=2 \cdot 10^{-6}$ atm, Figure 67. No phase analyses were obtained on selected samples. Therefore, conclusions on potential mineral influences have to be done with the help of phase analysis from other examinations, chapters 7.5.1 and 7.5.2.

The shear-depending flow behavior becomes more significant by increasing viscosity and decreasing temperature. Some samples show a well-developed shear-depending flow at a viscosity of 10 Pa s, e.g. S34 and S37. The presence of particles can be proofed for $B/A > 0.75$ when a similar crystallization behavior is supposed as found at oxidizing and reducing conditions. For B/A-ratios ranging from 0.50-0.75 at temperatures between 1200 °C and 1350 °C, the formation of particles is not to be supposed. This is in accordance with Newtonian flow of slag S24 at $\eta=10$ Pa s.

Slag S1 and S12 show a pseudo-plastic behavior at $\eta=25$ Pa s and $\eta=100$ Pa s, respectively. This is in accordance with observations from investigations under air for similar B/A-ratios.

The Newtonian flow behavior of S38 fits well to observations on S35 and S40. High solid volume fractions are assumed for S38 related XRD analysis on samples S35 and S40. In this case, the Newtonian flow behavior is not an indicator for particle absence.

Dilatant flow was found for samples S28 and S33. Same flow behaviors were also observed for oxidizing and reducing conditions within similar B/A-ratios. The formation of multi-mineral phases is to be supposed.

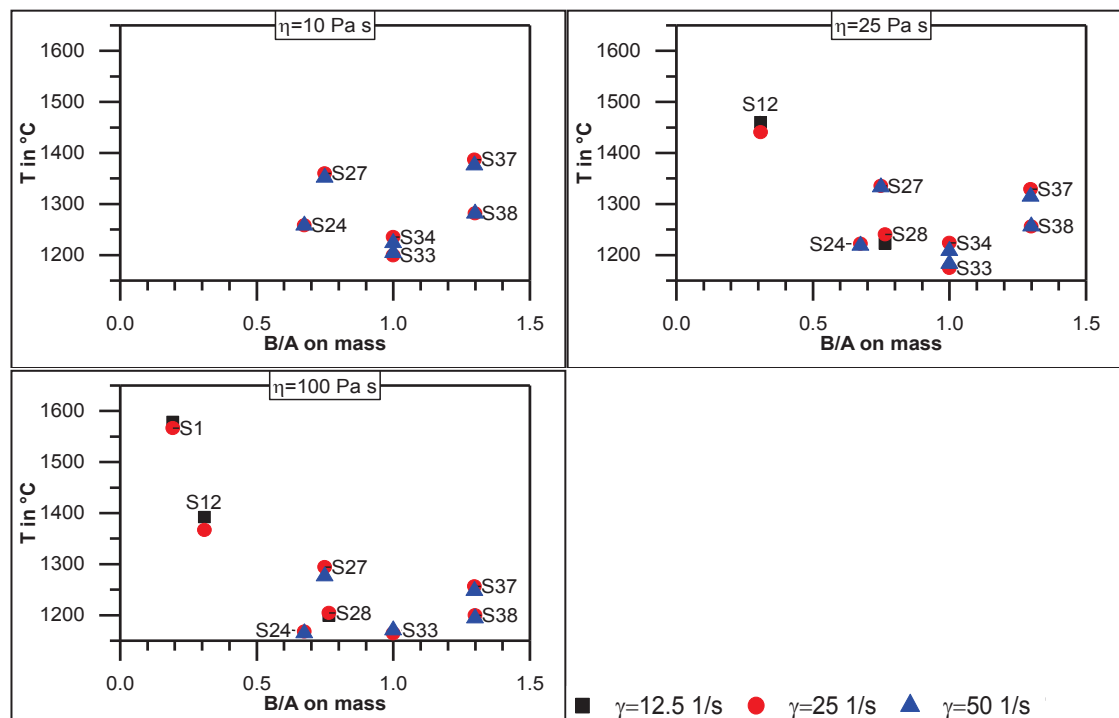


Figure 67: Temperatures of equal viscosities as function of shear rates under constant partial oxygen pressures.

Temperature differences by a variation in shear rate at constant viscosities under constant partial oxygen pressures are discussed for the sake of completeness. The small number of investigated shear rates limits the results. In general, the found flow behaviors are well depicted. For example, slags S28 and S33 were defined to be dilatant. This is proved by the negative temperature difference, Figure 68 and Figure 69.

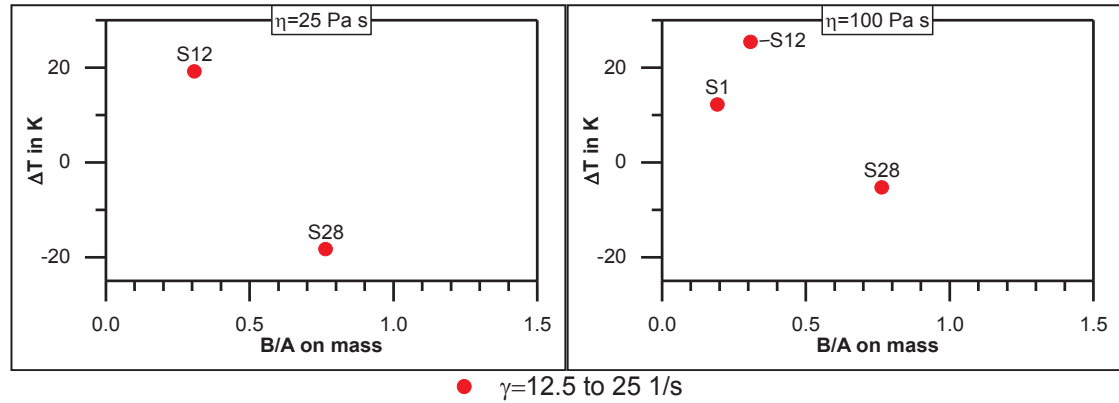


Figure 68: Temperature differences of viscosities measured at shear rates of 12.5 1/s and above, constant partial oxygen pressures.

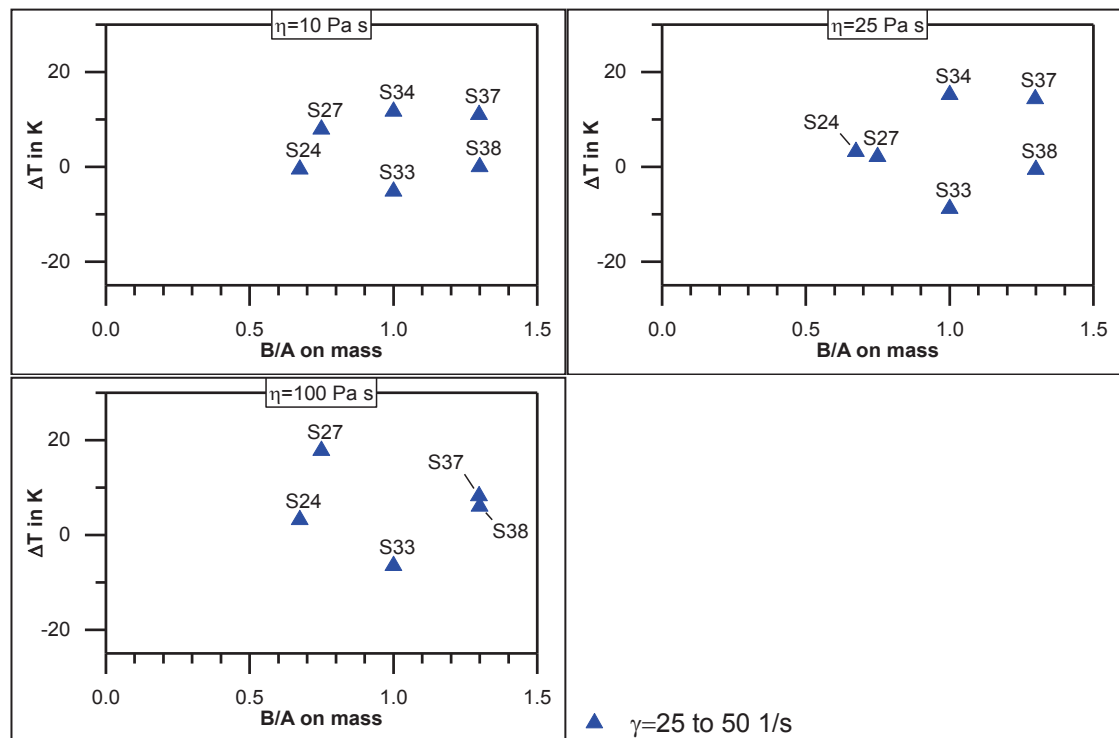


Figure 69: Temperature differences of viscosities measured at shear rates of 25 1/s and above, constant partial oxygen pressures.

7.5.4 Summary of chapter

- In general, a totally molten slag is Newtonian.
- Exceptions are slags S25, S26 and S30 where a dilatant flow behavior was observed without the presence of minerals.

- The onset of a non-Newtonian flow behavior in relation to the SVF is not clear defined. The occurrence of minerals does not guarantee the change of flow behavior.
- The number of mineral species is not indicating the onset of a non-Newtonian flow. Slags with a single mineral specie can be non-Newtonian, while slags with more mineral species are Newtonian, e.g. S40 and S34 at $\eta=25$ Pa s.
- An indicator of a possible change in flow behavior is the level of viscosity. Shear rate becomes more influencing flow behavior above 25 Pa s.
- Atmospheres are not significantly influencing the flow behavior.
- The flow behavior can be estimated from B/A-ratio.
- A pseudo-plastic flow was found on samples in the range $B/A < 0.25$
- A Newtonian flow over wide temperatures and viscosities is defined in the range $0.25 < B/A < 0.75$.
- Dilatant flow is found within ratios of $0.75 < B/A < 1.00$. Samples S25, S26, S28 and S29 seems to have structural reasons while crystals in sample S33 are providing shear-thickening flow.
- Mostly pseudo-plastic flow is found for $B/A > 1$. The small number of samples with elevated B/A-ratios is not adequate supporting a more extensive investigation.
- The change in viscosity is dramatic by comparing low and high shear rates. The influence of shear rate changes decreases when shear rate is changed from a high value to a much higher value.

7.6 Atmospheric Influence on Viscosity

A number of 10 slags were prepared under reducing and oxidizing conditions. Viscosity measurements were repeated with equal measurement parameters for both atmospheres and sample pairs. Pairs of slag samples were prepared from same ash sources. All data points show a significant atmospheric influence on viscosity.

A collection of results obtained at a shear rate of 50 1/s is given in Figure 70. The influence of oxidizing and reducing atmospheres is given on four viscosities, 5, 10, 25 and 100 Pa s. This viscosity and temperature range covers all mineral loads.

In general, the same viscosity is achieved at lower temperatures for reducing atmospheres. This indicates a lower viscosity for measurements at low partial oxygen pressures. The effect was expected due to the formation of Fe^{2+} under low partial oxygen pressure for Fe-containing samples in a large part.

An opposite observation was done on sample pairs S21/S22 and S26/S25. Here, the viscosity increases for reducing conditions. The formation of minerals and a change in slag composition can be excluded for the investigated samples due to the B/A-ratio. Samples S21 and S22 are Newtonian, while samples S25 and S26 show an uncommon

dilatant flow behavior. Both sample pairs are in the B/A-range of 0.58 to 0.74. There is no explicit evidence in all four compositions to explain the viscosity increase under reducing atmospheres. Errors in measurements are also excluded due to the number of four experiments. It is assumed that slags within the given B/A-ratios will show an elevated viscosity for reducing conditions.

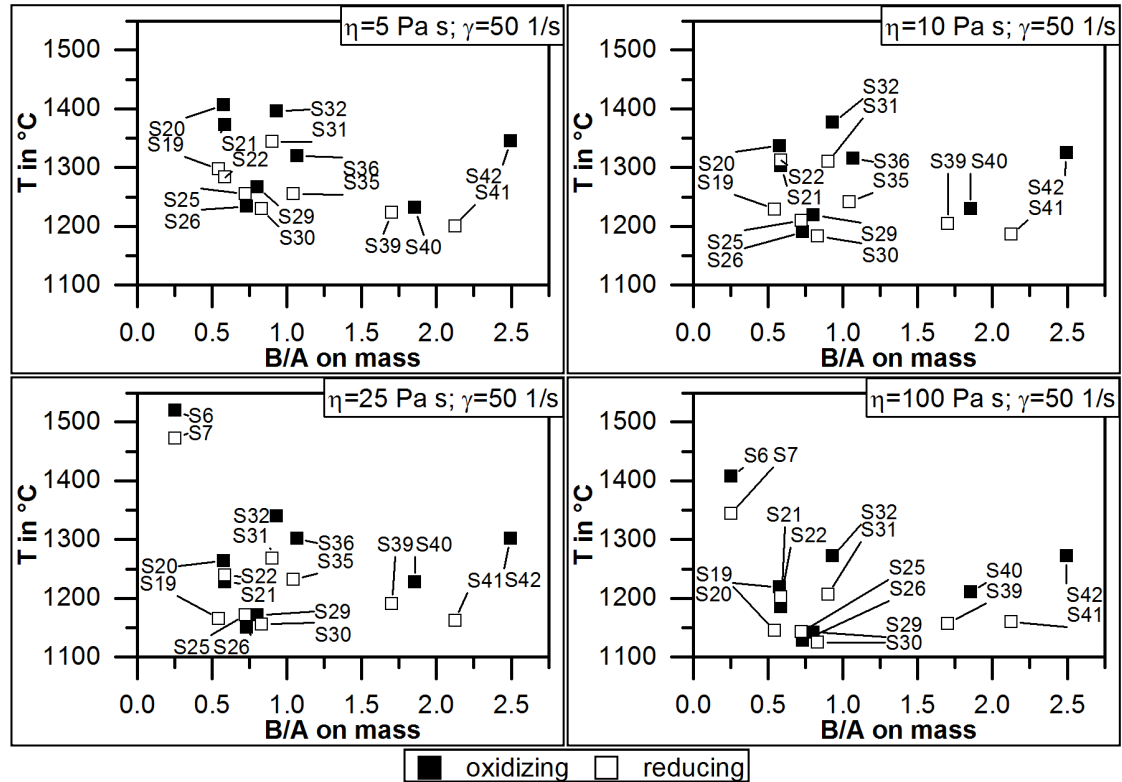


Figure 70: Temperatures of selected viscosities under oxidizing and reducing conditions at a shear rate of 50 1/s.

The absolute temperature difference to provide a defined viscosity is given in Figure 71. Additionally, shear rate was introduced to specify the occurring partial oxygen pressure effect.

The temperature differences of reducing and oxidizing conditions ranges from 1 K for S40/S39 at $\eta = 25 \text{ Pa s}$ and $\dot{\gamma} = 12.5 \text{ 1/s}$ to 158 K for S42/S41 at $\eta = 100 \text{ Pa s}$ and $\dot{\gamma} = 12.5 \text{ 1/s}$. The height of temperature differences is fluctuating over the B/A-ratio. From this follows that the temperature difference cannot certainly estimated from the B/A-ratio or bulk composition.

As pointed out in chapter 7.3, the formation of particles during cooling and their influence on slag flow is significant. The influence of temperature range, mineral formation, compositional change and flow behavior overlaps. Different shear rates are resulting in changed temperatures due to the enforcement of non-Newtonian flow.

The formation of minerals and therefore the change in slag composition has to be taken into account. Different minerals are formed under oxidizing and reducing conditions for slags with similar compositions.

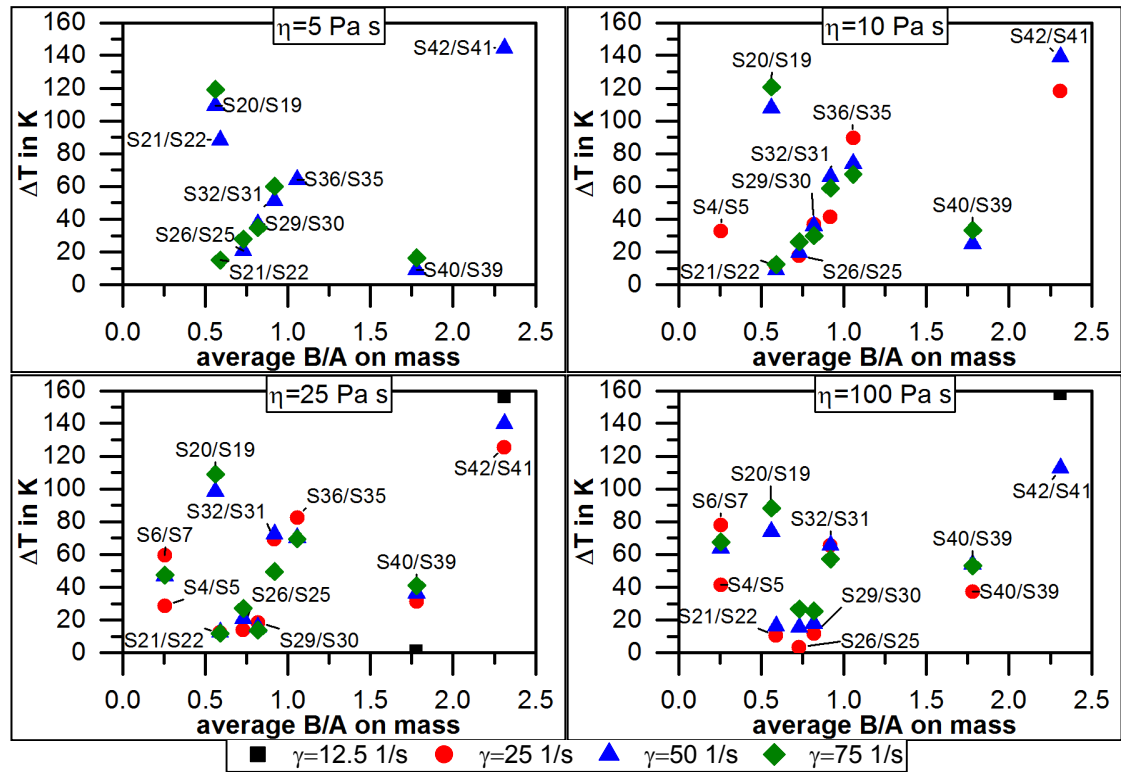


Figure 71: Temperature differences of selected viscosities for oxidizing and reducing conditions and changed shear rates.

7.6.1 Summary of Last Chapter

- A significant atmospheric influence was observed for all slag pairs.
- The viscosity changing effect becomes more noticeable the higher the investigated viscosity is while temperature is subordinated.
- The transformation of Fe^{3+} to Fe^{2+} is mostly cited in literature to explain the viscosity decreasing effect. No correlation between Fe-amount and temperature difference is found for molten slags.
- The viscosity decreasing behavior was also found for slags with an elevated mineral content. Here, the rheological impact of particles and compositional changes are overlapping at the same time. This complicates the estimation of atmospheric influences.
- In general, reducing atmospheres decrease viscosities. In other words, a smaller temperature is required to keep the same viscosity as under oxidizing contentions.
- Slags within the B/A-ratio of 0.58 and 0.74 have a viscosity increasing behavior under reducing conditions. A tenable reason is not found.

7.7 Cooling Rate Influence on Slag Viscosity

Samples S6, S7, S29, S30, S39 and S40 were measured under different cooling rates. The aim of these changes was to estimate the influence of cooling rates to the

temperature dependence of viscosity. Two main properties of slags should depend on cooling rates:

- The development of the silicate network and
- the formation of minerals by crystallization.

Both properties are found to change the flow behavior of slags. The polymerization of the silicate network is depending on temperature. It should also be a kinetic property due to the time consumption of network creation. The formation of minerals is effected by undercooling and the dwell within this temperature. When viscosity achieves a critical value, material transport will be inhibited to the particle.

Figure 72 shows the temperature to obtain a certain viscosity for cooling rates between -1 K/min to -60 K/min. The shear rate of 75 1/s is representative for lower shear rates. DTA measurements, Figure 56 a) and b), will be taken to find a correlation between possible crystallization for cooling rates different to -2 K/min. Relationships to mineral formation are also developed from results found in chapter 7.3. A separation of oxidizing and reducing atmosphere is not done. There was no influence of atmosphere to crystallization found.

Slags with B/A-ratios smaller 0.50 are nonsignificant influenced over wide viscosity ranges, S6 and S7. No temperature difference with more than 1 % was continuously recorded. The formation of minerals is not assumed. Results obtained by DTA measurements agree well with found data. Again, no mineral formation is supposed within the investigated temperature ranges. Therefore, no change in slag composition or rheological effects occurs. The sum of network formers, SiO_2 and Al_2O_3 , is around 80 wt.-%. This is resulting in an elevated number of available interconnections between silicate structures. Consequently, this circumstance compensates the number of interconnections which are not formed in a given time due to high cooling rates. Viscosity is kept on a high level.

Slags with a B/A-ratio around 0.75, S27 and S28, are becoming more affected by increasing the cooling rate. At viscosities of 25 Pa s and above, the temperature decreases to measure a certain viscosity. This is similar to a shear-thinning flow behavior. No formation of minerals is supposed within the interesting temperature ranges. DTA measurements show evidences of crystallizations for S30 and cooling rates lower than -20 K/min. Sample S29 should not form minerals in the discussed temperature ranges. Hence, the viscosity is decreasing due to changes in structural developments. The amount of network formers is reduced. SiO_2 and Al_2O_3 are around 55 wt.-% of the whole composition. It seems that the polymerization of the silicate network takes more time or the interconnection is not so powerful, respectively.

Therefore, viscosity is inhibited to increase by decreasing temperatures and is kept on a low level.

Slags with B/A-ratio above 0.80, S39 and S40, tend to a significant formation of minerals in all investigated viscosity ranges. The found dependence on cooling rate is overlapped by exothermic events recorded by DTA. No conclusion can be done on the exact reason for the viscosity-decreasing behavior, but crystallization is taken into account.

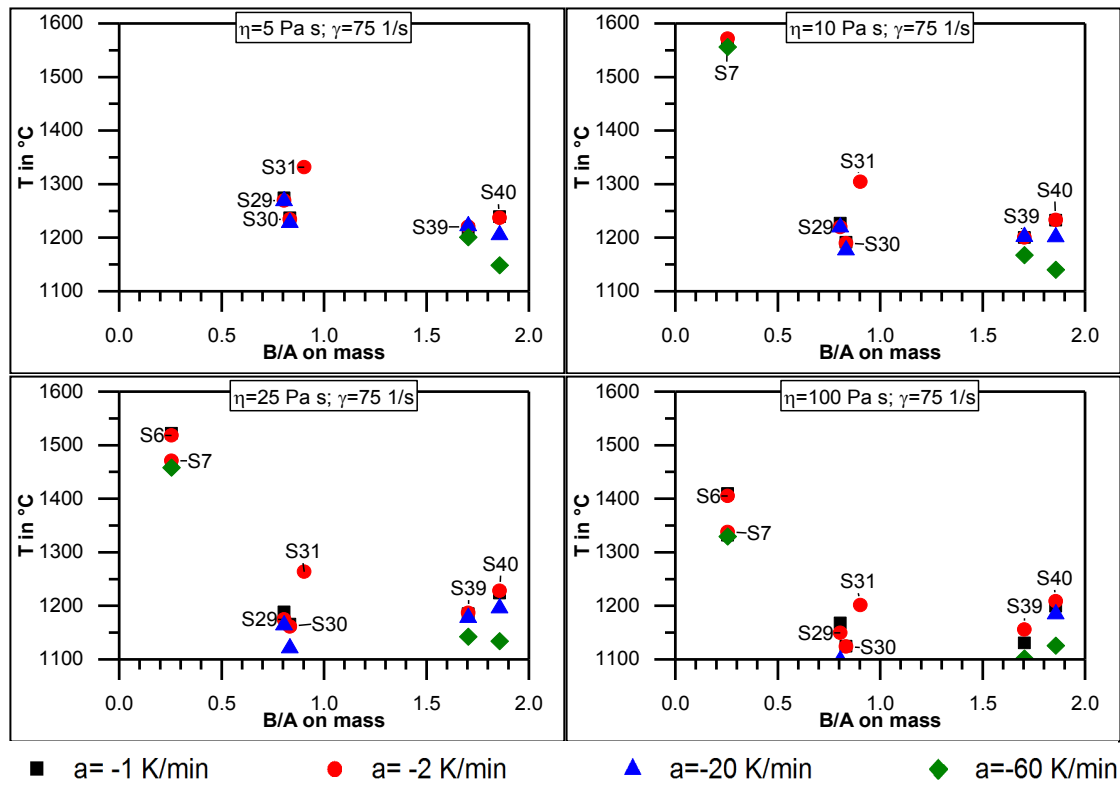


Figure 72: Temperatures to obtain a defined viscosity for different cooling rates at a constant shear rate.

7.7.1 Summary of Last Chapter

- Cooling rate is significantly influencing the viscosity at B/A > 0.8.
- An elevated amount of network formers, B/A < 0.8, seems to inhibit any effect by cooling rate.
- An intermediate amount of network formers decreases temperature for equal viscosities when cooling rates are elevated.
- Slags with B/A > 1.5 are identified to form minerals within the examined temperature ranges. There, the viscosity-decreasing behavior is well developed by increased shear rates.
- Structural reasons are pointed out for slags where no mineral formation occurs. The glass network has less time to polymerize, viscosity keeps at a low value. Overleaping effects of structural, compositional and rheological properties forces slags to crystallization.

- The number of measurements with different cooling rates has to be increased in future to support reliable conclusions.

8. Advanced Viscosity Modelling Approach

8.1 Prediction Quality of Classical Viscosity Models

The prediction quality of classical viscosity models was calculated on the AALE-performance function and plotted over the B/A-ratio, Figure 73. Viscosity predictions and measurements were compared on the viscosity range of 0-25 Pa s obtained by a cooling rate of -2 K/min. Within this range, mostly Newtonian flow behavior is existent. An introduction to the AALE-performance function is given in chapter 3.3.

Viscosities of samples measured under oxidizing atmospheres were calculated with Fe_2O_3 . The prediction performance is well for slags below B/A=1.0. Above this basicity, the AALE does continuously increase what indicates a loss in prediction quality.

Samples of reducing conditions were calculated by assuming ferric and ferrous, Fe^{3+} and Fe^{2+} , iron contents. An advantage of prediction performance was found for ferrous iron below B/A=0.6. There is no advantage using Fe^{3+} or Fe^{2+} for slag composition in the B/A-range of 0.5 to 1.0. Above B/A=1.0, a better agreement of predictions and measurements is calculated using Fe^{2+} . Applying ferrous Fe results in a continuously increase of AALE.

Slags measured under technical nitrogen atmosphere, to obtain a constant partial oxygen pressure of ca. $2 \cdot 10^{-6}$ atm, can also be calculated for reducing or oxidizing conditions. A small advantage in AALE is found for assuming an oxidizing character of the applied technical nitrogen atmosphere.

Finally, all atmospheres show a significant increase of AALE for elevated B/A-ratios. An influence of particle formation to slag flow cannot be excluded even at low viscosities in elevated B/A ranges. This is decreasing the prediction performance.

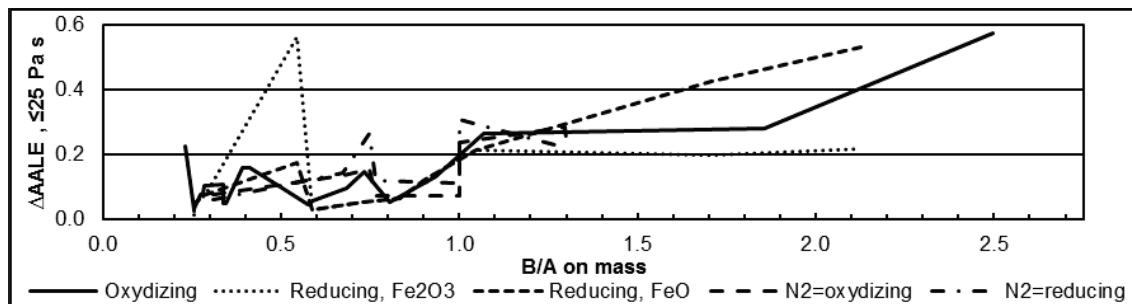


Figure 73: AALE of classic viscosity models, ≤ 25 Pa s, cooling rate -2 K/min, all shear rates.

8.1.1 Selecting the Best Viscosity Model for Newtonian Flow

A fundamental step is to select the best viscosity model for a certain slag composition. Three points are limiting the application of semi-empirical or artificial neural network viscosity models:

- The number of slag components,

- the mass fraction range of slag components and
- the restriction on Newtonian flow.

To find the best viscosity model for each slag composition, the absolute average logarithmic error (AALE) was applied. The AALE was calculated within the viscosity range ≤ 25 Pa s, including all shear rates. The viscosity range of ≤ 25 Pa s is sufficient for the balance of an adequate amount of viscosity measurements and covering data points with Newtonian flow behavior for almost all investigated slags.

Air atmosphere was assumed in the first calculation series for all slags, Table 47. No effort was given to changes in Fe^{3+} to Fe^{2+} for samples at reducing atmospheres. Figure 74 a) and b) depicting the devolution of AALE-value vs. B/A-ratio obtained from oxidizing conditions for all slags.

There is no obvious connection of the best viscosity model and the B/A-ratio. Some B/A-ranges are dominated by one viscosity model, e.g. the models of Kalmanovitch-Frank around 0.25, BBHLW around $\text{B/A}=0.5\text{-}0.6$, or Bomkamp in the range $\text{B/A}=1.0\text{-}1.3$. Above $\text{B/A}=1.5$, the models of Urbain and Kalmanovitch-Frank are dominating. This appearance is randomly. No dependence on parameters as composition or partial oxygen pressure was found even for narrow B/A-ranges.

The limitation of useful models is conducted in the following section. An examination on AALE was done by

- the minimum of the average AALE on all slags, best model is Kalmanovitch-Frank (AALE=0.381),
- the minimum of AALE on all slags, best model is Kalmanovitch-Frank (AALE=0.015) and
- the maximum of AALE on all slags, worst model is Lakatos (AALE=20.1).

The application of the selected models by the found values must be done with care. As pointed out, the Kalmanovitch-Frank model has the minimum average AALE what indicates best prediction performance over the total B/A-ratio. But, it was found only five times to be the best model. Also, the Lakatos model is not the worst prediction method over the entire B/A-range although it has the maximum AALE of all models. Above $\text{B/A}=1.3$, the model of Watt-Fereday turns into the worst prediction method.

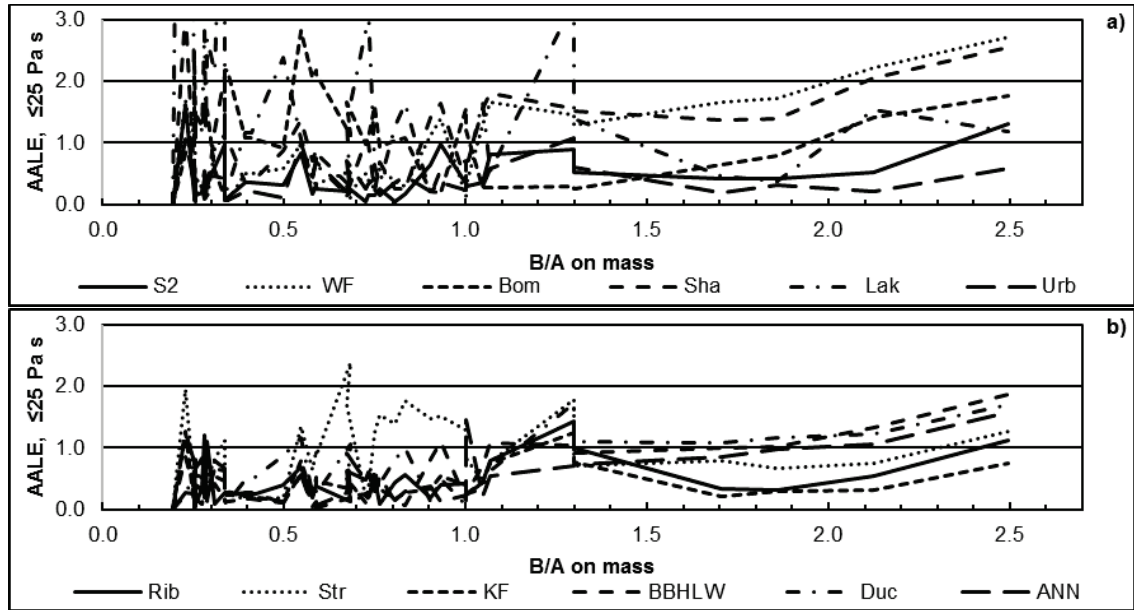


Figure 74: AALE obtained from classic viscosity models from a) S2 to Urbain and from b) Riboud to ANNliq, $\eta \leq 25$ Pa s, all shear rates, all slags, oxidizing conditions.

The calculation of AALE was repeated for samples under reducing atmospheres with respect to Fe^{2+} , Table 48. A depiction is given in Figure 114 a) and b). Tables and figures are placed in the appendix. The devolution is like the curves in Figure 74 a) and b). A difference ΔAALE can be found only for models where a differentiation in Fe_2O_3 and FeO is included. These are the models of Shaw, Urbain, Riboud, Streeter and Kalmanovitch-Frank, Figure 75. The difference ΔAALE was obtained by Eq. (41) where $\text{AALE}_{\text{oxidizing}}$ and $\text{AALE}_{\text{reducing}}$ are the AALE for the viscosity range ≤ 25 Pa s for oxidizing and reducing slags, respectively.

$$\Delta\text{AALE} = \text{AALE}_{\text{oxidizing}} - \text{AALE}_{\text{reducing}} \quad (41)$$

A positive ΔAALE indicates a higher AALE found at oxidizing than at reducing conditions. This implies a better agreement of predictions covering reducing conditions. A negative ΔAALE indicates a higher AALE found at reducing conditions than at oxidizing conditions. This implies a better agreement of predictions covering oxidizing conditions.

The graph shows a positive ΔAALE for almost all associated models for B/A-ranges below 0.7. Above this B/A, the advantage of models for slags adapted to reducing atmospheres fails. The error increases.

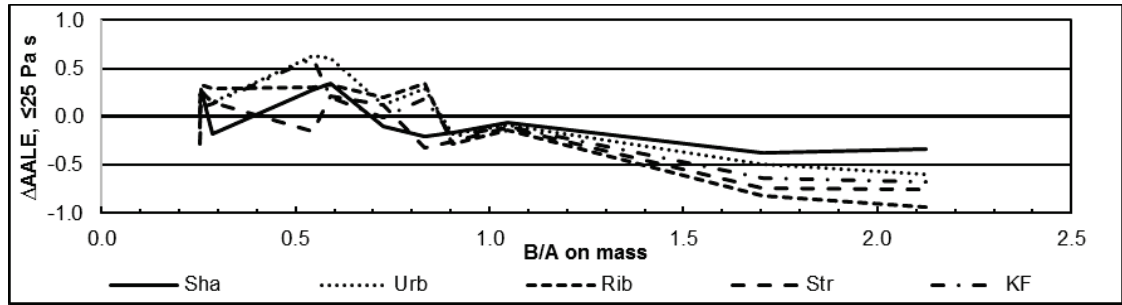


Figure 75: $\Delta AALE$ of slags measured under reducing conditions and calculated on oxidizing and reducing parameters.

The AALEs of samples measured under technical nitrogen gas to support a partial oxygen pressure of ca. $2 \cdot 10^{-6}$ atm are twice calculated. First, all Fe is ferric Fe^{3+} and second, all Fe is ferrous Fe^{2+} , Table 49 and Table 50. The plotted values of AALEs vs. the B/A-ratio are given in Figure 115 a) and b) for assuming oxidizing conditions and in Figure 116 a) and b) for reducing conditions. Tables and graphs are in the appendix. Values of slag S1 are not available due to the limited viscosity record range.

The difference of AALEs of oxidizing and reducing conditions is plotted in Figure 76 a) and b) for all used viscosity models. There are no significant advantages found to prefer viscosity predictions methods based on oxidizing or reducing conditions.

A trend can be found to use oxidizing calculation methods for the models of Shaw and Watt-Fereday. The model of Streeter agrees well for oxidizing conditions below $B/A < 1.0$. Reducing conditions are advantageous for the models of Urbain, Riboud and Kalmanovitch-Frank for a $B/A < 0.7$. The Streeter model deviates less to measurements assuming reducing conditions by nitrogen for a $B/A > 1.0$.

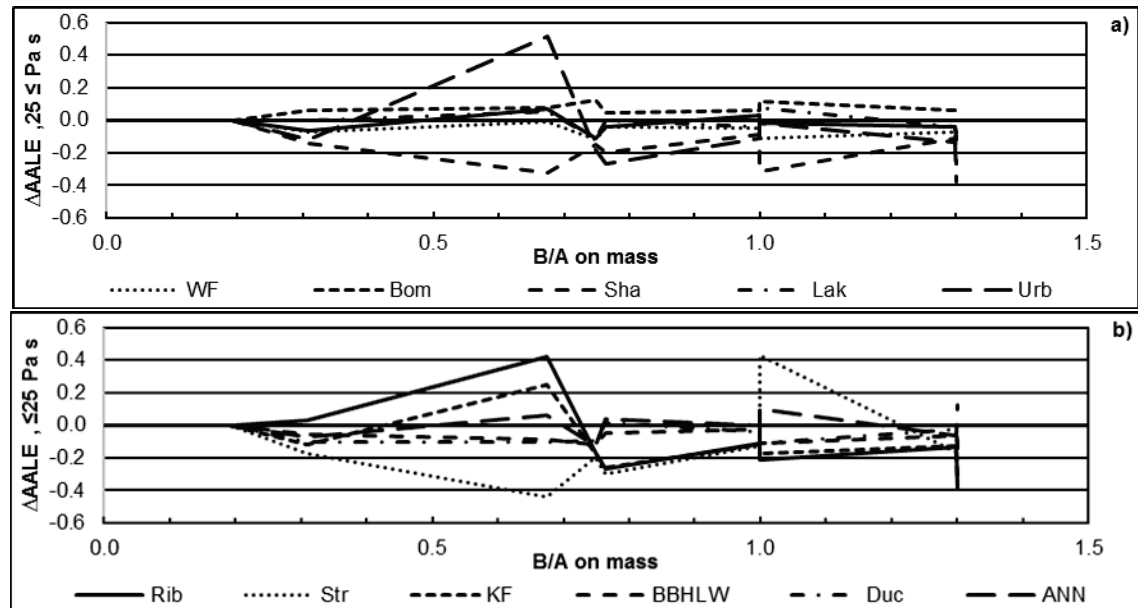


Figure 76: $\Delta AALE$ obtained from classical viscosity models a) S2 to Urbain and b) Riboud to ANNliq, $\eta \leq 25$ Pa s, all shear rates, nitrogen atmospheres.

8.1.2 Summary of Last Chapter

- Prediction quality changes with the model and the composition of the slag and the B/A-ratio, respectively.
- Selecting a suitable model to calculate slag viscosity can be done on the B/A-ratio.
- It is possible to introduce the atmospheric conditions to viscosity predictions by choosing Fe^{3+} and Fe^{2+} for oxidizing and reducing gases, respectively. Then, the prediction performance will change for models which separate into ferric and ferrous Fe.
- Slags measured under reducing atmospheres were better predicted including reducing parameters for $\text{B/A} < 0.7$. Above this limit, the improvement changed into a disadvantage.
- Nitrogen atmosphere was assumed to be oxidizing or reducing. Depending on the B/A-range and the model, the AALE was influenced. There is no strict recommendation which atmosphere must be selected on this kind of samples.
- Linear interpolation is recommended to select the best model for an uninvestigated slag.

8.2 Predicting Liquidus Temperature

8.2.1 Comparing Liquidus Calculations and Quenching Experiments

The liquidus temperature indicates the formation of minerals. Below this temperature, the onset of a non-Newtonian flow was verified, chapter 7.5. The liquidus temperature was computed by the Slag Viscosity Predictor (SVP), chapter 3.1. To calculate the thermochemical equilibrium, the software FactSageTM was applied. First, SlagA was selected. Later, SlagH was chosen to cover thermochemical equilibrium calculations with fluorine containing slags. The influence on predicted liquidus temperatures by different databases must be taken into account. Temperature differences were calculated by Eq. (42) where $T_{\text{liq,SlagH}}$ and $T_{\text{liq,SlagA}}$ are the liquidus temperature calculated on SlagH and SlagA, respectively.

$$\Delta T = T_{\text{liq,SlagH}} - T_{\text{liq,SlagA}} \quad (42)$$

As given in Figure 77, liquidus temperatures calculated by SlagA can vary between -40 and +30 K to SlagH. For oxidizing conditions, the disagreement fluctuates for the $\text{B/A} < 1$. For $\text{B/A} \geq 1$, the disagreement becomes close to 0 K. A trend can be found for reducing atmospheres. The deviation increases by an increasing B/A-ratio. The liquidus temperatures calculated by SlagA were up to 40 K higher than calculated by SlagH at a B/A-ratio of 2.126. The high amount of iron is responsible for the discovered behavior at

elevated B/A-ratios. While predictions at oxidizing conditions show an abundance of Fe^{3+} in liquid slag, reducing conditions are forming more Fe^{2+} . This results in deviations.

In conclusion, there is no dramatic difference in calculated liquidus temperatures in comparison with the investigated temperature ranges. A deviation of less than 50 K is acceptable at temperatures up to 1700 °C. Furthermore, the opportunity to calculate fluorine containing slags is available with SlagH. Finally, it is more important to compare the predicted liquidus temperatures to experimentally found ones. This is done in the following section.

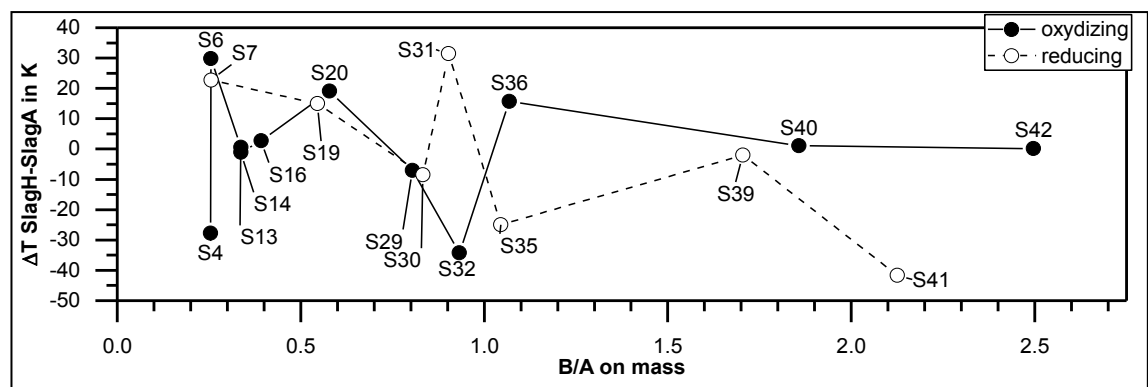


Figure 77: Differences of liquidus temperatures calculated by SlagH and SlagA solution species.

XRD-analysis on quenched samples were carried out to determine the temperature range of initial crystallization, chapter 7.3. These results were superimposed with liquidus temperatures computed by the Slag Viscosity Prediction Tool (SVP), Figure 78.

The experimentally obtained temperature range is pictured by double-T symbols. Some double-T symbols overlapping the maximum or minimum temperature of the plot. This indicates two properties. First, the overlapping of the maximum temperature means an insufficient temperature during sample quenching due to the limited temperature of the quench furnace, ca. 1575 °C. Second, the overlapping of the minimum temperature means no detection of minerals at the lowest quenching temperature. Slag is glassy.

The accordance between calculated and experimentally obtained temperatures fluctuates over the B/A-ratio.

Three groups of liquidus prediction exist:

- The first group of liquidus temperatures is predicted within or close to the measured liquidus temperatures; these are S31, S36, S39, and S42. Samples S4, S13, and S14 contained small mineral contents due to the limitation of attainable maximum quench furnace temperature. The calculated liquidus temperature seems to be valid. If these samples would be completely molten, supercooling would be expected due to the elevated amount of network modifiers.

- The second group of liquidus temperatures is overpredicted which means that the crystallization onset was experimentally proofed at lower temperatures. These are samples S6, S7, S16, S19, S20, S29, S30, S35, and S41. The disagreement can be several hundred Kelvins, e.g. sample S6. Additionally, some slags were not exhibiting crystallization, but liquidus temperatures were calculated, e.g. S7, S29 and S30. The observed slags are examples of the supercooling effect.
- The third group of liquidus temperatures is underpredicted which means that the crystallization onset was experimentally proofed at higher temperatures. These are samples S32 and S40. Several reasons are pointed out as improved crystallization by elevated amounts of Fe_2O_3 , CaO and MgO and formation of several minerals which increases the number of crystallization seeds, chapter 7.3

A significant influence of atmosphere was not observed.

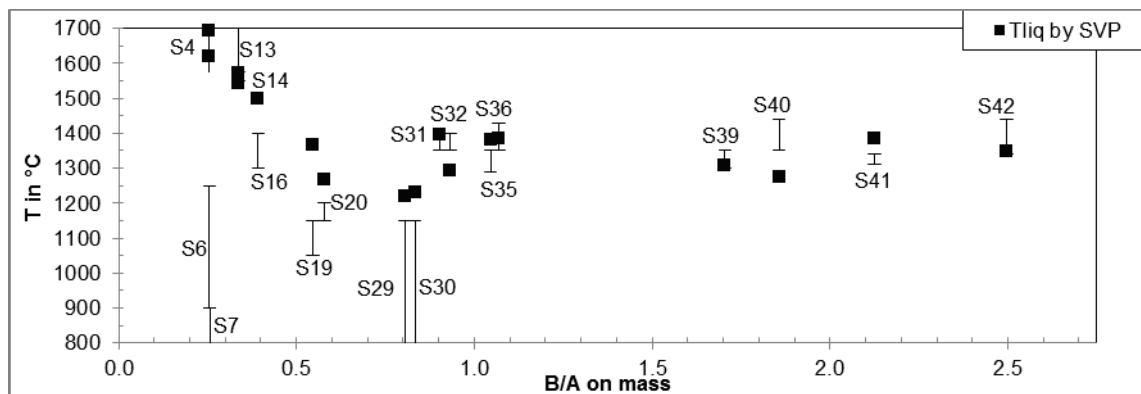


Figure 78: Liquidus temperatures obtained by slag quenching and by calculations with SVP.

8.2.2 Comparing DTA Results and Liquidus Calculations

DTA measurements with different cooling rates were performed on selected slags. The aim was the quick estimation of crystallization by the exothermal signal. Results of DTA measurements and quenching experiments are in good agreement for a cooling rate of -2 K/min, chapter 7.4. For that reason, DTA measurements will be compared to calculated liquidus temperatures.

Results are given in Figure 79. Liquidus temperatures were calculated by the SVP-tool. Calculations are based on the thermochemical equilibrium without respect to kinetics. In general, the liquidus temperature decreases with an increasing B/A-ratio. A minimum in calculated liquidus temperatures can be found around B/A=0.75. Samples S31 and S40 show unexpected liquidus temperatures in comparison to slags with similar B/A-ratios. This agrees with observations done by DTA, Figure 56. Thermochemical equilibrium calculation is in large part covering the course of the liquidus curve. Furthermore, the behavior of characteristic samples can be predicted. Therefore,

liquidus temperature calculations are an opportunity to estimate the onset of mineral formation.

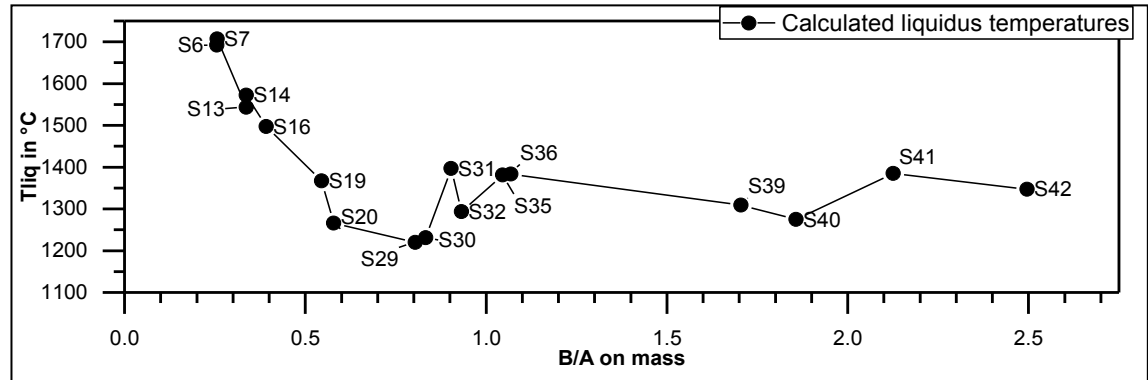


Figure 79: Calculated liquidus temperatures of selected slags.

Thermochemical equilibrium calculations cannot represent the influence of cooling rates. To overcome this problem, the temperature difference in Kelvins between predictions and measurements is calculated by Eq. (43) where T_{calc} and T_{DTA} are calculated liquidus temperature and experimentally obtained onset temperatures, respectively.

$$\Delta T = T_{calc} - T_{DTA} \quad (43)$$

The temperature difference obtained under oxidizing and reducing conditions is given in Figure 80 a) and b), respectively. No DTA signal was obtained for sample S14. Nevertheless, S14 was taken over to Figure 79 for completeness. Due to the lack of any DTA signal, no temperature difference was calculated for S14.

Two parameters are influencing the disagreement between calculations and measurements.

First, temperature differences decrease with an increasing B/A-ratio. This observation is explained by the improved crystallization. As pointed out in chapters 7.3 and 8.2.1, mineral formation was detected on all samples with B/A-ratios above 0.8. Crystallization unsteadily occurred below B/A=0.8, e.g. samples S6 and S7; S30 and S31.

Second, the temperature difference increases with an increasing cooling rate. This effect results in temperature differences up to 775 °C for cooling rates of -60 K/min and B/A-ratios below 0.5. The low B/A-ratio represents elevated amounts of network formers. Supercooling occurs and crystallization is suppressed. In reverse, low cooling rates result in temperatures close to calculated ones. The slag has more time to equilibrate. Crystallization is enhanced, e.g. by increased seed formation or improved material transport to growing minerals.

Almost all slags show a positive temperature difference. This implies the calculated liquidus temperature is above the experimentally obtained one. Only slags S30, S31 and

S32 exhibit negative differences. In other words, calculated temperatures are below the measured onset temperatures. A clear explanation cannot be given, but the crystallization mechanism seems to be part of the effect. Slag S30 exhibit no mineral formation for quenching experiments obtained under a cooling rate of -2 K/min. An exothermal event was detected by DTA at equal and lower cooling rates. Sample S31 belongs to the only pair of slags, where liquidus temperature calculation was above the liquidus temperature range estimated by quenching at -2 K/min. Sample S32 has high amounts of minerals in the range of 70 vol.-%, Figure 59.

There are no significant influences of atmospheric conditions. Temperature calculations for oxidizing conditions are slightly closer to measurements than for reducing atmospheres. An extensive investigation could not be carried out, because not all cooling rates could be repeated at reducing conditions.

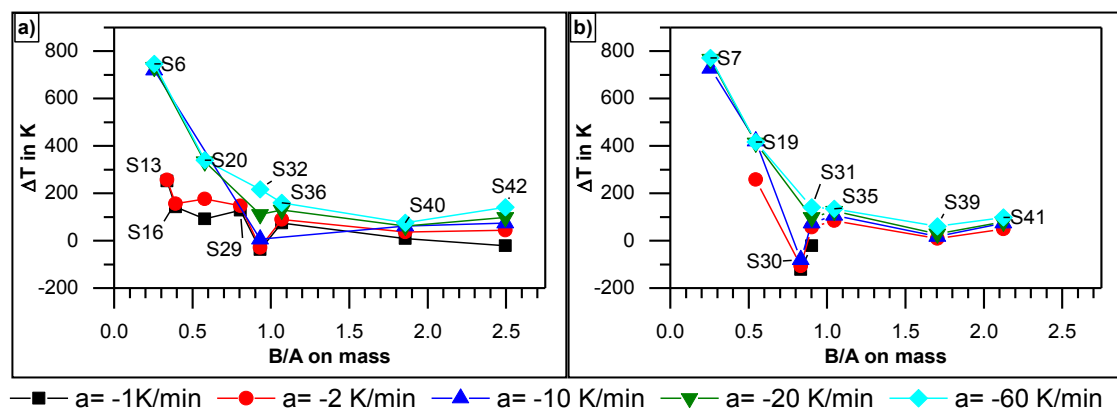


Figure 80: Temperature differences of calculated liquidus temperatures and onset temperatures obtained by DTA under a) oxidizing and b) reducing conditions.

8.2.3 Summary of Last Chapter

- Three groups of slags were found when the calculated liquidus temperature is compared with temperature ranges obtained by quenching experiments
- The first group is in accordance with calculations and crystallization ranges over wide B/A-ratio range.
- The second group overpredicts liquidus temperature. Supercooling due to elevated contents of network formers seems to be the reason. This effect is mostly observed on $B/A < 0.9$.
- The third group underestimate the liquidus temperature due to highly improved crystallization. The effect is especially observed on slags with elevated amounts of network modifiers and $B/A > 1.0$.
- Thermochemical equilibrium calculations are not covering cooling rate effects.
- Crystallization is supported by elevated B/A-ratios. Consequently, DTA measurements and thermochemical equilibrium calculations are in agreement.

- The atmospheric conditions seem not to significantly influence the obtained results.

8.3 Predicting Liquid Slag Composition

The liquid slag composition of extensively investigated samples was calculated by FactSage™ 6.4. The fixed set of data is given in Table 36 and Table 37. To estimate the influence of different solutions, two slag databases were chosen: SlagA and SlagH. SlagA database is mostly used for slags made from oxides and a sulfur content below 10 wt.-%. SlagH database was selected for this work to overcome fluoride F_2 containing slags, e.g. from blast furnaces or aluminum production.

Calculations were compared with results obtained from slag quenching experiments and further XRD analysis, chapter 7.3.3. The temperature-depending slag composition was recalculated based on found mineral species for each quenching point. This direction of examination has several advantages:

- First, the possible amount of predictable mineral species is high. This intensifies the effort of calculating the actual liquid slag composition.
- Second, thermochemical equilibrium calculations directly offering the liquid slag composition. The direct way minimizes the danger of miscalculation from the point above.

The temperature range between lowest viscosity and 100 Pa s is called “relevant temperature/viscosity range”. Some samples were quenched out of the necessary or relevant temperature range. For the sake of completeness, results beyond this temperature points are also discussed.

8.3.1 Results of Slag Composition Calculations at Oxidizing Conditions

Results of oxidizing conditions are given in the appendix, Figure 123 to Figure 125.

Cristobalite SiO_2 within slag S4 was experimentally determined to be 15 wt.-% while predictions were around 25 wt.-%. Iron was calculated to be mainly in Fe^{2+} state due to the elevated temperature of 1575 °C.

Slag S6 was not well predicted in case of mineral mass or slag consumption. The relevant temperature range is 1370 °C to 1600 °C. Predictions show the consumption of K_2O , Al_2O_3 and SiO_2 to form Leucite $KAlSi_2O_6$ at 1550 °C. Calculations at lower temperatures find a loss of Al_2O_3 , SiO_2 , Fe^{2+}/Fe^{3+} and CaO , e.g. by formation of Cordierite $Al_4Mg_2Si_5O_{18}$, Fe_2O_3 in Corundum structure and Anorthite $CaAl_2Si_2O_8$. As proven by XRD, no crystallization and therefore no slag consumption started within the relevant temperature ranges of 1420-1620 °C.

Artificial slags S13, S14 and S16 differ in prediction quality. S13 was calculated to be completely solid at 1360 °C. The formation of Hibonite $\text{CaAl}_{12}\text{O}_{19}$ was discovered by XRD analysis to be around 20 wt.-%. Thermochemical equilibrium software calculated Hibonite, Anorthite $\text{CaAl}_2\text{Si}_2\text{O}_8$ and Gehlenite $\text{Ca}_2\text{Al}_2\text{SiO}_7$ which consume all liquid slag starting at 1500 °C. The original XRD analysis showed 10 wt.-% of Hibonite at maximum quench temperature due to an insufficient dwell time. For further modelling, the mineral mass was set to 0 wt.-%.

Calculations on S14 agree with XRD analysis in the relevant temperature range of 1380 °C to 1600 °C. Formed mineral mass and the consumed slag species fit well. The consumption of SiO_2 was experimentally verified by the formation of Cristobalite, but calculated for Tridymite. Although phase predictions calculated a liquidus temperature of 1572 °C some minerals were discovered at maximum temperature point of circa 1575 °C. Similar to S13, the mineral mass was set to 0 at this temperature.

For S16, the liquidus temperature seems to be well computed between 1450 °C and 1500 °C. The depletion of slag species SiO_2 , Al_2O_3 and CaO is overestimated within the temperature range between 1400 °C and 1450 °C. At lower temperatures, the deviation is twisted. Equilibrium calculations and XRD analysis are in agreement by the formed mineral Anorthite $\text{CaAl}_2\text{Si}_2\text{O}_8$, but not by the mass development. Within the relevant temperature range, circa 30 wt.-% of mineral mass is over predicted.

The important temperature range of 1200 °C to 1410 °C is mostly well predicted for S20. An amorphous slag was observed by XRD analysis within this temperature range. Prediction weak points are at 1200 °C where SiO_2 , CaO and MgO form ca. 25 wt.-% of mineral matter, mostly Diopside $\text{CaMgSi}_2\text{O}_6$ and Tridymite SiO_2 . At lower temperatures and out of the relevant viscosity/temperature range, the deviation increases between calculations and measurements. There, SlagH overestimate the formation of minerals with 70 wt.-%. Additionally, iron is completely consumed by minerals. SlagA gives 40 wt.-%. The quenching experiment results in 10 wt.-%. The Fe_2O_3 content in slag is equal to XRD results.

A partial agreement in phase prediction was found for S29 within the relevant temperature/viscosity range of 1140 °C to 1340 °C. Below 1250 °C, the disagreement in slag consumptions grows between calculations and measurements. Calculations result in a total depletion of iron, followed by SiO_2 , Al_2O_3 and CaO . Predicted minerals are Anorthite $\text{CaAl}_2\text{Si}_2\text{O}_8$, Andradite $\text{Ca}_3\text{Fe}_2\text{Si}_3\text{O}_{12}$ and Gehlenite $\text{Ca}_2\text{Al}_2\text{SiO}_7$. Like S20, SlagH is more overestimating the formation of minerals than SlagA. Mass differences of circa 60 to 70 wt.-% occur.

The slag composition of Slag S32 deviates over the completely relevant temperature range of 1260 °C to 1400 °C. The formation of Gehlenite $\text{Ca}_2\text{Al}_2\text{SiO}_7$ was predicted and

verified by XRD analysis. Differences in mass are around 50 wt.-% to 60 wt.-% at 1300 °C. SlagA is also predicting the evaporation of Na₂O. There is good agreement with the remaining Fe₂O₃. The slag composition below 1300 °C has to be estimated.

Computation of the slag composition and therefore the mineral formation completely fail for slag S36 within the important temperature between 1270-1340 °C. XRD analysis proofed the complete consumption of SiO₂ and CaO by minerals like Hercynite Fe⁺⁺Al₂O₄ and Akermanite Ca₂MgSi₂O₇. This leads to a mineral amount of ca. 90 wt.-% suspended in slag. Predictions estimated the crystallization of 20 wt.-% Merwinite Ca₃MgSi₂O₈ and Spinels of MgO and Al₂O₃ in total.

A better accordance in view of mass consumption by minerals was achieved for S40. Although the crystallization onset was not predicted well, the sum of minerals differs between 15-25 wt.-% within the important temperature range of 1210-1250 °C. Similar S36, the preferred consumption of Fe₂O₃ by Magnetite Fe⁺⁺Fe⁺⁺⁺₂O₄ and Maghemite Fe⁺⁺⁺₂O₃ at 1250 °C was not predicted. Also, there are weak points in describing the consumption of SiO₂ and Al₂O₃. The calculated formation of Fe₂O₃-consuming minerals starts at 1200 °C.

Slag S42 is partly covered by equilibrium calculations within the relevant temperature range of 1270-1365 °C. Maghemite Fe₂O₃ was found by XRD analysis at 1300 °C. No consumption of Fe₂O₃ is calculated. Mass deviations of predictions and experimentally observations are ranging between 5-20 wt.-% within 1230 °C and 1350 °C. Like at S40, the consumption of SiO₂, Al₂O₃ and CaO is not sufficiently predicted. The verified MgO consumption by Spinel MgAl_{0.79}Fe_{1.21}O₄ and Bredigite Ca₁₄Mg₂(SiO₄)₈ is covered by the prediction of Merwinite Ca₃MgSi₂O₈.

8.3.2 Results of Slag Composition Calculations at Reducing Conditions

Results of reducing conditions are depicted in the appendix, Figure 126 and Figure 127.

The amorphous behavior of slag S7 was not predicted. Thermochemical equilibrium calculations indicated the formation of Leucite KAlSi₂O₆ around 1700 °C similar to S6. Other miss-predicted mineral phases like Cordierite Al₄Mg₂Si₅O₁₈ and ferro-Cordierite Al₄Fe₂Si₅O₁₈ consume Al₂O₃, SiO₂, MgO and Fe₂O₃ within the relevant temperature range of 1270 °C to 1640 °C.

Predictions on slag S19 deviates from XRD investigations at the relevant temperature/viscosity point of 1150 °C. Similar to S7, slag S19 is amorphous while calculations show huge consumptions of SiO₂, FeO, CaO and MgO to form Tridymite SiO₂, Diopside CaMgSi₂O₆ and Wollastonite CaSiO₃. Mineral phases are around of 60 wt.-%. Crystallization was experimentally verified below the relevant temperature range. Neither the ratios of consumed slag species nor the formed crystal masses agree.

The amorphous behavior of slag S30 is well computed within parts of the relevant temperature range 1120 °C to 1310 °C. Good agreement can be found for elevated temperatures. Gehlenite $\text{Ca}_2\text{Al}_2\text{SiO}_7$ was computed at 1150 °C to be around 10 wt.-%.

Huge deviations were found for phase predictions of slag S31. Crystallization was proofed by XRD analysis between 1350 °C to 1400 °C. SiO_2 , Al_2O_3 , CaO and MgO are consumed by solid phases like Gehlenite $\text{Ca}_2\text{Al}_2\text{SiO}_7$ and Akermanite $\text{Ca}_2\text{MgSi}_2\text{O}_7$. The depletion on CaO was not covered by calculations within the relevant temperature range of 1200 °C to 1370 °C. Mineral formation differs up to 60 wt.-% in view of experimentally proofed data.

Predictions also fail for S39. No agreement in slag specie consumption or formed crystal mass could be found. SiO_2 , CaO and MgO are primarily consumed by Gehlenite $\text{Ca}_2\text{Al}_2\text{SiO}_7$ and Akermanite $\text{Ca}_2\text{MgSi}_2\text{O}_7$. Predictions estimated the formation of Merwinite $\text{Ca}_3\text{MgSi}_2\text{O}_8$ and the Spinel MgAl_2O_4 . Mineral differences of around 50 wt.-% occurs between XRD analysis and calculations within the relevant temperature range of 1200 °C to 1275 °C.

The relevant temperature range from 1160 °C to 1220 °C of slag S41 is well covered by predictions. Experimentally proofed is the consumption of slag species SiO_2 , Al_2O_3 , CaO and MgO by the formation of Akermanite $\text{Ca}_2\text{MgSi}_2\text{O}_7$ and Gehlenite $\text{Ca}_2\text{Al}_2\text{SiO}_7$. The thermochemical equilibrium software predicts the crystallization of Merwinite $\text{Ca}_3\text{MgSi}_2\text{O}_8$ and spinels containing MgO and Al_2O_3 . FeO is used to create Monticellite $\text{CaFe}_{0.12}\text{Mg}_{0.88}\text{SiO}_4$ and Wuestite FeO. Computation does overpredict the consumption of FeO only by Wuestite.

8.3.3 Summary of Last Chapter

- Two main errors occur at mineral phase predictions: onset of crystallization and mass consumption of slag species.
- The prediction of the correct mineral phase is not necessary as long other phases with equal slag specie distributions are computed.
- Almost all predictions deviated to experimentally proofed data.
- Prediction quality was not influenced by oxidizing or reducing conditions.
- No advantage was found for amorphous slags. Predictions were partly in agreement or differed completely from XRD results.
- The B/A-factor and therefore the composition have no influences on prediction quality of mineral formation.
- The consumption of iron by Fe-containing minerals cannot be predicted in a sufficient good quality. Oxidizing or reducing atmospheres do not influence the

prediction. This is an error source for further viscosity modelling especially for slags with high Fe-contents.

- Leucite KAlSi_2O_6 was calculated for S6 and S7 but not found by XRD analysis. The elevated content of K_2O seems to be responsible for the false prediction. Excluding this mineral specie from thermochemical equilibrium calculations is possible but the formation of other minerals is still predicted. What is not in accordance with XRD.
- There are no significant differences in results obtained by SlagA or SlagH solution databases. Slag components of fluoride can be introduced by SlagH without restrictions in prediction quality.
- The search for selecting the best solid solution database to estimate mineral formation was not further followed. The number of possible selections within the software is huge. No dependence on the quality of mineral phase prediction was found, e.g. by atmosphere or B/A-ratio. In consequence, the probable mineral phase and its mass devolution must be estimated on XRD analysis.
- In summary, phase predictions by thermochemical equilibrium calculations are useful to estimate the liquidus temperature for heating up slags. The cooling behavior of slags is not satisfying simulated. Reasons are the cooling rate and the supposed supercooling of samples. Thermochemical equilibrium software cannot depict the cooling kinetic of a slag sample. A solution was not further followed.

8.4 Modelling Approach

Several slag samples were extensively investigated by

- viscosity measurements under reducing and oxidizing conditions,
- a variation in shear rates,
- DTA-measurements to estimate the onset of crystallization and
- XRD-analysis of quenched slag samples to verify the amount and specie of minerals.

The flow behavior was explained on these results. Crystallization was identified as origin of changes in flow behavior for mostly all slags. Software tools are available to predict mineral content in slags as function of composition and temperature. The kinetic nature of crystallization complicates the adequate calculation of mineral formation. Either the begin of crystallization nor the consumption of slag components could be satisfyingly depicted. For that reason, a slag viscosity modelling approach is provided to

- support the selection of the best model,
- calculate the SVF,

- assume the composition of remaining slag,
- compute the a-factor of the Einstein-Roscoe equation and
- predict viscosity for a given temperature, composition and shear rate.

The flowsheet of the viscosity modelling approach is depicted in Figure 81.

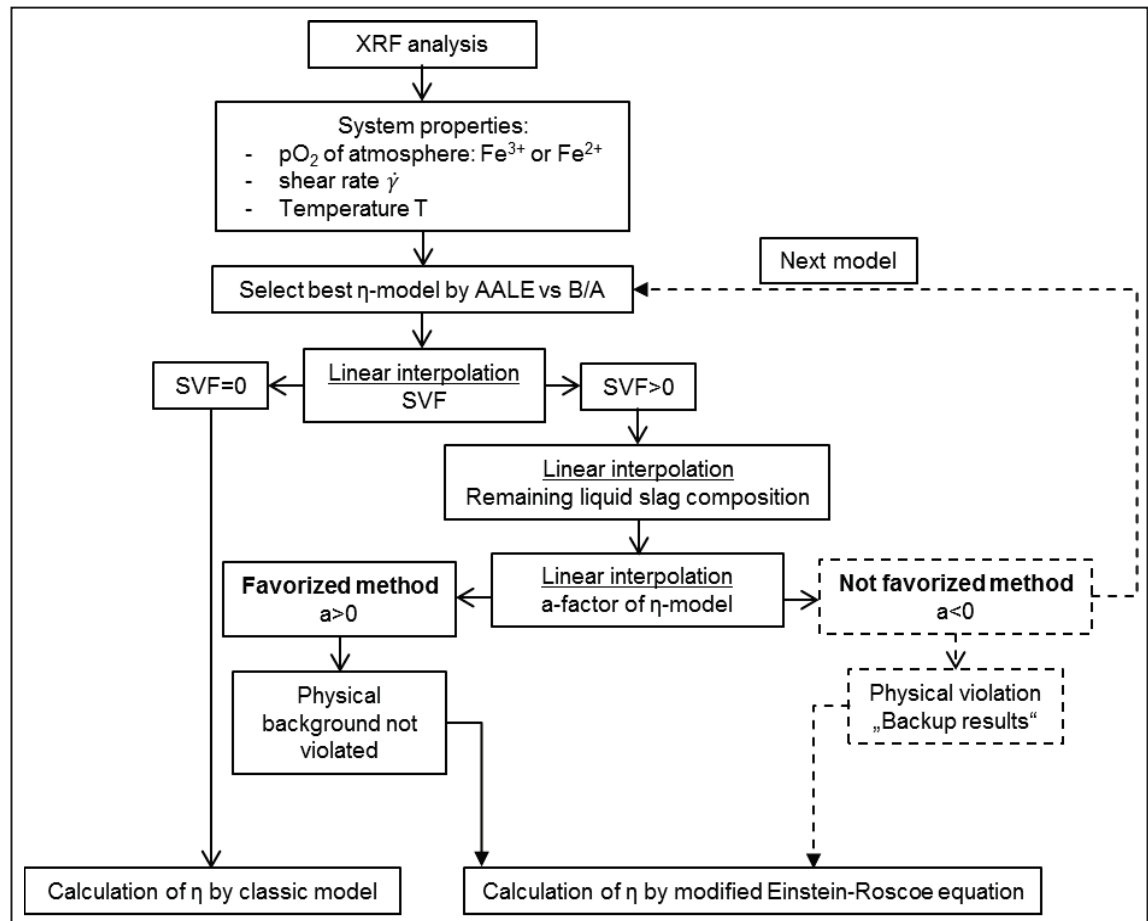


Figure 81: Recommended viscosity modelling approach.

8.4.1 Development of Datasets for Advanced Viscosity Modeling

The data of DTA measurements and quenching experiments of extensively investigated samples were selected. The change in slag composition due to partial crystallization was calculated on results of XRD analysis, chapter 7.3.3. DTA results defined the onset of crystallization, chapter 7.4. Afterwards, the Einstein-Roscoe equation was applied to introduce the influence of shear rate and solid volume fraction of minerals (SVF) to the slag flow behavior. The a-factor of each extensively investigated slag was fitted by the least squares method for all viscosity models. Each temperature and viscosity data point was defined by the best a-factor of a viscosity model. An increasing a-factor increases the viscosity of slag-mineral-suspension while a decreasing a-factor lowers the viscosity.

An example of the obtained a-factors is depicted in Figure 82 for the S2 model under oxidizing and reducing conditions. All models and their related a-factors are plotted in

Figure 117 and Figure 118. No effort was given to separate into related shear rate or solid volume fraction. The figures are only chosen for informative function.

The a-factors are varying in their value over B/A-ratio, temperature, solid volume fraction and shear rate. Some trends are pointed out:

- An oxidizing atmosphere shows huge variations of a-factors at low B/A-ratios while
- at reducing conditions the a-factors are huge deviating at low and high B/A-ratios.

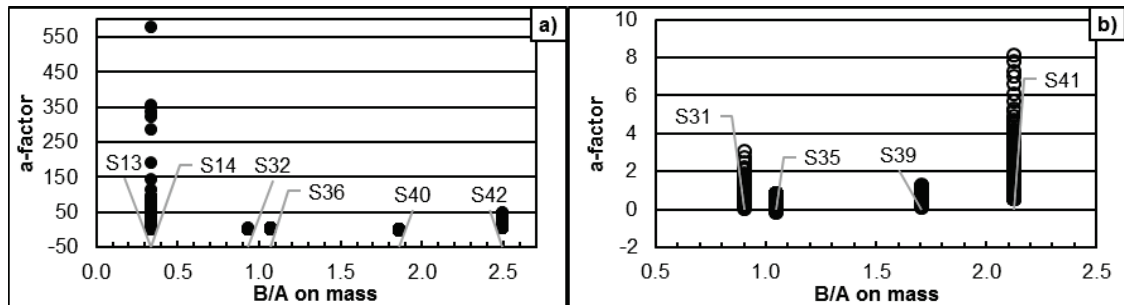


Figure 82: Devolution of fitted a-factors for S2 model under a) oxidizing and b) reducing conditions.

As discussed in chapter 5.3, the a-factor has the physical meaning of the particle influence to slag flow behavior. Consequently, a negative a-factor is unphysical. In mathematical meaning, there are two reasons of a negative a-factor.

- The liquid slag viscosity of the suspension is significantly overestimated or/and
- the solid volume fraction of the suspension is significantly overestimated.

Is the a-factor extended to describe the shear rate influence, the third reason is added.

- The applied shear rate dramatically lowers the suspension's viscosity.

There is no viscosity model available where all a-factors keep positive over the complete B/A-range, Table 18. Best models are Watt-Fereday, Shaw, Kalmanovitch-Frank and BBHLW with only one a-factor below zero. The model of Bomkamp violated for six slags the a-factor rule of a positive a-factor.

Table 18: Number of a-factor violations in view of models.

# Violating Rule $a \geq 0$	Model	Slag
1	Watt-Fereday, Shaw, Kalmanovitch-Frank, BBHLW	S14, S31, S40
2	S2, Urbain, Riboud	S13, S31, S35, S40
4	Lakatos, Streeter, ANNliq	S13, S14, S31, S32, S35, S39, S40, S41
5	Duchesne	S13, S14, S31, S35, S40
6	Bomkamp	S13, S14, S31, S35, S36, S40

The developed a-factors can also be discussed from the point of slags, Table 19. Only slag S42 is completely covered by positive a-factors. Slags S36, S39 and S41 are violating the a-factor rule by one viscosity model. Sample S31 is mostly fitted by negative a-factors. For seven models, a negative a-factor must be applied. There is no clear evidence of B/A-ratio or formed mineral phases to explain the scattering on calculated negative a-factors. Elevated B/A-ratios seem to improve the a-factor fitting, S36 to S42. In contrast, the B/A-ratio of slag S40 is 1.857, but the fitted a-factors fall below zero for six viscosity models.

Table 19: Number of a-factor violations in view of slags.

Violations Rule $a \geq$	Slag	B/A on mass	Model names
0	S42	2.497	-
1	S36	1.069	Bomkamp
1	S39	1.705	Lakatos
1	S41	2.126	Lakatos
2	S32	0.932	Streeter, ANNliq
4	S13	0.337	Bomkamp, Lakatos, Riboud, Duchesne
5	S35	1.046	S2, Bomkamp, Streeter, Duchesne, ANNliq
6	S14	0.337	Watt-Fereday, Bomkamp, Shaw, Streeter, Duchesne, ANNliq
6	S40	1.857	S2, Bomkamp, Lakatos, Urbain, BBHLW, Duchesne
7	S31	0.903	Bomkamp, Urbain, Riboud, Streeter, Kalmanovitch-Frank, Duchesne, ANNliq

The obtained a-factors show following properties which make it difficult to use a multi-parameter function, e.g. non-linear 3D-surface-fit:

- The slope of the fitted a-factors of several viscosity models can vary within a single slag (single B/A-ratio), Figure 83 a).
- The a-factor slope of a single viscosity model can vary for several slags (several B/A-ratios), Figure 83 b).

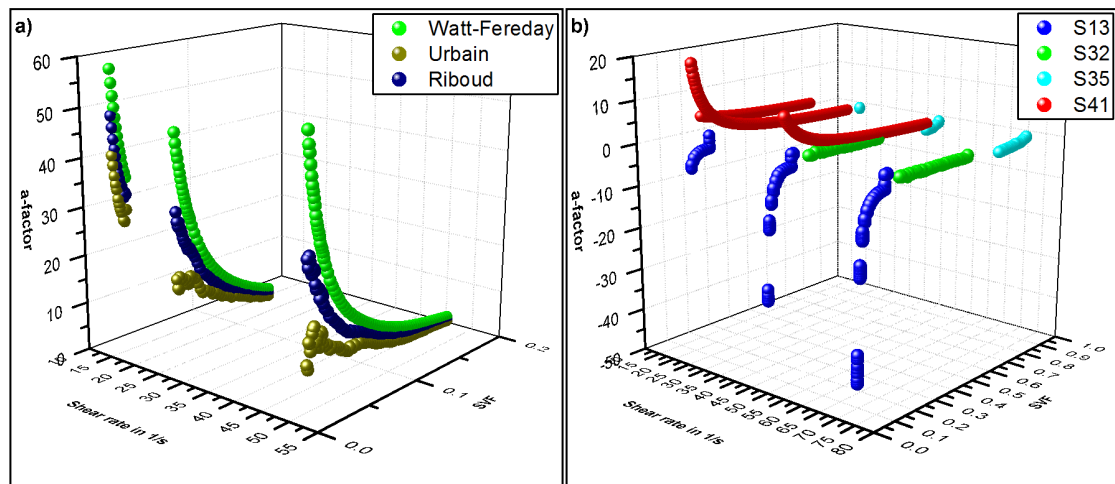


Figure 83: a-factors with different slopes of a) single slag (S42) and b) different slags (Bomkamp model).

8.4.2 Summary of Last Chapter

- The SVF is obtained from phase analysis taken from quenching experiments and XRD. To overcome temperature ranges without XRD information, the SVF is linear interpolated in steps of 10 K for a given slag in the range 1000-17000 °C. Linear interpolation is done with a look-up-table. The order is temperature, followed by B/A-ratio.
- Liquid slag composition is linear interpolated from same XRD datasets. The slag composition of extensively investigated slags was reduced by the components of formed minerals. The loss or the enrichment of slag components is indicated by factors below or above 1. The order is temperature, followed by B/A-ratio.
- The a-factor is calculated on the results of interpolated SVF. Again, a look-up-table is applied in the order shear rate, B/A-ratio and SVF.

8.5 Results of Advanced Slag Viscosity Modelling Approach

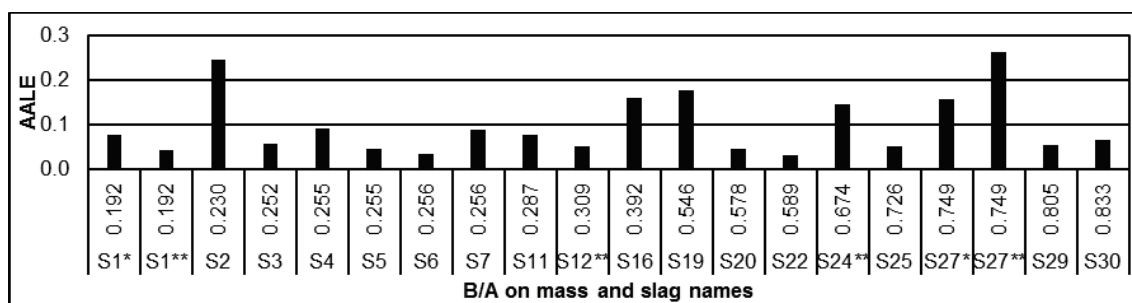
The viscosity of 42 slag samples was calculated by the recommended advanced slag viscosity modelling approach. Predictions and measurements are given in Figure 147 to Figure 227. The liquid slag composition was estimated from interpolation tables when the solid volume fraction (SVF) was above 0. The a-factor was calculated in the same way. If SVF is 0, the a-factor is also 0, read chapter 8.4. Afterwards, the best model by AALE of classical modelling was chosen for advanced viscosity modelling.

Not all slags show an interpolated mineral content of SVF>0. Therefore, no advanced viscosity modelling approach can be used. The found AALE is given in Figure 84 and a discussion starts in the sections below. A separation in different groups is done to characterize this kind of slags, Table 20, page 120.

Group 1 slags are Newtonian and no SVF was estimated by interpolation. This agrees with the theory of rheology. There is no need to introduce the shear rate influence. Results are not further discussed.

Group 2 slags are non-Newtonian, but the interpolated SVF is 0. This is not in agreement with the assumed particle-slag interactions. Several reasons are adduced. The interpolation of SVF for slag samples S1 to S7, $B/A \leq 0.256$, results in $SVF=0$ due to the limited phase information for oxidizing conditions. S4 was investigated by quenching and XRD phase determination in air atmosphere. Due to the high liquidus temperature of this slag, no amorphous sample was produced. Consequently, the extensive investigation program of several quenching points and phase analysis was not applied. Expecting the same behavior at reducing conditions, no further extensive investigation was done for pair slag S5. Other extensively investigated slags under reducing atmospheres are S7, S19 and S30. These slags were set to be amorphous in the given temperature ranges when the SVF table was developed. This influences SVF-interpolations at reducing atmospheres up to $B/A \leq 0.833$. An amorphous solidification behavior is estimated. Similar effects appear on slags under an oxidizing atmosphere and $B/A \leq 0.805$, S29. All extensively investigated slags under oxidizing atmospheres, S16, S20 and S29, were defined to be amorphous within the given temperature ranges.

A solution of this problem is to increase the number of extensively investigated samples of $B/A < 0.4$. Especially, the artificial slags should be replaced by natural melts. The lesser the B/A , the higher must be the maximum temperature of the quench furnace to support higher liquidus temperatures of samples. Oxidizing and reducing atmospheres are recommended to observe.



* - technical nitrogen atmosphere assumed to be oxidizing

** - technical nitrogen atmosphere assumed to be reducing

Figure 84: AALE of slags with interpolated $SVF=0$.

The next slag groups are defined by their modelling success. The formation of minerals, $SVF > 0$, was interpolated within the recorded temperature range. This allowed the application of interpolating the a-factor. To show the improvements of the recommended modelling approach, the AALE of used classic models before and after application of the advanced modelling approach is given. Modelling results of samples

measured under air are depicted in Figure 85. Results of slags measured under reducing conditions are given in Figure 86. Slags measured under technical nitrogen gas are separated into assuming an oxidizing or reducing effect, Figure 87 a) and b).

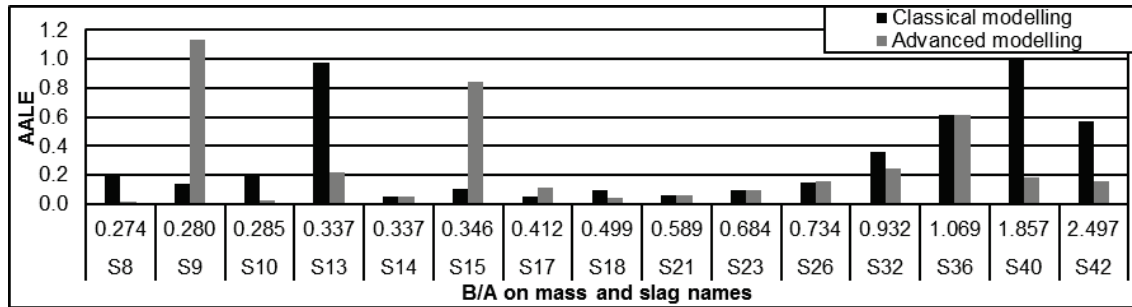


Figure 85: AALEs of best classic and advanced viscosity modelling under oxidizing atmosphere, SVF>0 and all shear rates.

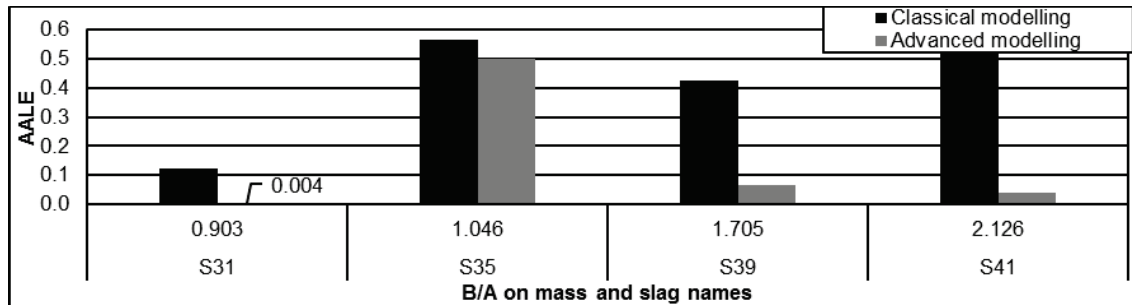


Figure 86: AALEs of best classic and advanced viscosity modelling under reducing atmosphere, SVF>0 and all shear rates.

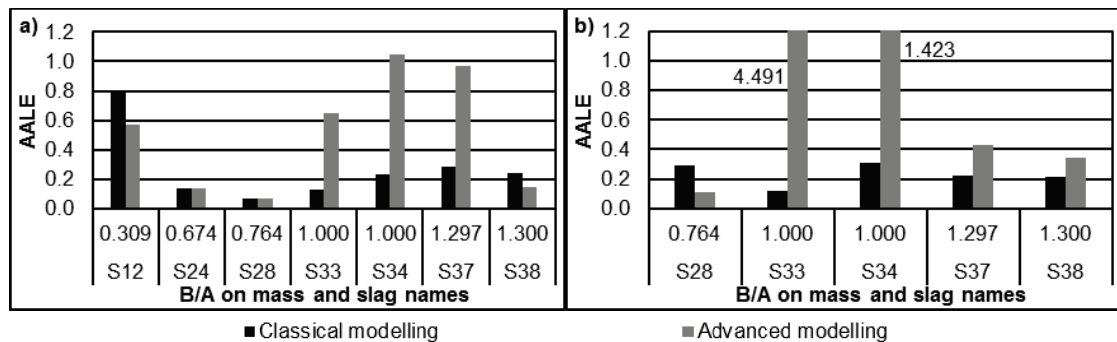


Figure 87: AALEs of best classic and advanced viscosity modelling under nitrogen atmosphere, SVF>0 and all shear rates, assuming a) oxidizing and b) reducing conditions.

Group 3 slags have an interpolated SVF>0, but the flow is Newtonian. This indicates an overestimation of particles. Only three slags exhibit this property: S17, S21, S23. In general, all interpolated SVF of this group became >0 above a viscosity of 40 Pa s and more. Additionally, the calculated SVF are at a low level, below 3 vol.-%. Slags S17 and S23 have a glassy viscosity curve, what can be in accordance to the interpolated low SVF. The viscosity of S21 rapidly increases below 1200 °C what is in accordance with the computed onset of SVF.

Group 4 slags have a SVF>0 as found by interpolation. A non-Newtonian flow indicates the presence of particles formed by partial mineralization. This supports the interpolated SVF>0. The a-factor was calculated in the next step. The AALE of classic

modelling was equal or higher than of advanced viscosity prediction. This indicates an improvement of viscosity forecasts. The quality of improvement fluctuates over ranges of B/A, shear rate and temperature/SVF. As pointed out in the beginning of this section, the best classic model was selected for advanced viscosity modelling. Not all slags support this method, e.g. S8, S10, S12 (assuming oxidizing conditions), S14, S32 and S40. In these cases, the second or third best classic model must be chosen for a satisfactory advanced modelling result. Reason can be the changes of remaining slag composition during the formation of minerals. The best model at classic modelling with a constant slag composition will become disadvantageous when a predicted compositional change occurs. Other slags were predicted with weak performance above a given viscosity range, e.g. S13. There, the a-factor is weak interpolated at elevated SVF. The remaining slag is not the error source. All slag compounds decrease in good proportions. No enrichment of a single slag component is forecasted. Other slags show a loss in prediction performance at a single shear rate, e.g. S35. There, only one shear rate was weak interpolated while others fit well. The reasons are similar as discussed before. Also, slags with a narrow temperature record range are considered to be well predicted, e.g. S36. Hence, the AALE of classic and advanced viscosity predictions are equal. In detail, only the flow behavior of $\dot{\gamma}=25$ 1/s does fail. Other properties as viscosity increase are well forecasted within a temperature range of 20 K.

Group 5 slags are non-Newtonian and a SVF>0 was interpolated, but no improvement of viscosity prediction quality was observed. Advanced viscosity modelling on S15 shows a dramatic failure. Computed viscosities decreased with decreasing temperature. The SVF seems to be too high for the recorded slag flow behavior. Although S15 is a multicomponent slag, only $\text{SiO}_2\text{-Al}_2\text{O}_3\text{-CaO}$ remain in a liquid mixture by SVF interpolation. The B/A of S15 is between the artificial slags S13, S14 and S16. These slags were extensively investigated and the phase determination results were included to create the look-up-tables of SVF and a-factor. This is resulting in an insufficient prediction of the remaining slag composition. For S26, the reason of insufficient prediction performance is hard to estimate. The mineral content was interpolated to be in the range of 2 vol.-%. Even in the case of a wrong assumed remaining liquid slag composition, the influence to viscosity should be less. An insufficient interpolated a-factor and a high amount of CaO are quoted as reasons. CaO is solidifying the glass network at small temperatures due to its strong field strength. Prediction performance of slags S24* and S28* (both nitrogen atmospheres supposed to be oxidizing) is also less. There, the a-factor is giving wrong results in view of shear rate influence. More extensively investigated slags must be introduced within the SVF- and a-factor-tables. The B/A-range 0.546 (S19) to 0.903 (S31) is not efficiently covered by experimental data. All other

group-5-slugs belong to the melts measured with technical nitrogen gas. Two main reasons are found:

- First, the interpolated SVF seems to be too high for the found flow behavior. Not all temperature ranges are covered by non-Newtonian flow.
- Second, dramatic elevated amounts of several slag components were interpolated.

P_2O_5 was computed up to 20 wt.-% for S33* and S34 or 38 wt.-% for S38*. The network modifiers K_2O and Na_2O were computed up to 31 wt.-% for S33** (nitrogen atmosphere supposed to be reducing) or 17 wt.-% for S37**. Especially the computed amounts of P_2O_5 are not covered by the used viscosity models.

Table 20: Slag groups by modelling results.

Group	Properties	Slags
1	○ Interpolated SVF=0	○ Oxidizing: S3, S4, S6
	○ Newtonian flow behavior	○ Reducing: S7, S22, S24**, S30
2	○ Interpolated SVF=0	○ Oxidizing: S1*, S2, S16, S17***, S20, S27*, S29
	○ non-Newtonian flow behavior	○ Reducing: S1**, S5, S11, S12**, S19, S25, S27**
3	○ Interpolated SVF>0	○ Oxidizing: S17***, S21, S23
	○ Newtonian flow behavior	
4	○ Interpolated SVF>0	○ Oxidizing: S8, S10, S12*, S13, S14, S32, S36, S38*, S40, S42
	○ non-Newtonian flow behavior	○ Reducing: S31, S35, S39, S41
	○ improvement by advanced modelling	
5	○ Interpolated SVF>0	○ Oxidizing: S15, S24*, S26, S28*, S33*, S34*, S37*
	○ non-Newtonian flow behavior	○ Reducing: S33**, S34**, S37**, S38**
	○ no improvement by advanced modelling	

* - technical nitrogen gas atmosphere assumed to be oxidizing

** - technical nitrogen gas atmosphere assumed to be reducing

*** - slag owns properties of *-group and **-group

Slags S9 and S18 were measured at a single shear rate. An estimation of the flow behavior cannot be done. Consequently, the forecasted SVF of maximum 0.25 and 0.35 is open for discussion. The advanced viscosity modelling totally failed for S9, while for S18 a partly agreement was found. A weak interpolated a-factor seems to be responsible

for this result. The remaining slag composition is not the source of error. All slag components decrease in a steady manner over the entire temperature range.

Slag S17 owns properties of group 2 and 3. A non-Newtonian flow was observed at temperatures of interpolated SVF=0 and vice versa. Errors during the measurement cannot be excluded, e.g. a not completely molten slag at the begin of viscosity recording. This supports non-Newtonian flow. After a certain time, the slag becomes totally molten and turns Newtonian.

8.5.1 Summary of Last Chapter

- The advanced viscosity modelling approach was applied on all 42 measured slags.
- The best classic model of a slag is chosen to be the best model for advanced viscosity modelling if no better data is available and advanced modelling is possible.
- It is recommended to adjust the Fe-species to the atmospheric conditions, e.g. all iron oxide is Fe_2O_3 at air atmosphere and FeO under reducing conditions.
- Measurements under technical nitrogen atmospheres can be defined as oxidizing or reducing. Viscosity prediction performance is mostly weak when advanced viscosity modelling is applied. A reason can be the ratio of $(\text{CaO}+\text{MgO})/(\text{SiO}_2+\text{Al}_2\text{O}_3)$.
- Five groups of slag were found.
- Group 1 slags exhibit a Newtonian flow behavior and an interpolated SVF=0.
- Group 2 slags were found to be non-Newtonian and SVF=0 what violates rheologic theory. There is not sufficient data of extensively investigated samples under reducing conditions for $B/A \leq 0.833$. Extensively investigated samples under an oxidizing atmosphere where set to be amorphous at elevated temperatures in a similar B/A-range. The number of extensively investigated samples of all atmospheres has to be increased to extend the look-up-tables of SVF and a-factors. This includes also higher quenching temperatures for $B/A < 0.4$.
- Group 3 slags where interpolated to become semi-liquid, SVF>0, but a Newtonian flow was measured. Only small SVF, below 3 vol.-%, were computed. In general, these slags can be shifted to group 1 due to the small calculated amounts of solids.
- Group 4 slags are in agreement with SVF>0 and non-Newtonian flow behavior. The prediction performance was improved by the advanced viscosity modelling approach. Some slags required the second or third best classic model to be improved by the advanced method.

- Group 5 slags are similar to group 4, but the advanced modelling approach turned into disadvantage. The minor part of samples show weak interpolated a-factors within the B/A-range 0.546 (S19) to 0.903 (S31). The number of extensively investigated samples has to be increased. The major part of group 5 samples was measured under nitrogen atmospheres. There is no influence to improve the prediction quality by assuming oxidizing or reducing conditions at elevated B/A-ratios. Reason is the elevated amount of interpolated K_2O , Na_2O and especially P_2O_5 within the remaining slag. Classic models are not covering these amounts.

9. Summary

Viscosity models were selected and the prediction quality of them was validated on own measurements. Slag density is calculated by the temperature and molar volume of slag components. The Einstein-Roscoe equation was chosen for interconnecting effects on slags by crystals and shear rates. The base/acid-ratio is sufficient to describe slag properties of several samples. The difference of calculated B/A-ratios on mass or molar base is neglectable. For this work, the mass-based value was taken.

A procedure was developed for sample preparation and following measurements. Viscosity investigations were carried out in an optimized high temperature viscometer. A self-constructed quench furnace was established to perform quenching experiments on slag samples for further phase analysis. Standard high temperature DTA devices are sufficient to measure the onset of crystallization.

The viscosity of natural and artificial slags was observed for different atmospheres, shear rates and cooling rates. Gasification processes were depicted by reducing conditions achieved by gas mixtures of CO and CO₂. Additional viscosity measurements were carried out under air atmosphere. Measurements under constant partial oxygen pressures on a small number of samples were also included to increase the amount of data. Several slags were extensively investigated by DTA and mineral phase analysis to explain observed viscosity data.

Selecting the best viscosity model of a liquid slag is depending on the B/A-ratio and the associated partial oxygen pressure of the prediction case. Tables for oxidizing and reducing conditions were developed to support the model selection. It is necessary to obtain the tabled values on measurements of low viscosities/high temperatures to avoid particle formation and changes in flow behavior.

Minimum viscosity was found for B/A-ratios around 0.75 for reducing and oxidizing atmospheres. This differs from literature, where the viscosity minimum is given with B/A=1. A significant atmospheric influence was observed. Reducing atmospheres decrease viscosities. No correlation between Fe-amount and temperature difference is found for molten slags in this work. The changing effect is more noticeable at elevated viscosities. This indicates a breakup of the slag network. Slags within $0.58 < B/A < 0.74$ have a viscosity increasing behavior under reducing conditions. A tenable reason is not found.

Mineral formation is influenced by atmospheric conditions. The number of mineral phases increases from oxidizing to reducing conditions. Ferric iron Fe³⁺ is found in minerals only in oxidizing conditions. Ferrous iron Fe²⁺ was observed in minerals for oxidizing and reducing atmospheres. Reason is presence of Fe²⁺ also under oxidizing conditions due to the thermochemical equilibrium.

The presence of minerals around 1 % was found for some samples due to insufficient heating power of the quench furnace. The number of formed minerals is elevated in comparison to completely molten slags. Minerals be supposed to act as crystallization nucleus.

Minerals were observed to decrease or disappear from an elevated temperature to a lower one. Dissolution into the remaining liquid slag is assumed. Additionally, a transformation from one mineral to another can occur. In the mentioned case, Fe^{2+} was built into the crystal structure of Merwinite to form Monticellite as found at S41.

Observations by DTA measurements exhibit decreasing onset temperatures of exothermic events when cooling rate is increased. These events were defined to indicate the begin of mineral formation. This implies the shift of crystallization from high to low temperatures. Atmospheres can influence the onset temperature especially at B/A-ranges from 0.80 to 0.93. There, the onset at oxidizing conditions was significant higher than under reducing atmospheres. Reasons can be the slag structure, indicated by a dilatant flow behavior without presence of minerals, and the formation of different minerals at varying atmospheres. Results of DTA measurements were used in further steps to estimate the onset of crystallization of a slag.

Molten slags are not Newtonian in all cases. A dilatant flow was found for slags within B/A-ranges of 0.73-0.83. Mostly pseudo-plastic flow is occurring. The amount of minerals is not strictly influencing flow behavior. Non-Newtonian flow was recorded for solid volume fractions below 0.1 (10 vol.-%) while slags with solid volume fractions of 0.6 (60 vol.-%) are still Newtonian.

Investigations on the influence of cooling rates were achieved for few slag samples. Slags with B/A-ratios around 0.75 seem to decrease in viscosity with increasing cooling rates and equal temperatures. Structural reasons are quoted. The number of measurements is not reliable.

Results of thermochemical equilibrium calculations on slags must be controversially discussed. The liquidus temperature can be estimated by a small number of samples over wide B/A-ratios. No evidence is found to explain this agreement. In general, liquidus temperatures were over- or underpredicted. Kinetic effects are not covered, too.

Almost all calculations fail in view of mineral phase prediction. Consideration of atmospheres is also not improving mineral phase prediction quality. Especially Fe-containing minerals were not sufficient covered. No relationship between prediction quality and B/A-ratio was found. Slag modelling by thermochemical equilibrium calculations was not further followed.

The recommended slag viscosity modelling approach starts with selecting the best classic viscosity model. Therefore, the absolute average logarithmic error (AALE) was

consulted. On the foundation of own measurements, the AALE of each viscosity model was calculated within all applied shear rates, atmospheres and recorded viscosities of ≤ 25 Pa s. The cooling rate was limited to -2 K/min due to the lack of XRD data at other cooling rates. These ranges were selected to obtain sufficient data points with almost Newtonian flow behavior. An advantage of model performance was found when iron was converted to Fe^{3+} at oxidizing conditions and Fe^{2+} at reducing atmospheres. The Einstein-Roscoe equation was applied to introduce the non-Newtonian flow behavior of slags in case of mineral-containing slags. Only the a-factor was changed and fitted to results of own viscosity measurements, SVF estimation and classic viscosity models. The a-factor becomes negative for few samples. The use of a negative a-factor is undesired due to non-physical background. Afterwards, look-up-tables of solid volume fractions, remaining slag composition and a-factors were developed from results of XRD and DTA investigations. Linear interpolation was applied to calculate slag properties as function of partial oxygen pressure, temperature, B/A-ratio and shear rate.

Five groups of slags were found when the advanced slag viscosity modelling approach was applied. Group 1 exhibit a Newtonian flow and predicted SVF is 0. Group 2 was found to be non-Newtonian and $\text{SVF}=0$ what violates rheologic theory. A lack of phase data especially for natural slag systems of $\text{B/A} < 0.833$ prevent successful calculations. Group 3 exhibit minerals by interpolation. The calculated mineral content is less and a-factor interpolation fails. Group 4 was improved by the advanced slag viscosity modelling approach. Group 5 is not improved and the advanced modelling turns into a disadvantage. Mostly slags measured under nitrogen atmosphere are represented. Enrichments on P_2O_5 and MgO are violating classic viscosity models which are the base of advanced modelling. The fluctuating ratio of $(\text{CaO}+\text{MgO})/(\text{SiO}_2+\text{Al}_2\text{O}_3)$ seems accountable.

The recommended advanced viscosity modelling approach can improve the prediction quality of classic models when certain points are fulfilled, e.g. sufficient tabled XRD, SVF and a-factor data. The development of a single viscosity model to cover wide compositional ranges and Newtonian flow behavior has to be supported. Such model can be extended later to introduce non-Newtonian flow caused by mineral particles. More quench experiments with smaller temperature steps, higher temperatures and a variation in cooling rates must be carried out. Hence, kinetic effects are mapped by these methods.

10. Appendix: Information on Classic Viscosity Modelling

10.1 Backgrounds of Applied Viscosity Models

As pointed out in Table 6, classical slag viscosity models depend on basic viscosity equations. These are Arrhenius, Weymann and Vogel-Fulcher-Tammann relations.

The Arrhenius relation is given in Eq. (44), where T is temperature in K, c_1 and c_2 are material constants in Pa s and K, E_A is flow activation energy in kJ/mol, and the gas constant $R_G=8.314 \cdot 10^{-3}$ kJ/mol K [158–160]. The flow activation energy describes E_A the potential barrier, a material-depending constant, where the temperature of viscous flow was found by viscosity measurements. A recommended application is the description of low-viscosity fluids in the temperature range 100 K above glass transformation T_g and higher. Also, a straight line with a constant slope of the exponential curve function in a semi-logarithmical diagram is assumed [4]. Slags with a non-straight line, a non-linear viscosity development over temperature, will be miss-interpreted by the unmodified Arrhenius function.

$$\eta(T) = c_1 \cdot \exp\left(-\frac{c_2}{T}\right) = c_1 \cdot \exp\left(\frac{\left[\frac{E_A}{R_G}\right]}{T}\right) \quad (44)$$

The Weymann model assumes that a liquid has a quasi-crystalline structure [161]. Molecules oscillate about equilibrium positions. A movement to a neighboring position is possible when

- the molecule's energy is high enough to pass an energy barrier
- and the equilibrium position next to the molecule is empty.

The emptiness of the place next to the molecule is described by transition probability κ . An outer shear stress can increase the frequency of transitions what results in a shear motion of the fluid. No reaction rate theory as within the Arrhenius assumption was applied, while statistical and mechanical concepts were employed to the Weymann theory, Eq. (45), where ε_0 is height of the potential barrier between equilibrium positions, m is mass of molecule, κ is transition probability, $v^{2/3}$ volume factor equal to the volume of a molecule. Referred to a previous work, k is the Boltzmann constant $1.381 \cdot 10^{-23}$ J/K and T is temperature in K [162].

$$\eta = \left(\frac{k \cdot T}{\varepsilon_0}\right)^{1/2} \cdot \frac{(2 \cdot m \cdot k \cdot T)^{1/2}}{-v^{2/3} \cdot \kappa} \cdot \exp\left(\frac{\varepsilon_0}{k \cdot T}\right) \quad (45)$$

The Vogel-Fulcher-Tammann equation (VFT) is an improvement of the Boltzmann approach to describe η - T -relationship, Eq. (46), where E_η is activation energy in J/mol to start viscous flow, R_G is gas constant, T the temperature in K and K the system constant.

$$\eta = K \cdot \exp\left(\frac{E_\eta}{R_G \cdot T}\right) \quad (46)$$

This relation is valid for simple liquids. Glasses do not offer a linear η - T -relationship and therefore calculations of E_η will become difficult. At high temperatures, the glass network is broken and E_η will be low to start viscous flow. For low temperatures, the glass network is well developed and a higher E_η is needed to overcome the energy barrier of flow. To include the described observations, the Boltzmann approach was complemented by an additional constant T_0 in K, Eq. (47).

$$\eta = K \cdot \exp\left(\frac{E_\eta}{T - T_0}\right) \quad (47)$$

The common relationship of VFT is given in Eq. (48), where A , B and T_0 are constants developed from three fixed points. These points are the temperature of glass transformation T_g , softening point estimated by the method of Littleton and the working point. Associated viscosities are $1 \cdot 10^{12.3}$ Pa s, $1 \cdot 10^{6.6}$ Pa s and $1 \cdot 10^3$ Pa s, respectively [10,36].

$$\log \eta = A + \frac{B}{T - T_0} \quad (48)$$

Especially in glass technology, detailed tables of constants A , B and T_0 were obtained for numerous melt compositions. Slag has a strongly differing composition in comparison to glasses. Therefore, a direct use of VFT is not possible for slag viscosity prediction without large adaptations.

Artificial Neural Network models are based on the principle of a communicating brain. As found in nature, neurons get information about a parameter, process this information and send it to a next neuron. Several kinds of ANN structures are available. A brief description of selected ANNs is given in Table 21.

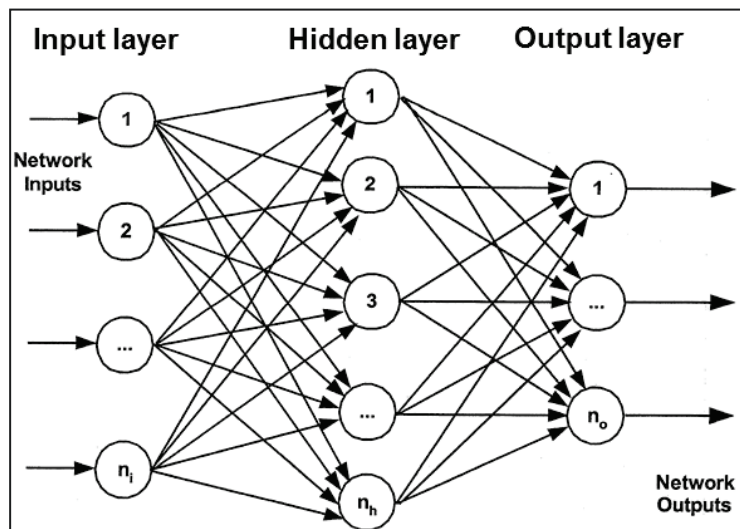
Table 21: Selected Artificial Neuronal Network structures [163].

Structure	Description
Multilayer perceptron (MLP)	<ul style="list-style-type: none"> each neuron output is connected to every neuron in next layer
Recurrent neural network (RNN), e.g. Hopfield	<ul style="list-style-type: none"> two sources of input external and internal flow of information
Non-recurrent Unsupervised Kohonen Network	<ul style="list-style-type: none"> structure of interconnected processing units consists of input layer and output (Kohonen) layer each input neuron is connected to all output neurons
Cerebellar Model Articulation Controller (CMAC)	<ul style="list-style-type: none"> multidimensional interlaces layers network decides by Boolean functions distribution of information to next layer

Important structures are

- the input layer, where data is coming from outside;
- the hidden layer, where data processing is performed; and
- the output layer for results.

See Figure 88 for schematic representation of ANN.

**Figure 88: Scheme of a MLP basic topology of an ANN [163].**

ANNs show advantages over conventional regression methods. Instead of developing an equation to describe a parameter in dependence of several others, e.g. viscosity as function of temperature and composition, ANNs are learning and interpreting dependencies of several parameters. Furthermore, an improved handling with scattered experimental data is reported. After selecting the structure of an ANN, setting input and output parameters, the ANN is trained. The stop criterion of training can be a specific performance function, e.g. the deviation between measured and calculated viscosity. It

is also recommended, to validate the ANN with another data than it was trained to exclude over-fitting [93,163,164].

10.2 Viscosity Model of the BCURA (S^2)

The compositional distribution of the fundamental 62 slag samples is given in Table 22.

Table 22: Compositional ranges covered by S^2 development [35].

Component	mass-%
SiO ₂	31-59
Al ₂ O ₃	19-37
Equivalent Fe ₂ O ₃	0-38
CaO	1-37
MgO	1-12
Na ₂ O + K ₂ O	1-6
Silica ratio S	45-75
SiO ₂ /Al ₂ O ₃	1.2-2.3

The original model predicted viscosity in Poise, while here the recalculation to Pa s was applied by introducing factor 0.1, Eq. (49). Temperature T is given in K and factor S is the silica ratio, Eq. (50). Slag components are in weight percent. The iron oxide equivalent $equiv.Fe_2O_3$ is a recalculation of the total iron content performed on weight basis if not other specified, Eq. (51). The background of $equiv.Fe_2O_3$ is to deal with different oxidation states of iron. The S^2 model was developed with assumption; all iron is in Fe³⁺ state [95]. The factors represent the mass relationship of iron for Fe₂O₃, FeO and Fe. 1 g of Fe₂O₃ contains the same amount of iron as 1/1.11 g of FeO and 1/1.43 g of Fe [35].

$$\log \eta = \left(4.468 \cdot \left(\frac{S}{100} \right)^2 + 1.265 \cdot \left(\frac{10^4}{T} \right) - 7.44 \right) \cdot 0.1 \quad (49)$$

$$S = \frac{100 \cdot SiO_2}{SiO_2 + equiv.Fe_2O_3 + CaO + MgO} \quad (50)$$

$$equiv.Fe_2O_3 = Fe_2O_3 + 1.11FeO + 1.43Fe \quad (51)$$

10.3 Watt-Fereday

Investigations were carried out on coals used for cyclone firing, Table 23.

Table 23: Compositional ranges covered by Watt-Fereday model [165].

Component	mass-%
SiO ₂	30-60
Al ₂ O ₃	15-35
Equivalent Fe ₂ O ₃	3-30
CaO	2-30
MgO	1-10
Silica ratio <i>S</i>	40-80
SiO ₂ /Al ₂ O ₃	1.4-2.4

Based on a modified Arrhenius equation, slag viscosity is predicted as given in Eq. (52). Factor 0.1 was applied to receive viscosity values in Pa s. Constants *m* and *c* are calculated by Eq. (53) and (54). Temperature *t* is in degrees Celsius [165].

$$\log \eta = \left(\frac{10^7 \cdot m}{(t - 150)^2} + c \right) \cdot 0.1 \quad (52)$$

$$m = 0.00835 \cdot SiO_2 + 0.00601 \cdot Al_2O_3 - 0.109 \quad (53)$$

$$c = 0.0415 \cdot SiO_2 + 0.0192 \cdot Al_2O_3 + 0.0276 \cdot equiv. Fe_2O_3 + 0.0160 \cdot CaO - 3.92 \quad (54)$$

The origin of *equiv. Fe₂O₃* was discussed above, Eq. (51). MgO is not ineffective, but covered by the recalculation to 100 wt.-% of the major components. On the other hand, MgO represents the major component with fewer amounts. Its influence should be therefore less to slag viscosity as pointed out in the original work. It is also noted, that a silica ratio *S* calculated for a British coal will fail when applied with a U.S. coal [165]. Misprints of the second term in the equation of *c* are reported for the works of Hoy et al. 1965 [166] and Quon et al. 1984 [167]. Also a misprint in the work of Vargas et al. 2001 [35] can be found for the last term in the *c*-equation.

10.4 Bomkamp

Modifications on *m* and *c* constants of the Watt-Fereday model were performed, Eq. (55) and (56). Viscosity is calculated by Eq. (52) in the same way as the Watt-Fereday model. Due to lack of references, equations were taken from secondary citation [41]. There is no indication about the use of *equiv. Fe₂O₃*. For regularity, the amount of iron should be calculated as described in section 4.1.2.

$$m = 0.0104291 \cdot SiO_2 + 0.0100297 \cdot Al_2O_3 - 0.296285 \quad (55)$$

$$c = 0.0154148 \cdot SiO_2 - 0.0388047 \cdot Al_2O_3 - 0.0167264 \cdot Fe_2O_3 - 0.0089096 \cdot CaO - 0.012932 \cdot MgO + 1.04678 \quad (56)$$

A probable misprint of the c constant is found in the work of Vargas et al. 2001. There, the last term is 0.04678 instead of 1.04678 [35].

10.5 Shaw

Base of the Bottinga-Weill model is the mixing relationship of simple mixtures, also called Arrhenius mixture rule, Eq. (57), where $\bar{\eta}$ is viscosity of mixture, η_i is characteristic viscosity of component i with mole fraction X_i . Characteristic viscosity η_i was achieved by minimizing the difference between measured and recalculated viscosity data. Data of η_i was published in steps of 35-45, 45-55, 55-65, 65-75 and 75-81 mole-% SiO_2 . Tabled temperature ranged from 1200-1800 °C in 50 K steps. Eleven pure oxides, namely SiO_2 , TiO_2 , FeO , MnO , MgO , CaO , SrO , BaO , Li_2O , Na_2O and K_2O are included. Alumina is covered by the theoretical formation of combined species, $KAlO_2$, $NaAlO_2$, $BaAl_2O_4$, $CaAl_2O_4$, $MgAl_2O_4$ and $MnAl_2O_4$ [45].

$$\ln \bar{\eta} = \sum_{i=1}^n X_i \cdot \ln \eta_i \quad (57)$$

Shaw applied the Arrhenius relation, to the found constants of Bottinga and Weill, Eq. (58), where η_0 is the pre-exponential factor, E^* is activation energy in kcal/mole, R is gas constant and T is temperature in K. The pre-exponential factor η_0 is treated as hypothetical viscosity.

$$\ln \eta = \ln \eta_0 + \left(\frac{E^*}{R} \right) \cdot \left(\frac{1}{T} \right) \quad (58)$$

Arrhenius graphs of $\ln \eta$ vs. $1/T$ were plotted for several mixtures and the slope is used to describe viscosity. By this assumption, viscosity is given by Eq. (59) in Pa s, where s is the characteristic slope for a given multicomponent mixture, and c_T and c_η are coordinates of the point of intersection. The intersection point coordinates were chosen by weighted means of investigated viscosity-temperature-relationships. The slope, characterizing each slag mixture, is computed by Eq. (61) with help of component-depending factor s_i^0 , Table 24.

For further investigations, the modification of [35] was achieved in this work.

$$\eta = \exp \left(\left(s \cdot \left(\frac{10^4}{T} \right) - c_T \cdot s + c_\eta \right) \right) \cdot 0.1 \quad (59)$$

$$\eta = 10^{\left(s \cdot \left(\frac{10^4}{T} \right) - c_T \cdot s + c_\eta \right)} \quad (60)$$

$$s = \frac{\sum (X_i \cdot s_i^0) \cdot X_{SiO_2}}{(1 - X_{SiO_2})} \quad (61)$$

Table 24: Factors for the Shaw model referenced by [90] and [35].

	Shaw 1972	Vargas et al. 2001
Metal oxide – silica pair	Slope intercept s_i^0	
K ₂ O-, Na ₂ O-, Li ₂ O-	2.8	1.2
MgO-, FeO-	3.4	1.5
CaO-, TiO ₂ -	4.5	2.0
“AlO ₂ ”-	6.7	2.9
Coordinates of the point of intersection		
c_η	-6.40	-3.78
c_T	1.50	

For the sake of completeness, the further discussed relationship between activation energy E^* , characteristic viscosity η_0 , s , c_T and c_η is given in Eq. (62) and (63), respectively. Shaw was not defining a clear physical relationship between these constants.

$$E^* = 10^4 \cdot s \cdot R = 19.87 \text{ kcal/mol} \cdot s \quad (62)$$

$$\ln \eta_0 = c_\eta - c_T \cdot s \quad (63)$$

For predicting slag viscosity, recalculate the slag components to the amount of model-covered species. All iron within the sample has to be recalculated to FeO. Depending on the explanation by Bottinga and Weill, iron is assumed to be a network modifier. Al₂O₃ is changed to “AlO₂” in moles simply by multiplying the mass with two [90].

The influence of H₂O on slag viscosity is also covered by the Shaw model, but insufficient data does not allow a proofed statement. Viscosity data taken from geological pressure ranges (≤ 20 kbars) is not comparable to gasification techniques (≤ 100 bars).

10.6 Lakatos Model

The compositional range of investigated samples is given in Table 25. As common in glass technology, silica content has a small range of approximately 60-75 wt.-%.

Table 25: Compositional ranges for Lakatos model development [68].

Oxide	Wt.-%
SiO ₂	59.5-77.4
Al ₂ O ₃	0.0-8.3
CaO	8.2-13.3
MgO	0.0-6.7
Na ₂ O	10.4-15.3
K ₂ O	0.0-8.7

Lakatos applied the Vogel-Fulcher-Tammann (VFT) equation to calculate viscosity, Eq. (64). Viscosity η is given in Pa s by including factor 0.1, T is temperature in °C and T_0 , B and A are constants related to glass composition. Constants were developed by multiple regressions of minimum temperature deviations, Eq. (65) to (67). Factors Na₂O, K₂O, CaO, MgO and Al₂O₃ represent the glass composition in *mole component / 1 mole SiO₂*.

$$\log \eta = \left(-A + \frac{B}{T - T_0} \right) \cdot 0.1 \quad (64)$$

$$B = -6039.7 \cdot Na_2O - 1439.6 \cdot K_2O - 3919.3 \cdot CaO + 6285.3 \cdot MgO + 2253.4 \cdot Al_2O_3 + 5736.4 \quad (65)$$

$$A = -1.4788 \cdot Na_2O + 0.8350 \cdot K_2O + 1.6030 \cdot CaO + 5.4936 \cdot MgO - 1.5183 \cdot Al_2O_3 + 1.4550 \quad (66)$$

$$T_0 = -25.07 \cdot Na_2O - 321.0 \cdot K_2O + 544.3 \cdot CaO - 384.0 \cdot MgO + 294.4 \cdot Al_2O_3 + 198.1 \quad (67)$$

10.7 Urbain Model

Urbain assumes the melt flow as position changes of ionic structures into free places, depending on the free volume probability P_v . Also, viscosity is a function of the “jumping” probability P_e of the melt ions. Furthermore, the model separates into network forming, network modifying and amphoteric ions, Table 26.

Table 26: Separation of network formers, modifiers and amphoterics by [91,100].

Group	Ion
Network formers	Si ⁴⁺ , Ge ⁴⁺ , P ⁵⁺
Network modifiers	Na ⁺ , K ⁺ , Ca ²⁺ , Fe ²⁺ , Cr ³⁺ , Ti ⁴⁺
Amphoterics	Al ³⁺ , B ³⁺ , Fe ³⁺

The Urbain viscosity model bases on the Weymann relation written in a modified form, Eq. (68), where viscosity η is in Pa s by application of factor 0.1, T is temperature in K, A and B are parameters depending only on the melt composition. The parameters A and B are empirical linked, Eq. (69), where A has the unit of Pa s/K and B has the unit of K.

A cubic function describes B , Eq. (70), where N is the molar fraction of silica. The numerical values of B_i can be calculated by Eq. (71)-(74) under support of constant α .

$$\eta = \left(A \cdot T \cdot \exp\left(\frac{10^3 \cdot B}{T}\right) \right) \cdot 0.1 \quad (68)$$

$$-\ln A = 0.2693 \cdot B + 11.6725 \quad (69)$$

$$B = B_0 + B_1 \cdot N + B_2 \cdot N^2 + B_3 \cdot N^3 \quad (70)$$

$$B_0 = 13.8 + 39.9355 \cdot \alpha - 44.049 \cdot \alpha^2 \quad (71)$$

$$B_1 = 30.481 - 117.1505 \cdot \alpha + 129.9978 \cdot \alpha^2 \quad (72)$$

$$B_2 = -40.9429 + 234.0486 \cdot \alpha - 300.04 \cdot \alpha^2 \quad (73)$$

$$B_3 = 60.7619 - 153.9276 \cdot \alpha + 211.1616 \cdot \alpha^2 \quad (74)$$

As introduced above, viscosity is driven by the probabilities P_v and P_e . Urbain used the parameters to describe also the occurrence of free volume. All melts used by Urbain show a linear relationship between $\ln A$ and B [168].

Constant α describes the fraction of network modifiers and amphoteric. The equation was extended from the first publication to a final version, Eq. (75) and (76). MO is mole fraction of network modifiers and A_2O_3 is mole fraction of amphoteric.

$$\alpha = \frac{CaO}{CaO + Al_2O_3} \quad (75)$$

$$\alpha = \frac{\sum MO}{\sum MO + \sum A_2O_3} \quad (76)$$

Urbain recommended also the use of composition-depending calculation methods for MO or N , e.g. Fe_2O_3 has to be treated as network modifier [100]. To limit the possibilities of calculation methods, a proposal for factors is given below, Eq. (77) and Eq. (78). Components are in mole fractions [35]. Another work mentioned SO_3 instead of CaF_2 as network modifier [95].

$$MO = FeO + CaO + MgO + Na_2O + K_2O + MnO + NiO + 2 \cdot (TiO_2 + ZrO_2) + 3 \cdot CaF_2 \quad (77)$$

$$A_2O_3 = Al_2O_3 + Fe_2O_3 + B_2O_3 \quad (78)$$

10.8 Riboud Model

Investigated slags were separated into ternary SiO_2 - CaO - CaF_2 , SiO_2 - CaO - Na_2O and SiO_2 - CaO - Al_2O_3 ; quaternary SiO_2 - CaO - CaF_2 - Na_2O , SiO_2 - CaO - Al_2O_3 - Na_2O ; and

quintuple $\text{SiO}_2\text{-CaO-Al}_2\text{O}_3\text{-CaF}_2\text{-Na}_2\text{O}$. Contents ranged from 0 to over 50 %, Table 27. SiO_2 dominates the compositional ranges.

Table 27: Content ranges for the development of Riboud model.

Component	Wt.-%
SiO_2	34-56
Al_2O_3	0-12
CaO	8-46
CaF_2	0-18
Na_2O	0-22

Depending on further investigations done by Urbain [99,169], the authors decided to use the Weymann (or Frenkel) viscosity relation. The derived form is given in Eq. (79), where A and B are viscosity parameters in Pa s/K and K, respectively. Temperature T is in K.

$$\eta = A \cdot T \cdot \exp\left(\frac{B}{T}\right) \quad (79)$$

Parameters A and B have been computed on synthetic slags by the least squares method. Furthermore, the compositional influence on slag viscosity was described by first order polynomial expression, Eq. (80) and Eq. (81). Constituents are represented in molar fractions.

$$\begin{aligned} \ln A = & -19.81 + 1.73 \cdot (X_{\text{CaO}} + X_{\text{MnO}} + X_{\text{MgO}} + X_{\text{FeO}}) + 5.82 \cdot X_{\text{CaF}_2} + 7.02 \\ & \cdot (X_{\text{Na}_2\text{O}} + X_{\text{K}_2\text{O}}) - 35.76 \cdot X_{\text{Al}_2\text{O}_3} \end{aligned} \quad (80)$$

$$\begin{aligned} B = & +31140 - 23896 \cdot (X_{\text{CaO}} + X_{\text{MnO}} + X_{\text{MgO}}) - 46356 \cdot X_{\text{CaF}_2} - 39159 \\ & \cdot (X_{\text{Na}_2\text{O}} + X_{\text{K}_2\text{O}}) + 68833 \cdot X_{\text{Al}_2\text{O}_3} \end{aligned} \quad (81)$$

The original work of Riboud exhibits presumably a twist of digits. Eq. (81) is given twice: In the beginning of the paper in a simple and at the end in a more detailed form. There, factor “31519” is printed as “39159”. Because the amount of Na_2O and K_2O in slags is less than 10 mole-%, no explicit discussion has to be done on this circumstance.

10.9 Streeter Model

Table 28 includes slag compositional ranges of the initial 17 slags [95].

Table 28: Compositional range of slags for Streeter model development [95].

Oxide	Wt.-%
SiO ₂	20.0-63.5
Al ₂ O ₃	13.3-36.7
Fe ₂ O ₃	0.9-18.9
TiO ₂	0.6-2.3
P ₂ O ₅	0.0-0.8
CaO	6.0-29.4
MgO	2.5-8.2
Na ₂ O	0.0-9.9
K ₂ O	0.1-2.2
SO ₃	0.0-1.8

Adapted from the Urbain model [91], the basic viscosity formulation is given by Eq. (82), where temperature T is in K, B is the parameter defined by slag composition, A is function of B , Eq. (69) and Eq. (70). Viscosity is given in Pa s by application of factor 0.1.

$$\ln \eta = \ln A + \ln T + \frac{1000 \cdot B}{T} \quad (82)$$

To fit the Urbain equation to the experimental obtained data, an additional term Δ has to be applied, Eq. (83). The fourth term is calculated by Eq. (84). It describes the difference (positive or negative) between computed and measured viscosity points. Factor b is a function of m and best fitted by Eq. (85).

$$\ln \eta = \ln A + \ln T + \frac{1000 \cdot B}{T} + \Delta \quad (83)$$

$$\Delta = m \cdot T + b \quad (84)$$

$$b = -1.6870 \cdot (1000 \cdot m) + 0.2343 \quad (85)$$

In the next step, a correlation for m was developed. It was pointed out, that a single formulation of m is not able to cover the complete slag compositional range. As a result, the m -function was separated into three formulae depending on the value of B . Oxides are in mole fractions.

- High-silica slags, $B > 28$

$$b = -1.7137 \cdot (1000 \cdot m) + 0.0509 \quad (86)$$

$$1000 \cdot m = -1.7264 \cdot F + 8.4404 \quad (87)$$

$$F = \frac{SiO_2}{CaO + MgO + Na_2O + K_2O} \quad (88)$$

- Intermediate-silica slags, $24 < B < 28$

$$b = -2.0356 \cdot (1000 \cdot m) + 1.1094 \quad (89)$$

$$1000 \cdot m = -1.3101 \cdot F' + 9.9279 \quad (90)$$

$$F' = B \cdot (Al_2O_3 + FeO) \quad (91)$$

- Low-silica slags, $24 < B$

$$b = -1.8244 \cdot (1000 \cdot m) + 0.9416 \quad (92)$$

$$1000 \cdot m = -55.3649 \cdot F'' + 37.9186 \quad (93)$$

$$F'' = \frac{CaO}{CaO + MgO + Na_2O + K_2O} \quad (94)$$

10.10 Kalmanovitch-Frank Model

Parameter A and α were adapted to the datasets of [53,54,109], Eq. (95) and (96). Factor α received changes. Use Eq. (70) to calculate factor B as introduced in section 4.1.6. Components are expressed as mole fractions [92].

$$\ln A = -0.2812 \cdot B - 11.8279 \quad (95)$$

$$\alpha = \frac{CaO + MgO + Na_2O + K_2O + FeO + TiO_2}{Al_2O_3 + CaO + MgO + Na_2O + K_2O + FeO + TiO_2} \quad (96)$$

10.11 BBHLW Model

A number of 117 slag samples was taken into account for the model development. See Table 29 for compositional ranges. The melts ranged from binary mixtures to multi-component systems.

Table 29: Compositional range of slags for BBHLW model development [92].

Oxide	Wt.-%	
	coal ash slags	synthetic slags
SiO ₂	26.5-60.9	18.5-70
Al ₂ O ₃	4.7-31.5	0-40
CaO	0.3-40.1	0-55
FeO	0.2-29.2	0-80
K ₂ O	0-7.1	0
MgO	0.1-4.7	0-25
Na ₂ O	0.05-2.1	0
TiO ₂	0.3-1.6	0-19
SO ₃	0.03-1.57	0
MnO	0.01-0.72	0-7.9

The BBHLW model bases on the observation of Nicholls and Reid, Eq. (97). They declared that at a given viscosity, the gradient of the viscosity-temperature relation is the same. Newtonian flow behavior is assumed.

$$\frac{d\eta}{dT} = f(\eta) \neq f(T) \quad (97)$$

Different slag compositions will be distributed over along the temperature axis. By the help of a temperature shift, the viscosity curves can be shifted to overlay each other. This temperature shift is characteristic for any slag composition. The resulting expression is given in Eq. (98) where experimental temperature T and temperature shift T_S are in K. Viscosity in Pa s is calculated by transposing Eq. (98) to Eq. (99).

$$\log\left(\frac{\eta}{T - T_S}\right) = \frac{14788}{T - T_S} - 10.931 \quad (98)$$

$$\eta = 10^{(14788/(T-T_S)-10.931)} \cdot (T - T_S) \quad (99)$$

Temperature shift T_S was correlated to slag composition by introducing a weighted molar ratio A . This fitting included three steps:

1. Weighting each slag component by a coefficient,
2. calculate coefficients by least square regression, and
3. moving coefficients to other side of divisor in factor A when coefficient became negative.

Following expressions were found for temperature shift T_S and weighted molar ratio A , Eq. (100) and (101). Slag components given in molar fractions normalized to 1.

$$T_S = 306.63 \cdot \ln A - 574.31 \quad (100)$$

$$A = (3.19 \cdot Si^{4+} + 0.855 \cdot Al^{3+} + 1.6 \cdot K^+) / (0.93 \cdot Ca^{2+} + 1.50 \cdot Fe^{n+} + 1.21 \cdot Mg^{2+} + 0.69 \cdot Na^+ + 1.35 \cdot Mn^{n+} + 1.47 \cdot Ti^{4+} + 1.91 \cdot S^{2-}) \quad (101)$$

The authors discovered a linear relationship between octahedral (fluxing) cation radii and the value of fluxing ion coefficient. K_2O is assumed to change the equilibrium between network-forming AlO_2^- and network-modifying Al^{3+} ions.

10.12 Duchesne Model

Duchesne used Artificial Neural Network model technology. It was created using MATLAB® 7.6 [170].

Input data and ranges were transferred to first hidden layer for model regression, Table 30. Data sources include reducing and oxidizing atmospheres as soon as artificial and natural slag systems. Number of oxides ranged from single to multi-component melts. Digits of values are necessary due to calculation precision.

Table 30: Development input data and parameter ranges of Duchesne model [93].

Input	Minimum	Maximum
Temperature in °C	809	2482
Si mole fraction	0.1347	1.00
Al mole fraction	0.00	0.8235
Fe mole fraction	0.00	0.8053
Ca mole fraction	0.00	0.60
Mg mole fraction	0.00	0.651
Na mole fraction	0.00	0.50
K mole fraction	0.00	0.5081
Mn mole fraction	0.00	0.688
Log (viscosity in Pa s)	-3.81	11.16

Calculations of Temperature T_{norm} in K, normalized slag composition X_{norm} with component X_i in moles and normalized elements mole fractions \bar{X}_i are done by Eq. (102) to (111). As declared in Eq. (106), all iron is transferred into Fe_2O_3 . A separation between reducing and oxidizing conditions is not possible by the principle of the model.

$$T_{norm} = \frac{T - 1082}{2755 - 1082} \quad (102)$$

$$X_{norm} = X_{SiO_2} + 2 \cdot X_{Al_2O_3} + 2 \cdot X_{Fe_2O_3} + X_{FeO} + X_{Fe} + X_{CaO} + 2 \cdot X_{Na_2O} + 2 \cdot X_{K_2O} + X_{MnO} \quad (103)$$

$$\bar{X}_{SiO_2} = X_{SiO_2} / X_{norm} \quad (104)$$

$$\bar{X}_{Al_2O_3} = (2 \cdot X_{Al_2O_3}) / X_{norm} \quad (105)$$

$$\bar{X}_{Fe2O3} = (2 \cdot X_{Fe2O3} + X_{FeO} + X_{Fe})/X_{norm} \quad (106)$$

$$\bar{X}_{CaO} = X_{CaO}/X_{norm} \quad (107)$$

$$\bar{X}_{MgO} = X_{MgO}/X_{norm} \quad (108)$$

$$\bar{X}_{Na2O} = (2 \cdot X_{MgO})/X_{norm} \quad (109)$$

$$\bar{X}_{K2O} = (2 \cdot X_{K2O})/X_{norm} \quad (110)$$

$$\bar{X}_{MnO} = X_{MnO}/X_{norm} \quad (111)$$

To adjust input data as required by the ANN, normalized temperature T_{norm} and normalized elements mole fractions \bar{X}_i have to be linearized into \bar{T}_{norm} and $\bar{\bar{X}}_i$, Eq. (112) and (113). As result, the individual linearization ranges from -1 to +1. Values of Max and Min of each component i can be found in Table 30 for investigated compositional ranges.

$$\bar{T}_{norm} = \frac{2 \cdot T_{norm} - 1 - 0}{1 - 0} \quad (112)$$

$$\bar{\bar{X}}_i = \frac{(2 \cdot \bar{X}_i - Max(i) - Min(i))}{Max(i) - Min(i)} \quad (113)$$

Input data to hidden layer nodes is computed by Eq. (114), where $w_H(i, j)$ represent signal weights i going to node j . Weights for signals (parameters) going to the hidden layer are given in Table 31.

$$Input_{node}(j) = T_{norm} \cdot w_H(0, j) + \sum_{i=1}^9 \bar{\bar{X}}_i \cdot w_H(i, j) \quad (114)$$

Table 31: Weights to first hidden layer within ANN Duchesne model [93].

Parameter i	Name	Node 1 $w_H(i, 1)$	Node 2 $w_H(i, 2)$	Node 3 $w_H(i, 3)$
0	Temperature	-0.7939	1.1056	-0.1516
1	Si	1.1249	0.1558	-0.4868
2	Al	-0.5146	-1.7803	0.997
3	Fe	0.0577	0.6035	-0.2673
4	Ca	0.7364	0.3918	-0.5305
5	Mg	-1.6109	-1.1210	1.3102
6	Na	0.6952	0.1849	-0.4222
7	K	0.2251	0.9112	-0.4758
8	Mn	0.859	1.4353	-1.0365
9	Bias	-0.2809	-0.0547	0.1204

After sending data to the hidden layer nodes, outputs of hidden layer nodes have to be interpreted. Therefore, Eq. (115) has to be applied for each of the three output nodes.

$$Output_{node}(j) = \frac{2}{1 + \text{Exp}(-2 \cdot Input_{node}(j))} - 1 \quad (115)$$

In the next step, an additional input node is calculated from all three output nodes, Eq. (116). The necessary output weights $w_o(j)$ are given in Table 32.

$$Input_{node}(4) = w_o(4) + \sum_{j=1}^3 Output_{node}(j) \cdot w_o(j) \quad (116)$$

Table 32: Weights for output nodes of Duchesne model [93].

Node j	Output weight $w_o(j)$
1	1.3008
2	1.0609
3	2.2571
4	-0.2587

Afterwards, the output of nodes has to be normalized by Eq. (117). As recognized from the used factors, this step is supported by the maximum and minimum of $\log \eta$ taken from model development.

$$Output = \frac{(Input_{node}(4) \cdot (11.156 + 3.81218) + 11.156 - 3.81218)}{2} \quad (117)$$

Finally, predict slag viscosity η in Pa s by Eq. (118).

$$\eta = 10^{Output} \quad (118)$$

10.13 ANNliq Model

Temperature and compositional ranges varying to Duchesne model are given in Table 33. Digits of values are necessary due to calculation precision.

Table 33: Input data and parameter ranges used to develop the ANNliq model [83].

Input	Minimum	Maximum
Temperature in °C	1100	2482
Si mole fraction	0.00	1.00
Al mole fraction	0.00	1.00
Fe mole fraction	0.00	0.88334
Ca mole fraction	0.00	0.60
Mg mole fraction	0.00	0.651
Na mole fraction	0.00	0.51944

Continuation of Table 33

Input	Minimum	Maximum
K mole fraction	0.00	0.540791
Mn mole fraction	0.00	0.50
Log (viscosity in Pa s)	-2.5	3.00

Calculation steps to not differ strongly from Duchesne model. Changes were done on temperature linearization, signal weights $w_H(i, j)$ going to hidden layer, output weights $w_o(j)$ and the calculation of the nodes' output. Linearization of temperature is done in one step. All changed formulations and values are given below, Eq. (119) and (120), Table 34 and Table 35. Any effort to the atmospheric regime, reducing or oxidizing, was not included.

$$\bar{T}_{norm} = \frac{2 \cdot T - 2755 - 1373}{2755 - 1373} \quad (119)$$

$$Output = \frac{(Input_{node(4)} \cdot (3 + 2.49485) + 3 - 2.49485)}{2} \quad (120)$$

Table 34: Weights to first hidden layer within ANNliq model [83].

Parameter i	Name	Node 1 $w_H(i, 1)$	Node 2 $w_H(i, 2)$	Node 3 $w_H(i, 3)$
0	Temperature	-0.8122	-0.608	0.372
1	Si	0.4779	1.3219	-6.4457
2	Al	0.2338	0.3832	-4.5697
3	Fe	-0.9978	-3.4329	-4.0402
4	Ca	0.1647	0.9149	-2.2416
5	Mg	0.1559	0.8349	-2.3479
6	Na	1.3006	2.023	13.8132
7	K	0.536	1.1477	-0.4666
8	Mn	-0.1862	0.3596	-1.986
9	Bias	-0.2444	-0.4375	3.1203

Table 35: Weights for output nodes for ANNliq model [83].

Node j	Output weight $w_o(j)$
1	2.7936
2	-2.3112
3	-0.5613
4	0.387

11. Appendix: Settings of Equilibrium Calculations

Table 36: Solution species selected for phase calculations by SVP.

Miscibility	Base-Phase	Miscibility	Base-Phase
I	FTmisc-FeLQ	I	FToxid-aC2S
I	FTmisc-BCCS	I	FToxid-Cord
I	FTmisc-FCCS	I	FToxid-Mull
I	FToxid-SLAGH	I	FToxid-CAF1
I	FToxid-MeO_A	I	FToxid-CORU
+	FToxid-WOLLA	I	FToxid-Neph
I	FToxid-bC2S	I	FToxid-AlSp

I immiscibility gap; + single phase

Table 37: Compound species of FactSage selected for phase calculations.

Compound species, gases, FactPS + FToxid					
position	name	position	name	position	name
1	O(g)	26	Al ₂ O(g)	51	KO(g)
2	O ₂ (g)	27	Al ₂ O ₂ (g)	52	KF(g)
3	O ₃ (g)	28	Al ₂ O ₃ (g)	53	(KF) ₂ (g)
4	F(g)	29	AlF(g)	54	Ca(g)
5	F ₂ (g)	30	AlF ₂ (g)	55	Ca ₂ (g)
6	OF(g)	31	AlF ₃ (g)	56	CaO(g)
7	O ₂ F(g)	32	(AlF ₃) ₂ (g)	57	CaF(g)
8	O ₂ F(g ₂)	33	OAlF(g)	58	CaF ₂ (g)
9	OF ₂ (g)	34	AlOF ₂ (g)	59	Ti(g)
10	F ₂ O ₂ (g)	35	NaAlF ₄ (g)	60	TiO(g)
11	Na(g)	36	Na ₂ AlF ₅ (g)	61	TiO ₂ (g)
12	Na ₂ (g)	37	NaAl ₂ F ₇ (g)	62	TiF(g)
13	NaO(g)	38	(NaAlF ₄) ₂ (g)	63	TiF ₂ (g)
14	NaF(g)	39	Si(g)	64	TiF ₃ (g)
15	(NaF) ₂ (g)	40	Si ₂ (g)	65	TiF ₄ (g)
16	Mg(g)	41	Si ₃ (g)	66	OTiF(g)
17	Mg ₂ (g)	42	SiO(g)	67	OTiF ₂ (g)
18	MgO(g)	43	SiO ₂ (g)	68	Mn(g)
19	MgF(g)	44	SiF(g)	69	Fe(g)
20	MgF ₂ (g)	45	SiF ₂ (g)	70	FeO(g)
21	(MgF ₂) ₂ (g)	46	SiF ₃ (g)	71	FeF(g)
22	Al(g)	47	SiF ₄ (g)	72	FeF ₂ (g)
23	Al ₂ (g)	48	OSiF ₂ (g)	73	FeF ₃ (g)
24	AlO(g)	49	K(g)		
25	AlO ₂ (g)	50	K ₂ (g)		

Continuation of Table 37

Liquid iron mixtures selected for phase calculations by SVP					
position	name	position	name	position	name
74	Fe(FeLQ)	80	Ti(FeLQ)	86	SiO(FeLQ)
75	Al(FeLQ)	81	Mg(FeLQ)	87	MnO(FeLQ)
76	Ca(FeLQ)	82	MgO(FeLQ)	88	Al ₂ O(FeLQ)
77	Mn(FeLQ)	83	CaO(FeLQ)	89	Ti ₂ O(FeLQ)
78	O(FeLQ)	84	AlO(FeLQ)		
79	Si(FeLQ)	85	TiO(FeLQ)		
Iron alloys in BCC structure selected for phase calculations by SVP					
position	name	position	name	position	name
106	Fe:Va(BCCS)	109	Mn:Va(BCCS)	112	Fe:Va(FCCS)
107	Mn:Va(BCCS)	110	Fe:Va(FCCS)	113	Mn:Va(FCCS)
108	Fe:Va(BCCS)	111	Mn:Va(FCCS)		
Slag species selected for phase calculations by SVP					
position	name	position	name	position	name
114	MgO(SLAGH)	120	Ti ₂ O ₃ (SLAGH)	126	KF(SLAGH)
115	FeO(SLAGH)	121	CaO(SLAGH)	127	CaF ₂ (SLAGH)
116	MnO(SLAGH)	122	Al ₂ O ₃ (SLAGH)	128	MgF ₂ (SLAGH)
117	Na ₂ O(SLAGH)	123	K ₂ O(SLAGH)	129	FeF ₂ (SLAGH)
118	SiO ₂ (SLAGH)	124	Fe ₂ O ₃ (SLAGH)	130	MnF ₂ (SLAGH)
119	TiO ₂ (SLAGH)	125	NaF(SLAGH)	131	Mn ₂ O ₃ (SLAGH)
Metal oxides with rock salt structure selected for phase calculations by SVP					
position	name	position	name	position	name
150	FeO(MeO_A)	153	MgO(MeO_A)	156	TiO ₂ (MeO_A)
151	Fe ₂ O ₃ (MeO_A)	154	Al ₂ O ₃ (MeO_A)		
152	CaO(MeO_A)	155	MnO(MeO_A)		
Wollastonite selected for phase calculations by SVP					
position	name	position	name		
164	MgSiO ₃ (WOLLA)	166	CaSiO ₃ (WOLLA)		
165	FeSiO ₃ (WOLLA)	167	MnSiO ₃ (WOLLA)		

Continuation of Table 37

Alpha-prime Ca ₂ SiO ₄ selected for phase calculations by SVP			
position	name	position	name
168	Mg ₂ SiO ₄ (bC2S)	170	Ca ₂ SiO ₄ (bC2S)
169	Fe ₂ SiO ₄ (bC2S)	171	Mn ₂ SiO ₄ (bC2S)
Alpha Ca ₂ SiO ₄ selected for phase calculations by SVP			
position	name	position	name
176	Mg ₂ SiO ₄ (aC2S)	178	Mn ₂ SiO ₄ (aC2S)
177	Ca ₂ SiO ₄ (aC2S)	179	Fe ₂ SiO ₄ (aC2S)
Corderite selected for phase calculations by SVP			
position	name	position	name
184	Al ₄ Fe ₂ Si ₅ O ₁₈ (Cord)	185	Al ₄ Mg ₂ Si ₅ O ₁₈ (Cord)
Mullite selected for phase calculations by SVP			
position	name	position	name
188	Al ₂ Al ₁ O ₅ (Mull)	190	Al ₂ Si ₁ O ₅ (Mull)
189	Al ₂ Al ₁ Va ₅ (Mull)	191	Al ₂ Si ₁ Va ₅ (Mull)
Ca-Al-Fe-O compositions selected for phase calculations by SVP.			
position	name	position	name
196	Ca ₁ Al ₂ O ₄ (CAF1)	197	Ca ₁ Fe ₂ O ₄ (CAF1)
Corundum structure selected for phase calculations by SVP			
position	name	position	name
200	Al ₂ O ₃ (CORU)	202	Mn ₂ O ₃ (CORU)
201	Fe ₂ O ₃ (CORU)	203	Ti ₂ O ₃ (CORU)
Nepheline structure selected for phase calculations by SVP			
position	name	position	name
208	NaAlSiO ₄ (Neph)	209	Si ₂ O ₄ (Neph)
Al-Spinel selected for phase calculations by SVP			
position	name	position	name
212	MgAl ₂ O ₄ (AlSp)	214	MnAl ₂ O ₄ (AlSp)
213	FeAl ₂ O ₄ (AlSp)	215	Al ₈ O ₁₂ (AlSp)

Continuation of Table 37

Compound species for pure liquids, taken from FToxid, FactPS			
position	name	position	name
220	Na ₂ O(liq)	241	K ₂ Si ₂ O ₅ (liq)
221	MgO(liq)	242	K ₂ Si ₄ O ₉ (liq)
222	Al ₂ O ₃ (liq)	243	Ca(liq)
223	SiO ₂ (liq)	244	CaF ₂ (liq)
224	K ₂ O(liq)	245	Ti(liq)
225	CaO(liq)	246	TiO(liq)
226	TiO ₂ (liq)	247	Na ₄ TiO ₄ (liq)
227	Ti ₂ O ₃ (liq)	248	Na ₈ Ti ₅ O ₁₄ (liq)
228	MnO(liq)	249	MgTi ₂ O ₅ (liq)
229	Na(liq)	250	Al ₂ TiO ₅ (liq)
230	NaF(liq)	251	K ₄ TiO ₄ (liq)
231	Mg(liq)	252	CaTiO ₃ (liq)
232	MgF ₂ (liq)	253	CaSiTiO ₅ (liq)
233	Al(liq)	254	Mn(liq)
234	AlF ₃ (liq)	255	MnF ₂ (liq)
235	MgAl ₂ O ₄ (liq)	256	Mn ₂ TiO ₄ (liq)
236	Si(liq)	257	Fe(liq)
237	K(liq)	258	FeO(liq)
238	KF(liq)	259	FeF ₂ (liq)
239	KAlO ₂ (liq)	260	FeNaO ₂ (liq)
240	K ₂ SiO ₃ (liq)	261	(FeO) ₂ (TiO ₂)(liq)
Compound species for pure solids, taken from FToxid, FactPS			
position	name	position	name
262	FeAl ₃ (s)	387	K ₈ Ti ₅ O ₁₄ (s)
263	Na ₂ O(s)	388	K ₂ Ti ₆ O ₁₃ (s)
264	Na ₂ O(s ₂)	389	CaTiO ₃ (s)
265	Na ₂ O(s ₃)	390	CaTiO ₃ (s ₂)
266	MgO(s)	391	Ca ₂ Ti ₂ O ₅ (s)
267	Al ₂ O ₃ (s)	392	Ca ₂ Ti ₂ O ₅ (s ₂)
268	Al ₂ O ₃ (s ₂)	393	Ca ₃ Ti ₂ O ₆ (s)
269	Al ₂ O ₃ (s ₃)	394	Ca ₃ Ti ₂ O ₇ (s)
270	Al ₂ O ₃ (s ₄)	395	Ca ₅ Ti ₄ O ₁₃ (s)
271	NaAlO ₂ (s)	396	CaSiTiO ₅ (s)
272	NaAlO ₂ (s ₂)	397	MnO(s)
273	NaAl ₉ O ₁₄ (s)	398	MnO ₂ (s)
274	Na ₂ Al ₁₂ O ₁₉ (s)	399	Mn ₂ O ₃ (s)
275	SiO ₂ (s)	400	Mn ₂ O ₃ (s ₂)
276	SiO ₂ (s ₂)	401	MnAl ₂ O ₄ (s)

Continuation of Table 37

Compound species for pure liquids, taken from FToxid, FactPS			
position	name	position	name
277	SiO2(s3)	402	MnSiO3(s)
278	SiO2(s4)	403	Mn2SiO4(s)
279	SiO2(s5)	404	Mn2Al4Si5O18(s)
280	SiO2(s6)	405	Mn3Al2Si3O12(s)
281	SiO2(s7)	406	MnTiO3(s)
282	SiO2(s8)	407	MnTi2O4(s)
283	Na2SiO3(s)	408	MnTi2O5(s)
284	Na4SiO4(s)	409	Mn2TiO4(s)
285	Na2Si2O5(s)	410	Mn2TiO4(s2)
286	Na2Si2O5(s2)	411	Fe2O3(s)
287	Na2Si2O5(s3)	412	Fe2O3(s2)
288	Na6Si2O7(s)	413	Fe2O3(s3)
289	Na6Si8O19(s)	414	Na2Fe2O4(s)
290	MgSiO3(s)	415	Al2Fe2O6(s)
291	MgSiO3(s2)	416	FeSiO3(s)
292	MgSiO3(s3)	417	FeSiO3(s2)
293	MgSiO3(s4)	418	FeSiO3(s3)
294	MgSiO3(s5)	419	Fe2SiO4(s)
295	MgSiO3(s6)	420	Fe2SiO4(s2)
296	MgSiO3(s7)	421	Fe2SiO4(s3)
297	Mg2SiO4(s)	422	Fe2Al4Si5O18(s)
298	Mg2SiO4(s2)	423	Fe3Al2Si3O12(s)
299	Mg2SiO4(s3)	424	CaFe2O4(s)
300	Na2MgSi4O10(s)	425	Ca2Fe2O5(s)
301	Na2Mg2Si6O15(s)	426	CaFe4O7(s)
302	Al2Si2O7(s)	427	CaFeSi2O6(s)
303	NaAlSiO4(s)	428	Ca2FeSi2O7(s)
304	NaAlSiO4(s2)	429	Ca3Fe2Si3O12(s)
305	NaAlSi2O6(s)	430	(FeO)(TiO2)(s)

Table 38: Details of used density data to estimate density model performance.

# points	216			
# references	10			
References	[131,171,171–176,176,177]			
Temperature	Min °C		Max °C	
	1230		1700	
Oxides	Wt.-%		Mole-%	
	Min	Max	Min	Max
SiO ₂	0.0	74.0	0.0	76.4
Al ₂ O ₃	0.0	51.8	0.0	35.9
Fe ₂ O ₃	0.0	40.0	0.0	19.2
FeO	0.0	70.4	0.0	68.7
CaO	0.0	60.0	0.0	61.9
MgO	0.0	28.8	0.0	41.0
Na ₂ O	0.0	0.4	0.0	0.4
K ₂ O	0.0	0.2	0.0	0.1
MnO	0.0	4.0	0.0	4.0
TiO ₂	0.0	11.1	0.0	8.9
CaF ₂	0.0	23.7	0.0	22.0

Table 39: Recommended densities of minerals found in crystallized slags.

Mineral	Formula	Density g/cm ³	Temp. K	Ref.
-	-	-	-	-
Akermanite (melilite)	Ca ₂ MgSi ₂ O ₇	2.94	298	[178]
Anorthite	CaAl ₂ Si ₂ O ₈	2.75	298	[179]
Augite	(Ca,Na)(Mg,Fe,Al,Ti)(Si,Al) ₂ O ₆	3.19	298	[179]
Brownmillerite	Ca ₂ Al _{1.1} Fe ₂ +0.9O ₅	3.75	298	[179]
Calcium Iron Aluminum Oxide	CaFe ⁺⁺⁺ 3AlO ₇	4.16	298	TOPAS 4.0
Corundum	Al ₂ O ₃	3.88	1273	FS 6.4; FToxid; SlagA
		3.87	1373	FS 6.4; FToxid; SlagA
		3.86	1473	FS 6.4; FToxid; SlagA
		3.84	1573	FS 6.4; FToxid; SlagA
		3.83	1673	FS 6.4; FToxid; SlagA
		3.82	1773	FS 6.4; FToxid; SlagA
		3.80	1873	FS 6.4; FToxid; SlagA
		3.79	1973	FS 6.4; FToxid; SlagA
Cristobalite (high)	SiO ₂	1.92	1750	FS 6.4; FToxid; SlagA
		1.91	1773	FS 6.4; FToxid; SlagA
		1.88	1873	FS 6.4; FToxid; SlagA
		1.84	1973	FS 6.4; FToxid; SlagA
Diopside iron	Ca(Mg _{0.75} Fe _{0.25})Si ₂ O ₆	3.23	1323	FS 6.4; FToxid; I SlagA; + FToxid-LcPy

Continuation of Table 39

Mineral	Formula	Density g/cm ³	Temp. K	Ref.
-	-	-	-	-
Fayalite magnesian	Fe ⁺⁺ 2SiO ₄	4.19	1273	FS 6.4; FToxid; SlagA
		4.15	1473	FS 6.4; FToxid; SlagA
		4.10	1673	FS 6.4; FToxid; SlagA
		4.05	1873	FS 6.4; FToxid; SlagA
Ferrobustamite	(CaFe)(SiO ₃) ₂	3.42	1273	FS 6.4; FToxid; SlagA
		3.40	1373	FS 6.4; FToxid; SlagA
		3.37	1473	FS 6.4; FToxid; SlagA
		3.37	1497	FS 6.4; FToxid; SlagA
Forsterite, ferroan	Mg ₂ SiO ₄	3.12	1273	FS 6.4; FToxid; SlagA
		3.10	1473	FS 6.4; FToxid; SlagA
		3.07	1673	FS 6.4; FToxid; SlagA
		3.04	1873	FS 6.4; FToxid; SlagA
Gehlenite	Ca ₂ Al ₂ SiO ₇	2.98	298	Enc. of Minerals, 2nd ed., 1990
		2.97	1273	FS 6.4; FToxid; SlagA
		2.95	1473	FS 6.4; FToxid; SlagA
		2.94	1673	FS 6.4; FToxid; SlagA
Grossular	Ca ₃ Al ₂ (SiO ₄) ₃	3.57	298	[180]
Hibonite	CaAl ₁₂ O ₁₉	3.84	298	[181]
Kirschsteinite	CaFe ⁺⁺ (SiO ₄)	3.43	298	[181]
	Ca(Fe _{0.69} Mg _{0.31})SiO ₄	3.43	298	[181]

Continuation of Table 39

Mineral	Formula	Density g/cm ³	Temp. K	Ref.
-	-	-	-	-
Larnite	Ca ₂ (SiO ₄)	F.I.O.	F.I.O.	[181]
Maghemite γ -Fe ₂ O ₃	Fe ⁺⁺⁺ 2O ₃	4.90	298	[181]
Magnesioferrite	MgAl _{0.79} Fe _{1.21} O ₄	4.150	298	[182]
Magnesioferrite aluminian	MgFe ⁺⁺⁺ 2O ₄	4.50	298	[183]
Magnesium Silicate (taken from Forsterite, ferroan)	Mg ₂ SiO ₄	3.12	1273	FS 6.4; FToxid; SlagA
		3.10	1473	FS 6.4; FToxid; SlagA
		3.07	1673	FS 6.4; FToxid; SlagA
		3.04	1873	FS 6.4; FToxid; SlagA
Magnetite	Fe ⁺⁺ Fe ⁺⁺⁺ 2O ₄	5.15	298	[179]
		5.20	298	[179]
		5.20	298-2500	FS 6.4; FactPS - FACT 2013
Merwinite	Ca ₃ Mg(SiO ₄) ₂	3.34	298	FS6.4 FTdemo
		3.22	1273	FS6.4 Equilib-Calc. FToxid+FactPS+FTmisc
		3.20	1473	FS6.4 Equilib-Calc. FToxid+FactPS+FTmisc
Merwinite	Ca ₃ Mg(SiO ₄) ₂	3.18	1673	FS6.4 Equilib-Calc. FToxid+FactPS+FTmisc
Monticellite	CaMgSiO ₄	3.17	1773	FS6.4 Equilib-Calc. FToxid+FactPS+FTmisc
Monticellite with 0.12 moles Fe ⁺⁺	CaFe ⁺⁺ 0.12Mg _{0.88} SiO ₄	3.20	298	TOPAS 4.0
Mullite 2:1	(Al ₂ O ₃) ₂ (SiO ₂) ₁	3.05	298	[179]
Porcelainite	Al ₆ Si ₂ O ₁₃	3.17	298	[179]

Continuation of Table 39				
Mineral	Formula	Density g/cm ³	Temp. K	Ref.
-	-	-	-	-
ps-Wollastonite	CaSiO ₃	2.80	1398.3	FS 6.4; FToxid; SlagA
		2.79	1473.	FS 6.4; FToxid; SlagA
		2.77	1573.	FS 6.4; FToxid; SlagA
		2.76	1673.	FS 6.4; FToxid; SlagA
		2.75	1773.	FS 6.4; FToxid; SlagA
		2.75	1813.18	FS 6.4; FToxid; SlagA
Quartz (high)	SiO ₂	2.54	1139.92	FS6.4 Equilib-Calc. FToxid + FactPS + FTmisc
Spinel	MgAl ₂ O ₄	3.65	298	[179]
Spinel-hercynite	Fe ⁺⁺ Al ₂ O ₄	3.95	298	[181]
Srebrodolskite	Ca ₂ Fe ⁺⁺⁺ 2O ₅	4.04	298	[179]
Wollastonite	CaSiO ₃	2.80	1398.3	FS 6.4; FToxid; SlagA
Wuestite	FeO	5.83	1273	FS 6.4; FToxid; SlagA
		5.83	1373	FS 6.4; FToxid; SlagA
		5.83	1473	FS 6.4; FToxid; SlagA
		5.83	1573	FS 6.4; FToxid; SlagA

12. Appendix: Parameters of Einstein-Roscoe Equation

Table 40: Values of a and n factors of Einstein-Roscoe equation taken from several references.

a-factor	Conditions / Remarks	Size ratio	Distributions	Ref.
1.00	○ spheres of very diverse sizes	1.71:1	25 vol.-%; <3.4 μm	[135]
	○ valid for all concentrations 0.05< f <0.45 water-based mixture	2.74:1	25 vol.-%; >6.0 μm 25 vol.-%; <150 μm 25 vol.-%; > 90 μm	[136]
1.35	○ spheres of equal sizes			
	○ high and medium concentrations			
	○ invalid for $f \geq \frac{1}{1.35} \geq 0.7401$ (close-packing) ○ water-based mixture	n.d.	n.d.	[129], [134]
1.35	○ spheres of equal sizes			
	○ low concentrations $f > 0.05$			
	○ formed particle doublets are increasing effective concentration ○ water-based mixture	2:1	n.d.	[134]
1.35	○ flow behavior studies on SiO_2 - Na_2O - B_2O_3 melts	n.d.	n.d.	[184]
	○ solid NaBO_2 separated			
2.25 1.34	○ flow behavior investigations within the garnet composition, e.g. $\text{Mg}_3\text{Al}_2\text{Si}_3\text{O}_{12}$		10-51 vol.-% 180-400 μm	
	○ viscosity in the range of 10^8 - 10^{14} Pa s	n.d.		[185]
	○ non-Newtonian behavior found for $f \geq 0.4$			
	○ n varies from 1.3 to 3.4			
4.24	○ introducing of MgAl_2O_4 spinel into completely molten CaO - MgO - Al_2O_3 - SiO_2 slag at 1373 °C		0-20 vol.-% 0.10-0.21 mm	
	○ fine particle size	n.d.		
	○ $n = -1.28$			
3.29	○ medium particle size			[124]
	○ $n = -2.36$	n.d.	0-20 vol.-% 0.21-0.44 mm	
3.56	○ coarse particle size			
	○ $n = -2.24$	n.d.	0-20 vol.-% 0.44-0.99 mm	

Continuation of Table 40

a-factor	Conditions / Remarks	Size ratio	Distributions	Ref.
1.158	<ul style="list-style-type: none"> viscosity investigations on 45 coal ash slags calculation of solid volume fraction by support of FactSage no analysis of formed particles use of Eq. (33) for $f \leq 0.1$ with 1.158 instead of 2.5 	n.d.	$f < 0.1$	[112]
1.00	<ul style="list-style-type: none"> modified Eq (35) where maximum $f=0.62$ $n = -4.62 \cdot \dot{\gamma}^{-0.572}$ 	n.d.	$f \geq 0.1$	

If not noted $n=-2.5$

n.d. – not determined data

f – solid volume fraction (SVF)

13. Appendix: Ash and Slag Sample Preparation

Ashing process started with extraction of coal samples from transport containments by a standard sampling method. Proximate analyses were carried out to detect the ash content of rare coal. When the ash content is known, an adequate amount of coal was ashed to receive enough products for further preparation steps. Coal was ashed under air for 36 h according to DIN 51719. If necessary, coal was milled to a grain size <10 mm to improve ashing success within THERCONCEPT furnace (THERMCONCEPT Dr. Fischer GmbH & Co. KG, Bremen), Figure 89. Ultimate analysis and X-ray fluorescence (XRF) of melted bead were applied to estimate ash composition.



Figure 89: Ashing furnace chamber.

Slagging under air was the second process step. After XRF analysis of ash, the liquidus temperature was estimated by thermoequilibrium software FactSage 6.4TM. Liquidus temperature prediction was based on the composition of metal oxides. The use of phase diagrams is also possible but limited due to the availability of certain data for multicomponent ashes. All ash sample was filled into a platinum-gold (Pt95-Au5, mass-related) dish and slagged under air with at least 50 K more than calculated liquidus temperature. A Carbolite 1500 RHFTM chamber furnace (Carbolite Gero GmbH & Co. KG, Neuhausen, Germany) was used for samples with liquidus temperature below 1450 °C. In case of ashes with liquidus temperatures from 1450-1700 °C, the TOMMI plusTM furnace (Fraunhofer Institut für Silicatiforschung, Bronnbach, Germany) was engaged, Figure 90 a) and b). Initial temperatures were 600 °C.

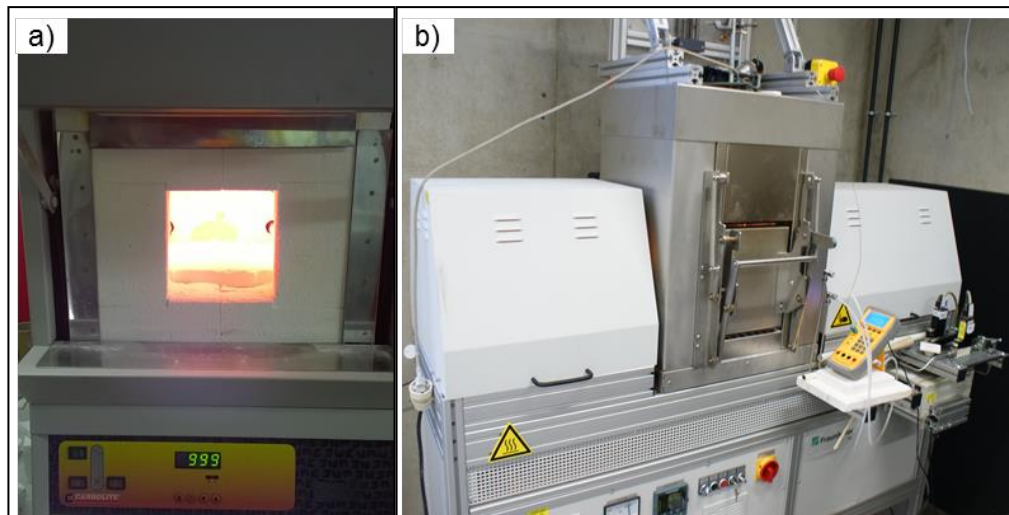


Figure 90: High-temperature furnace a) of Carbolite and b) TOMMI plus.

Heating rates varied from 1-10 K/min depending on the swelling or bubbling behavior. The swelling behavior was not in agreement with the ash composition, i.e. ashes with high sulfur, sodium or other contents were similarly bubbling than ashes with a moderately amount of volatiles. The melting state has to be eye-proofed due to the non-predictability of bubbling behavior. In summary, a heating rate of 2 K/min is recommended. A boil over of ash/slag can cause serious damages on the furnace, Figure 91. When the liquidus temperature was passed by 50-100 K, the sample was hold for 1-3 h and cooled down with 10 K/min afterwards to room temperature. The remaining slag was removed from the Pt95-Au5 crucible and milled to powder in a swinging disc mill (Herzog HSM, HERZOG Maschinenfabrik GmbH & Co. KG, Osnabrück, Germany). Milling is required for further XRF-analysis and to provide a well homogenized slag powder.



Figure 91: Damages caused by slag boil over within a high temperature furnace.

Slagging under reducing conditions was done in a vertical furnace with atmospheric control, Reetz VRO 1650 (HTM Reetz GmbH, Berlin, Germany), Figure 92. Preparation of slag samples under reducing conditions was introduced before viscosity measurements were carried out under reducing conditions. This ensures a defined sample condition in the beginning of viscosity measurements.



Figure 92: Reetz vertical tube furnace 1650 to adjust oxidation state.

Slag powder prepared under air was divided into two equal portions. One half was taken for reducing conditions preparation. The powder was filled in a Platinum-Rhodium (Pt80-Rh20, mass-related) crucible and inserted within the furnace. A heating rate of 10 K/min was achieved up to 50-100 K above liquidus temperature predicted for reducing conditions by FactSage 6.4TM. From startup to 1000 °C, the furnace tube was purged by argon gas (ALPHAGAZTM 1, AIR LIQUIDE Deutschland GmbH, Düsseldorf). At 1000 °C, a mixture of carbon monoxide (CO) and carbon dioxide (CO₂) was achieved to maintain a reducing atmosphere. Primary goal was to change all Fe³⁺ into Fe²⁺. Depending on temperature and slag composition, the CO:CO₂ ratio was set to 6:4 and in later experiments 7:3. This causes partial oxygen pressures p_{O_2} in the range $1 \cdot 10^{-7}$ to $1 \cdot 10^{-15}$ atm in the investigated temperature ranges, Figure 93 a). The ratio Fe₂O₃/FeO is shifted to lower values, more FeO is formed, Figure 93 b). Values are taken from FactSage 6.4TM calculations with FactPS, FToxid, FTmisc, pure solids, liquids and gases whereas real gas behavior is switched on. The mechanism of iron reducing can be related to

- thermochemical equilibrium and/or to
- chemical reaction, e.g. by free C from the Boudouard reaction or directly by CO from the gas atmosphere.

A detailed discussion on the impact of thermochemical equilibrium and chemical reaction in view of iron reducing will be not given.

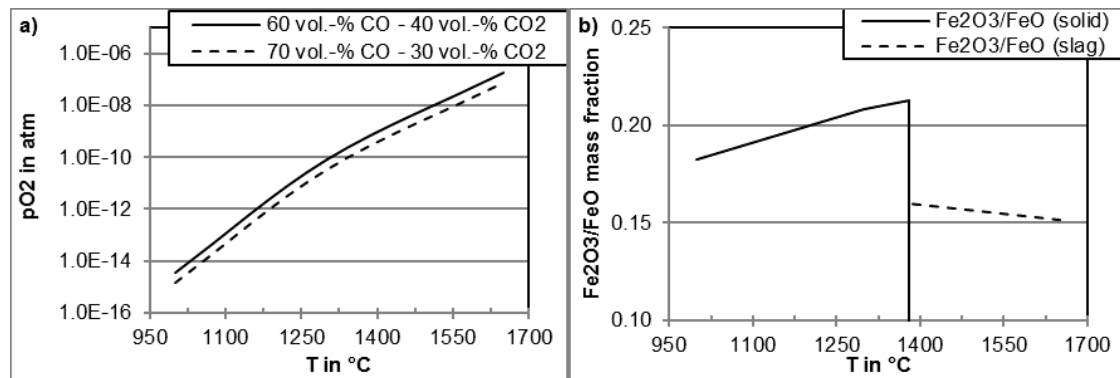


Figure 93: Influence of temperature a) to partial oxygen pressure of different $\text{CO}:\text{CO}_2$ ratios and b) on the $\text{Fe}_2\text{O}_3/\text{FeO}$ mass ratio at 70 vol.-% CO and 60 vol.-% CO_2 . Input is pure Fe_2O_3 , liquidus temperature is 1375.3 $^\circ\text{C}$.

The dwell time for melting and the fixed $\text{CO}:\text{CO}_2$ gas ratio has to be discussed. Information about sample preparation varies in literature. A selection is given below:

- No time information [43,64,186],
- short holding times of 1-3 h for sample fusing [58,187] and
- several hours [151]

Also, the influence of atmosphere on the formation of the $\text{Fe}^{3+}/\text{Fe}_{\text{total}}$ ratio is less discussed. Authors who are explicit studied the influence of ferrous and ferric iron are using a gas mixture of CO/CO_2 to adjust $p\text{O}_2$ and later validate the $\text{Fe}^{3+}/\text{Fe}_{\text{total}}$ by Mössbauer spectra [58]. Also, the use of sacrificial graphite crucibles to remove all O_2 from atmosphere or as measuring system later in viscosity investigations is reported [92]. It is not reported that researchers changed the gas composition for each temperature to achieve a constant $p\text{O}_2$.

In view of application to gasification processes, the dwell time and the distribution of $p\text{O}_2$ has to be close to experiences with technical facilities. A review resulted in resting times >10 min for entrained gasification processes [188] and >15 min for BGL gasifiers. The partial oxygen pressures vary over the length of the reactor but should be predictable by the gas composition and the temperature of each section.

14. Appendix: Experimental Procedures: Viscometer

14.1 General Viscometer Description

The high temperature viscometer manufactured by Bähr Thermoanalyse GmbH (Hüllhorst, Germany) is depicted in Figure 94 a) and b). Main parts are (1) the viscometer measuring head, (2) the measuring chamber, (3) the gas supply, and (4) the exhaust system essential to run under reducing conditions. Inside the sample chamber, there are (5) the crucible within the insulation, (6) the crucible holder made from alumina with internal thermocouple, and (7) the spindle going through the chamber upper side.

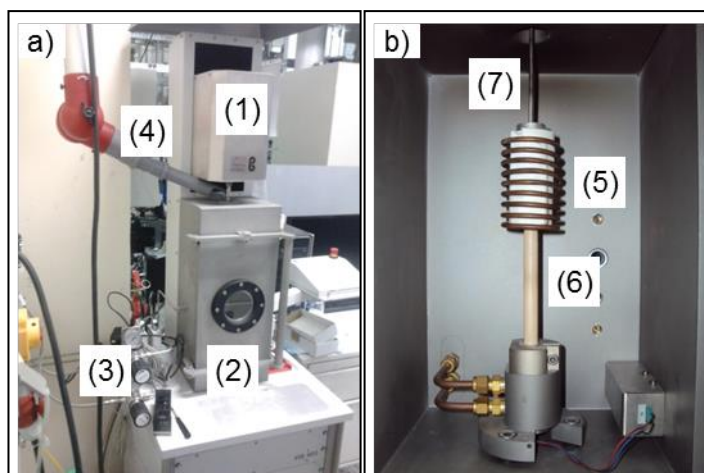


Figure 94: HT-Viscometer a) from outside with closed door and b) open measurement chamber.

The dimensions of crucible and rotating bob are given in Figure 95 a). R_S and R_C are the bob radius and crucible inner radius with 4.5 and 11.45 mm, respectively. Crucible and bob are made from a Pt-Rh alloy (80-20 wt.-%). Read section 14.6 for a review of the material influence on viscosity results.

The heat loss by radiation has to be taken into account. First measurements showed irregular temperature distributions, i.e. the sample was liquid but covered by a solid layer. To counteract, the crucible was wrapped in and covered by layers of silica-alumina-fiber sheets of “thermopaper” (Altra™ KP, Rath AG, Vienna, Austria). It withstands temperatures up to 1700 °C. The difference in heat loss before and after insulation enhancement can be easily recognized by the brightness at same temperatures, Figure 95 b) and c).

The low total mass of sample and crucible, circa 300 g, is beneficial for high heating or cooling rates. Several measurements at a single sample can be shortly done.

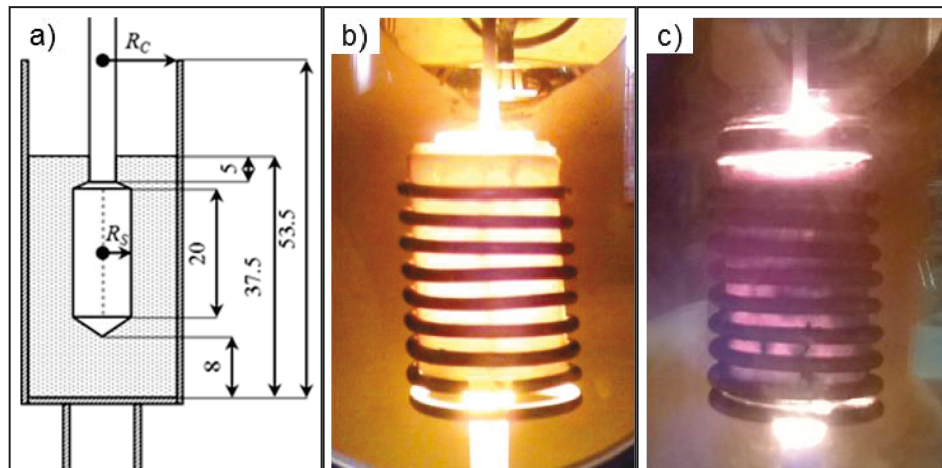


Figure 95: a) Dimensions of crucible and spindle, b) crucible with poor insulation and c) crucible with enhanced insulation at high temperatures.

14.2 Temperature Calibration

Crucible and the sample inside were heated up inductively. Temperature was measured using a B-type thermocouple, placed under the crucible. A temperature calibration with an additional thermocouple was done before each single slag. The additional thermocouple was moved from above into the crucible and deposited on the bottom of the crucible. Two calibration methods were applied:

1. Setting three temperature points and recording the difference between set and measured temperature. This process was repeated three times to find an average.
2. The influence of cooling rate on real temperature was obtained as shown below. Starting from highest experimental temperature, the difference between real temperature and set temperature was recorded. Furthermore, the cooling rate was proofed by taking time information.

Linear functions were later developed to calculate the real temperature from mean measurement data. Also, the correct cooling rate was set depending on cooling rate to time investigations described in point 2.

14.3 Viscometer Calibration

In need of the non-standard measurement system, viscometer calibration was done at

1. room temperature and
2. at operating temperatures.

At room temperature, silicon oils Brookfield 5000, 12500 and 30000 (Brookfield Engineering Laboratories, Inc., Middleboro, Massachusetts, USA). Due to the temperature sensitivity of silicone oils, temperature measurements were done with a K-

type thermocouple to determine temperature up to one-tenth degree Celsius. A factor was developed to adjust measured viscosities to real viscosities. For rotational velocities (shear rates) in the range 1-300 rpm (0.25-75 1/s) and viscosities from 0-100 Pa s, the factor was set to 2.2. All measured viscosities were multiplied with this factor after measurements.

The found viscosity calibration factor was furthermore tested for high temperatures with a calibration glass standard DGG1, Deutsche Glastechnische Gesellschaft [189]. There were no significant deviations detected between the factor at room temperature and at highest temperatures. Details are discussed in section 14.4.

14.4 Accuracy and Reproducibility of HT-Viscosity Measurements

The reproducibility of high temperature (HT) viscosity measurement faces several challenges which are:

1. accuracy of temperature measurements,
2. accuracy of viscosity measurements,
3. temperature deviation within the furnace/heating system,
4. changing in slag composition, and
5. crystallization behavior of molten samples for cooling conditions.

In general, the accuracy of a rotational viscometer is reported within wide ranges. Authors often do not inform about calibration methods, the temperature range for high temperature calibration or the accuracy of temperature measurement method. Additionally, some authors measure deviations on a logarithmical scale [190]. A selection of deviations is given below:

- up to 5 % of error at 1250 °C for glass standard sample in viscosity for the high temperature viscometer of the British Coal Utilization Research Association [165],
- $\pm 3 \cdot 10^{-3}$ Pa s or 0.5 % of maximum viscosity range of 3 Pa s for a rotational viscometer with molybdenum spindle/crucible [191],
- 2 % of accuracy for viscosity values $\leq 1 \cdot 10^5$ Pa s while the precision of rotating cup viscometry deteriorates for viscosities $> 1 \cdot 10^5$ Pa s [52],
- deviation is ≤ 5 % for a calibration at room temperature with silicone oil and with standard glass at elevated temperatures [192],
- uncertainties of ± 25 -50 % in viscosity are reported for apparatuses, where dissolution of bob and crucible occur [34]

Temperature indication underlies the characteristic error of applied thermocouples. All temperature measurements at the viscometer were achieved by B-type thermocouples, accuracy class 2. The error in measurement is given in the German

industrial standard DIN EN 605842 [193]. Commonly, the deviation $\pm\Delta T$ in K is specified by Eq. (121) where t represents the indicated temperature in °C. For example, the deviation results in ± 10 K at 1000 °C and in ± 15 K for 1500 °C. The equation is valid in the temperature range 600 to 1700 °C.

$$\pm\Delta T = 0.01 \cdot t \quad (121)$$

Viscosity measurements for standard silicon oils at room temperature are given in Figure 96. Standard silicone oils S-5000 and S-30000 were measured three times to clarify reproducibility and standard deviation. Some scattering is recorded. Average absolute errors taken from minimum and maximum data recorded are in the range of 1.5-1.8 % of the indicated value.

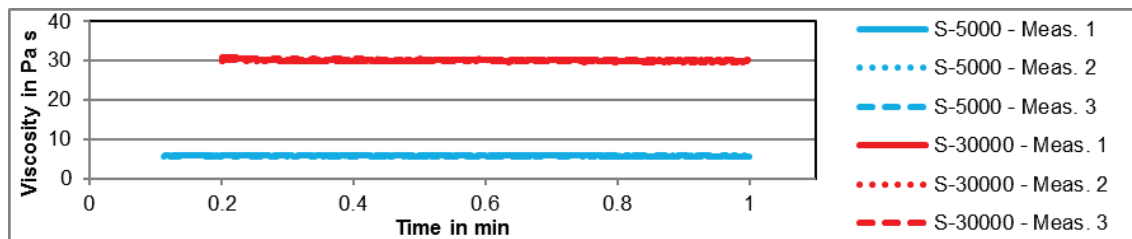


Figure 96: Reproducibility of silicon oil viscosity calibration for shear rate $\dot{\gamma}=75$ 1/s.

The developed calibration factor for silicon oils at room temperature has to be validated. Therefore, viscosity measurements on glass standard DGG1 was carried out, see section 14.3. Different shear rates were applied and Newtonian behavior is indicated, Figure 97. Measurements are in good agreement to the tabulated reference viscosity. Average absolute errors are between 3-6.9 % of the indicated value in the viscosity range of $1 < \eta < 100$ Pa s. The calibration factor is not changed within the viscosity and temperature range. To avoid any effort, no need for calibration constant adaption is necessary in a viscosity range of $1 < \eta < 100$ Pa s.

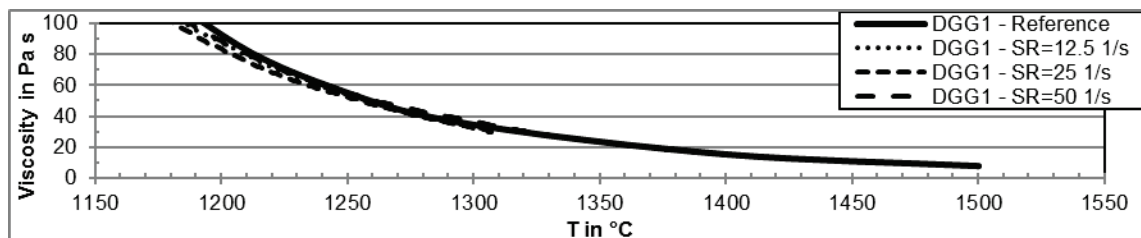


Figure 97: Calibration of measuring system with standard glass DGG1 with different shear rates. Cooling rate is -2 K/min.

Reproducibility at elevated temperatures is shown in Figure 98. Standard glass DGG1 was heated up to 1300 °C, hold for 15 min and chilled with a rate of -2 K/min. Scattering is in the range of 1-4.3 %.

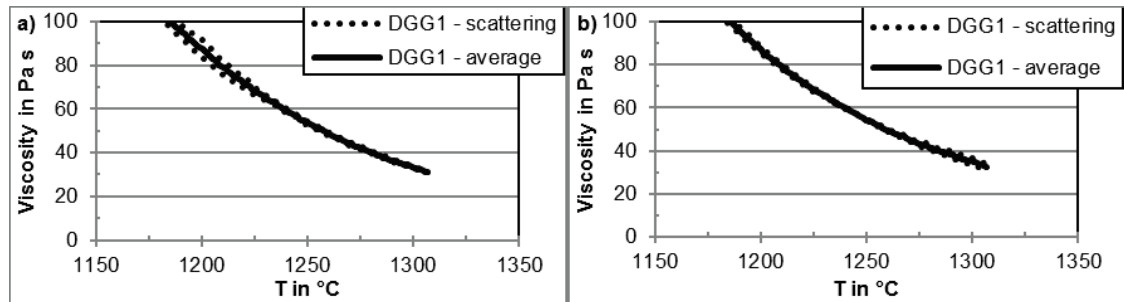


Figure 98: Reproducibility of high temperature viscosity measurements of DGG1 at a shear rate of a) $\dot{\gamma}=25$ 1/s and b) $\dot{\gamma}=50$ 1/s

A critical point is the investigated temperature range. Only one measurement achieved 1400 °C resulting in a minimum viscosity of 15 Pa s. Higher temperatures lead to a loss of glass components and resulting in varying viscosities. It is recommended to minimize the time of temperature treatment. No change in viscosity is reported for 1000-1200 °C within 40 h, 1200-1300 °C within 20 h and 1300-1400 °C within 15 h. The manufacturer provides tabulated viscosity data for $T > 1400$ °C but does not mention the processing time before compositional changes [194].

14.5 Influence of Inductive Heating

A literature survey was done to estimate the influence of the electromagnetic field radiated for inductive heating. Less information is found for investigations on pure slag melts. Most information can be found from metallurgic sciences obtained on pure metallic samples.

Experimental and computational work on electromagnetic fields within an Electro Slag Remelter (ESR) showed the formation of complex velocity fields. At room temperature, mercury replaced molten metal [195]. This transportation effect is called electromagnetic stirring and is caused by interactions between the magnetic field and the electrical field formed within the melt of an Al-Ti-B alloy. In this work, slag was moved to the wall due to the convection of the metallic melt [196]. When the electromagnetic field was caused by alternating current, slag and iron melt were less influenced as by direct current [197]. Simulations and CFD-modelling on Cr-Ni-alloys doped with CaO-CaF₂ slag showed stronger vortex within the slag as within the metal melt. The slag vortex was introduced by Lorentz force, which is smaller in metal [198]. A separating effect of Fe²⁺ and Fe³⁺ was found for electromagnetic fields and high temperatures out of slag into refractory. MgFe₂O₄ spinel was formed by this effect. There is no evidence of well-formed slag convections caused by electromagnetic fields or forces [199].

An influence of electromagnetic fields to samples in ESR process was found, but a clear separation is not given. Mostly, convection of slag depends on the convection of the metallic melt or to temperature differences within the slag zone. Also, the electromagnetic fields were directly given into the smelter by electrodes. At the

viscometer, the electromagnetic field is introduced by a coil. The field is not directly interacting with the metal free slag, but rather with the Pt-Rh crucible. An effect on the slag is not excluded, but was not detected in experiments.

14.6 Influence of Measurement System Materials

Crucible and bob are covered by slag. Consequentially, emphasis has to be given on the interactions between slag and the material of the measurement system. The wetting behavior of slag on the walls of bob and crucible influences the shear rate and shear stress. Viscosity depends on these rheological properties.

A possible effect is “slipping” between crucible wall and the fluid. There, no or less force is applied to the fluid and viscosity results are falsified. Another effect is the formation of different developed menisci between crucible wall and slag surface which result in changed slag levels and finally in an insufficient immersed bob. To keep the meniscus effect low, a crucible with a ratio of height/radius ≥ 6 should be preferred [200]. The information above was discussed on an oscillating viscometer, but cannot be excluded for rotational ones.

Corrosion of the measurement system has to be avoided for several reasons. First, the crucible/spindle material is solved by slag. This changes the slag composition and therefore the slag viscosity. Second, while the measurement system is dissolved, the radius of spindle and crucible are varied. Calibration constants are developed for a unique measurements system and viscosity data is wrong interpreted for a changed crucible/bob diameter. An enrichment of 2.4-4.9 wt.-% in Al_2O_3 was found after measurements under reducing and oxidizing conditions. In comparison to an indissoluble Pt-crucible, differences are up to 300 % [201]. Own investigations detected a significant dissolution of molybdenum in slag, Table 41. Coal ash was directly given to a molybdenum crucible, heated up to 1700 °C under argon atmosphere and cooled down at a cooling rate of -2 K/min. Composition obtained by XRF of powders.

Table 41: Increase of molybdenum within a coal ash after high temperature measurements.

Oxyde	ash, 815 °C	after measurement
Al ₂ O ₃	2.1	2.6
BaO	0.1	0.1
CaO	28.4	29.3
Fe ₂ O ₃	12.7	15.4
K ₂ O	0.1	0.1
MgO	2.4	2.4
MoO ₃	0.0	17.5
P ₂ O ₅	0.0	0.2
SiO ₂	29.6	31.2
SO ₃	24.2	0.5
TiO ₂	0.1	0.3

Numerous crucible materials are available. Most important properties are a high melting point and good resistance to oxidation or reduction to face the high temperatures necessary in slag viscosity research. A summarized listing is given in Table 42.

Although molybdenum is recommended for measurements under reducing atmospheres by Nentwig [190], other investigators found molybdenum spheres in the size of 10 µm distribute in slag [201].

Alloys of platinum-rhodium is best selection. All kinds of atmospheres can be covered with this material. Care on the partial oxygen pressure has to be taken for Fe-rich slags to avoid the formation of metallic iron under reducing.

Table 42: Selected crucible and bob materials.

Material	Properties
Platinum Pt	<ul style="list-style-type: none"> melting point 1769.9 °C [202] resistance to reactions with slag under inert conditions [203] reference material [203] stable under oxidizing and reducing conditions forms alloy in presence of metallic iron (reducing conditions)
Platinum-Rhodium alloys	<ul style="list-style-type: none"> increased melting point, e.g. 1837.8 °C (Pt-Rh 80-20 wt.-%) [84] rhodium imparts greater rigidity and mechanical strength [201] no significant reactions with oxygen under air multiple useable after melt-out of slag but expensive forms alloy in presence of metallic iron (reducing conditions)
Molybdenum Mo	<ul style="list-style-type: none"> melting point 2610 °C [202] reduction of iron to Fe(II) is possible [203] not stable in oxygen atmospheres and temperatures above 770 °C [203]
Graphite C	<ul style="list-style-type: none"> sublimation temperature 3730 °C [202] strong reducing effect on iron oxide to pure iron [203] slag penetration observed [203] CaO-SiO₂ melts with >50 mole % of SiO₂ attacked graphite crucibles [56]
hexagonal Boron nitride α-BN	<ul style="list-style-type: none"> melting point 2967 °C [204] reduces iron oxide [203] penetrated by slag [203] not stable under air at high temperatures [203]
Corundum α-Al ₂ O ₃	<ul style="list-style-type: none"> melting point 2045 °C [202] reactions found between slag and corundum and not recommended for viscosity determination [203]
tetragonal Zirconia ZrO ₂	<ul style="list-style-type: none"> melting temperature 2677 °C [205] slags react severely with stabilized ZrO₂ at highest temperatures [203] recommended for temperatures below 1600 °C [203]

15. Appendix: Experimental Procedures: Quenching Furnace

A quench furnace with atmospheric control was self-constructed, Figure 99 a) and b). Parameters are given in Table 43. The construction is described as follows. A vertical furnace with an inner alumina tube houses a Pt-Au (95-5 mass-%) crucible with slag. The crucible is suspended in the isothermal furnace area on a wire made from thermocouple alloy (B-type, Pt-Rh 94-6 mass-%). This alloy is preferred due to the advantages of a high melting point and good mechanical properties at elevated temperatures and stresses. Three gasses can be set by mass flow controllers: CO, CO₂ and N₂. Purging gases are removed by an exhaust system. Alternatively, experiments can be run under air. Temperature indication is done by a B-type thermocouple directly placed above the crucible. The furnace temperature has to be manually adjusted to satisfy the targeted sample temperature.

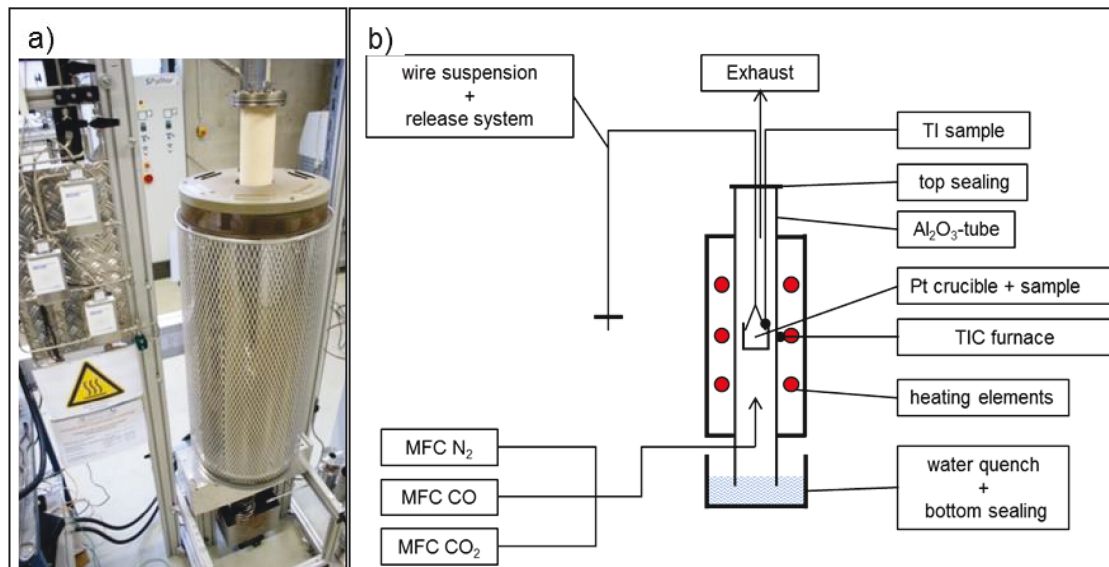


Figure 99: a) Quench furnace installed at the laboratory and b) schematic representation.

Table 43: Parameters of quenching furnace.

Furnace	Ströhnlein
Tube	alumina
Maximum heating rate in K/min	20
Maximum cooling rate in K/min	10
T _{max} in °C	1575
Gases	N ₂ , CO, CO ₂ , air
Crucible	Pt95-Au5 wt.-%

16. Appendix: Slag Sample Parameters and Composition

Table 44: Slag composition, weight basis, before viscosity measurements.

Sample	Atm.	Reducing gas compositions in vol.-%		B/A	Composition in mass-%, normalized, traces free, XRF on melt bead									
		CO ₂	CO		SiO ₂	Al ₂ O ₃	Fe ₂ O ₃	CaO	MgO	Na ₂ O	K ₂ O	TiO ₂	P ₂ O ₅	SO ₃
S1	N ₂	0.00	0.00	0.192	69.5	13.6	9.3	3.0	1.2	1.3	1.3	0.6	0.1	0.1
S2	air	0.00	0.00	0.230	18.9	62.4	0.0	18.2	0.2	0.3	0.0	0.0	0.0	0.0
S3	air	0.00	0.00	0.252	53.7	24.3	8.4	6.2	2.1	0.4	2.8	1.1	0.5	0.5
S4	air	0.00	0.00	0.255	78.4	1.2	3.6	13.0	2.8	0.5	0.4	0.1	0.0	0.0
S5	red	0.60	0.40	0.255	78.4	1.2	3.6	13.0	2.8	0.5	0.4	0.1	0.0	0.0
S6	air	0.00	0.00	0.256	53.0	25.4	8.1	4.1	2.7	0.9	4.5	1.0	0.3	0.0
S7	red	0.30	0.70	0.256	52.8	25.6	8.1	4.1	2.7	0.9	4.5	1.0	0.3	0.0
S8	air	0.00	0.00	0.274	52.4	24.2	8.5	7.5	2.8	0.7	1.8	1.1	0.5	0.5
S9	air	0.00	0.00	0.280	40.7	32.8	6.6	7.5	3.1	2.0	1.7	1.1	4.4	0.0
S10	air	0.00	0.00	0.285	53.5	22.3	8.4	8.1	3.0	0.9	1.5	1.1	0.5	0.7
S11	red	0.40	0.60	0.287	40.3	32.5	6.3	7.4	3.0	1.9	2.6	1.1	4.8	0.0
S12	N ₂	0.00	0.00	0.309	38.6	36.5	2.1	16.7	2.7	0.3	1.8	1.1	0.3	0.0
S13	air	0.00	0.00	0.337	26.5	48.3	0.0	25.0	0.2	0.0	0.0	0.0	0.0	0.0
S14	air	0.00	0.00	0.337	70.6	4.2	0.0	25.2	0.0	0.0	0.0	0.0	0.0	0.0
S15	air	0.00	0.00	0.346	51.0	21.0	8.6	9.6	3.9	1.5	1.6	1.0	0.4	1.4
S16	air	0.00	0.00	0.392	43.6	28.3	0.0	28.0	0.2	0.0	0.0	0.0	0.0	0.0
S17	air	0.00	0.00	0.412	47.9	20.5	9.1	10.6	4.3	1.7	2.9	1.0	0.4	1.7
S18	air	0.00	0.00	0.499	35.8	30.9	0.0	33.0	0.3	0.0	0.0	0.0	0.0	0.0
S19	red	0.40	0.60	0.546	62.1	2.3	8.2	20.9	4.9	1.0	0.3	0.3	0.0	0.0

Continuation of Table 44

Sample	Atm.	Reducing gas compositions in vol.-%		B/A	Composition in mass-%, normalized, traces free, XRF on melt bead									
		CO ₂	CO		SiO ₂	Al ₂ O ₃	Fe ₂ O ₃	CaO	MgO	Na ₂ O	K ₂ O	TiO ₂	P ₂ O ₅	SO ₃
S20	Air	0.00	0.00	0.578	59.8	3.2	9.2	21.1	5.1	0.9	0.3	0.3	0.0	0.1
S21	air	0.00	0.00	0.589	59.8	2.9	11.3	19.6	5.0	0.7	0.4	0.2	0.0	0.0
S22	red	0.50	0.50	0.589	59.8	2.9	11.3	19.6	5.0	0.7	0.4	0.2	0.0	0.0
S23	air	0.00	0.00	0.684	43.2	16.2	0.0	40.3	0.3	0.0	0.0	0.0	0.0	0.0
S24	N ₂	0.00	0.00	0.674	46.0	13.2	14.2	9.6	11.4	3.8	0.9	0.0	0.9	0.0
S25	red	0.40	0.60	0.726	32.9	22.5	5.0	24.6	8.7	1.3	1.2	0.8	3.0	0.0
S26	air	0.00	0.00	0.734	32.8	22.4	5.4	24.4	8.7	1.3	1.3	0.8	3.0	0.0
S27	N ₂	0.00	0.00	0.749	48.6	8.0	1.0	30.9	2.4	2.0	6.1	0.0	1.0	0.0
S28	N ₂	0.00	0.00	0.764	38.5	15.0	5.6	30.1	2.4	2.7	1.0	1.2	2.4	1.0
S29	air	0.00	0.00	0.805	38.7	15.6	8.4	33.0	1.7	0.5	0.5	0.5	1.0	0.1
S30	red	0.30	0.70	0.833	37.8	16.2	8.6	34.1	1.8	0.5	0.5	0.6	0.0	0.0
S31	red	0.30	0.70	0.903	30.7	21.3	9.6	32.5	1.6	3.3	0.4	0.5	0.1	0.0
S32	air	0.00	0.00	0.932	30.3	20.9	10.7	32.2	1.6	3.3	0.4	0.5	0.1	0.0
S33	N ₂	0.00	0.00	1.000	42.4	6.9	1.3	35.6	3.3	2.9	6.2	0.0	1.4	0.0
S34	N ₂	0.00	0.00	1.000	39.2	10.0	9.9	22.8	9.4	4.3	2.8	0.0	1.5	0.0
S35	red	0.40	0.60	1.046	31.6	16.1	4.0	33.1	11.6	0.5	1.3	0.6	1.3	0.0
S36	air	0.00	0.00	1.069	31.8	15.6	5.5	32.3	11.9	0.2	1.4	0.6	0.7	0.0
S37	N ₂	0.00	0.00	1.297	36.7	6.0	1.5	39.8	4.1	3.7	6.3	0.0	1.8	0.0
S38	N ₂	0.00	0.00	1.300	34.7	8.0	7.1	31.6	8.1	4.6	4.1	0.0	1.8	0.0
S39	red	0.30	0.70	1.705	30.5	6.1	23.4	31.3	7.7	0.1	0.4	0.3	0.1	0.0
S40	air	0.00	0.00	1.857	29.0	5.7	27.2	30.0	7.3	0.1	0.4	0.3	0.0	0.0

Continuation of Table 44

Sample	Atm.	Reducing gas compositions in vol.-%		B/A	Composition in mass-%, normalized, traces free, XRF on melt bead									
-	-	CO ₂	CO	-	SiO ₂	Al ₂ O ₃	Fe ₂ O ₃	CaO	MgO	Na ₂ O	K ₂ O	TiO ₂	P ₂ O ₅	SO ₃
S41	red	0.30	0.70	2.126	24.4	7.1	25.8	32.3	8.7	0.4	0.4	0.3	0.0	0.6
S42	air	0.00	0.00	2.497	21.9	6.4	28.7	33.8	8.3	0.1	0.5	0.3	0.0	0.0

Atm. - atmosphere

Table 45: Slag composition, molar basis, before viscosity measurements.

Sample	Atm.	Reducing gas compositions in vol.-%		B/A	Composition in mole-%, normalized, traces free, XRF on melt bead									
-	-	CO ₂	CO	-	SiO ₂	Al ₂ O ₃	Fe ₂ O ₃	CaO	MgO	Na ₂ O	K ₂ O	TiO ₂	P ₂ O ₅	SO ₃
S1	N ₂	0.00	0.00	0.192	69.5	13.6	9.3	3.0	1.2	1.3	1.3	0.6	0.1	0.1
S2	air	0.00	0.00	0.230	18.9	62.4	0.0	18.2	0.2	0.3	0.0	0.0	0.0	0.0
S3	air	0.00	0.00	0.252	53.7	24.3	8.4	6.2	2.1	0.4	2.8	1.1	0.5	0.5
S4	air	0.00	0.00	0.255	78.4	1.2	3.6	13.0	2.8	0.5	0.4	0.1	0.0	0.0
S5	red	0.60	0.40	0.255	78.4	1.2	3.6	13.0	2.8	0.5	0.4	0.1	0.0	0.0
S6	air	0.00	0.00	0.256	53.0	25.4	8.1	4.1	2.7	0.9	4.5	1.0	0.3	0.0
S7	red	0.30	0.70	0.256	52.8	25.6	8.1	4.1	2.7	0.9	4.5	1.0	0.3	0.0
S8	air	0.00	0.00	0.274	52.4	24.2	8.5	7.5	2.8	0.7	1.8	1.1	0.5	0.5
S9	air	0.00	0.00	0.280	40.7	32.8	6.6	7.5	3.1	2.0	1.7	1.1	4.4	0.0
S10	air	0.00	0.00	0.285	53.5	22.3	8.4	8.1	3.0	0.9	1.5	1.1	0.5	0.7
S11	red	0.40	0.60	0.287	40.3	32.5	6.3	7.4	3.0	1.9	2.6	1.1	4.8	0.0
S12	N ₂	0.00	0.00	0.309	38.6	36.5	2.1	16.7	2.7	0.3	1.8	1.1	0.3	0.0
S13	air	0.00	0.00	0.337	26.5	48.3	0.0	25.0	0.2	0.0	0.0	0.0	0.0	0.0
S14	air	0.00	0.00	0.337	70.6	4.2	0.0	25.2	0.0	0.0	0.0	0.0	0.0	0.0

Continuation of Table 45

Sample	Atm.	Reducing gas compositions in vol.-%		B/A	Composition in mole-%, normalized, traces free, XRF on melt bead									
		CO ₂	CO		SiO ₂	Al ₂ O ₃	Fe ₂ O ₃	CaO	MgO	Na ₂ O	K ₂ O	TiO ₂	P ₂ O ₅	SO ₃
S15	air	0.00	0.00	0.346	51.0	21.0	8.6	9.6	3.9	1.5	1.6	1.0	0.4	1.4
S16	air	0.00	0.00	0.392	43.6	28.3	0.0	28.0	0.2	0.0	0.0	0.0	0.0	0.0
S17	air	0.00	0.00	0.412	47.9	20.5	9.1	10.6	4.3	1.7	2.9	1.0	0.4	1.7
S18	air	0.00	0.00	0.499	35.8	30.9	0.0	33.0	0.3	0.0	0.0	0.0	0.0	0.0
S19	red	0.40	0.60	0.546	62.1	2.3	8.2	20.9	4.9	1.0	0.3	0.3	0.0	0.0
S20	air	0.00	0.00	0.578	59.8	3.2	9.2	21.1	5.1	0.9	0.3	0.3	0.0	0.1
S21	air	0.00	0.00	0.589	59.8	2.9	11.3	19.6	5.0	0.7	0.4	0.2	0.0	0.0
S22	red	0.50	0.50	0.589	59.8	2.9	11.3	19.6	5.0	0.7	0.4	0.2	0.0	0.0
S23	air	0.00	0.00	0.684	43.2	16.2	0.0	40.3	0.3	0.0	0.0	0.0	0.0	0.0
S24	N ₂	0.00	0.00	0.674	46.0	13.2	14.2	9.6	11.4	3.8	0.9	0.0	0.9	0.0
S25	red	0.40	0.60	0.726	32.9	22.5	5.0	24.6	8.7	1.3	1.2	0.8	3.0	0.0
S26	air	0.00	0.00	0.734	32.8	22.4	5.4	24.4	8.7	1.3	1.3	0.8	3.0	0.0
S27	N ₂	0.00	0.00	0.749	48.6	8.0	1.0	30.9	2.4	2.0	6.1	0.0	1.0	0.0
S28	N ₂	0.00	0.00	0.764	38.5	15.0	5.6	30.1	2.4	2.7	1.0	1.2	2.4	1.0
S29	air	0.00	0.00	0.805	38.7	15.6	8.4	33.0	1.7	0.5	0.5	0.5	1.0	0.1
S30	red	0.30	0.70	0.833	37.8	16.2	8.6	34.1	1.8	0.5	0.5	0.6	0.0	0.0
S31	red	0.30	0.70	0.903	30.7	21.3	9.6	32.5	1.6	3.3	0.4	0.5	0.1	0.0
S32	air	0.00	0.00	0.932	30.3	20.9	10.7	32.2	1.6	3.3	0.4	0.5	0.1	0.0
S33	N ₂	0.00	0.00	1.000	42.4	6.9	1.3	35.6	3.3	2.9	6.2	0.0	1.4	0.0
S34	N ₂	0.00	0.00	1.000	39.2	10.0	9.9	22.8	9.4	4.3	2.8	0.0	1.5	0.0
S35	red	0.40	0.60	1.046	31.6	16.1	4.0	33.1	11.6	0.5	1.3	0.6	1.3	0.0

Continuation of Table 45

Sample	Atm.	Reducing gas compositions in vol.-%		B/A	Composition in mole-%, normalized, traces free, XRF on melt bead									
		CO ₂	CO		SiO ₂	Al ₂ O ₃	Fe ₂ O ₃	CaO	MgO	Na ₂ O	K ₂ O	TiO ₂	P ₂ O ₅	SO ₃
S36	air	0.00	0.00	1.069	31.8	15.6	5.5	32.3	11.9	0.2	1.4	0.6	0.7	0.0
S37	N ₂	0.00	0.00	1.297	36.7	6.0	1.5	39.8	4.1	3.7	6.3	0.0	1.8	0.0
S38	N ₂	0.00	0.00	1.300	34.7	8.0	7.1	31.6	8.1	4.6	4.1	0.0	1.8	0.0
S39	red	0.30	0.70	1.705	30.5	6.1	23.4	31.3	7.7	0.1	0.4	0.3	0.1	0.0
S40	air	0.00	0.00	1.857	29.0	5.7	27.2	30.0	7.3	0.1	0.4	0.3	0.0	0.0
S41	red	0.30	0.70	2.126	24.4	7.1	25.8	32.3	8.7	0.4	0.4	0.3	0.0	0.6
S42	air	0.00	0.00	2.497	21.9	6.4	28.7	33.8	8.3	0.1	0.5	0.3	0.0	0.0

Atm. – atmospheres

Table 46: Slag composition, weight basis, after viscosity measurements.

Sample	Atm.	Reducing gas compositions in vol.-%		B/A*	Composition in mass-%, normalized, traces free, XRF on melt bead									
		CO ₂	CO		SiO ₂	Al ₂ O ₃	Fe ₂ O ₃	CaO	MgO	Na ₂ O	K ₂ O	TiO ₂	P ₂ O ₅	SO ₃
S1	N ₂	0.00	0.00	0.192	n.a.	n.a.	n.a.	n.a.	n.a.	n.a.	n.a.	n.a.	n.a.	n.a.
S2	air	0.00	0.00	0.230	29.2	48.2	0.1	22.1	0.0	0.4	0.0	0.0	0.0	0.0
S3	air	0.00	0.00	0.252	57.9	22.4	7.6	5.9	1.9	0.6	2.2	1.1	0.6	0.0
S4	air	0.00	0.00	0.255	72.6	3.9	4.6	14.0	3.6	0.5	0.5	0.1	0.0	0.0
S5	red	0.60	0.40	0.255	n.a.	n.a.	n.a.	n.a.	n.a.	n.a.	n.a.	n.a.	n.a.	n.a.
S6	air	0.00	0.00	0.256	53.0	25.4	8.1	4.1	2.7	0.9	4.5	1.0	0.3	0.0
S7	red	0.30	0.70	0.256	52.7	25.5	8.1	4.1	2.7	0.9	4.5	1.0	0.3	0.0
S8	air	0.00	0.00	0.274	55.5	23.2	8.0	6.8	2.2	0.5	2.0	1.1	0.6	0.0
S9	air	0.00	0.00	0.280	40.9	32.3	6.0	7.5	3.1	1.9	2.6	1.1	4.7	0.0

Continuation of Table 46

Sample	Atm.	Reducing gas compositions in vol.-%		B/A*	Composition in mass-%, normalized, traces free, XRF on melt bead									
		CO ₂	CO		SiO ₂	Al ₂ O ₃	Fe ₂ O ₃	CaO	MgO	Na ₂ O	K ₂ O	TiO ₂	P ₂ O ₅	SO ₃
S10	air	0.00	0.00	0.285	55.7	22.6	8.0	7.1	2.3	0.6	2.0	1.1	0.6	0.0
S11	red	0.40	0.60	0.287	40.4	32.7	6.1	7.4	3.1	1.9	2.6	1.1	4.7	0.0
S12	N ₂	0.00	0.00	0.309	37.6	34.6	2.1	16.4	2.5	0.2	1.6	1.1	0.3	0.0
S13	air	0.00	0.00	0.337	30.0	41.6	0.0	28.4	0.0	0.0	0.0	0.0	0.0	0.0
S14	air	0.00	0.00	0.337	n.a.	n.a.	n.a.	n.a.	n.a.	n.a.	n.a.	n.a.	n.a.	n.a.
S15	air	0.00	0.00	0.346	54.6	22.0	8.0	8.2	2.7	0.7	2.1	1.1	0.6	0.0
S16	air	0.00	0.00	0.392	42.6	28.9	0.2	28.0	0.3	0.0	0.0	0.0	0.0	0.0
S17	air	0.00	0.00	0.412	53.8	22.1	8.0	8.6	2.9	0.8	2.2	1.0	0.6	0.0
S18	air	0.00	0.00	0.499	41.4	26.3	0.1	31.7	0.2	0.0	0.0	0.0	0.1	0.0
S19	red	0.40	0.60	0.546	n.a.	n.a.	n.a.	n.a.	n.a.	n.a.	n.a.	n.a.	n.a.	n.a.
S20	air	0.00	0.00	0.578	59.8	3.1	9.2	21.1	5.1	0.9	0.3	0.3	0.0	0.1
S21	air	0.00	0.00	0.589	60.3	3.0	11.2	19.3	5.0	0.7	0.4	0.2	0.0	0.0
S22	red	0.50	0.50	0.589	60.9	3.0	10.4	19.4	5.0	0.7	0.4	0.2	0.0	0.0
S23	air	0.00	0.00	0.684	50.5	14.1	0.2	34.9	0.1	0.0	0.0	0.0	0.1	0.0
S24	N ₂	0.00	0.00	0.674	47.2	10.5	13.3	10.2	12.2	2.5	0.9	2.4	0.8	0.0
S25	red	0.40	0.60	0.726	34.4	20.3	4.8	26.0	7.9	1.3	1.3	0.8	3.1	0.0
S26	air	0.00	0.00	0.734	34.1	20.1	6.1	25.5	7.7	1.3	1.2	0.8	3.1	0.0
S27	N ₂	0.00	0.00	0.749	52.9	6.2	1.0	28.0	2.2	1.8	6.4	0.3	1.0	0.2
S28	N ₂	0.00	0.00	0.764	41.1	18.6	5.2	27.4	2.3	1.8	0.3	1.2	2.2	0.0
S29	air	0.00	0.00	0.805	38.5	15.5	8.6	33.2	1.7	0.5	0.5	0.5	1.0	0.1
S30	red	0.30	0.70	0.833	39.2	15.7	7.0	33.7	1.8	0.5	0.5	0.6	1.0	0.0

Continuation of Table 46

Sample	Atm.	Reducing gas compositions in vol.-%		B/A*	Composition in mass-%, normalized, traces free, XRF on melt bead									
		CO ₂	CO		SiO ₂	Al ₂ O ₃	Fe ₂ O ₃	CaO	MgO	Na ₂ O	K ₂ O	TiO ₂	P ₂ O ₅	SO ₃
S31	red	0.30	0.70	0.903	31.6	21.8	6.8	33.9	1.6	3.3	0.3	0.6	0.1	0.0
S32	air	0.00	0.00	0.932	29.7	23.0	11.1	30.5	1.5	3.2	0.4	0.5	0.1	0.0
S33	N ₂	0.00	0.00	1.000	45.1	5.7	1.2	33.4	3.3	2.6	7.2	0.3	1.3	0.0
S34	N ₂	0.00	0.00	1.000	41.2	8.4	8.6	21.7	9.8	3.2	3.9	1.7	1.4	0.0
S35	red	0.40	0.60	1.046	30.4	17.4	3.9	32.8	11.8	0.4	1.0	0.6	1.3	0.0
S36	air	0.00	0.00	1.069	31.8	14.9	5.5	33.1	11.7	0.2	1.4	0.6	0.8	0.0
S37	N ₂	0.00	0.00	1.297	40.3	5.1	1.2	37.0	4.0	3.4	7.0	0.3	1.6	0.1
S38	N ₂	0.00	0.00	1.300	35.4	7.0	6.4	30.6	8.3	4.2	5.1	1.3	1.6	0.0
S39	red	0.30	0.70	1.705	30.5	6.1	23.4	31.3	7.7	0.1	0.4	0.3	0.1	0.0
S40	air	0.00	0.00	1.857	28.9	5.7	27.4	29.8	7.3	0.1	0.4	0.3	0.0	0.0
S41	red	0.30	0.70	2.126	n.a.	n.a.	n.a.	n.a.	n.a.	n.a.	n.a.	n.a.	n.a.	n.a.
S42	air	0.00	0.00	2.497	24.0	5.9	26.4	34.0	8.9	0.1	0.4	0.3	0.0	0.0

Atm. – atmosphere; B/A* - B/A-ratio was taken from samples before measurements and not from above tabled data.

17. Appendix: Slag Viscosity Measurements Results

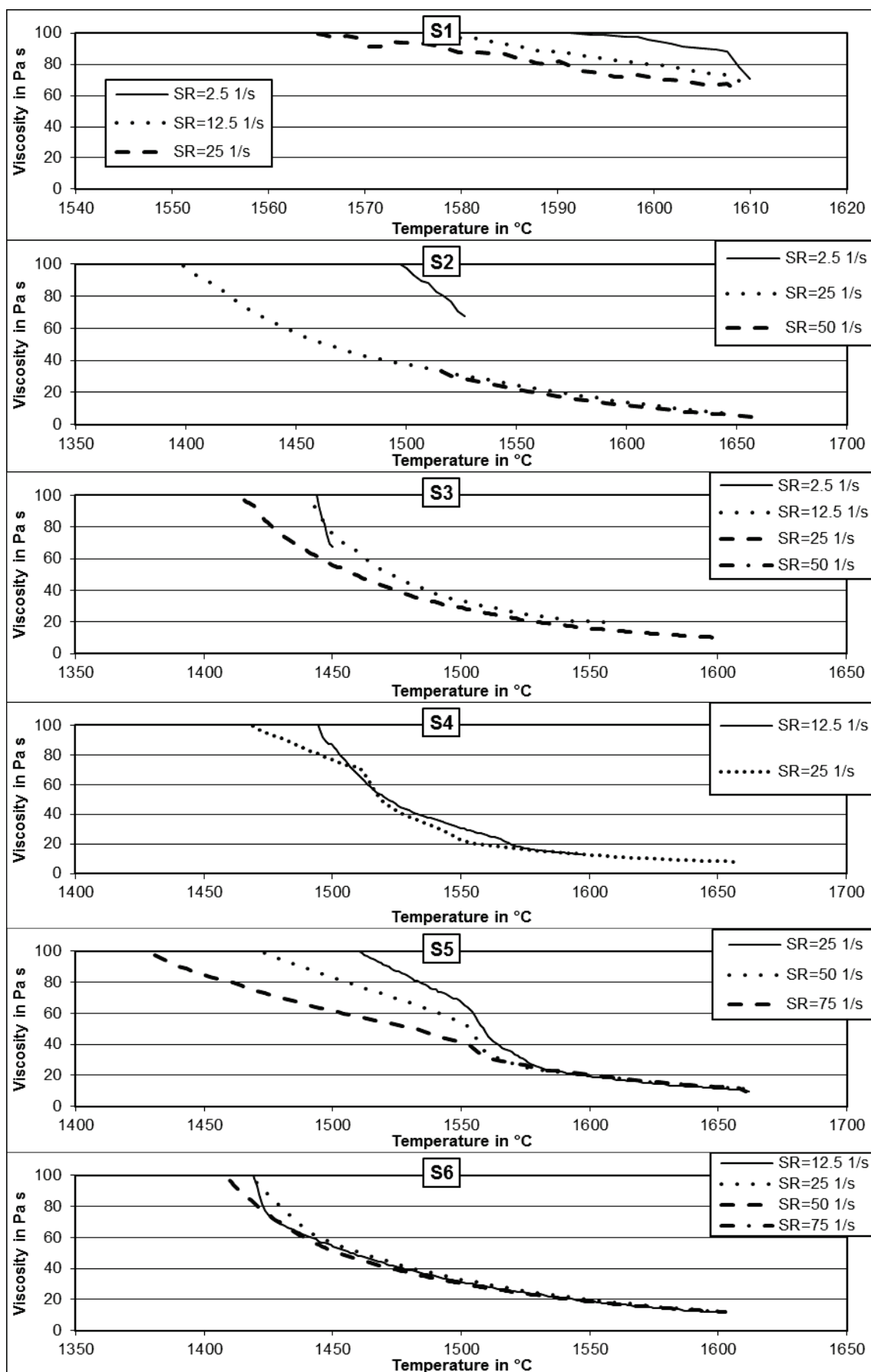


Figure 100: Slag viscosity measurements on slags S1 to S6 at a cooling rate of -2 K/min.

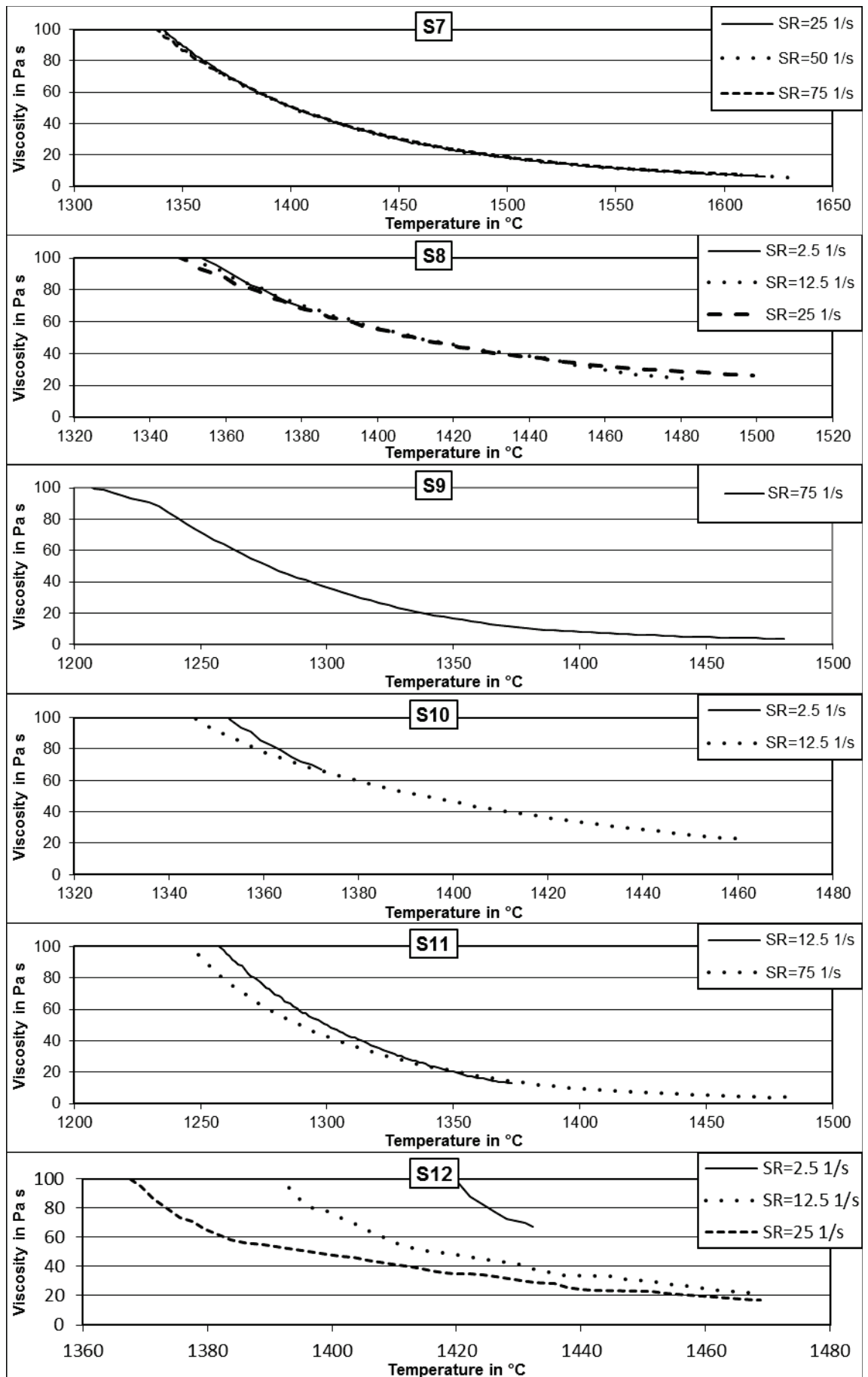


Figure 101: Slag viscosity measurements on slags S7 to S12 at a cooling rate of -2 K/min.

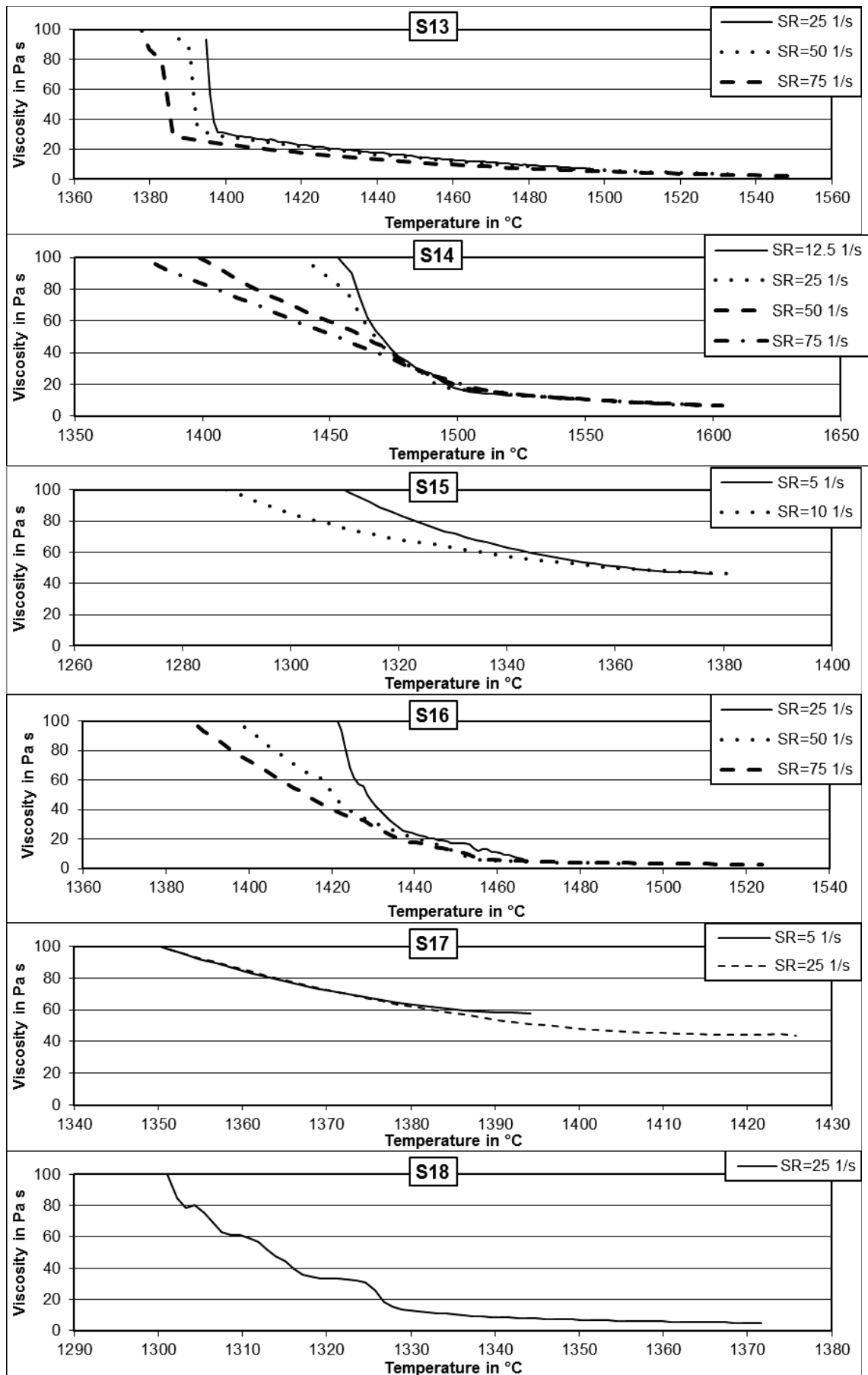


Figure 102: Slag viscosity measurements on slags S13 to S18 at a cooling rate of -2 K/min.

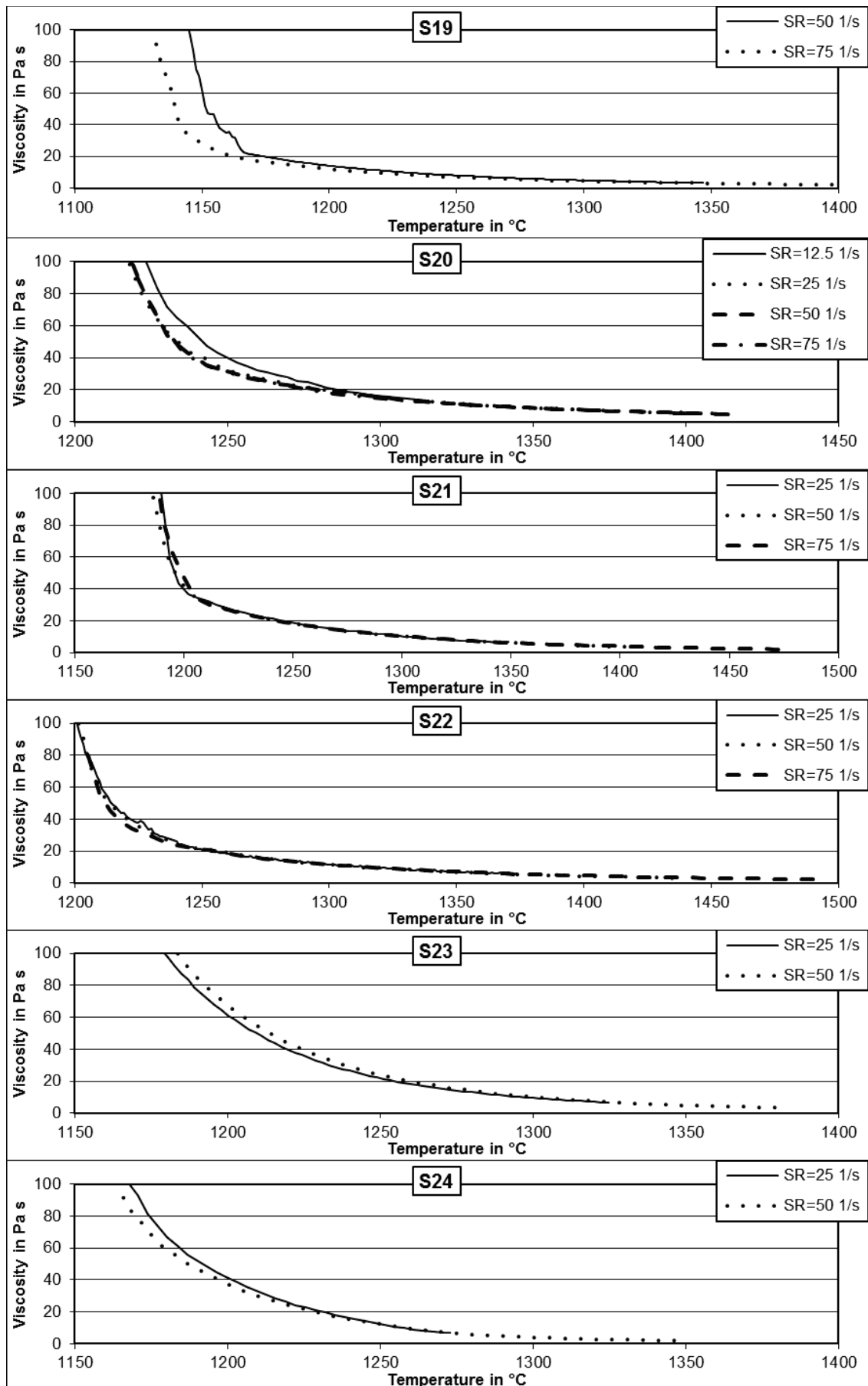


Figure 103: Slag viscosity measurements on slags S19 to S24 at a cooling rate of -2 K/min.

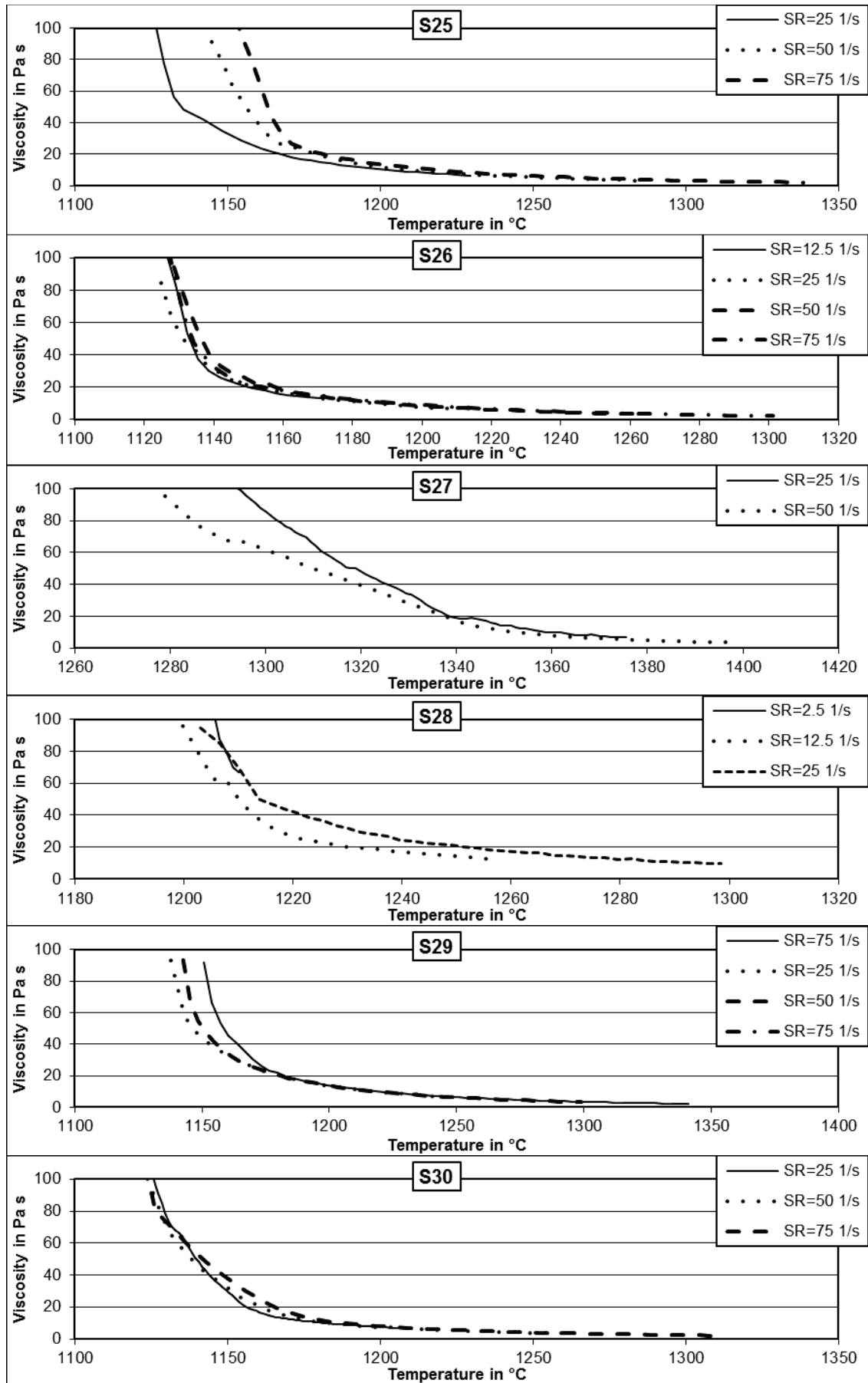


Figure 104: Slag viscosity measurements on slags S25 to S30 at a cooling rate of -2 K/min.

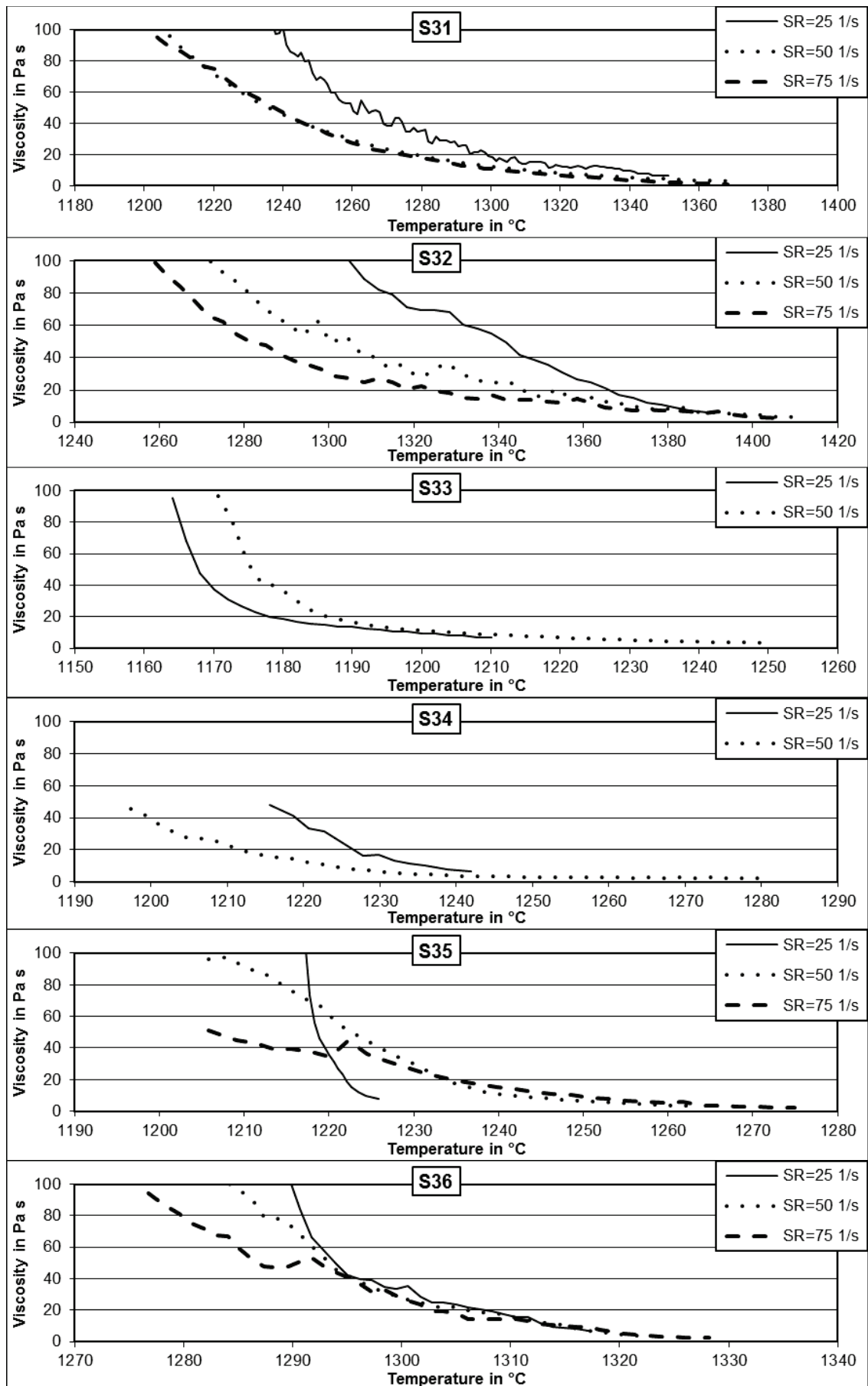


Figure 105: Slag viscosity measurements on slags S31 to S36 at a cooling rate of -2 K/min.

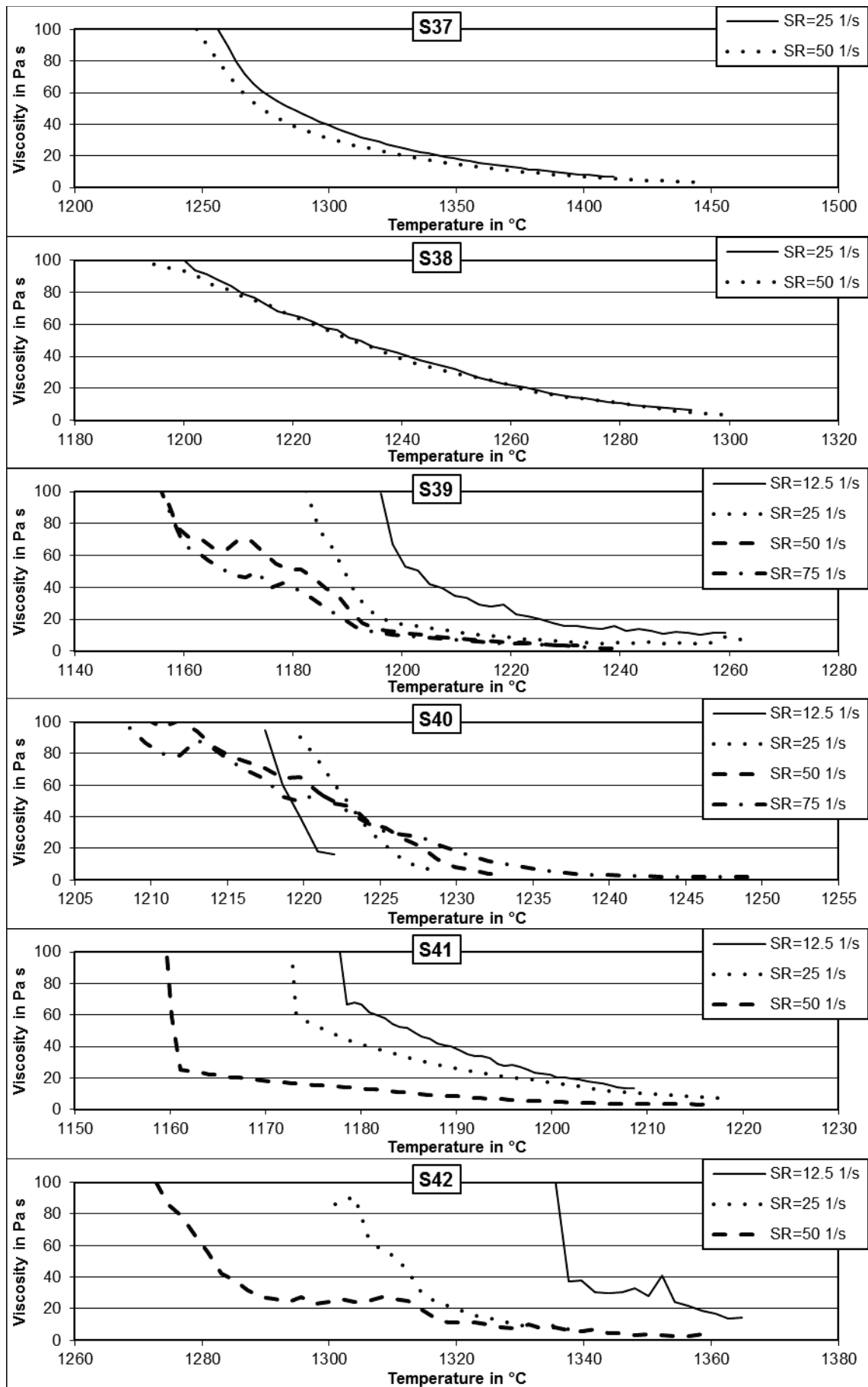


Figure 106: Slag viscosity measurements on slags S37 to S42 at a cooling rate of -2 K/min.

18. Appendix: Viscosities at Different Cooling Rates

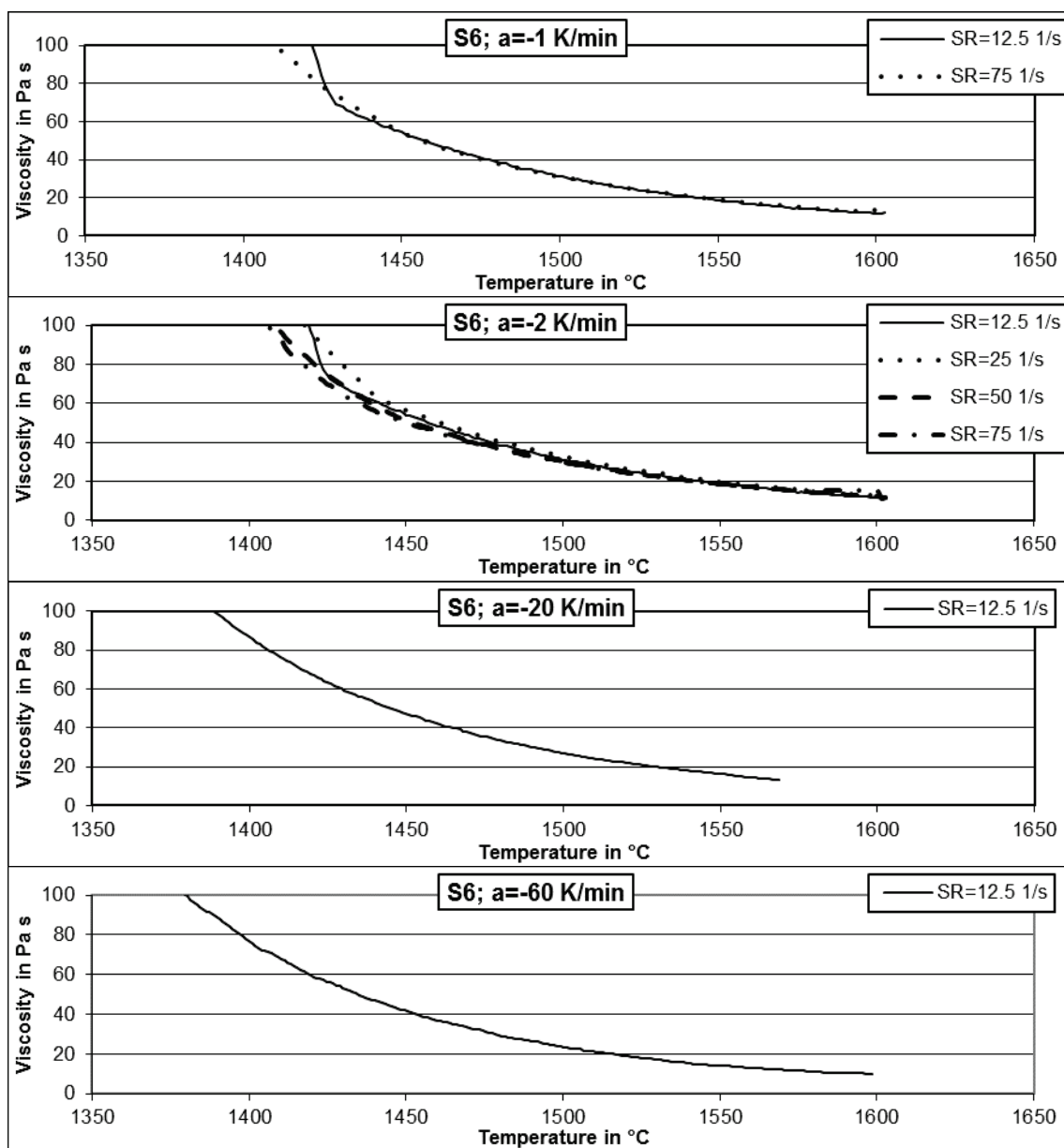


Figure 107: Slag S6 measured at different cooling rates.

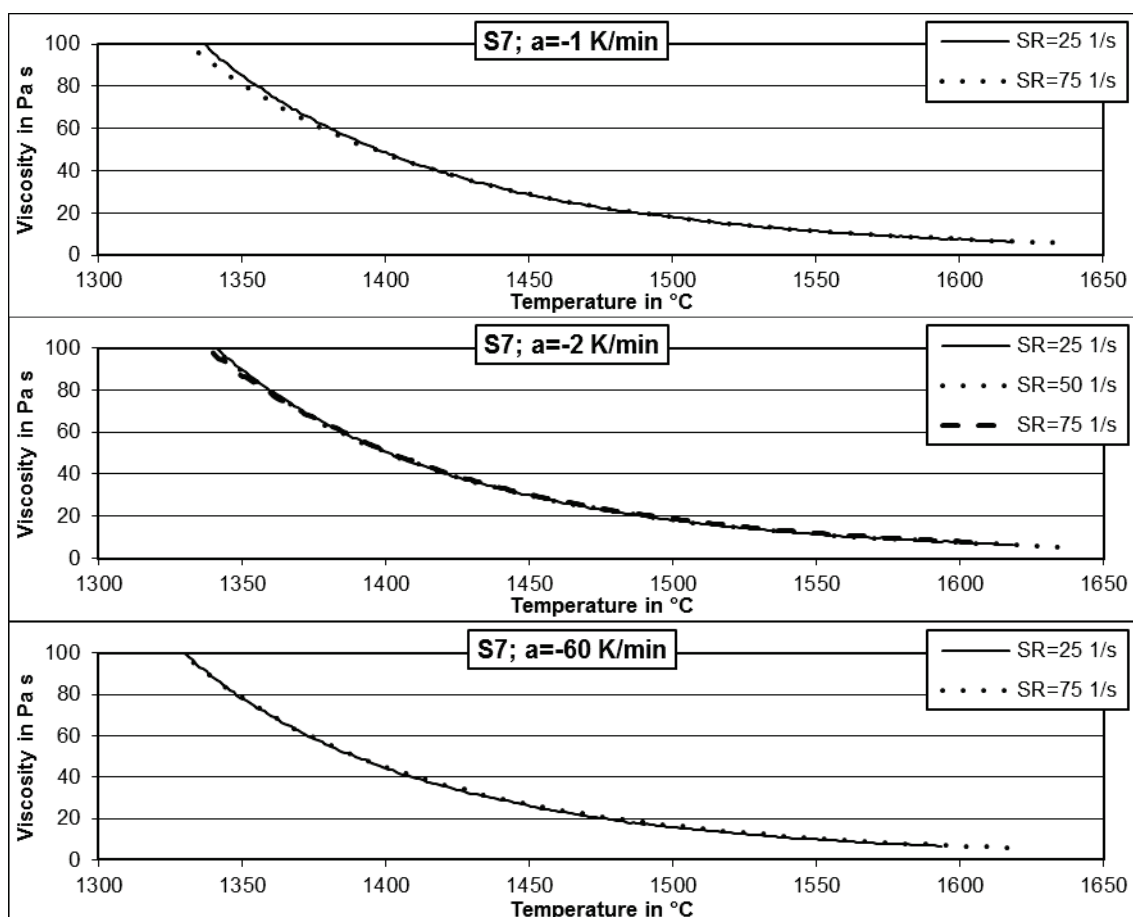


Figure 108: Slag S7 measured at different cooling rates.

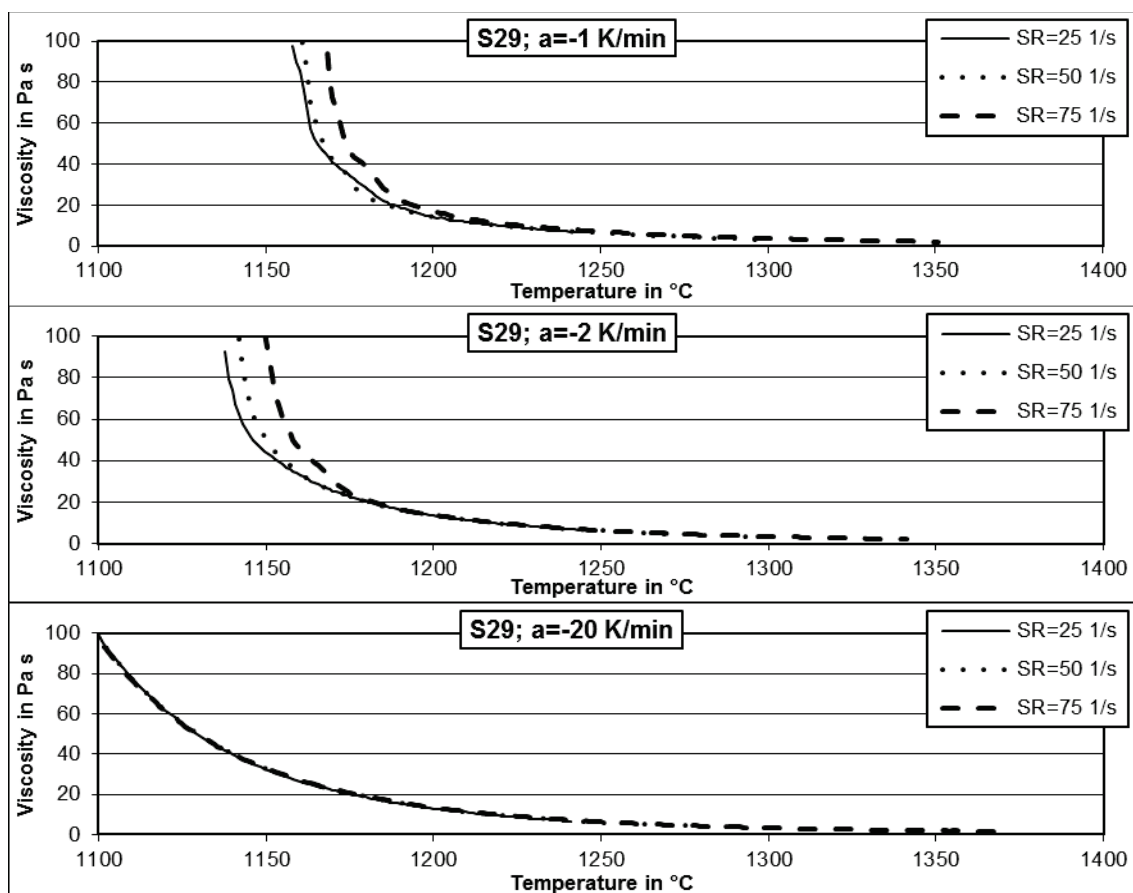


Figure 109: Slag S29 measured at different cooling rates.

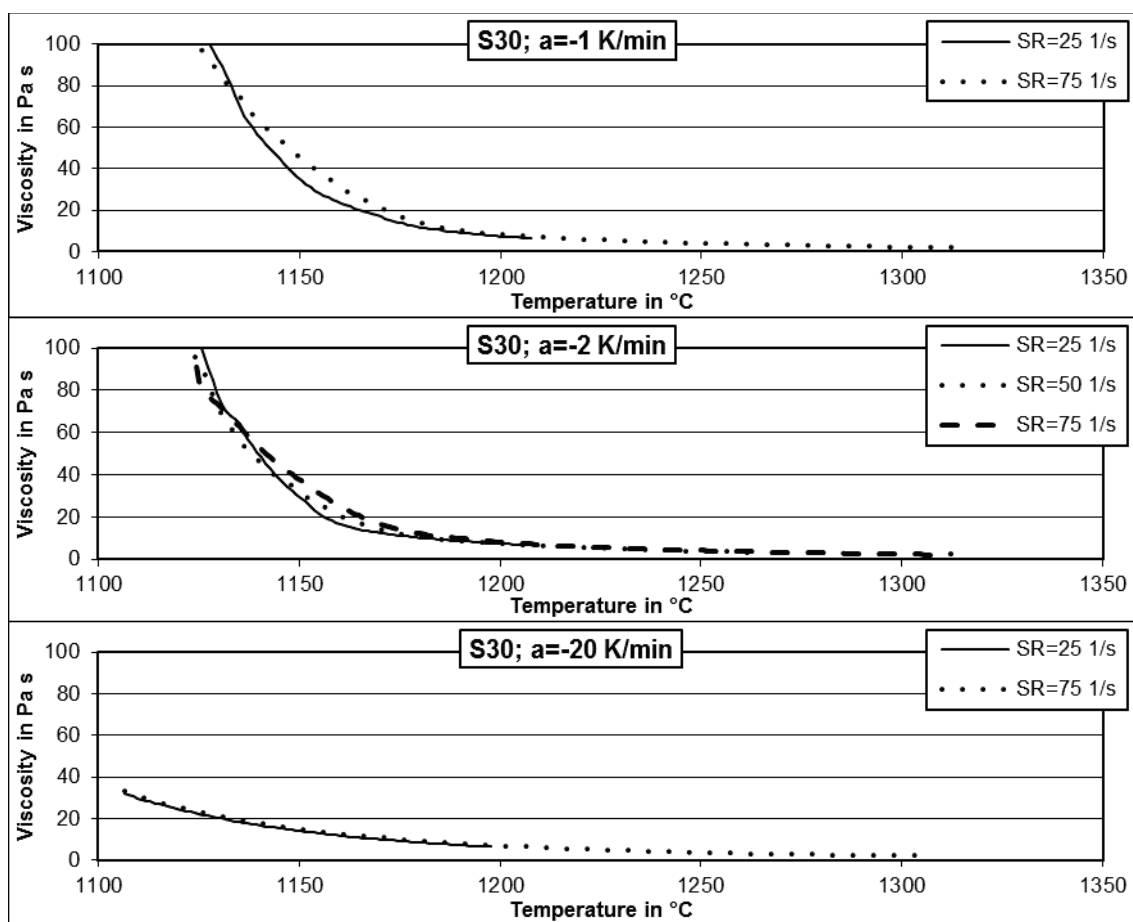


Figure 110: Slag S30 measured at different cooling rates.

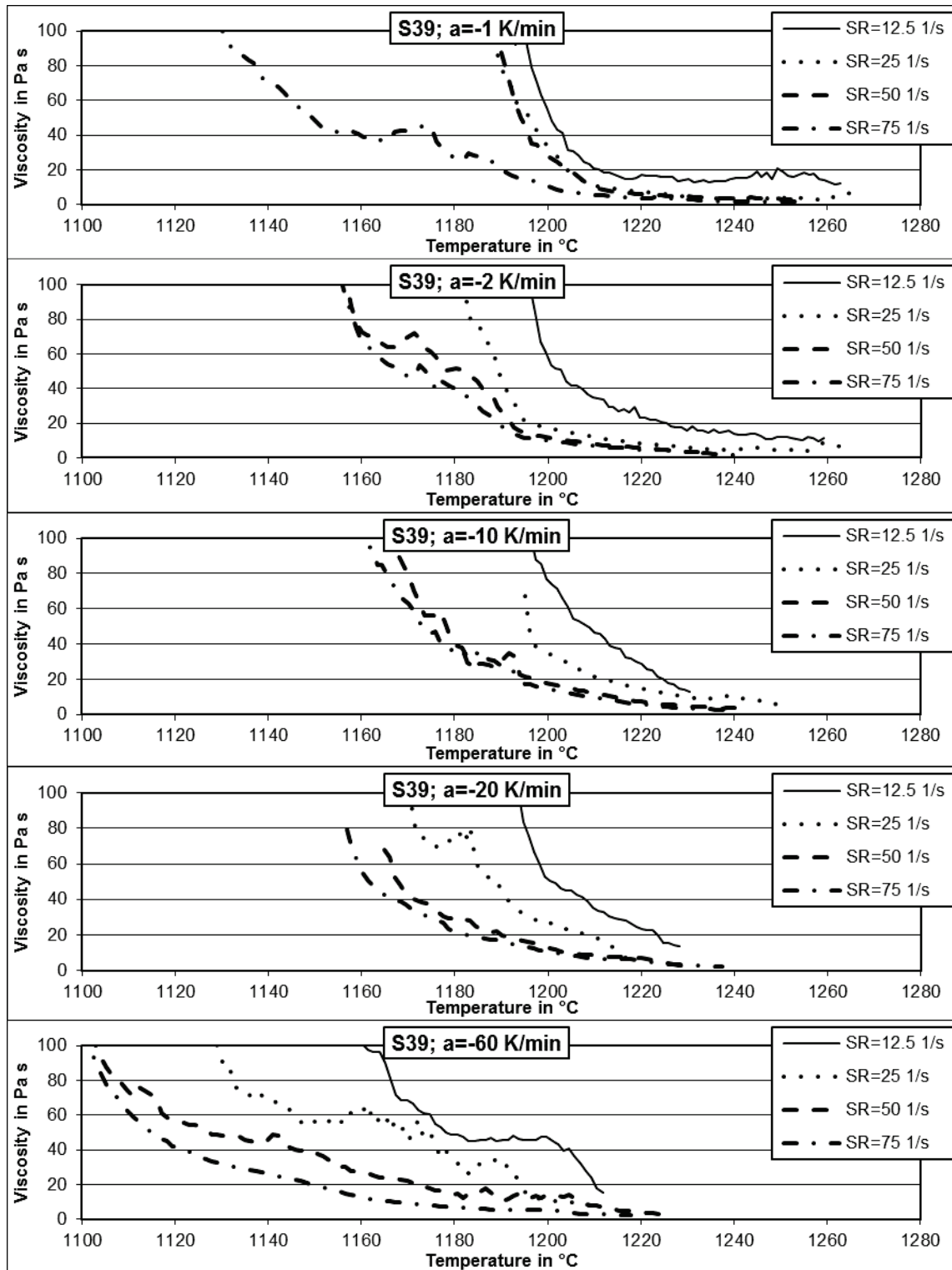


Figure 111: Slag S39 measured at different cooling rates.

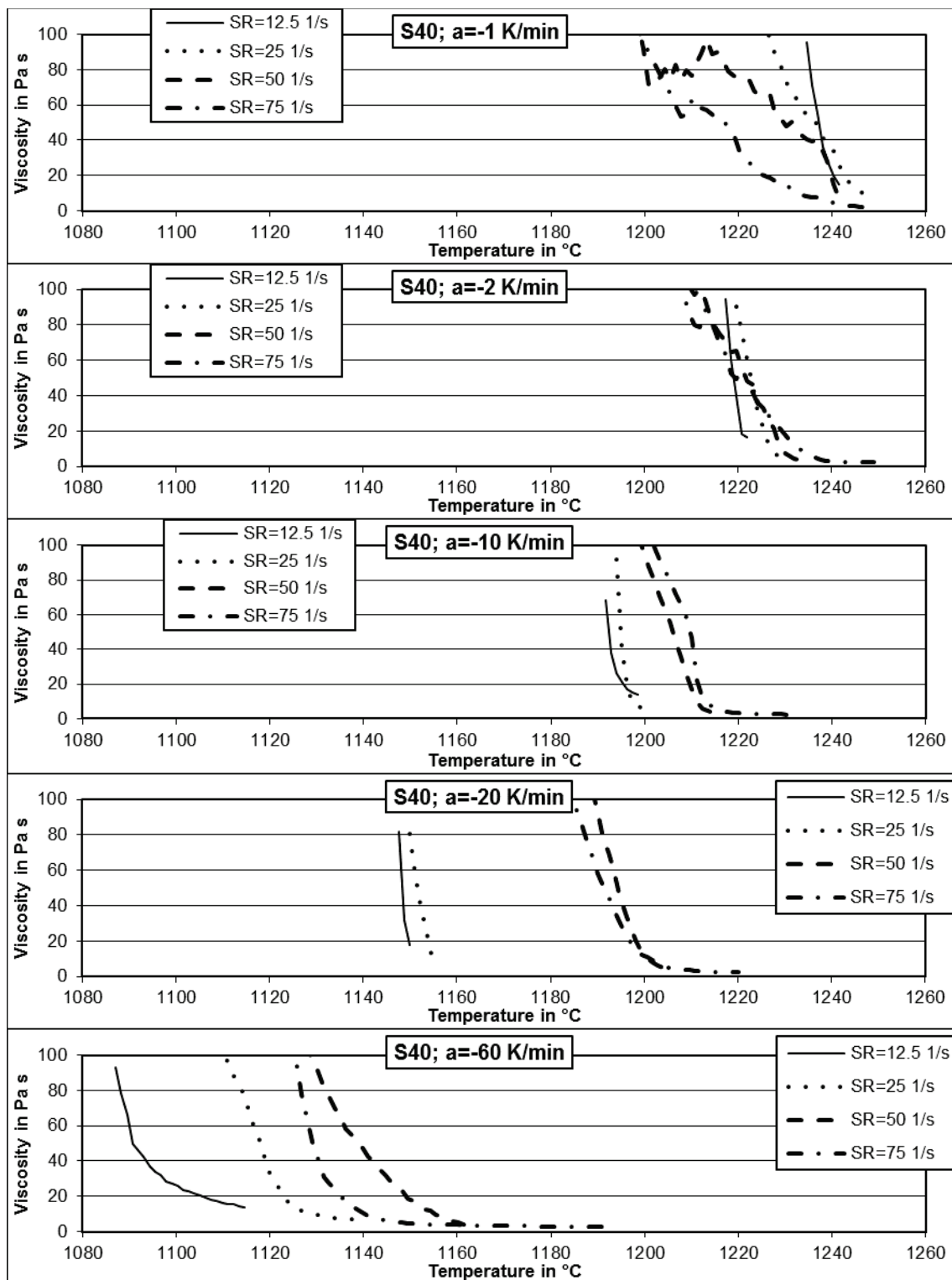


Figure 112: Slag S39 measured at different cooling rates.

19. Appendix: Slag Viscosity Modelling: AALE Calculations

Table 47: AALE calculated on viscosity predictions and measurements in the ranges $\eta=0-25$ Pa s, $a=-2$ K/min, all shear rates, B/A on mass, air.

Sample	B/A	S2	WF	Bom	Sha	Lak	Urb	Rib	Str	KF	BBHLW	Duc	ANN	Best model
S1	0.192	n.a.	n.a.	n.a.	n.a.	n.a.	n.a.	n.a.	n.a.	n.a.	n.a.	n.a.	n.a.	n.a.
S2	0.230	1.627	1.703	0.823	3.125	20.067	1.067	0.263	1.947	1.261	0.851	0.226	1.239	Duc
S3	0.252	0.136	0.312	1.274	0.358	1.127	0.305	0.248	0.247	0.057	0.322	0.619	0.769	KF
S4	0.255	0.073	0.247	2.469	0.822	0.092	0.457	0.148	0.349	0.193	0.172	0.083	0.026	ANN
S5	0.255	0.094	0.083	2.308	0.645	0.241	0.275	0.298	0.154	0.015	0.362	0.108	0.159	KF
S6	0.256	0.053	0.306	1.271	0.168	1.120	0.218	0.168	0.151	0.033	0.252	0.757	0.872	KF
S7	0.256	0.146	0.103	1.473	0.352	1.343	0.423	0.394	0.358	0.172	0.050	0.559	0.660	BBHLW
S8	0.274	0.189	0.328	1.270	0.269	1.197	0.324	0.338	0.267	0.077	0.377	0.521	0.833	KF
S9	0.280	0.408	0.143	1.598	0.082	2.818	0.537	1.212	0.580	0.314	0.277	0.154	0.179	Sha
S10	0.285	0.104	0.209	1.430	0.415	1.159	0.449	0.391	0.410	0.202	0.329	0.411	0.721	S2
S11	0.287	0.347	0.076	1.538	0.197	2.693	0.435	1.100	0.486	0.212	0.242	0.117	0.150	WF
S12	0.309	0.614	0.886	0.564	1.208	2.169	0.453	0.079	0.808	0.664	0.548	0.412	0.795	Rib
S13	0.337	0.978	1.152	0.110	2.105	7.047	0.417	0.275	1.115	0.617	0.465	0.172	0.655	Bom
S14	0.337	0.111	0.050	2.170	1.057	0.241	0.056	0.274	0.256	0.285	0.124	0.099	0.228	WF
S15	0.346	0.111	0.050	2.170	1.057	0.241	0.056	0.274	0.256	0.285	0.124	0.099	0.228	WF
S16	0.392	0.360	0.509	1.080	0.350	1.172	0.202	0.224	0.161	0.209	0.167	0.474	0.279	Str
S17	0.412	0.360	0.509	1.080	0.350	1.172	0.202	0.224	0.161	0.209	0.167	0.474	0.279	Str
S18	0.499	0.324	0.581	0.913	0.870	2.377	0.110	0.398	0.178	0.119	0.100	0.861	0.105	BBHLW
S19	0.546	0.826	0.982	2.827	1.361	1.070	0.997	0.692	1.347	0.783	0.571	1.155	0.565	ANN
S20	0.578	0.168	0.227	2.063	0.705	0.468	0.427	0.186	0.639	0.214	0.092	0.247	0.044	ANN

Continuation of Table 47

Sample	B/A	S2	WF	Bom	Sha	Lak	Urb	Rib	Str	KF	BBHLW	Duc	ANN	Best model
S21	0.589	0.308	0.395	2.182	0.894	0.704	0.741	0.419	0.959	0.523	0.059	0.335	0.118	BBHLW
S22	0.589	0.246	0.331	2.127	0.838	0.637	0.683	0.371	0.870	0.465	0.030	0.258	0.062	BBHLW
S23	0.684	0.215	0.532	1.116	0.284	0.097	0.153	0.116	2.374	0.339	0.191	1.068	0.297	Lak
S24	0.674	0.295	0.138	1.670	0.170	1.356	0.715	0.613	1.698	0.506	0.210	0.252	0.907	WF
S25	0.726	0.052	0.509	0.987	1.039	2.812	0.243	0.469	0.191	0.096	0.244	0.137	0.457	S2
S26	0.734	0.150	0.403	1.074	0.997	3.206	0.333	0.597	0.335	0.151	0.164	0.148	0.573	Duc
S27	0.749	0.156	0.250	1.604	0.221	0.620	0.409	0.503	1.241	0.595	0.190	0.600	0.291	S2
S28	0.764	0.249	0.593	0.926	0.691	0.331	0.146	0.073	1.543	0.335	0.535	0.424	0.428	Rib
S29	0.805	0.054	0.372	1.041	0.251	1.263	0.349	0.436	1.389	0.160	0.125	0.817	0.138	S2
S30	0.833	0.178	0.302	1.071	0.259	1.637	0.469	0.554	1.772	0.278	0.065	0.994	0.281	BBHLW
S31	0.903	0.649	1.114	0.219	1.421	0.156	0.216	0.194	1.477	0.337	0.800	0.123	0.370	Duc
S32	0.932	0.985	1.389	0.188	1.646	0.571	0.362	0.396	1.514	0.546	1.091	0.496	0.130	ANN
S33	1.000	0.327	0.131	1.558	0.351	0.697	0.224	0.412	1.282	0.391	0.139	0.073	0.221	Duc
S34	1.000	0.287	0.313	1.210	0.576	0.549	0.313	0.238	0.835	0.245	0.239	0.240	1.454	Rib
S35	1.046	0.345	1.286	0.272	1.550	1.661	0.299	0.429	0.452	0.439	0.709	0.339	0.215	ANN
S36	1.069	0.804	1.653	0.264	1.805	0.546	0.575	0.784	0.773	0.750	1.083	0.616	0.548	Bom
S37	1.297	0.900	1.453	0.283	1.558	3.302	1.071	1.440	1.776	1.237	1.041	1.713	0.715	Bom
S38	1.300	0.519	1.290	0.245	1.507	1.387	0.595	0.988	0.697	0.768	0.903	1.089	0.732	Bom
S39	1.705	0.425	1.669	0.653	1.371	0.458	0.199	0.326	0.788	0.217	0.999	1.086	0.844	Urb
S40	1.857	0.419	1.715	0.786	1.387	0.383	0.319	0.304	0.658	0.282	1.014	1.163	0.976	KF
S41	2.126	0.530	2.230	1.403	2.048	1.533	0.219	0.548	0.753	0.302	1.319	1.224	1.053	Urb
S42	2.497	1.313	2.716	1.767	2.553	1.183	0.575	1.115	1.268	0.753	1.856	1.697	1.577	Urb

Table 48: AALE calculated on viscosity predictions and measurements in the ranges $\eta \leq 25$ Pa s, $a = -2$ K/min, all shear rates, B/A on mass, reducing atmospheres.

Sample	B/A	S2	WF	Bom	Sha	Lak	Urb	Rib	Str	KF	BBHLW	Duc	ANN	Best model
S5	0.255	0.094	0.083	2.308	0.501	0.241	0.044	0.413	0.164	0.293	0.362	0.108	0.159	Urb
S7	0.256	0.146	0.103	1.473	0.073	1.343	0.162	0.066	0.097	0.077	0.050	0.560	0.660	BBHLW
S11	0.287	0.347	0.076	1.538	0.376	2.693	0.285	0.806	0.337	0.078	0.241	0.117	0.149	WF
S19	0.546	0.826	0.982	2.827	1.086	1.070	0.371	0.381	1.501	0.176	0.571	1.154	0.565	KF
S22	0.589	0.246	0.331	2.127	0.491	0.637	0.076	0.045	0.658	0.269	0.030	0.257	0.062	BBHLW
S25	0.726	0.052	0.509	0.987	1.134	2.812	0.121	0.265	0.067	0.105	0.245	0.137	0.457	S2
S30	0.833	0.178	0.302	1.071	0.461	1.637	0.173	0.209	2.087	0.084	0.065	0.994	0.281	BBHLW
S31	0.903	0.649	1.114	0.219	1.587	0.156	0.390	0.472	1.729	0.548	0.801	0.123	0.370	Duc
S35	1.046	0.345	1.286	0.272	1.611	1.661	0.383	0.567	0.564	0.545	0.709	0.339	0.215	ANN
S39	1.705	0.425	1.669	0.653	1.747	0.458	0.693	1.150	1.526	0.853	0.999	1.087	0.845	S2
S41	2.126	0.530	2.230	1.403	2.386	1.533	0.813	1.488	1.501	0.970	1.319	1.225	1.054	S2

Table 49: AALE calculated on viscosity predictions and measurements in the ranges $\eta \leq 25$ Pa s, $a = -2$ K/min, all shear rates, B/A on mass, nitrogen gas is oxidizing.

Sample	B/A	S2	WF	Bom	Sha	Lak	Urb	Rib	Str	KF	BBHLW	Duc	ANN	Best model
S1	0.192	n.a.	n.a.	n.a.	n.a.	n.a.	n.a.	n.a.	n.a.	n.a.	n.a.	n.a.	n.a.	n.a.
S12	0.309	0.614	0.886	0.564	1.208	2.169	0.453	0.079	0.808	0.664	0.548	0.412	0.795	Rib
S24	0.674	0.295	0.138	1.670	0.170	1.356	0.715	0.613	1.698	0.506	0.210	0.252	0.907	WF
S27	0.749	0.156	0.250	1.604	0.221	0.620	0.409	0.503	1.241	0.595	0.190	0.600	0.291	S2
S28	0.764	0.249	0.593	0.926	0.691	0.331	0.146	0.073	1.543	0.335	0.535	0.424	0.428	Rib
S33	1.000	0.327	0.131	1.558	0.351	0.697	0.224	0.412	1.282	0.391	0.139	0.073	0.221	Duc
S34	1.000	0.287	0.313	1.210	0.576	0.549	0.313	0.238	0.835	0.245	0.239	0.240	1.454	Rib
S37	1.297	0.900	1.453	0.283	1.558	3.302	1.071	1.440	1.776	1.237	1.041	1.713	0.715	Bom
S38	1.300	0.519	1.290	0.245	1.507	1.387	0.595	0.988	0.697	0.768	0.903	1.089	0.732	Bom

Table 50: AALE calculated on viscosity predictions and measurements in the ranges $\eta \leq 25$ Pa s, $a = -2$ K/min, all shear rates, B/A on mass, nitrogen gas is reducing.

Sample	B/A	S2	WF	Bom	Sha	Lak	Urb	Rib	Str	KF	BBHLW	Duc	ANN	Best model
S1	0.192	n.a.	n.a.	n.a.	n.a.	n.a.	n.a.	n.a.	n.a.	n.a.	n.a.	n.a.	n.a.	n.a.
S12	0.309	0.682	0.956	0.503	1.347	2.171	0.574	0.051	0.982	0.783	0.607	0.518	0.864	Rib
S24	0.674	0.229	0.146	1.596	0.490	1.305	0.203	0.191	2.137	0.256	0.295	0.356	0.846	WF
S27	0.749	0.265	0.373	1.477	0.369	0.735	0.588	0.669	1.442	0.772	0.307	0.698	0.417	S2
S28	0.764	0.290	0.637	0.877	0.886	0.332	0.415	0.343	1.845	0.598	0.585	0.414	0.389	S2
S33	1.000	0.295	0.181	1.500	0.442	0.740	0.336	0.520	1.408	0.507	0.164	0.114	0.223	Duc
S34	1.000	0.308	0.422	1.097	0.889	0.472	0.330	0.453	0.407	0.423	0.350	0.350	1.351	S2
S37	1.297	0.943	1.529	0.221	1.672	3.342	1.203	1.573	1.945	1.368	1.106	1.735	0.779	Bom
S38	1.300	0.642	1.431	0.214	1.779	1.474	0.973	1.373	1.061	1.139	1.044	1.210	0.610	Bom

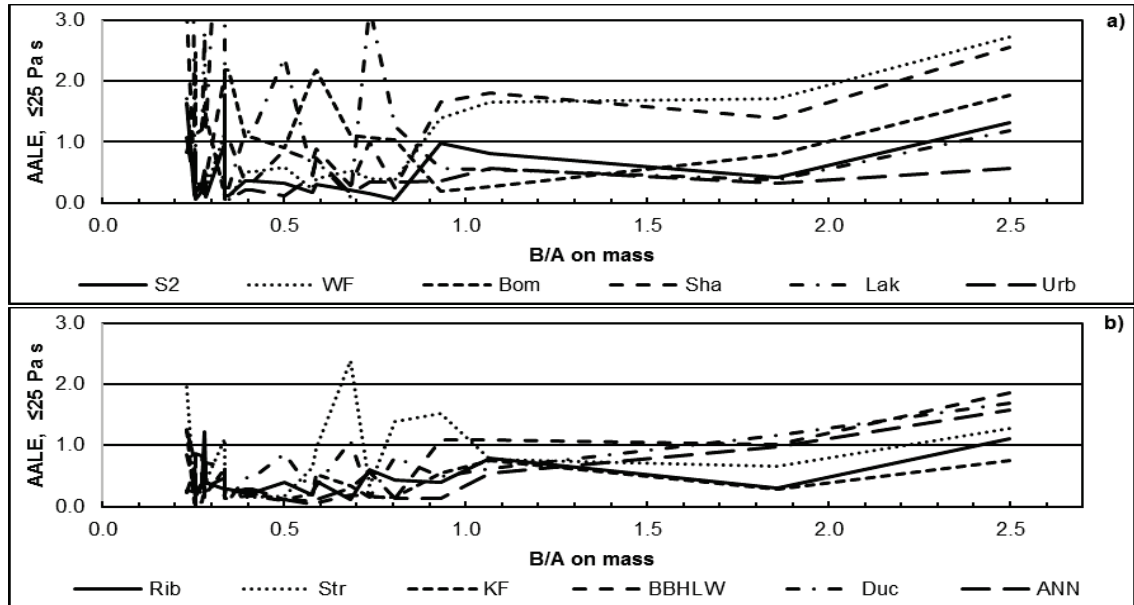


Figure 113: AALE as function of B/A-ratio obtained from classical viscosity models a) S2 to Urbain and b) Riboud to ANNliq, $\eta \leq 25 \text{ Pa s}$, all shear rates, oxidizing conditions.

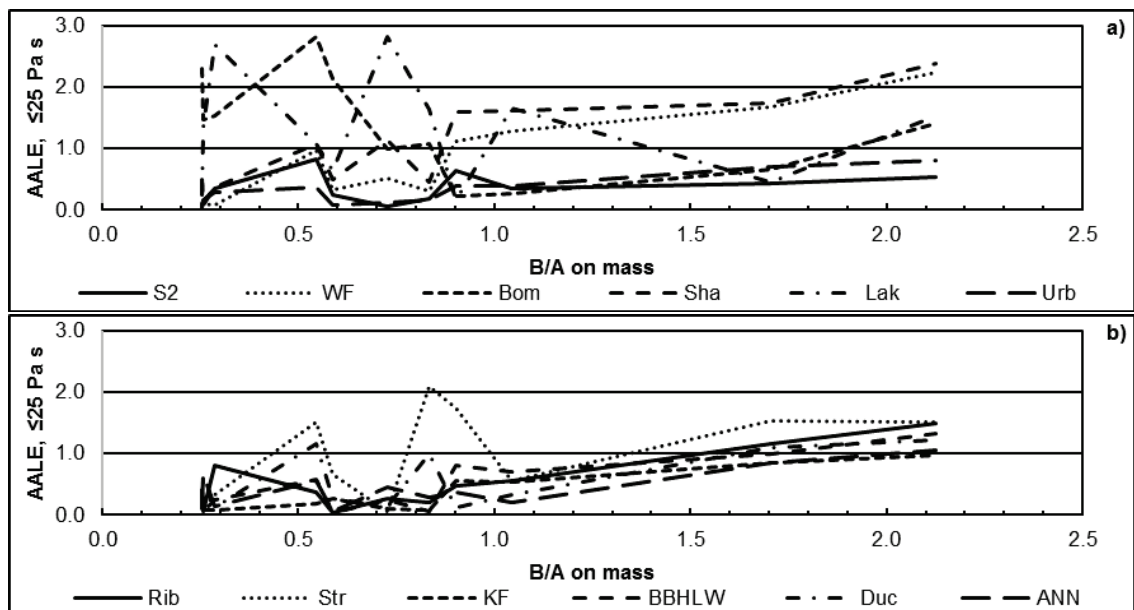


Figure 114: AALE as function of B/A-ratio obtained from classical viscosity models a) S2 to Urbain and b) Riboud to ANNliq, $\eta \leq 25 \text{ Pa s}$, all shear rates, reducing conditions.

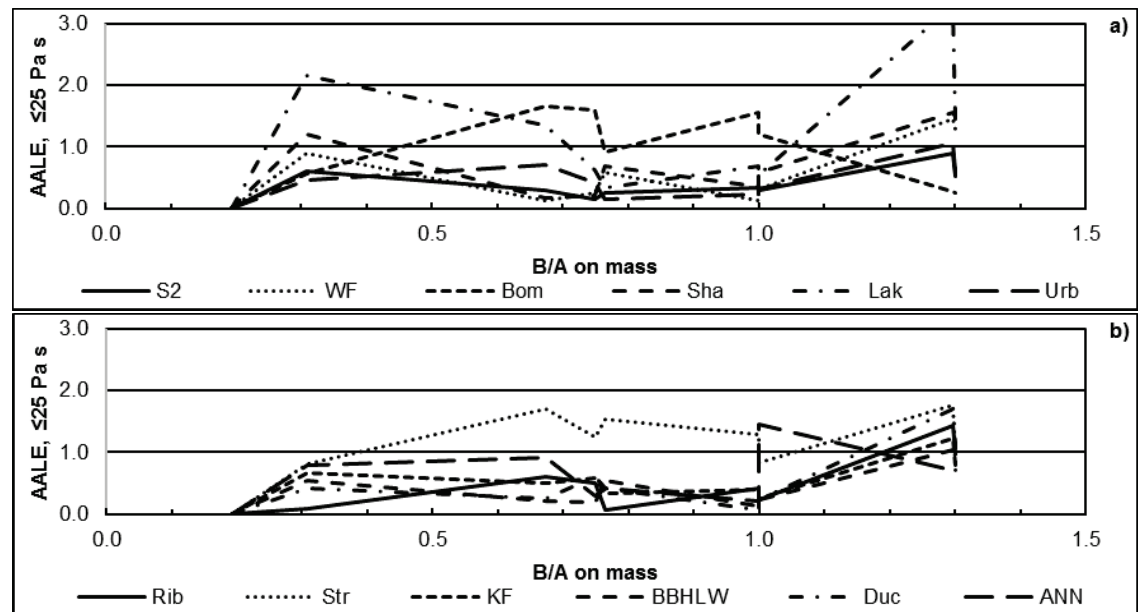


Figure 115: AALE obtained from classical viscosity models a) S2 to Urbain and b) Riboud to ANNliq, $\eta \leq 25$ Pa s, all shear rates, nitrogen atmosphere assumed to be oxidizing.

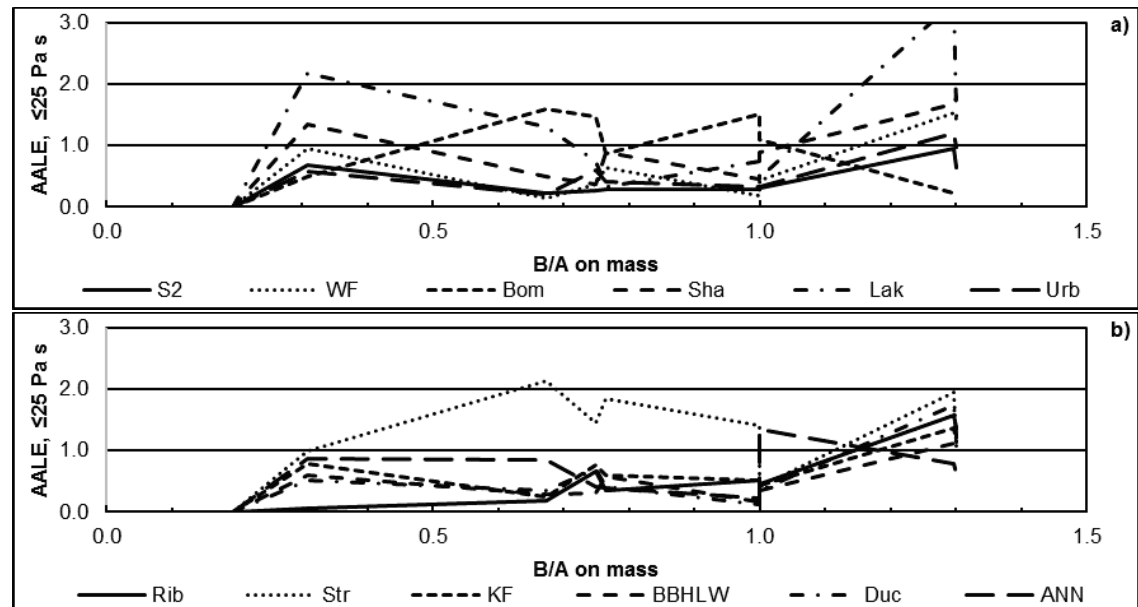


Figure 116: AALE obtained from classical viscosity models a) S2 to Urbain and b) Riboud to ANNliq, $\eta \leq 25$ Pa s, all shear rates, nitrogen atmosphere assumed to be reducing.

20. Appendix: Advanced Viscosity Modelling: a-factors

Table 51: Minimum and maximum a-factors of extensively investigated samples, oxidizing conditions, all shear rates, all solid volume fractions.

Sample	S13		S14		S32		S36		S40		S42	
B/A	0.337		0.338		0.932		1.069		1.857		2.497	
AALe	max.	min.	max.	min.	max.	min.	max.	min.	max.	min.	max.	min.
S2	578.2	4.7	355.1	1.6	3.7	1.1	5.6	1.1	1.2	-1.8	50.0	4.9
W-F	646.4	5.3	4.2	-240.2	4.1	1.3	7.5	1.3	2.0	1.3	57.4	5.7
Bom	2.7	-514.8	-4.8	-26650.5	2.1	0.1	3.2	-8.7	0.9	-8.2	52.6	4.8
Sha	974.5	6.3	0.4	-6686.0	4.3	1.3	7.4	1.3	1.9	1.2	56.9	5.6
Lak	-106.7	-281164	735.4	2.1	3.5	1.3	6.4	1.2	1.4	-3.6	51.2	3.2
Urb	71.5	3.0	170.9	0.7	2.7	0.6	6.3	1.2	1.5	-0.1	40.1	4.9
Rib	3.1	-575.5	820.1	2.1	2.9	0.9	6.8	1.3	1.7	0.6	48.1	5.3
Str	600.1	4.4	971.5	-0.2	4.2	-2.5	6.6	1.1	2.5	1.4	49.6	5.4
K-F	269.2	3.8	907.3	2.2	3.1	0.8	6.6	1.2	1.6	0.5	43.2	5.0
BBHLW	171.5	3.5	493.3	1.2	3.9	1.4	6.5	1.2	1.5	-0.1	53.8	5.3
Duc	3.6	-751.9	3.6	-392.9	3.4	1.4	6.2	1.2	1.0	-1.7	52.7	5.0
ANN	322.8	3.9	3.8	-1049.7	1.3	-1.9	6.4	1.1	1.7	0.5	51.4	4.8

Table 52: Minimum and maximum a-factors from extensively investigated samples, reducing conditions, all shear rates, all solid volume fractions.

Sample	S31		S35		S39		S41	
B/A	0.903		1.046		1.705		2.126	
AALE	max.	min.	max.	min.	max.	min.	max.	min.
S2	3.1	0.0	0.8	-0.1	1.3	0.1	8.1	0.6
W-F	4.9	0.8	1.1	0.8	1.9	1.2	19.5	1.1
Bom	0.8	-9.2	0.9	-0.8	1.6	1.1	19.7	1.0
Sha	6.3	1.1	1.1	1.0	2.0	1.2	19.8	1.2
Lak	2.8	0.7	1.1	0.9	1.4	-1.53E+18	16.5	-3.17E+28
Urb	1.1	-2.3	1.0	0.5	1.2	0.1	14.2	0.8
Rib	2.0	-1.0	1.1	0.8	1.6	0.8	17.9	1.0
Str	6.5	-0.2	-3.2	-42.1	2.1	1.2	19.4	1.1
K-F	2.1	-0.9	1.0	0.6	1.3	0.3	14.9	0.8
BBHLW	3.7	0.7	1.0	0.5	1.6	0.9	18.5	1.0
Duc	1.3	-3.4	0.8	-0.2	1.8	1.0	17.5	1.0
ANN	-2.4	-12.6	0.6	-1.0	1.8	1.1	17.4	1.0

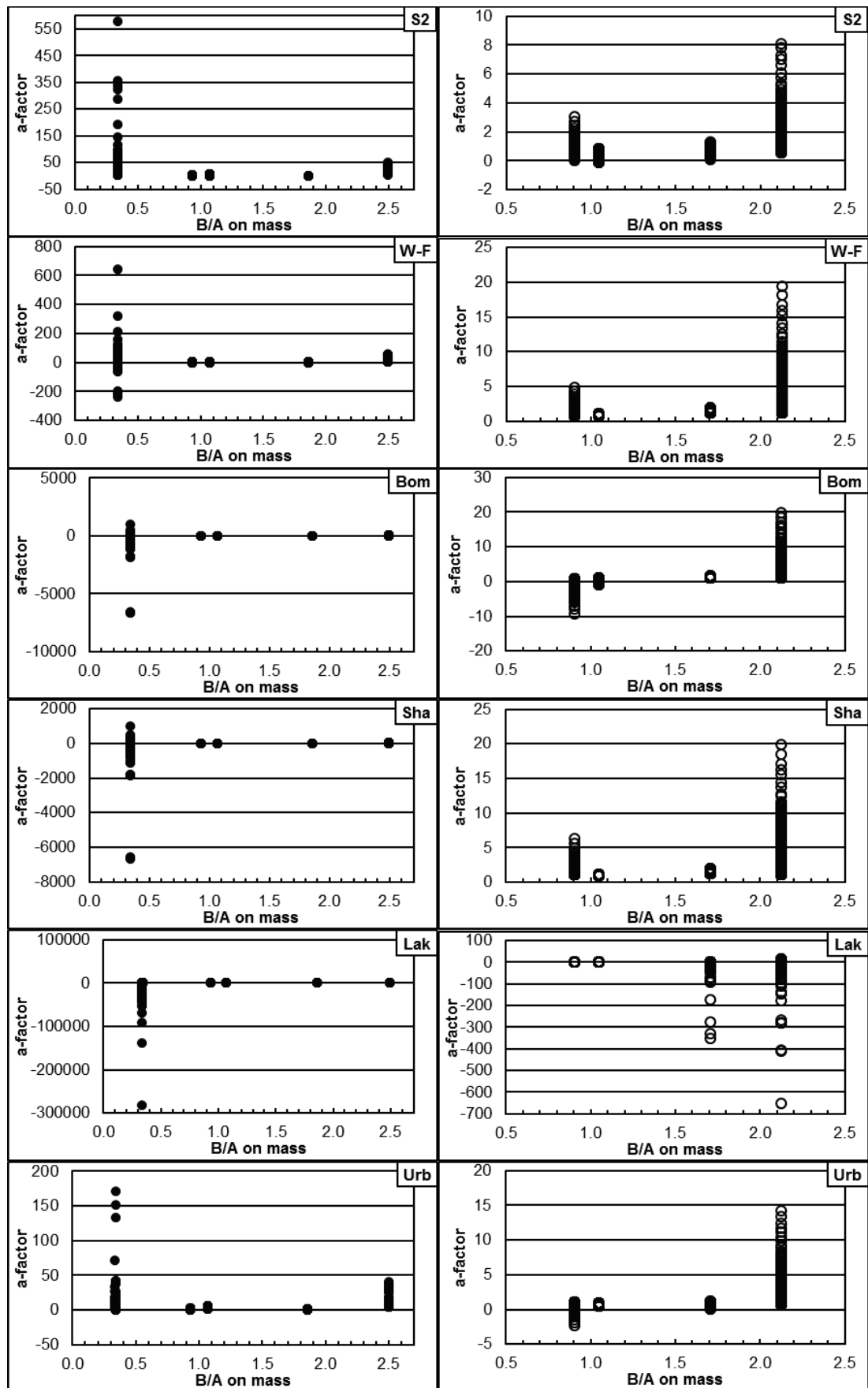


Figure 117: Fitted a-factors of extensively investigated slags, all shear rates, all solid volume fractions, S2 to Urbain. Left hand: oxidizing conditions, right hand: reducing conditions.

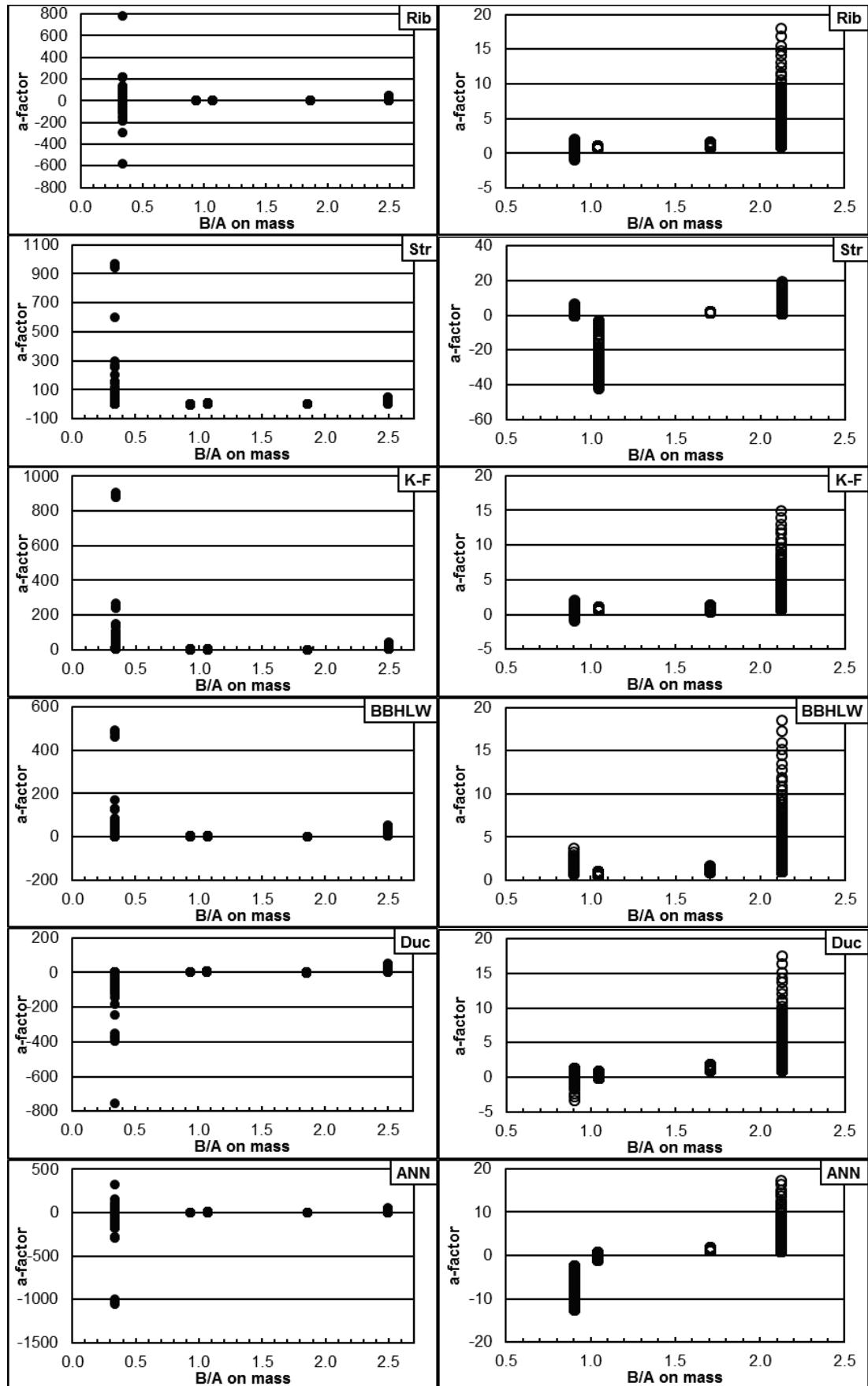


Figure 118: Fitted a-factors of extensively investigated slags, all shear rates, all solid volume fractions, Riboud to ANNliq. Left hand: oxidizing conditions, right hand: reducing conditions.

21. Appendix: Slag Mineral Phase Investigations and Modelling

Table 53: Minerals, abbreviations and chemical formulas.

Abbr.	Mineral name	Mineral formula	Abbr.	Mineral name	Mineral formula
Ake	Akermanite	$\text{Ca}_2\text{MgSi}_2\text{O}_7$	Hol	Hollandit	$\text{K}_{0.75}\text{Ti}_{3.25}\text{Al}_{0.75}\text{O}_8$
Alu	Alumina	$\gamma\text{-Al}_2\text{O}_3$	Kir	Kirschsteinite	$\text{Ca}(\text{Fe}^{++}0.69\text{Mg}_{0.31})\text{SiO}_4$
Ano	Anorthite	$\text{CaAl}_2\text{Si}_2\text{O}_8$	Lar	Larnite	$\text{Ca}_2(\text{SiO}_4)$
Aug	Augite	$(\text{Ca},\text{Fe})(\text{Mg},\text{Fe})[\text{Si}_2\text{O}_6]$	Magh	Maghemite	$\text{Fe}^{+++}\text{O}_3$
Bre	Bredigite	$\text{Ca}_{14}\text{Mg}_2(\text{SiO}_4)_8$	Magn	Magnetite	$\text{Fe}^{++}\text{Fe}^{+++}\text{O}_4$
Brow	Brownmillerite	$\text{Ca}_2(\text{Al},\text{Fe}^{+++})_2\text{O}_5$	MagSi	Magnesium Silicate	Mg_2SiO_4
Cor	Corundum	Al_2O_3	Mer	Merwinite	$\text{Ca}_3\text{MgSi}_2\text{O}_8$
Cri	Cristobalite	SiO_2	Mon	Monticellite	CaMgSiO_4
DioFe	Diopside-Fe	$\text{Ca}(\text{Mg}_{0.75}\text{Fe}_{0.25})\text{Si}_2\text{O}_6$	MonFe	Monticellite-Fe ⁺⁺	$\text{CaFe}_{0.12}\text{Mg}_{0.88}\text{SiO}_4$
Fay	Fayalite	$\text{Fe}^{++}\text{SiO}_4$	Mul 2:1	Mullite 2:1	$(\text{Al}_2\text{O}_3)_2(\text{SiO}_2)$
Fer	Ferrobustamite	$(\text{CaFe}^{++})(\text{SiO}_3)_2$	Por	Porcelainite	$\text{Al}_6\text{Si}_2\text{O}_{13}$
For	Forsterite	Mg_2SiO_4	Qua	Quartz	SiO_2
Geh	Gehlenite	$\text{Ca}_2\text{Al}_2\text{SiO}_7(\text{s})$	SpFA	Spinel Hercynite	$\text{Fe}^{++}\text{Al}_2\text{O}_4$
Gro	Grossularia	$\text{Ca}_3\text{Al}_2(\text{SiO}_4)_3$	SpMAF	Spinel	$\text{MgAl}_{0.79}\text{Fe}^{+++}1.21\text{O}_4$
Hed	Hedenbergite	$\text{CaFe}^{++}\text{Si}_2\text{O}_6$	SpiMA	Spinel	MgAl_2O_4
Her	Hercynite	$\text{Fe}^{++}\text{Al}_2\text{O}_4$	Wol	Wollastonite	CaSiO_3
Hib	Hibonite	$\text{CaAl}_{12}\text{O}_{19}$	Wue	Wuestite	Fe^{++}O

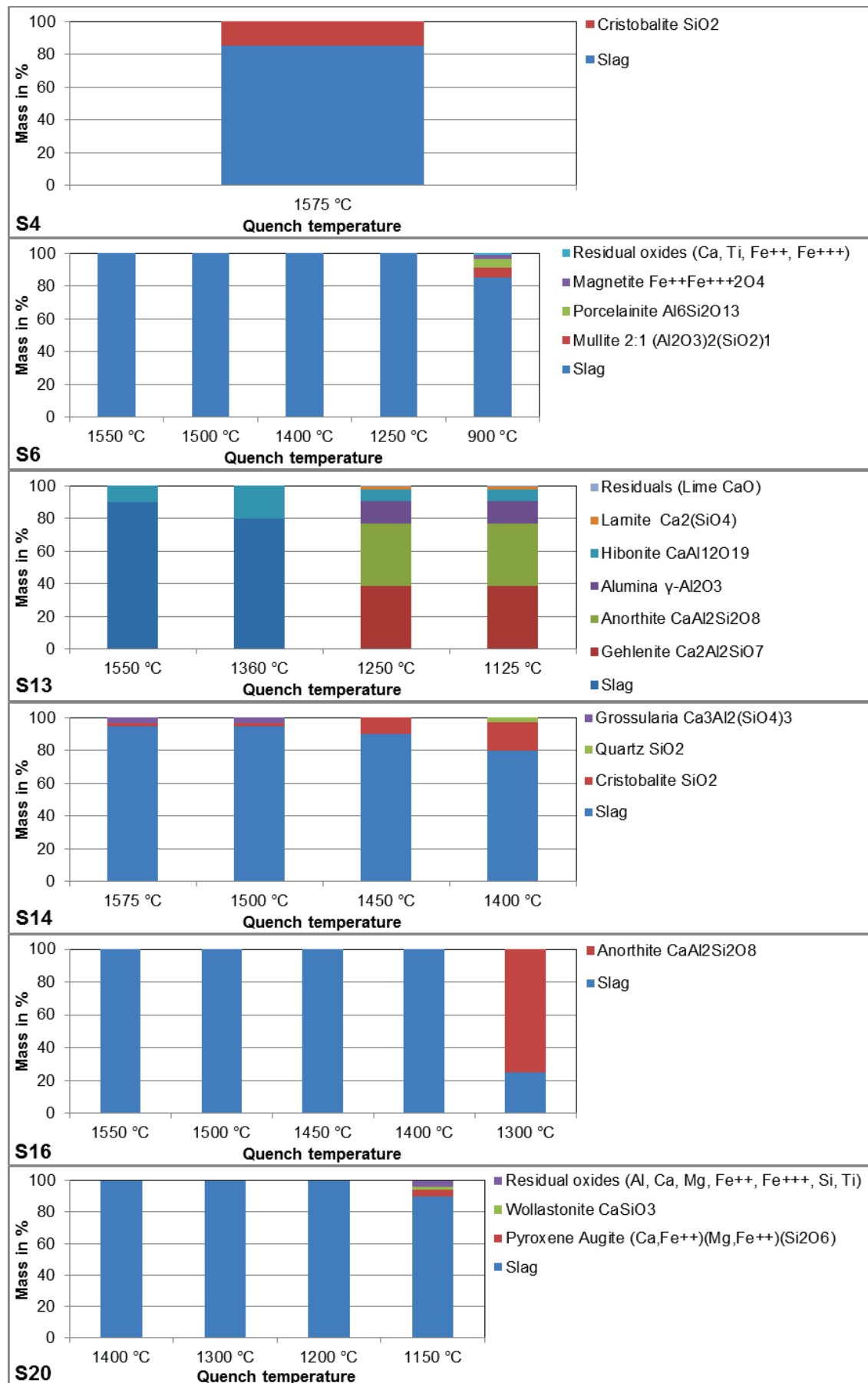


Figure 119: Phase analysis for samples under oxidizing conditions, S4 to S20.

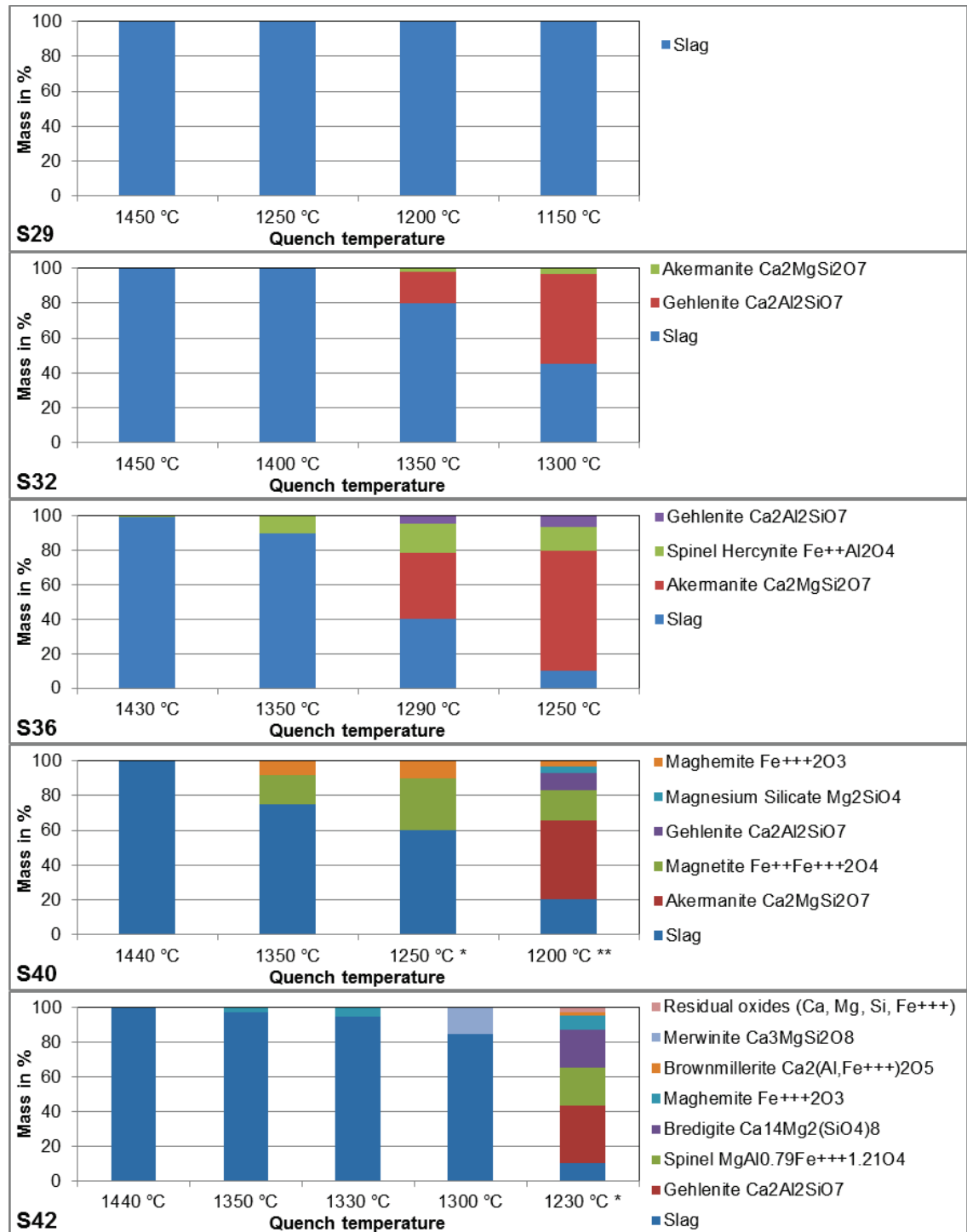


Figure 120: Phase analysis for samples under oxidizing conditions, S29 to S42.

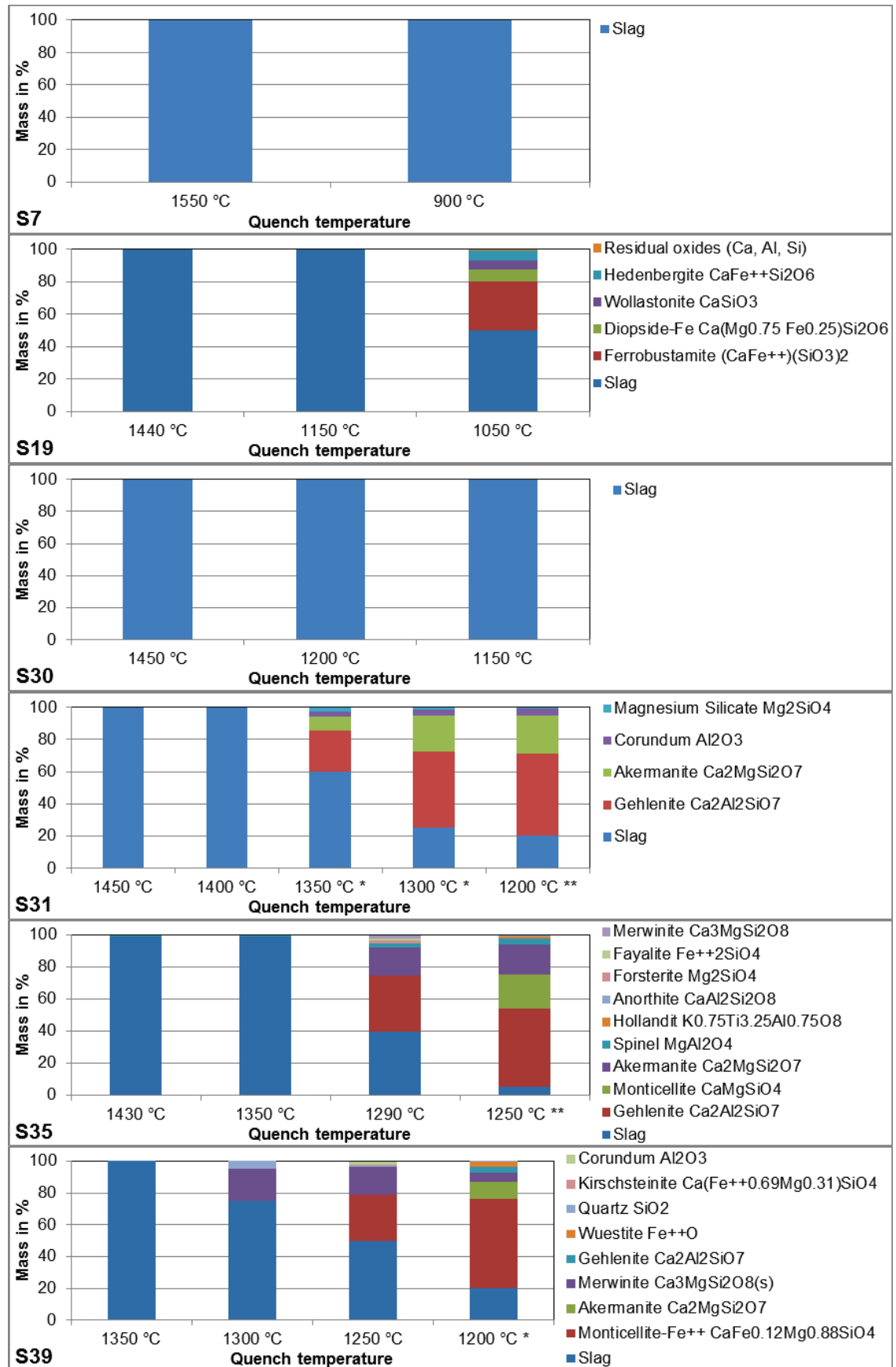


Figure 121: Phase analysis of samples prepared under reducing conditions, slags S7 to S39.

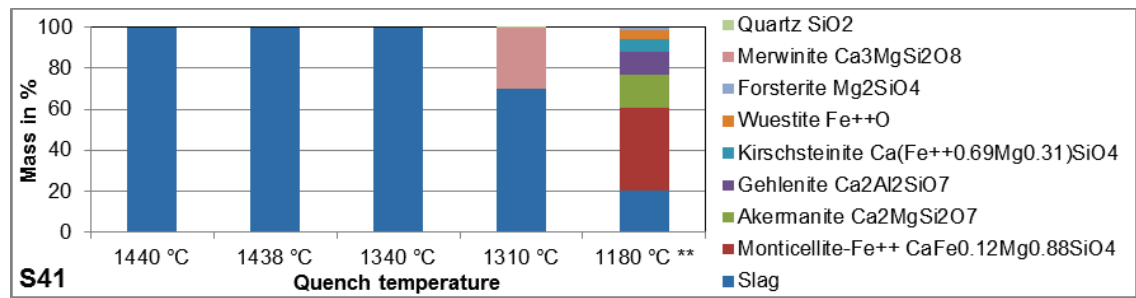


Figure 122: Phase analysis of samples prepared under reducing conditions, S41.

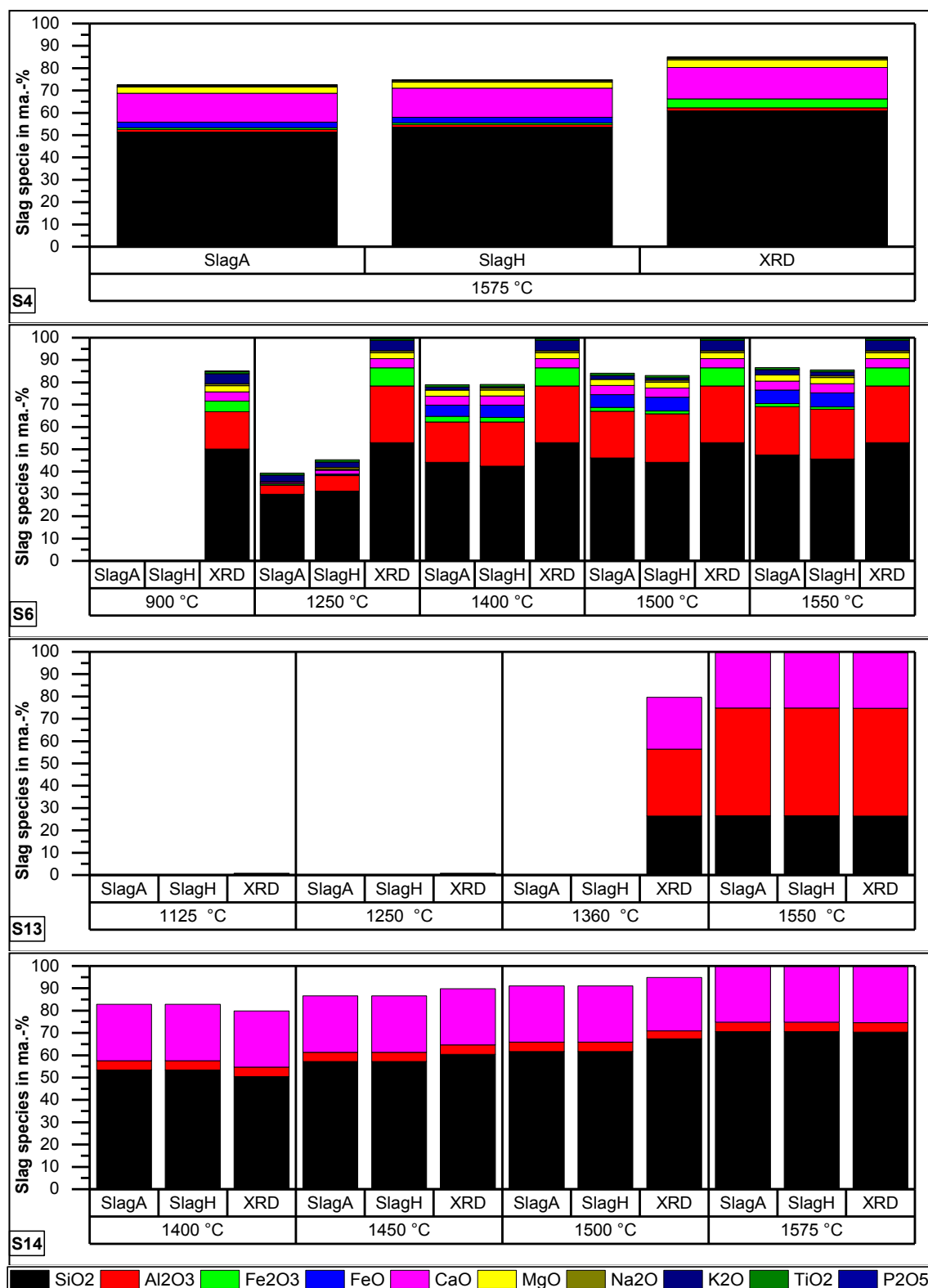


Figure 123: Liquid slag composition obtained by quenching experiments and calculations at oxidizing conditions, S4 to S14.

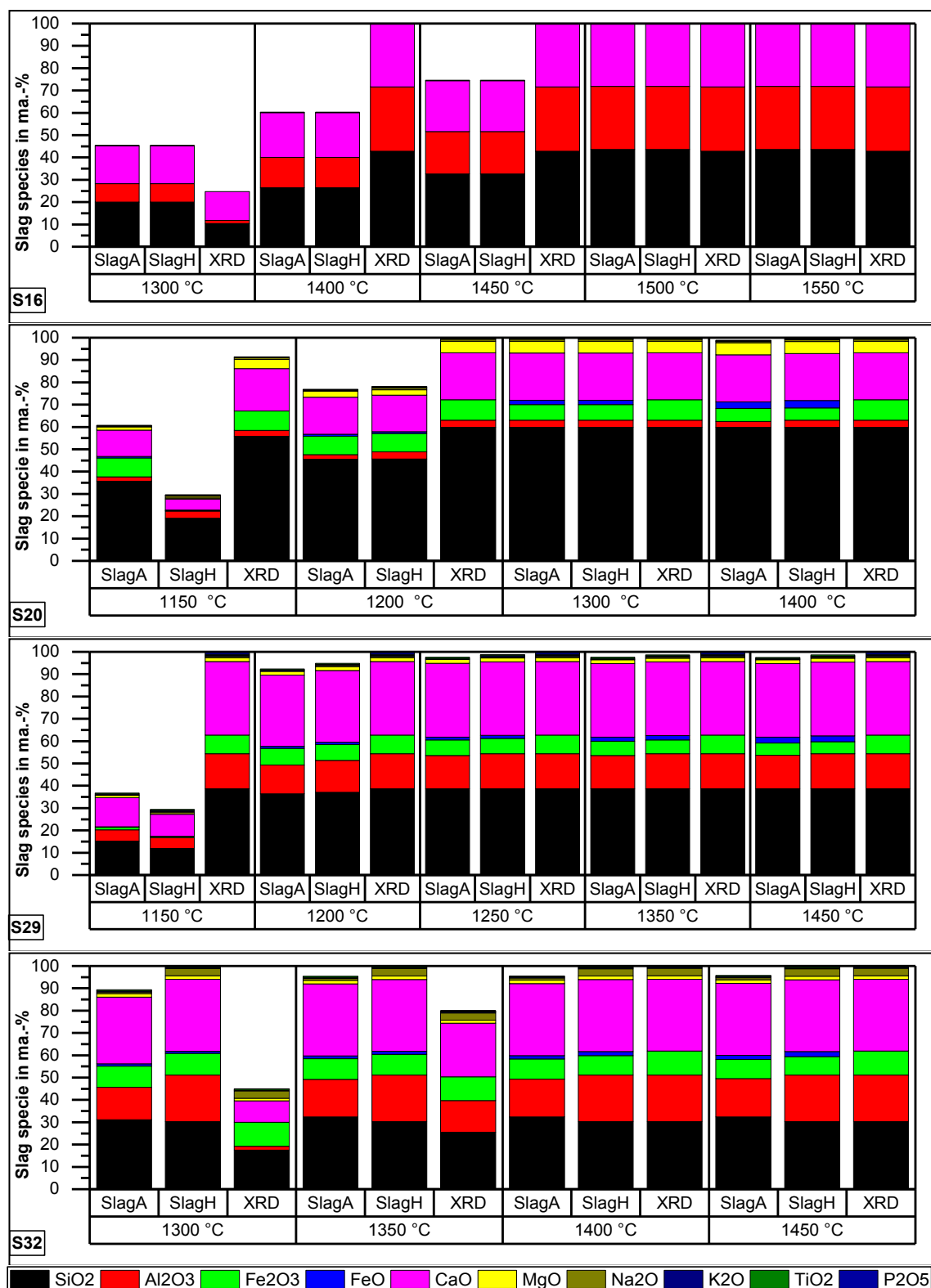


Figure 124: Liquid slag composition obtained by quenching experiments and calculations at oxidizing conditions, S16 to S32.

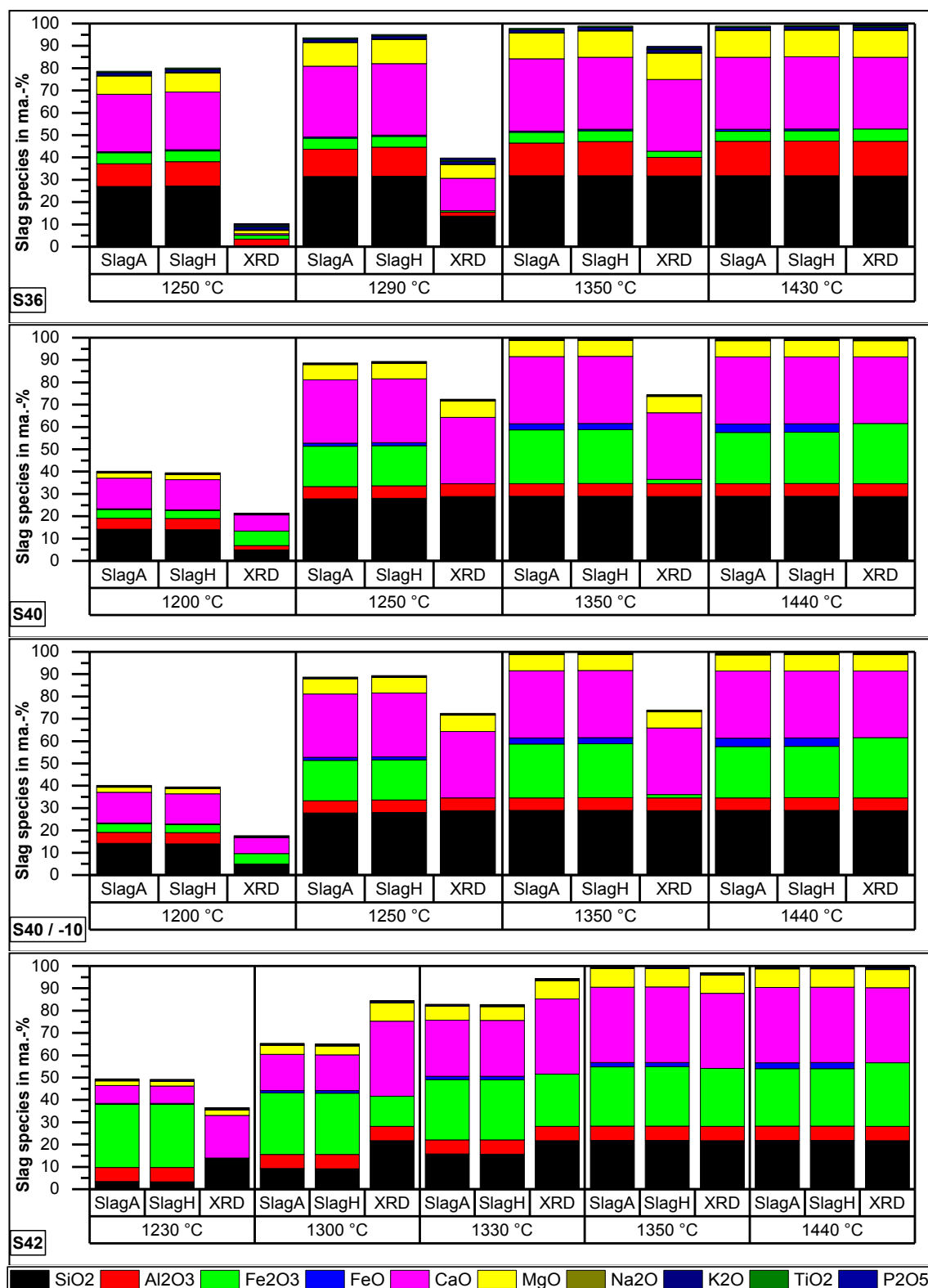


Figure 125: Liquid slag composition obtained by quenching experiments and calculations at oxidizing conditions, S36 to S42.

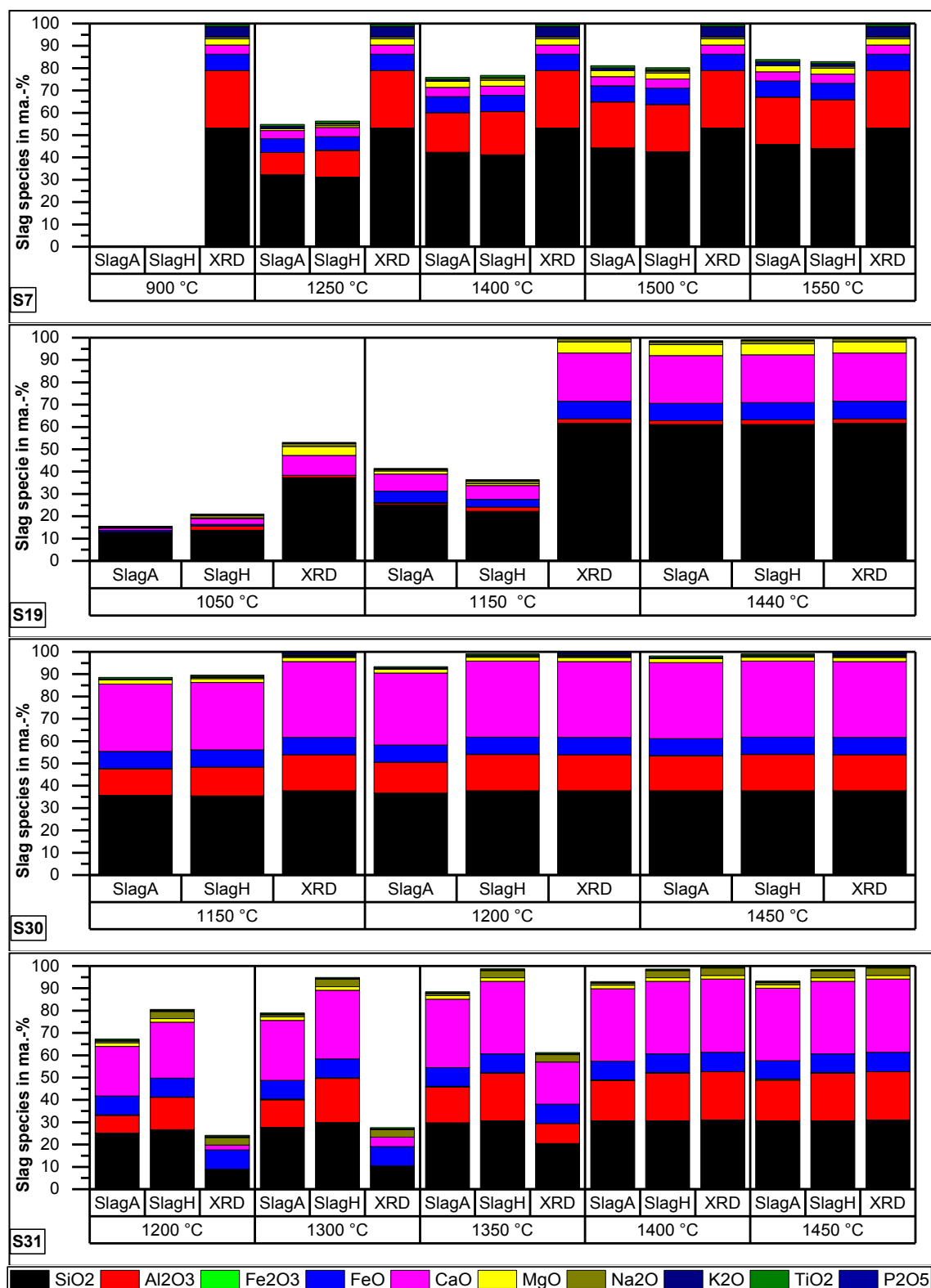


Figure 126: Liquid slag composition obtained by quenching experiments and calculations at reducing conditions, S7 to S31.

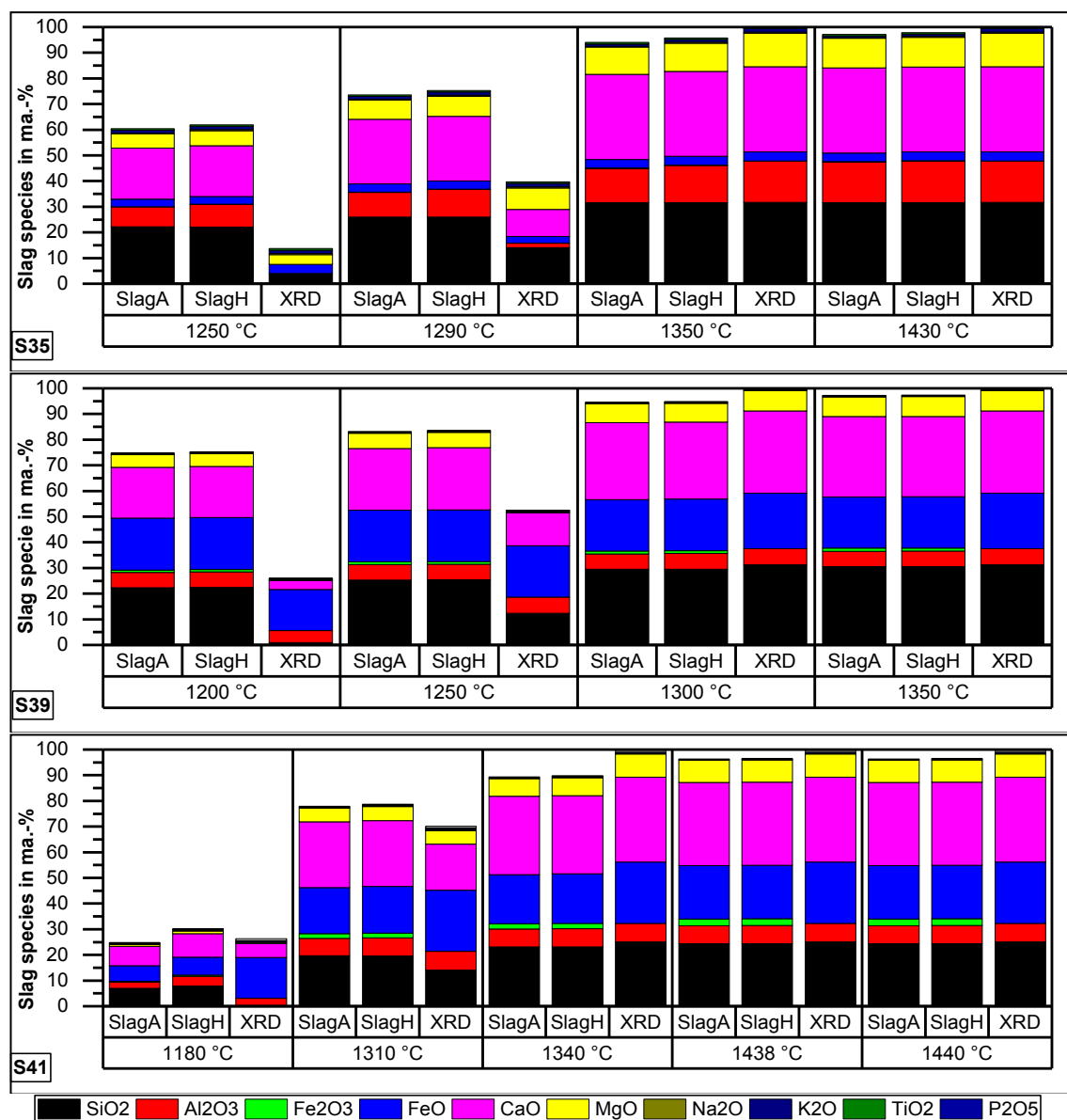


Figure 127: Liquid slag composition obtained by quenching experiments and calculations at reducing conditions, S35 to S41.

22. Appendix: Results of DTA Measurements on Slags

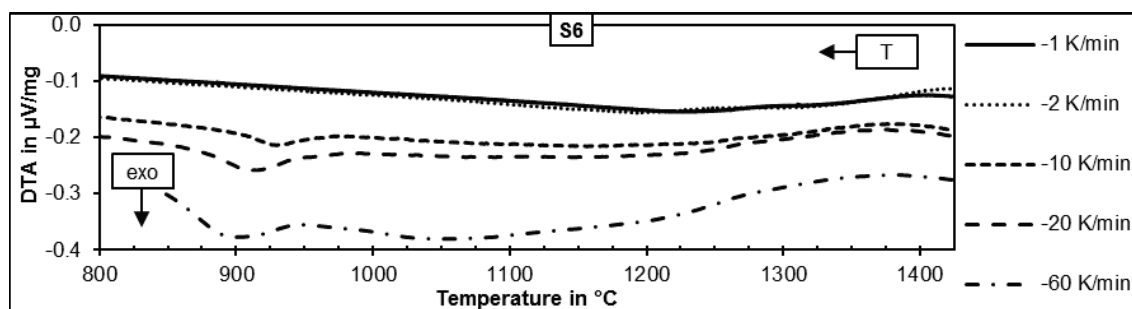


Figure 128: DTA curves of slag S6, oxidizing atmospheres.

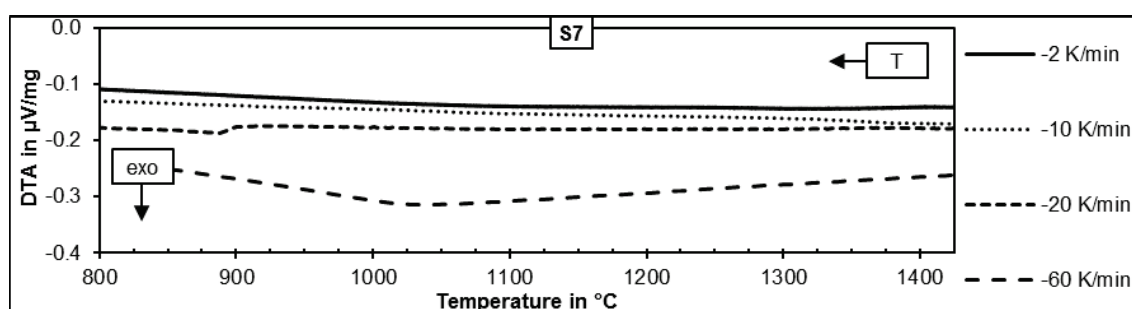


Figure 129: DTA curves of slag S7, reducing atmospheres.

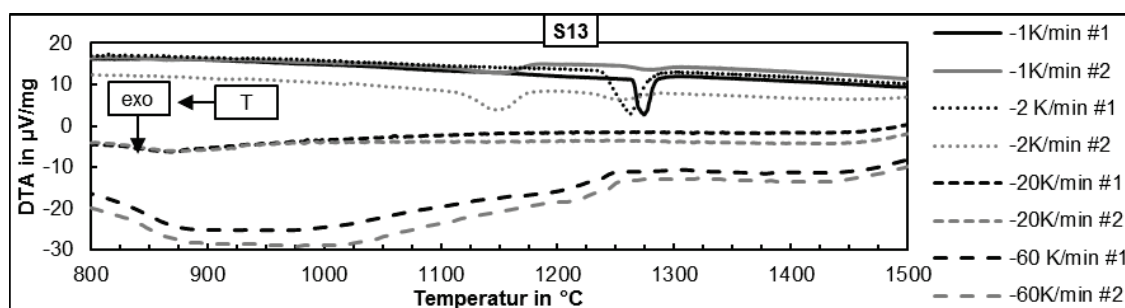


Figure 130: DTA curves of slag S13, oxidizing atmospheres, including repetitions.

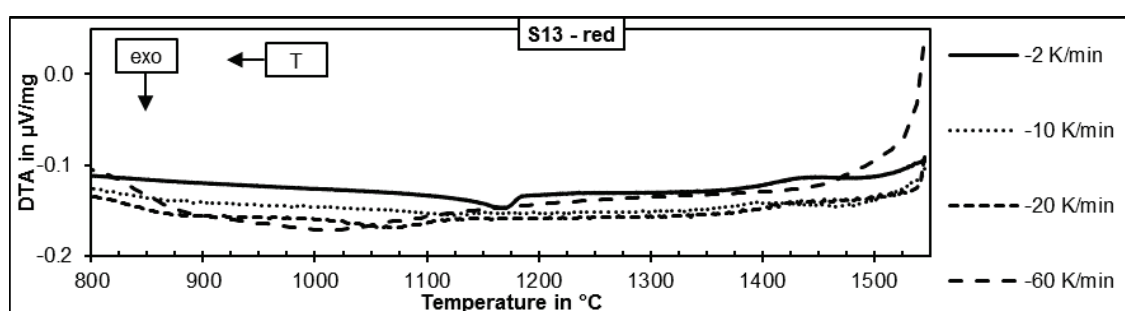


Figure 131: DTA curves of slag S13, reducing atmospheres.

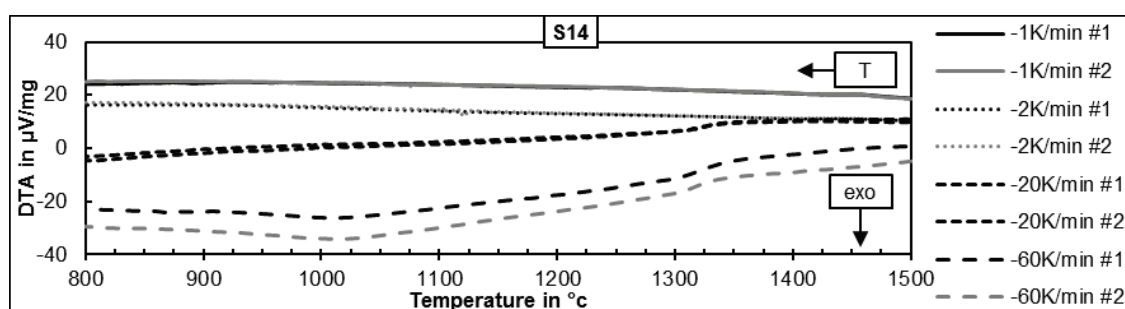


Figure 132: DTA curves of slag S14, oxidizing atmospheres, including repetitions.

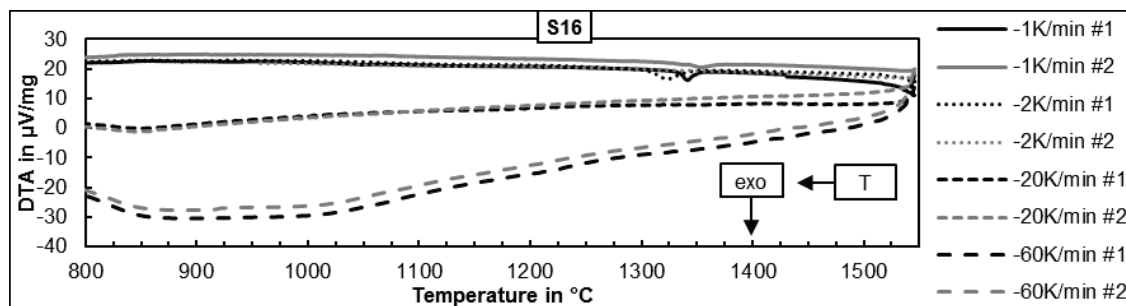


Figure 133: DTA curves of slag S16, oxidizing atmospheres, agreement to viscosity measurements.

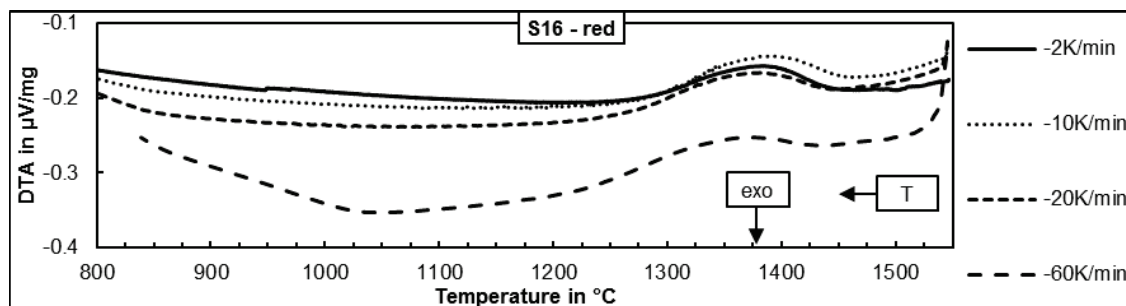


Figure 134: DTA curves of slag S16, reducing atmospheres.

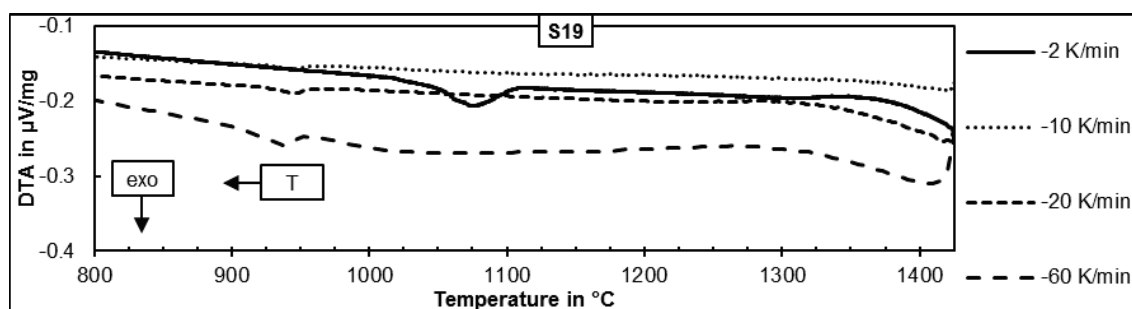


Figure 135: DTA curves of slag S19, reducing atmospheres.

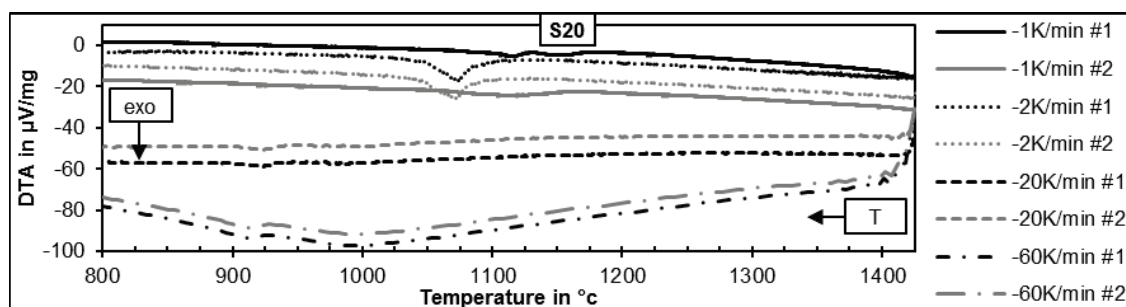


Figure 136: DTA curves of slag S20, oxidizing atmospheres, including repetitions.

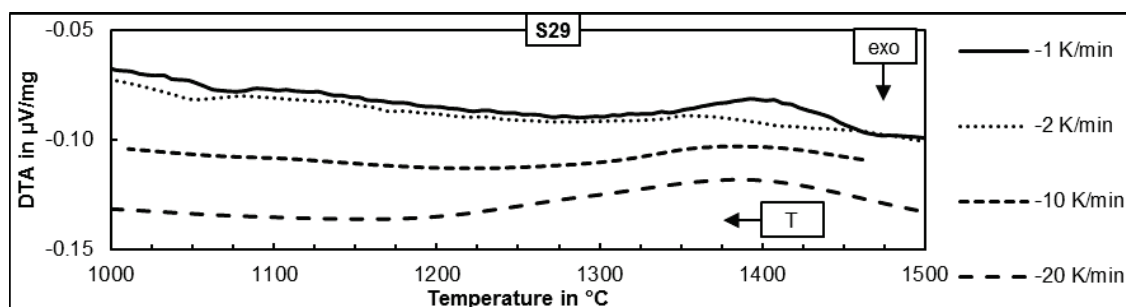


Figure 137: DTA curves of slag S29, oxidizing atmospheres.

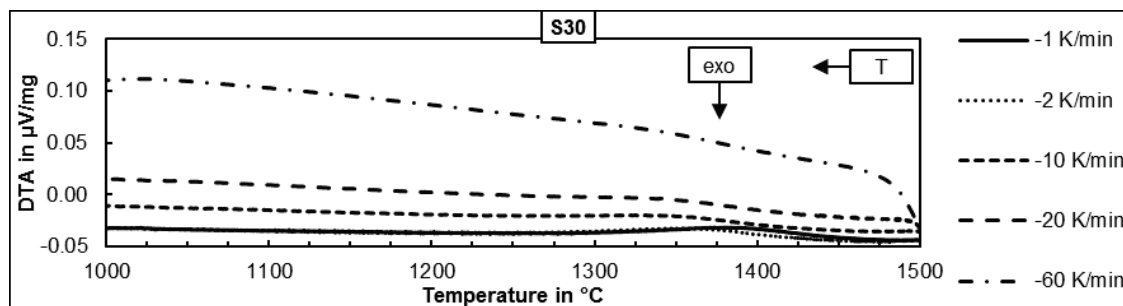


Figure 138: DTA curves of slag S30, reducing atmospheres.

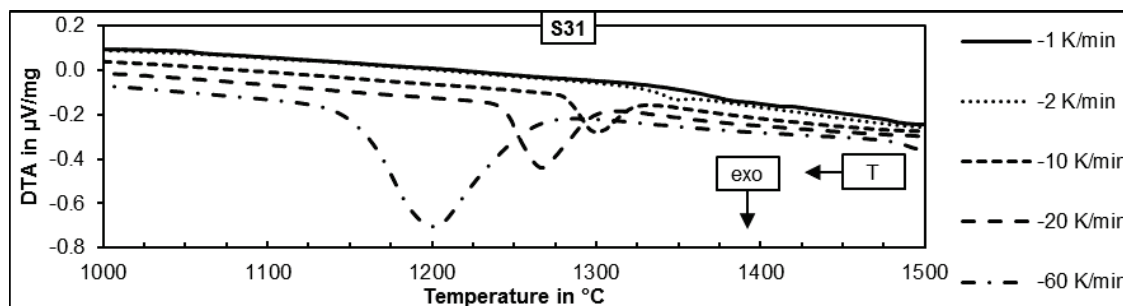


Figure 139: DTA curves of slag S31, reducing atmospheres.

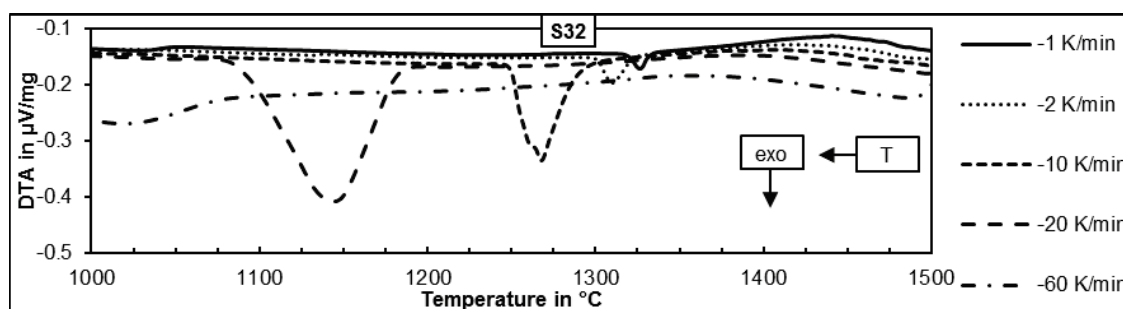


Figure 140: DTA curves of slag S32, oxidizing atmospheres.

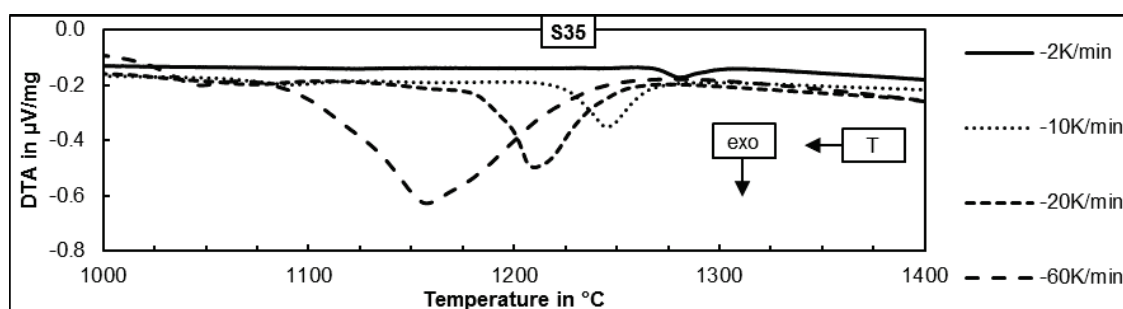


Figure 141: DTA curves of slag S35, reducing atmospheres.

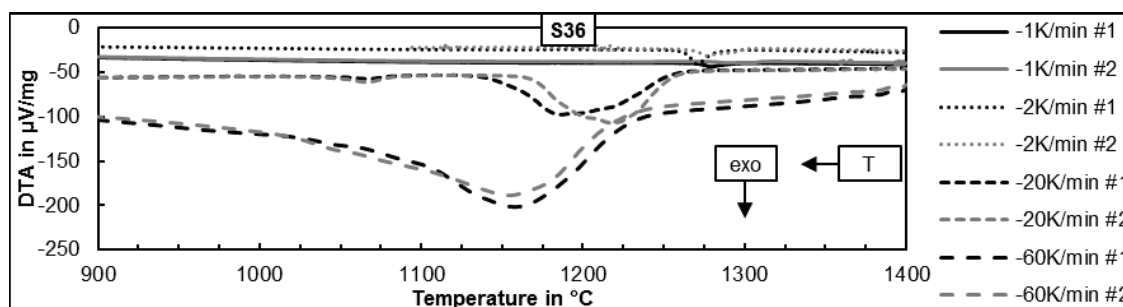


Figure 142: DTA curves of slag S36, oxidizing atmospheres, including repetitions.

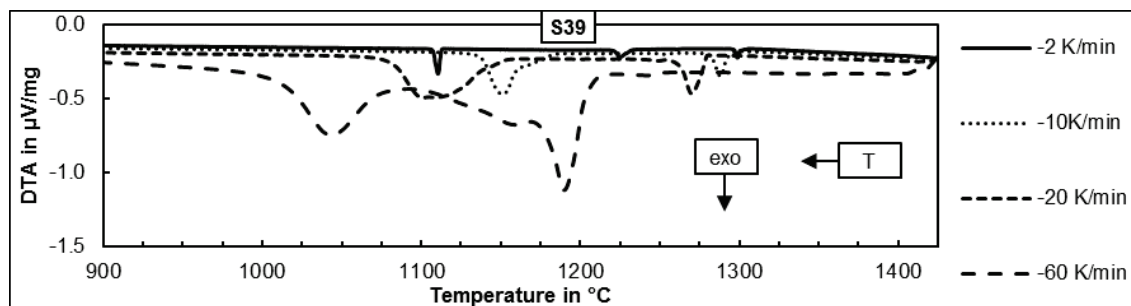


Figure 143: DTA curves of slag S39, reducing atmospheres.

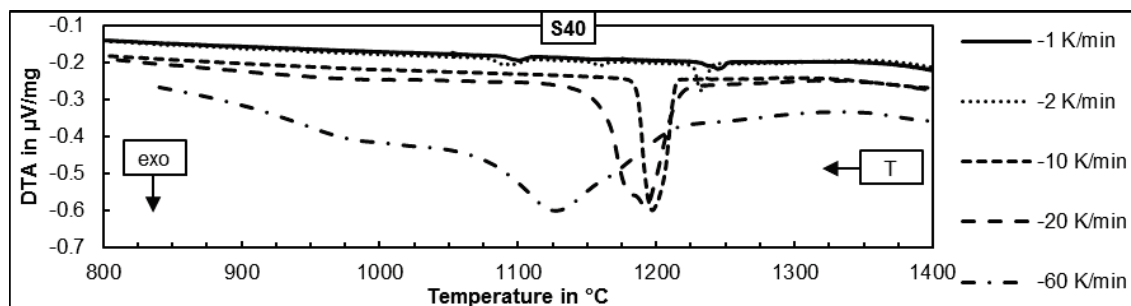


Figure 144: DTA curves of slag S40, oxidizing atmospheres.

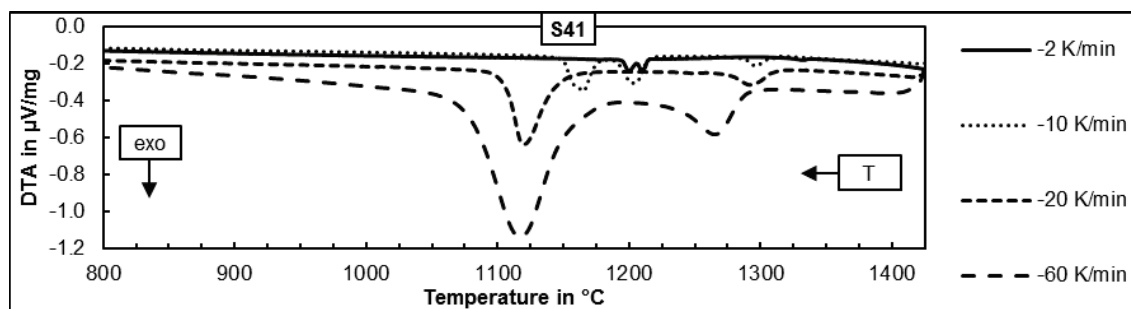


Figure 145: DTA curves of slag S41, reducing atmospheres.

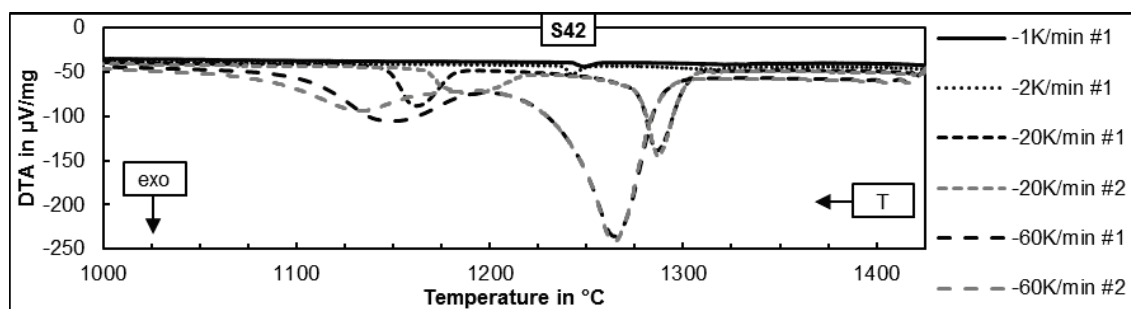


Figure 146: DTA curves of slag S42, oxidizing atmospheres, including repetitions.

23. Appendix: Advanced Slag Viscosity Modelling Approach

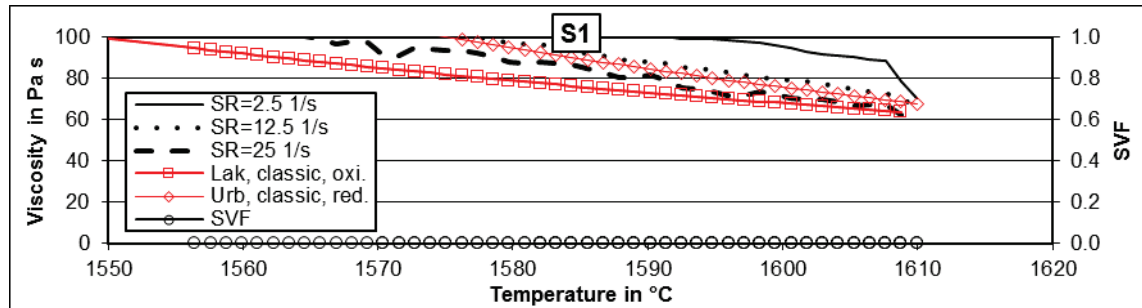


Figure 147: Slag S1, nitrogen atmosphere, classic modelling assuming oxidizing and reducing conditions.

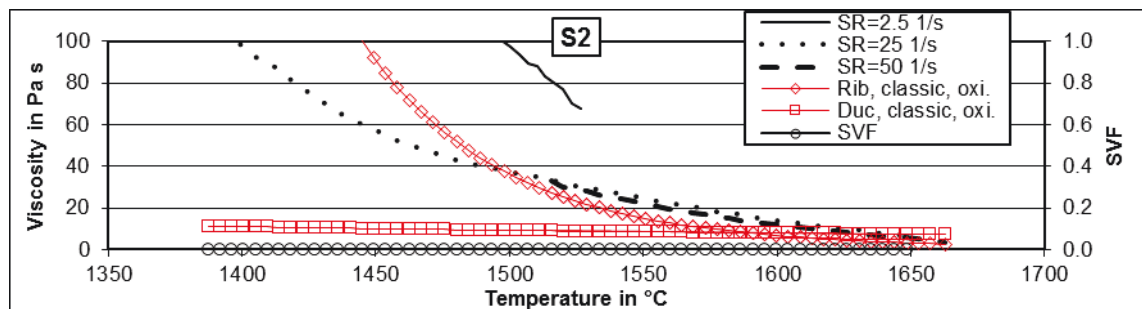


Figure 148: Slag S2, oxidizing atmosphere, AALE by $\eta \leq 25$ Pa s and $\eta \leq 100$ Pa s.

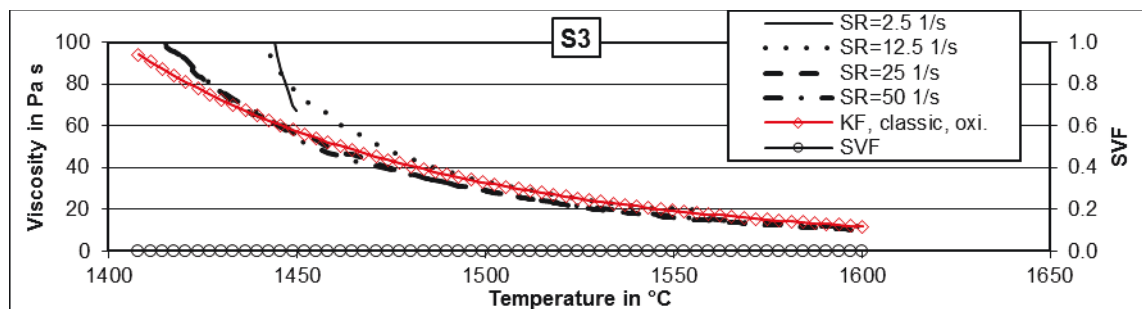


Figure 149: Slag S3, oxidizing atmosphere.

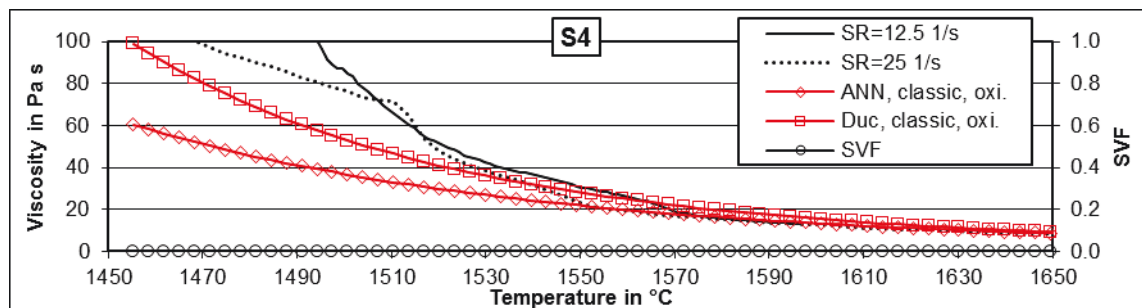


Figure 150: Slag S4, oxidizing atmosphere, classic modelling, AALE by $\eta \leq 25$ Pa s and $\eta \leq 100$ Pa s.

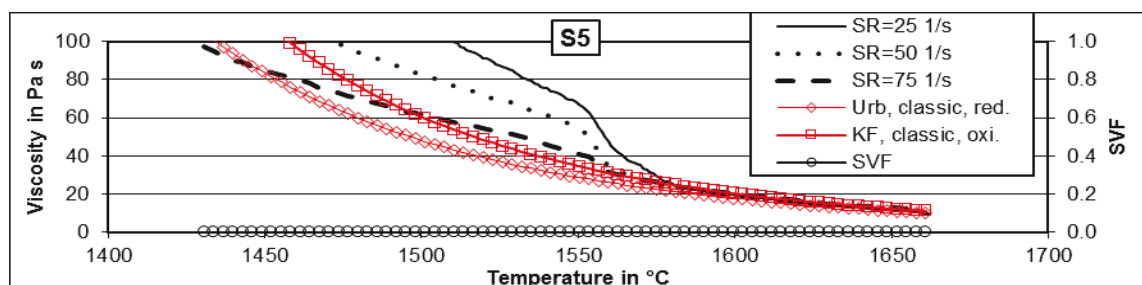


Figure 151: Slag S5, reducing atmosphere, classic modelling, additional oxidizing atmosphere.

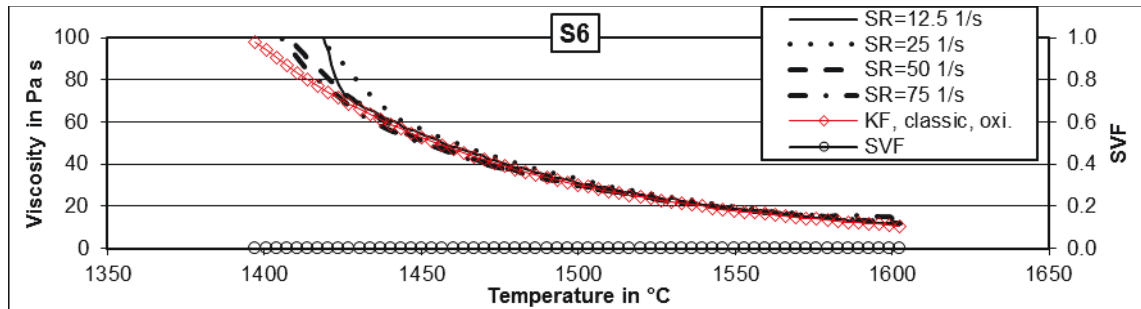


Figure 152: Slag S6, oxidizing atmosphere, classic modelling.

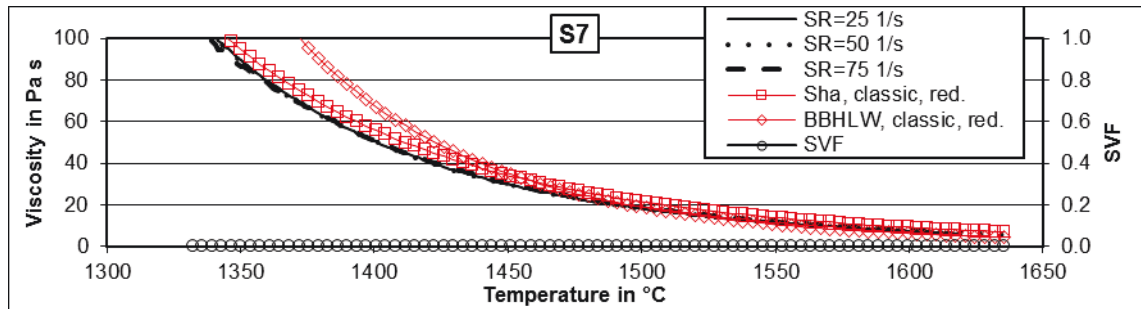
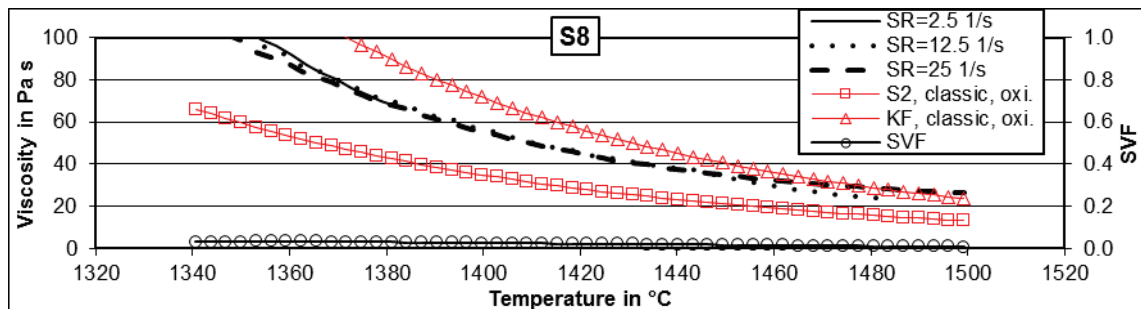
Figure 153: Slag S7, reducing atmosphere, classic modelling, AALE by $\eta \leq 25$ Pa s and $\eta \leq 100$ Pa s.

Figure 154: Slag S8, oxidizing atmosphere, classic modelling.

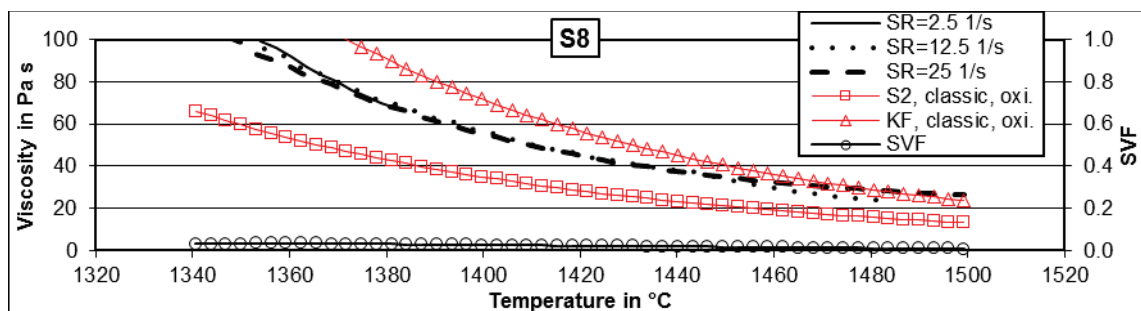
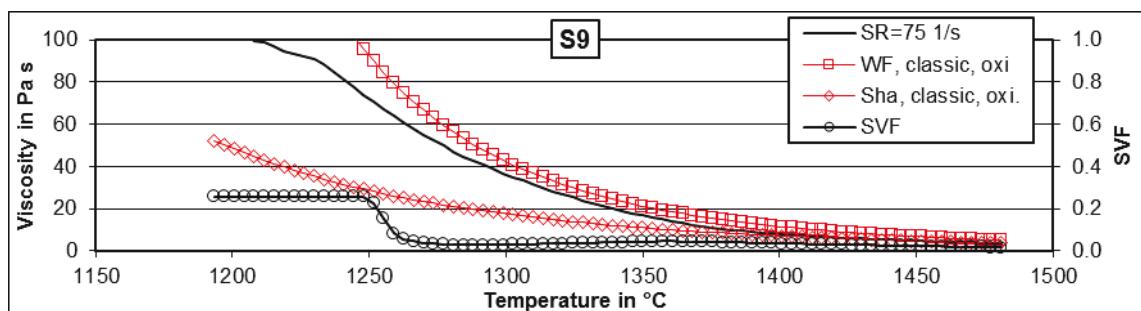


Figure 155: Slag S8, oxidizing atmosphere, advanced modelling.

Figure 156: Slag S9, oxidizing atmospheres, classic modelling, AALE by $\eta \leq 25$ Pa s and $\eta \leq 100$ Pa s.

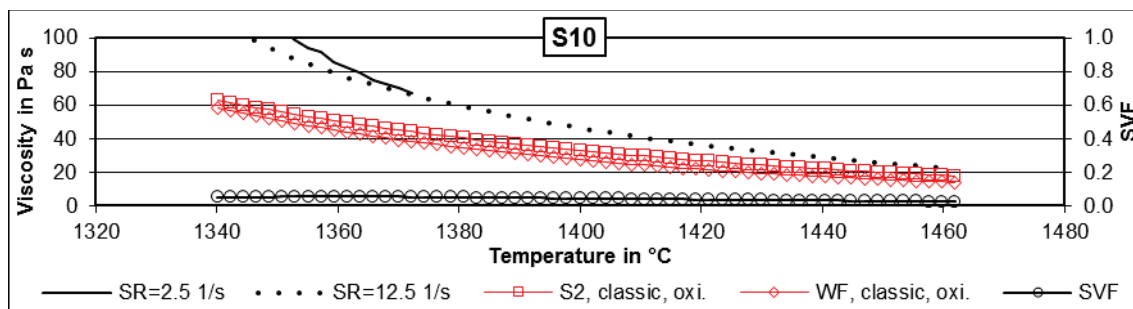


Figure 157: Slag S10, oxidizing atmospheres, classic modelling.

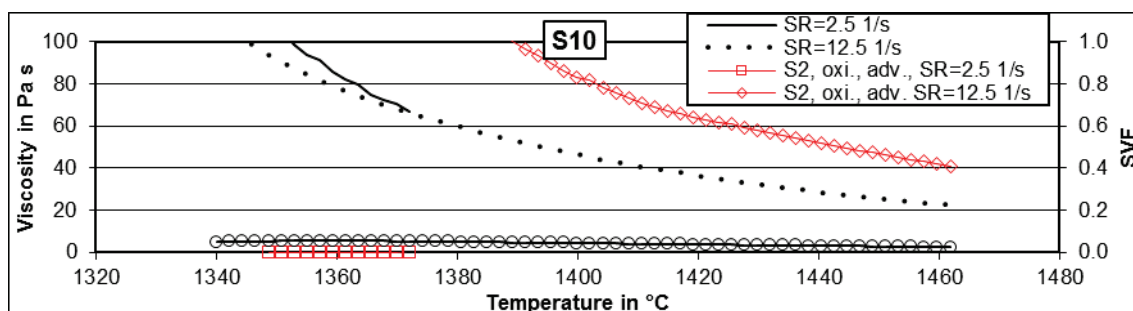


Figure 158: Slag S10, oxidizing atmospheres, advanced modelling, best classic model S2 by AALE.

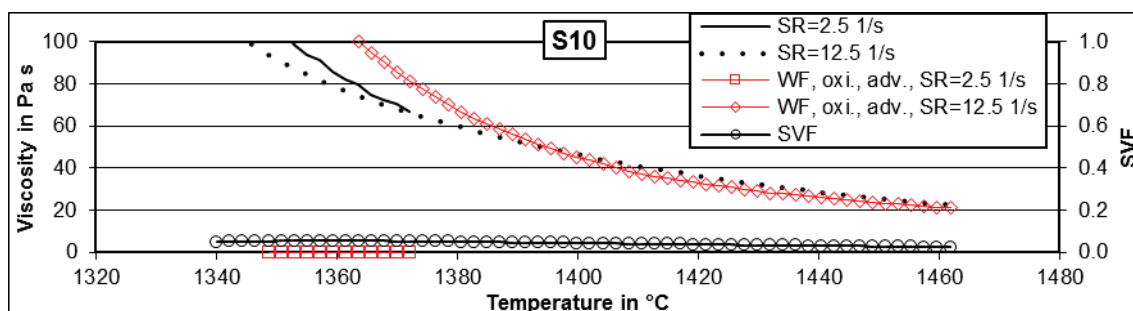


Figure 159: Slag S10, oxidizing atmospheres, advanced modelling, best advanced model Watt-Fereday by AALE.

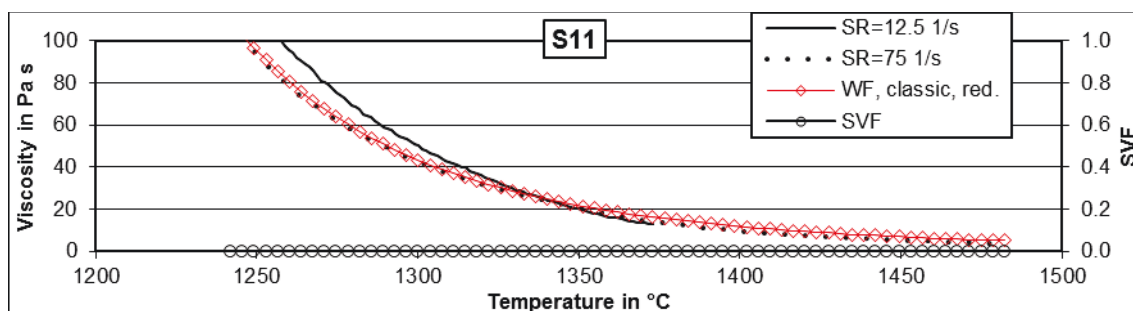


Figure 160: Slag S11, reducing atmospheres, classic modelling.

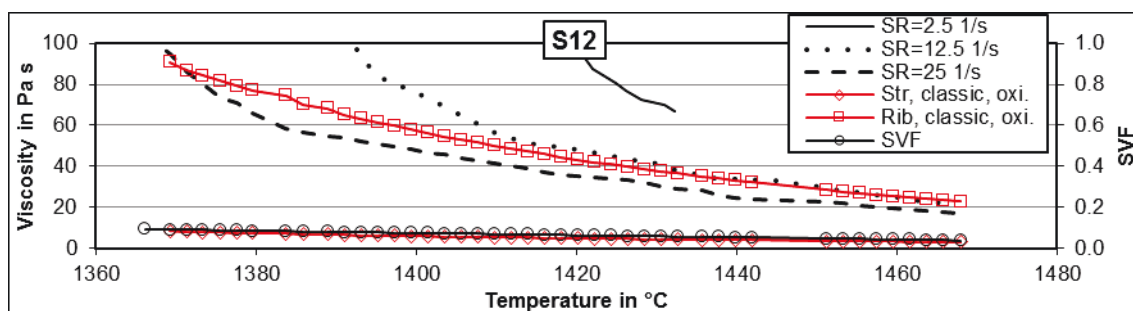


Figure 161: Slag S12, nitrogen atmospheres, oxidizing atmosphere for classic modelling.

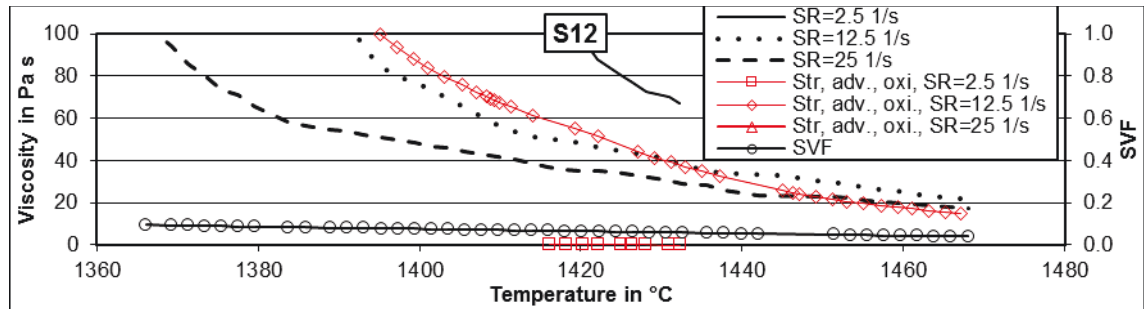


Figure 162: Slag S12, nitrogen atmospheres, oxidizing conditions and Streeter model for advanced modelling.

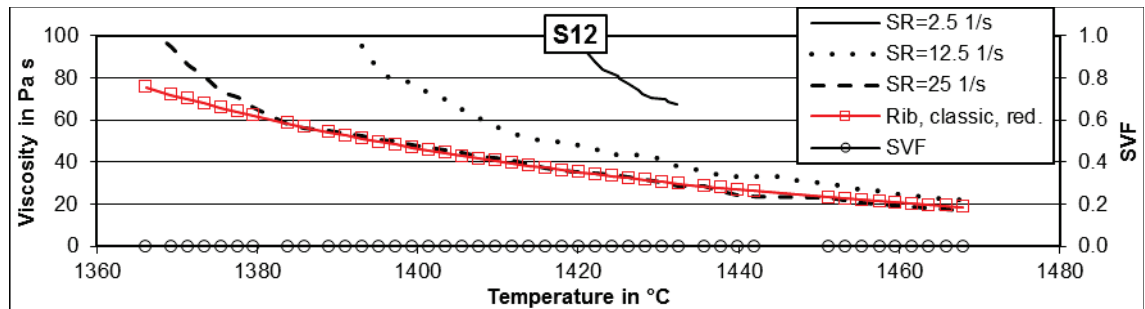


Figure 163: Slag S12, nitrogen atmospheres, reducing conditions, classic viscosity modelling.

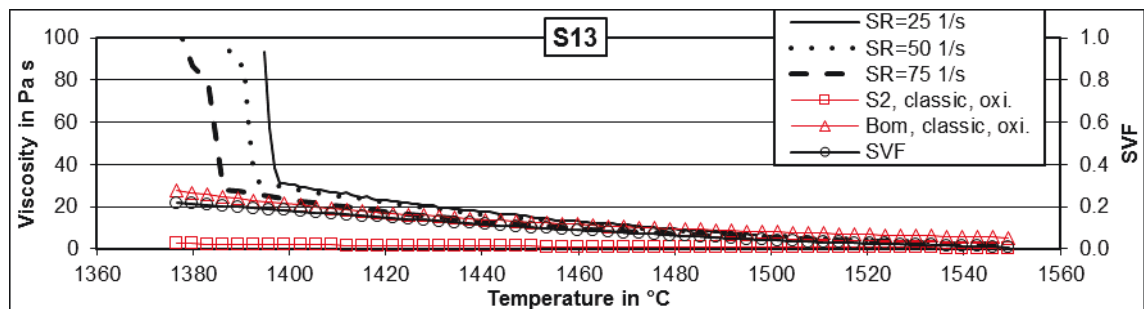


Figure 164: Slag S13, oxidizing atmospheres, classic modelling.

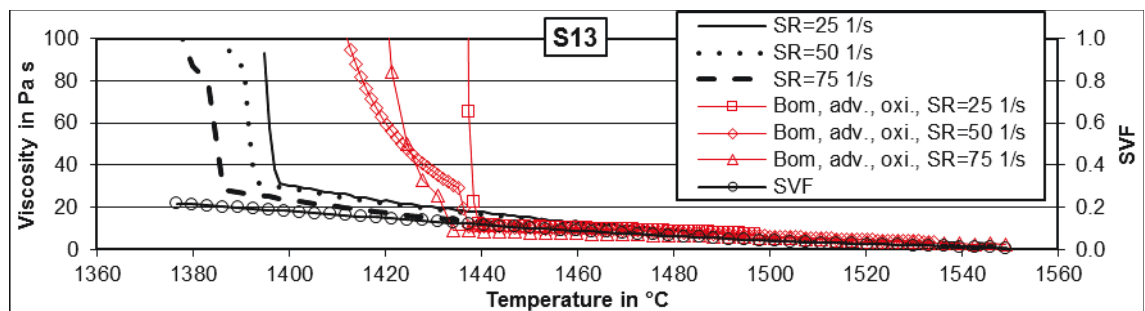


Figure 165: Slag S13, oxidizing atmospheres, advanced modelling by Bomkamp model.

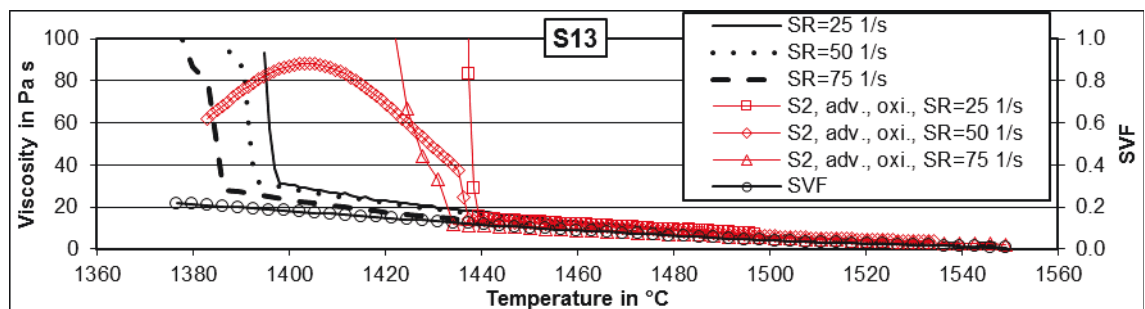


Figure 166: Slag S13, oxidizing atmospheres, advanced modelling by S2 model.

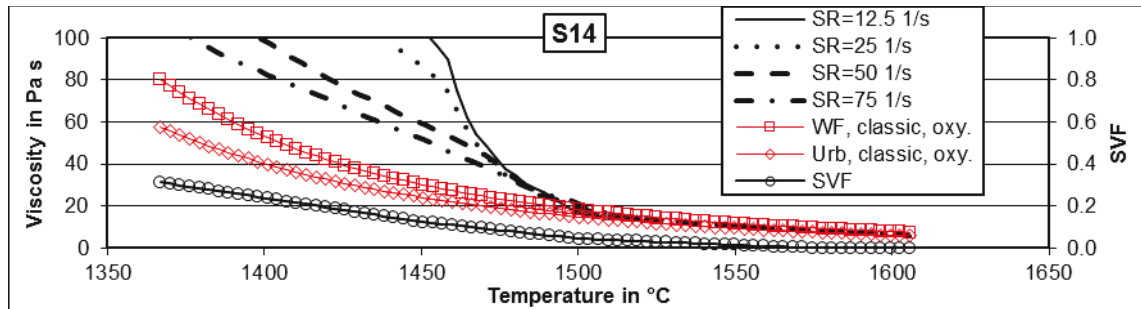


Figure 167: Slag S14, oxidizing atmospheres, classic modelling.

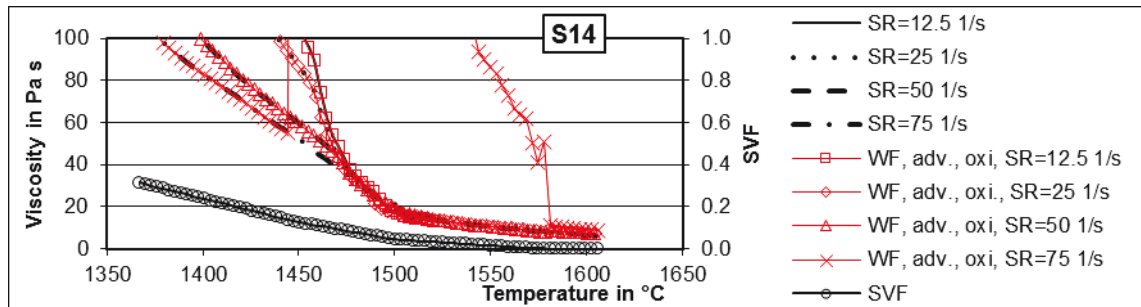


Figure 168: Slag S14, oxidizing atmospheres, advanced modelling, best classic model.

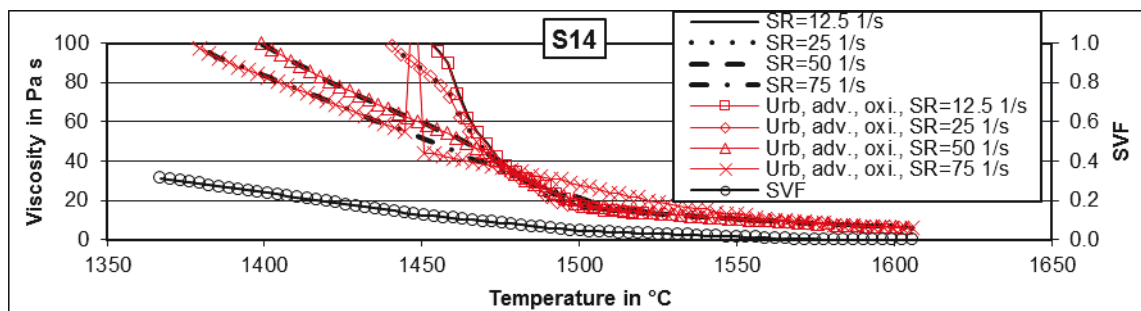


Figure 169: Slag S14, oxidizing atmospheres, advanced modelling, best advanced model.

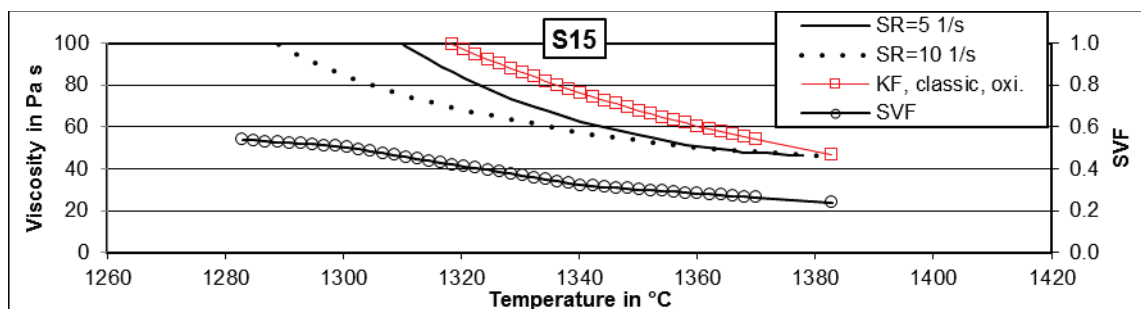


Figure 170: Slag S15, oxidizing atmospheres, classic viscosity modelling.

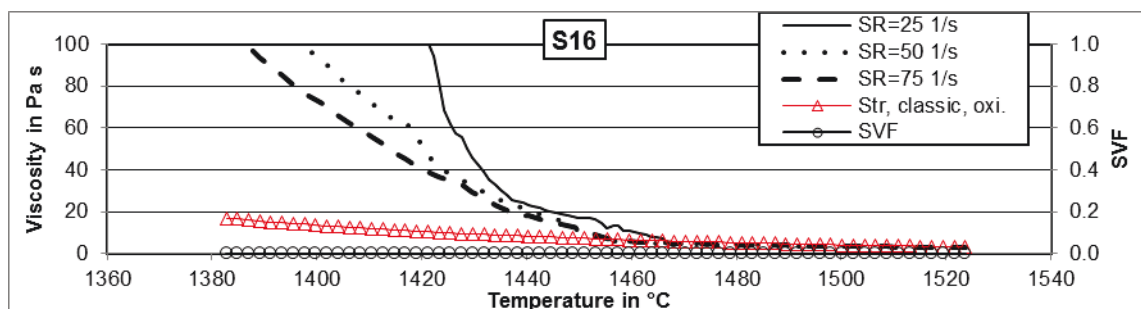


Figure 171: Slag S16, oxidizing atmosphere, classic viscosity modelling.

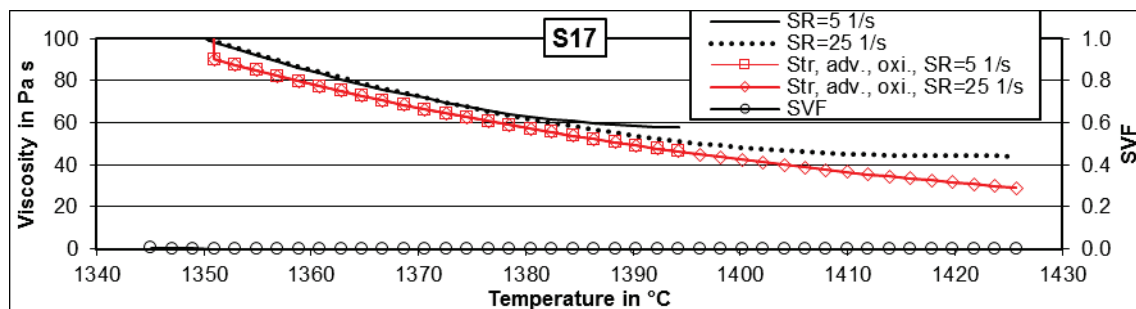


Figure 172: Slag S17, oxidizing conditions, classic and advanced modelling close to each other.

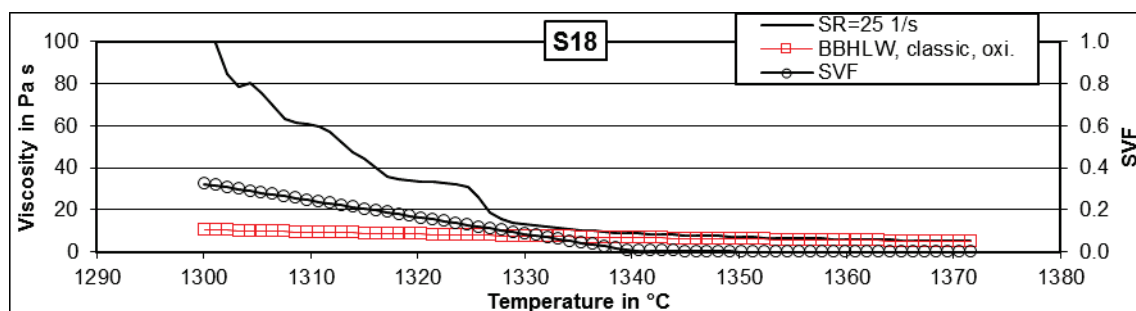


Figure 173: Slag S18, oxidizing atmospheres, classic modelling.

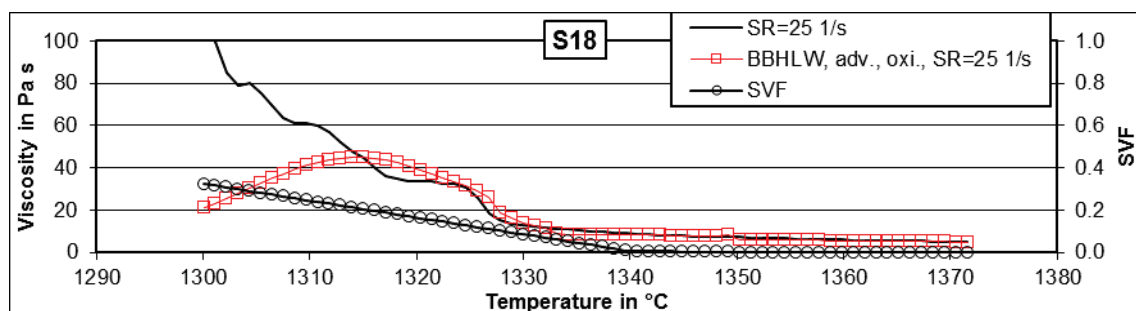


Figure 174: Slag S18, oxidizing atmosphere, advanced modelling of best classic model.

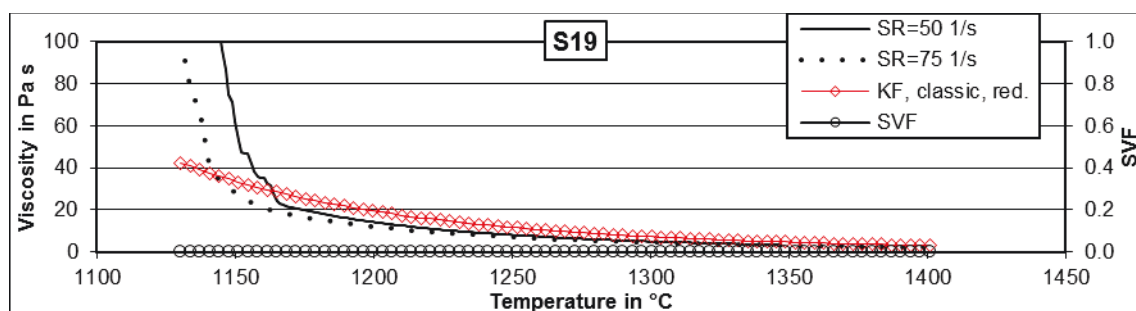


Figure 175: Slag S19, reducing atmosphere, classic modelling.

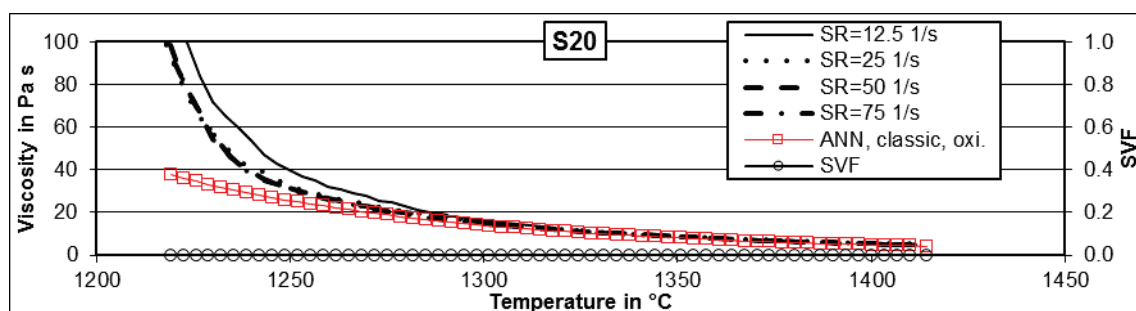


Figure 176: Slag S20, oxidizing atmosphere, classic modelling.

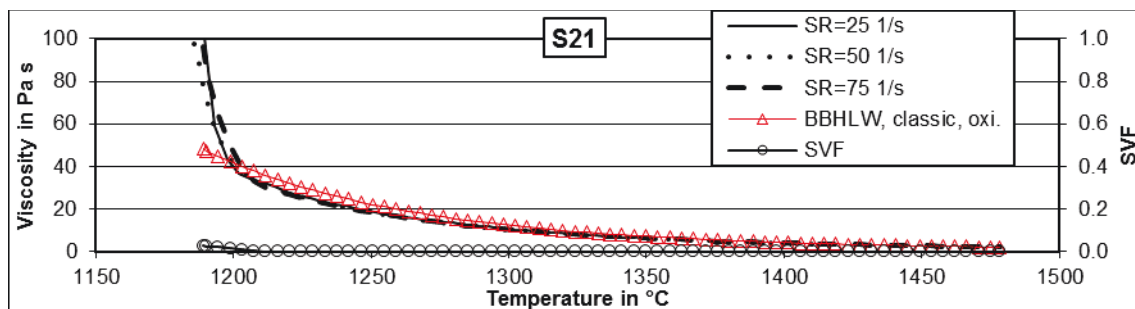


Figure 177: Slag S21, oxidizing atmosphere, classic modelling.

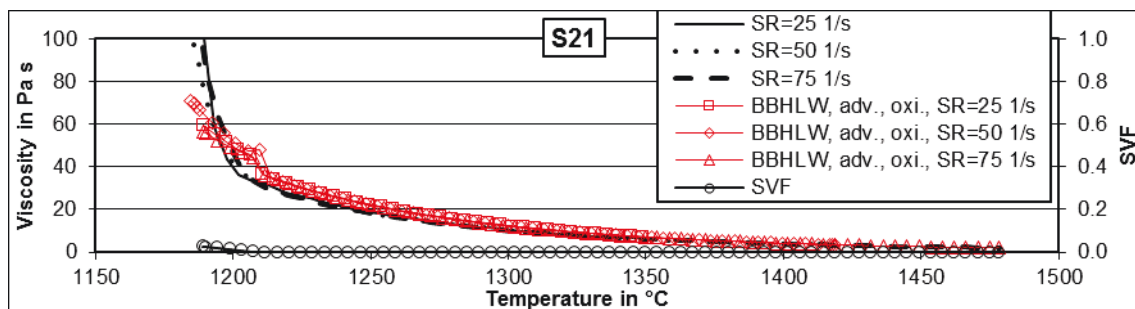


Figure 178: Slag S21, oxidizing atmosphere, advanced modelling.

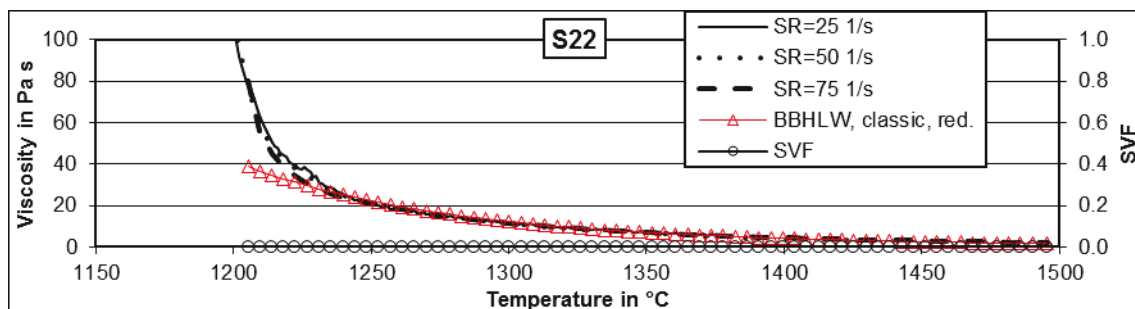


Figure 179: Slag S22, reducing atmosphere, classic modelling.

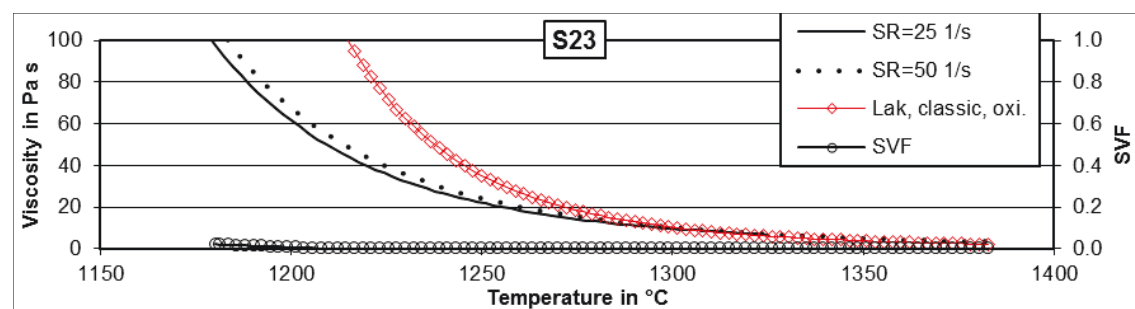


Figure 180: Slag S23, oxidizing atmosphere, classic modelling.

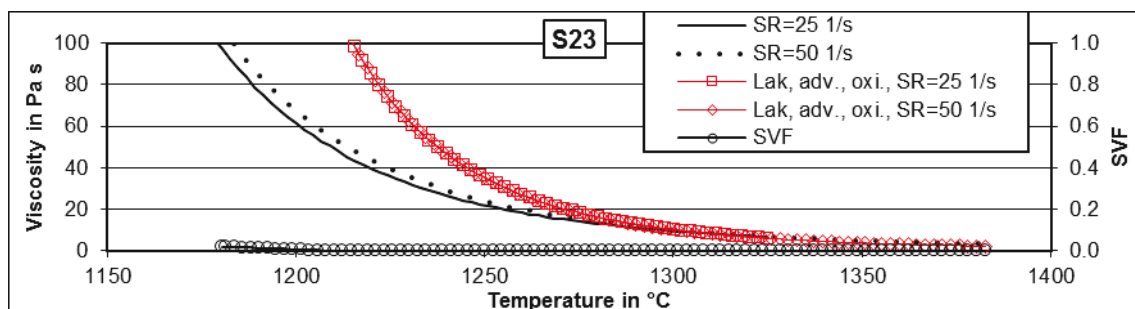


Figure 181: Slag S23, oxidizing atmosphere, advanced modelling.

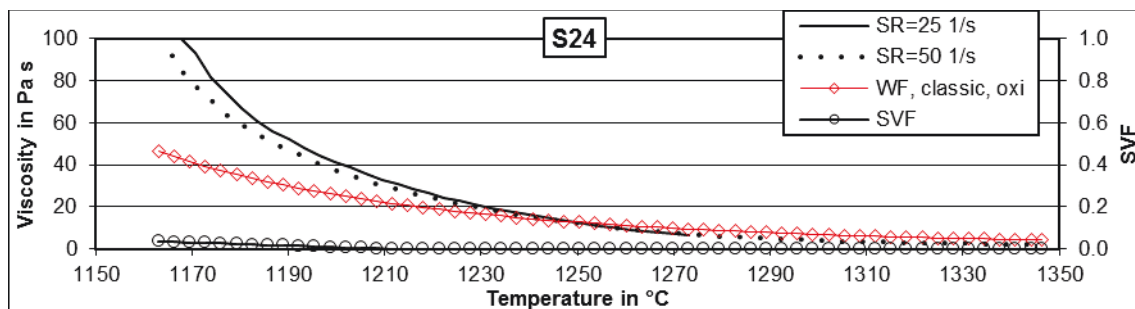


Figure 182: Slag S24, nitrogen atmospheres, oxidizing conditions assumed for classic modelling.

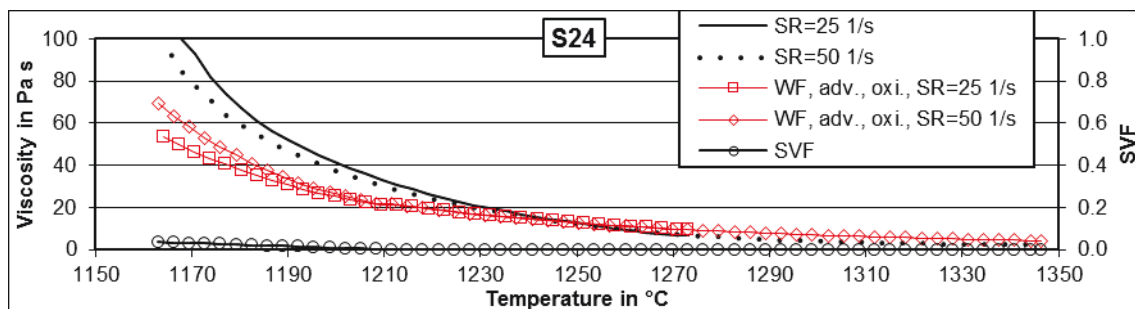


Figure 183: Slag S24, nitrogen atmospheres, oxidizing conditions assumed for advanced modelling.

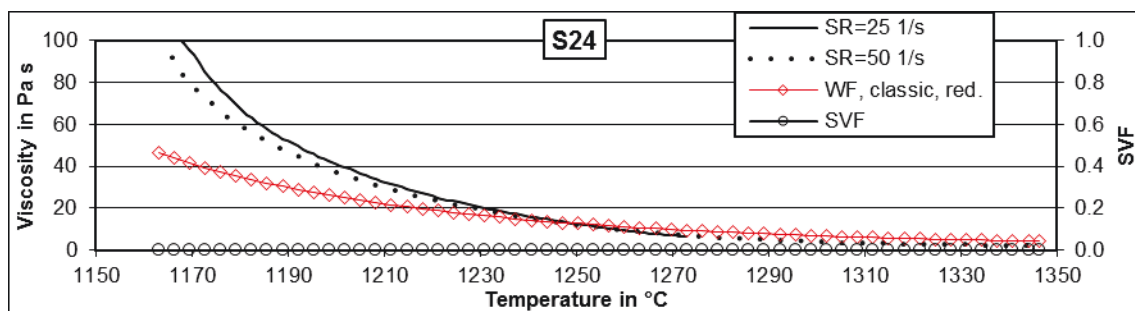


Figure 184: Slag S24, nitrogen atmospheres, reducing conditions assumed for classic modelling.

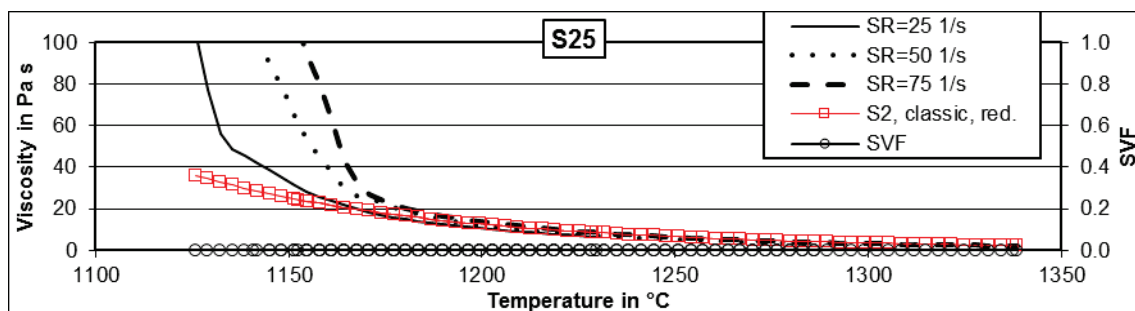


Figure 185: Slag S25, reducing conditions, classic modelling.

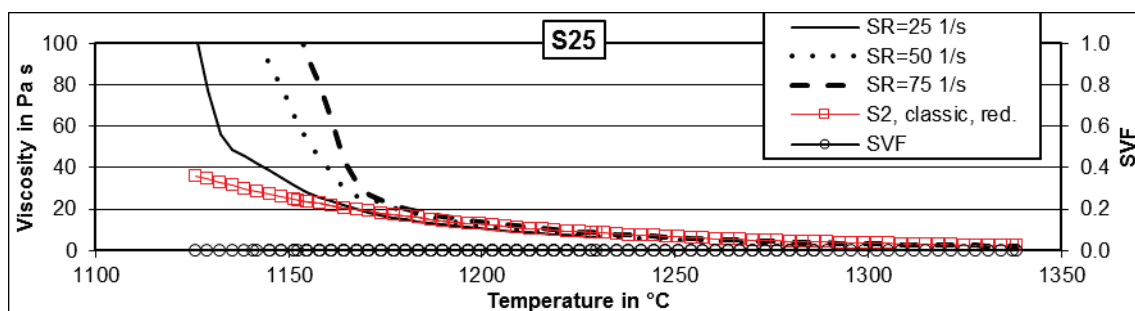


Figure 186: Slag S25, reducing conditions, advanced modelling.

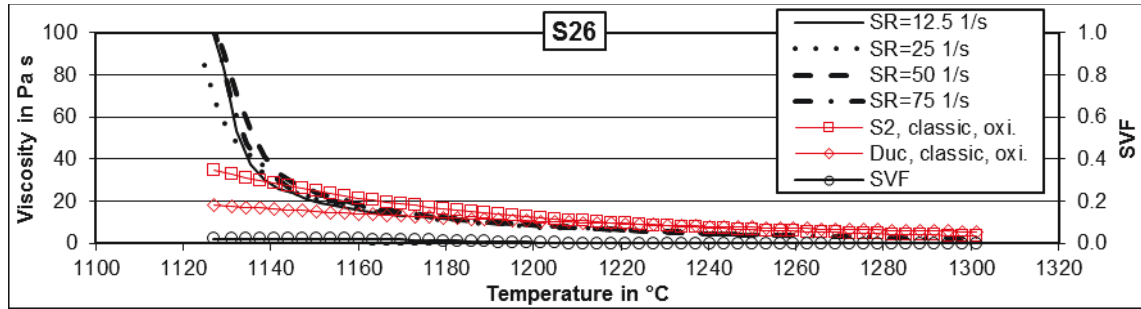


Figure 187: Slag S26, oxidizing atmosphere, classic modelling, best AALE of ≤ 25 Pa s (Duchesne) and ≤ 100 Pa s (S2).

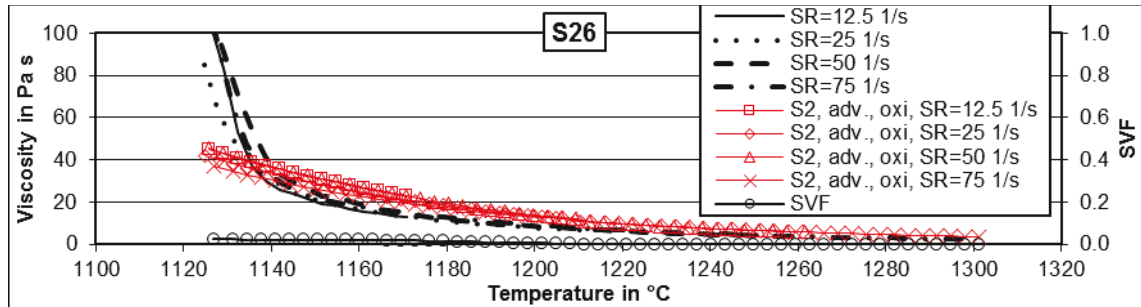


Figure 188: Slag S26, oxidizing atmosphere, advanced modelling, best AALE of ≤ 100 Pa s.

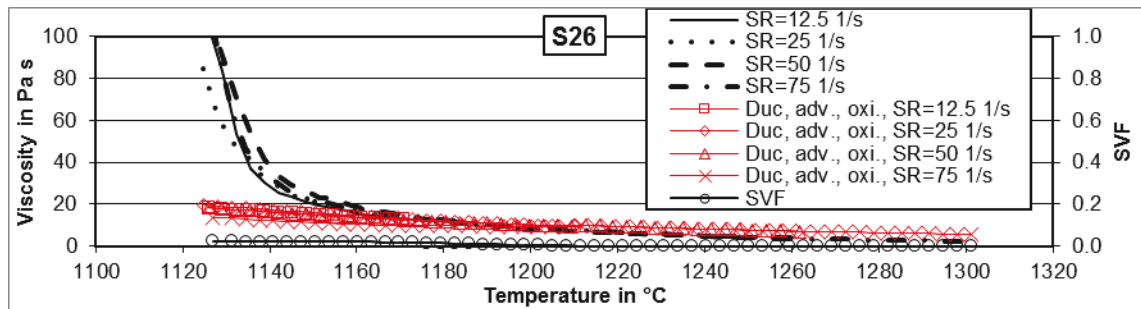


Figure 189: Slag S26, oxidizing atmosphere, advanced modelling, best AALE ≤ 25 Pa s (Duchesne).

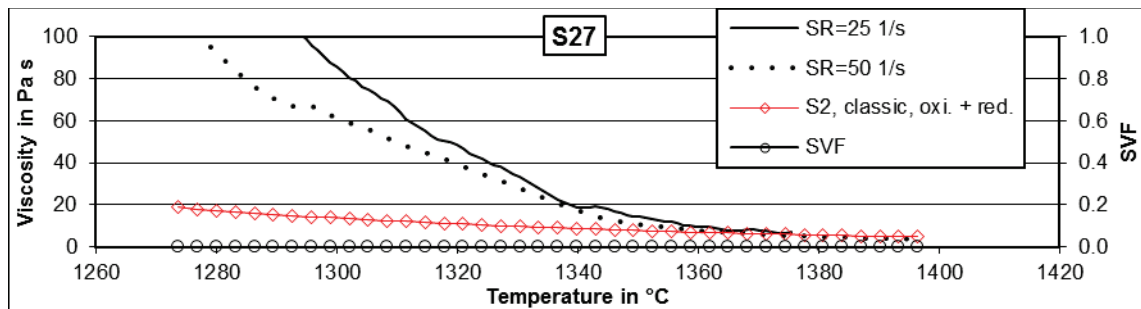


Figure 190: Slag S27, nitrogen atmosphere, classic modelling of oxidizing and reducing conditions.

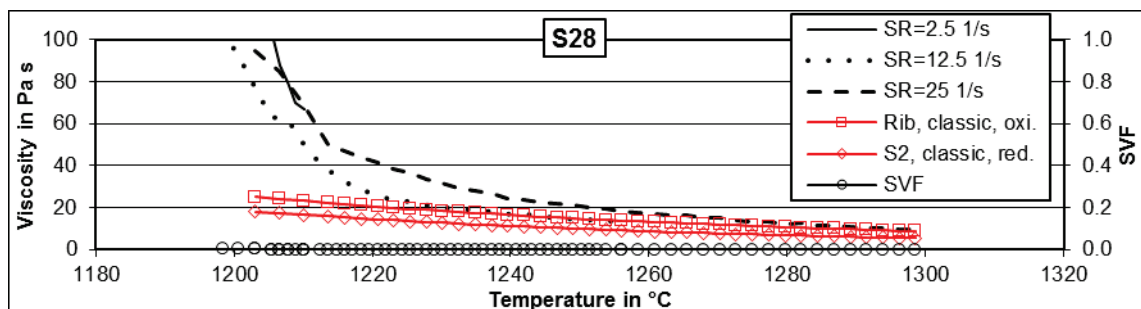


Figure 191: Slag S28, nitrogen atmosphere, classic modelling assuming oxidizing and reducing conditions.

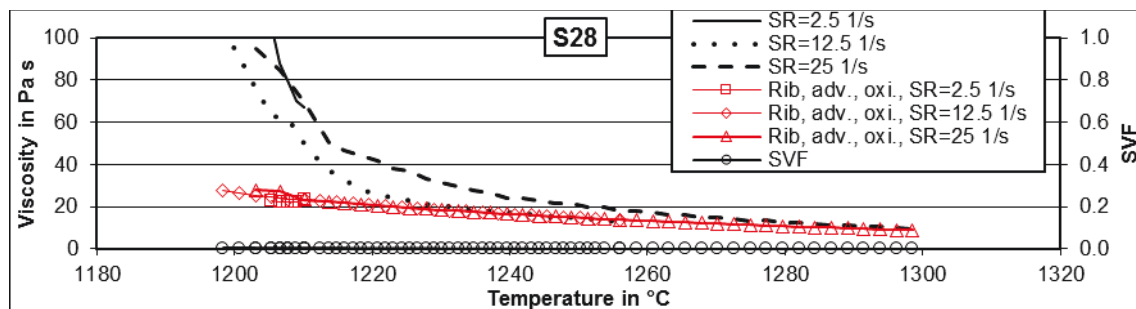


Figure 192: Slag S28, nitrogen atmosphere, advanced modelling assuming oxidizing conditions.

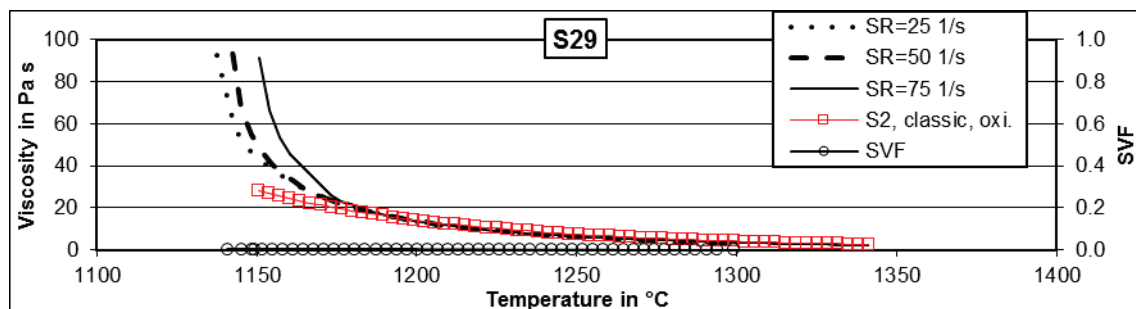


Figure 193: Slag S29, oxygen atmosphere, classic modelling.

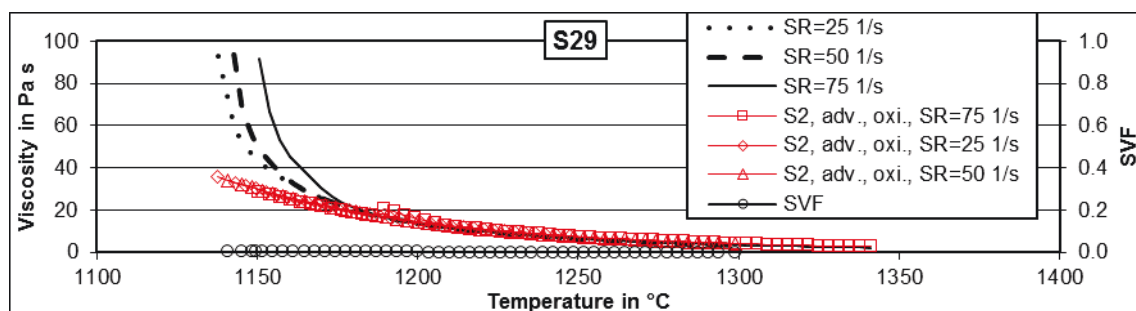


Figure 194: Slag S29, oxygen atmosphere, advanced modelling.

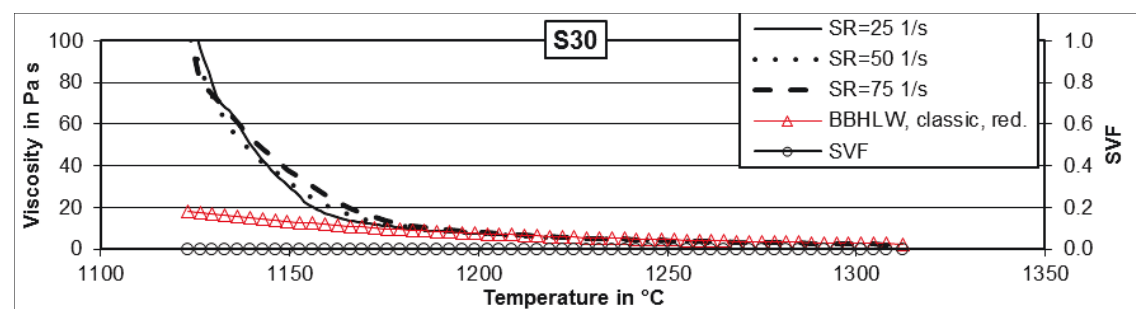


Figure 195: Slag S30, reducing atmosphere, classic modelling.

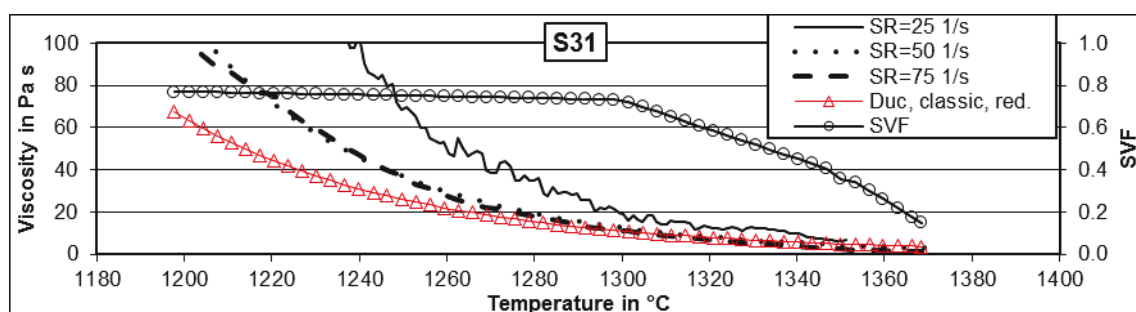


Figure 196: Slag S31, reducing atmosphere, classic modelling.

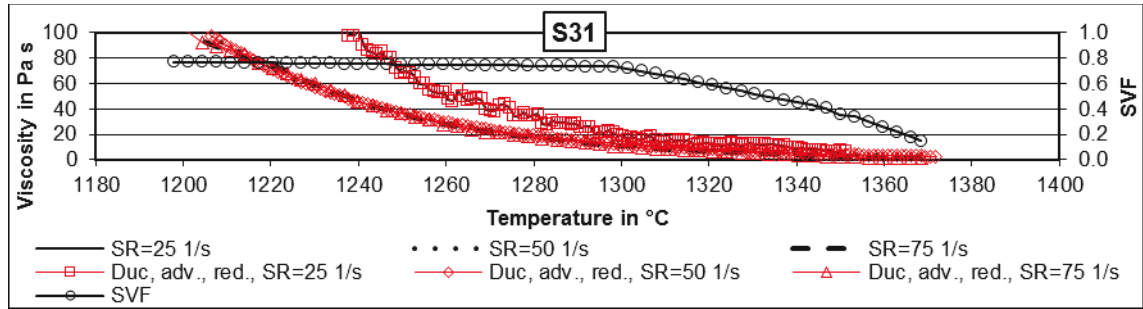


Figure 197: Slag S31, reducing atmosphere, advanced modelling.

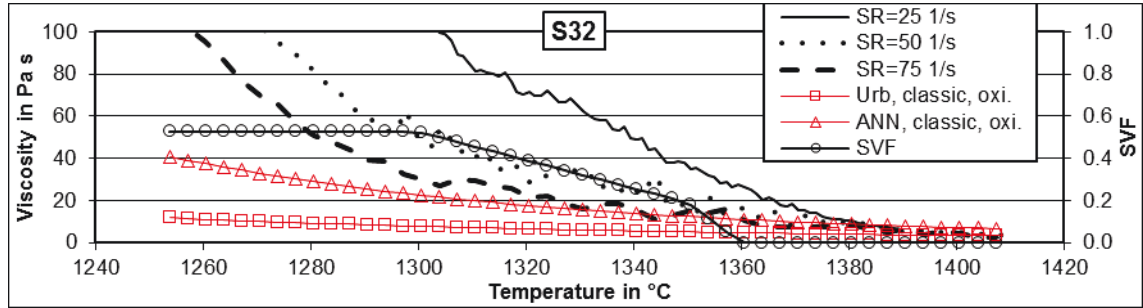


Figure 198: Slag S32, oxidizing atmosphere, classic modelling.

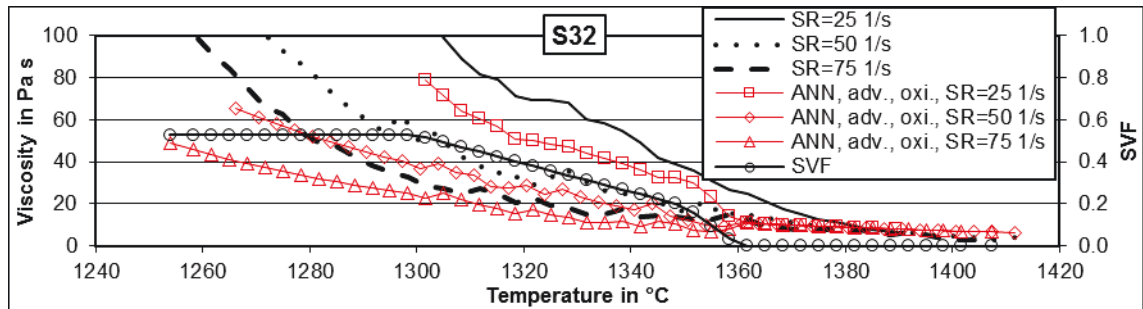


Figure 199: Slag S32, oxidizing atmosphere, advanced modelling by best classic AALE (ANNliq).

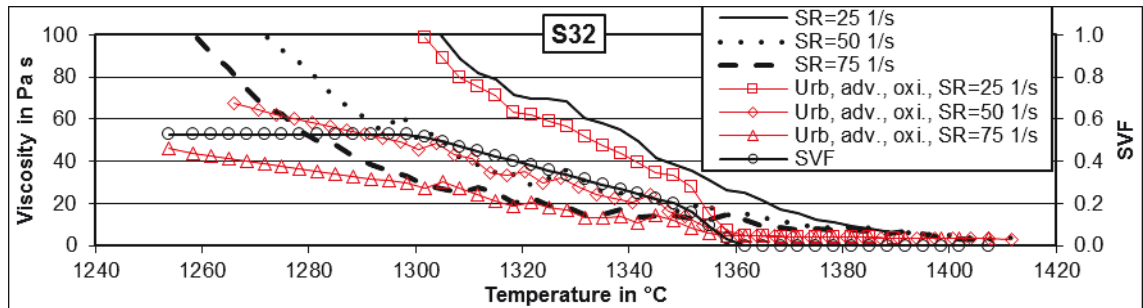


Figure 200: Slag S32, oxidizing atmosphere, advanced modelling by best fitting model (Urbain).

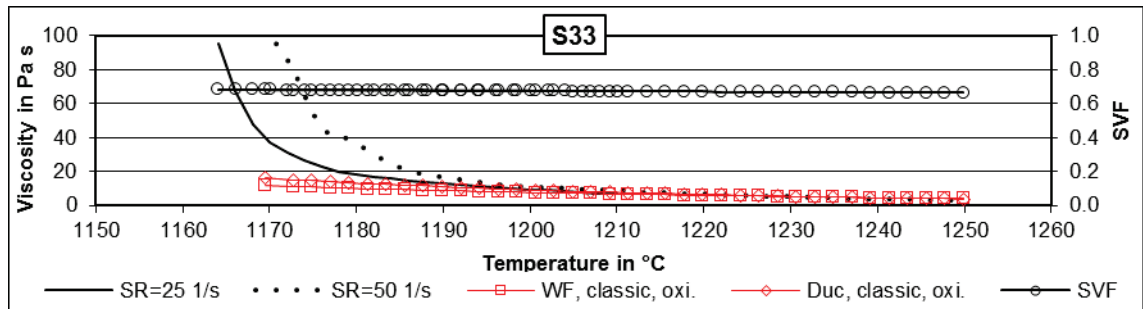
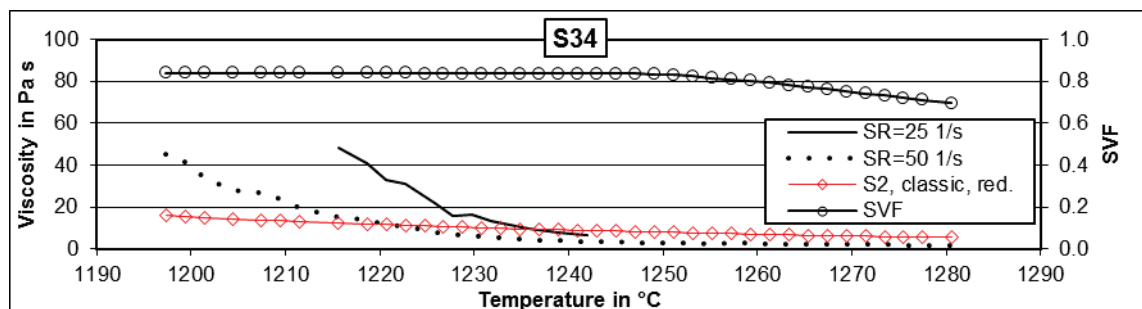
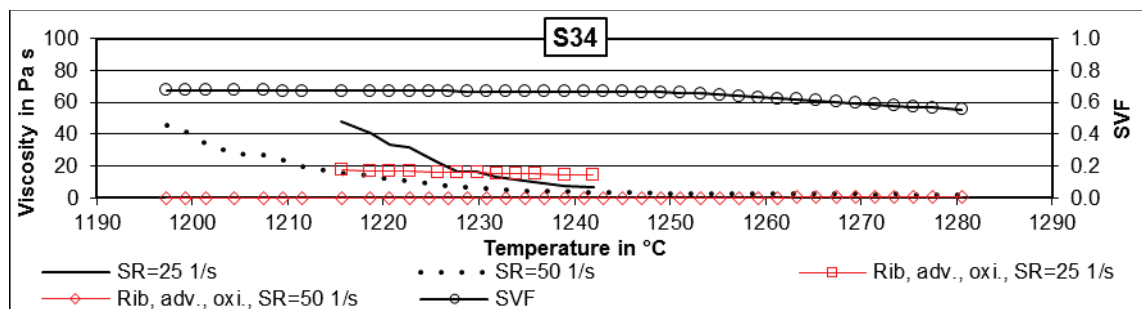
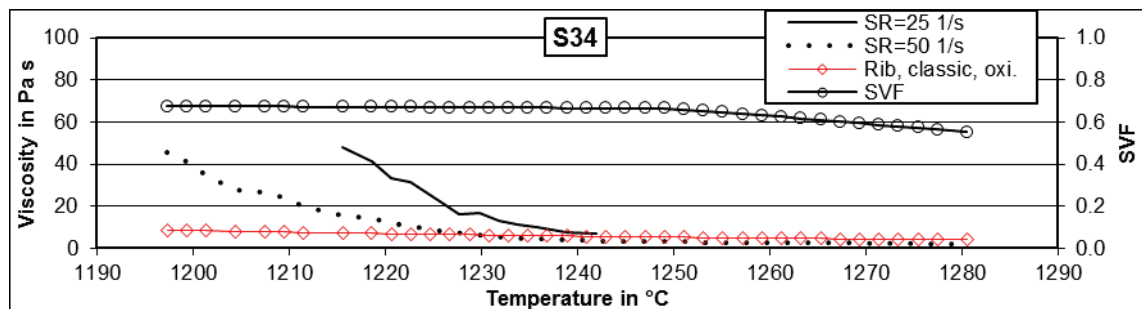
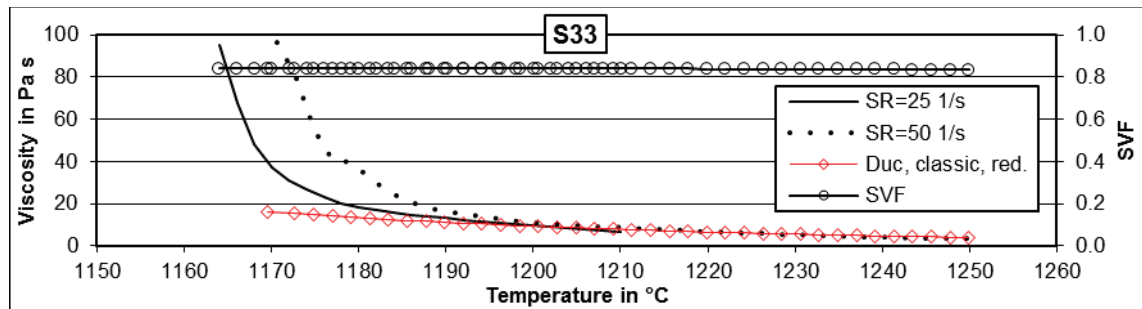
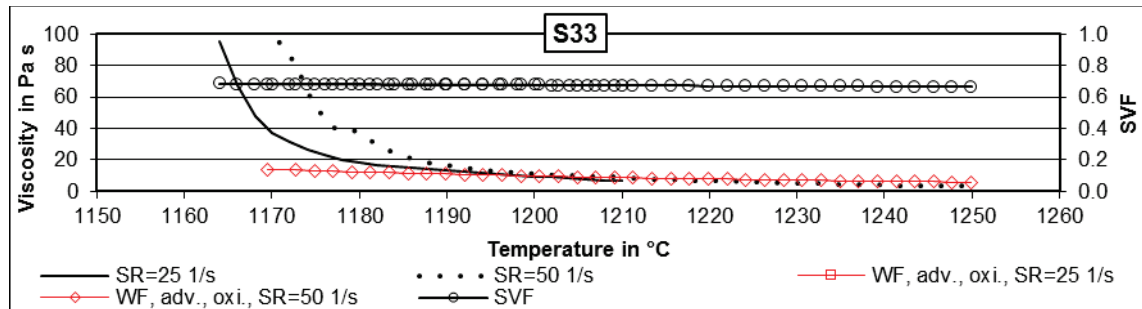


Figure 201: Slag S33, nitrogen atmosphere, classic modelling assuming oxidizing conditions, best AALE (Duchesne) and best advanced model (Watt-Fereday).



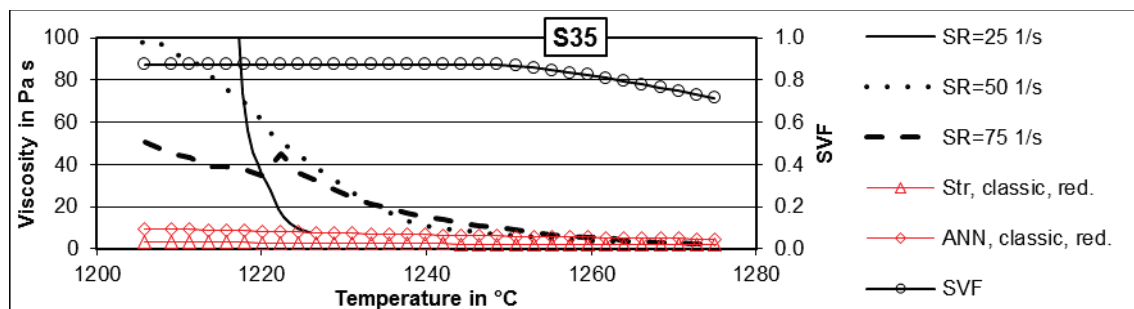


Figure 207: Slag S35, reducing atmosphere, classic modelling by best classic model (ANNliq) and best advanced model (Streeter).

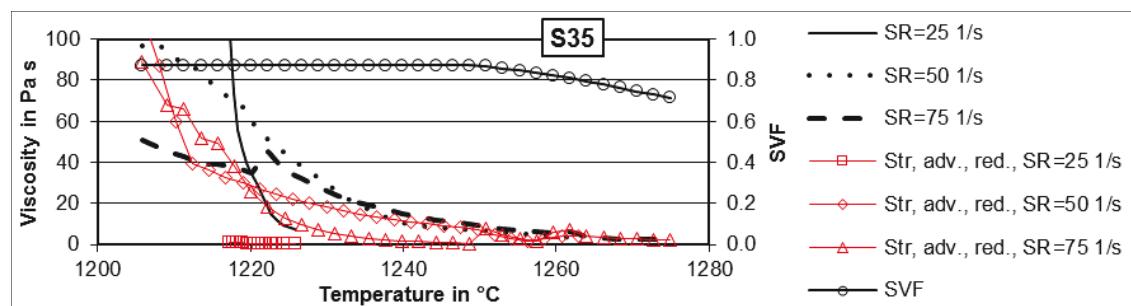


Figure 208: Slag S35, reducing atmosphere, advanced modelling by best advanced model.

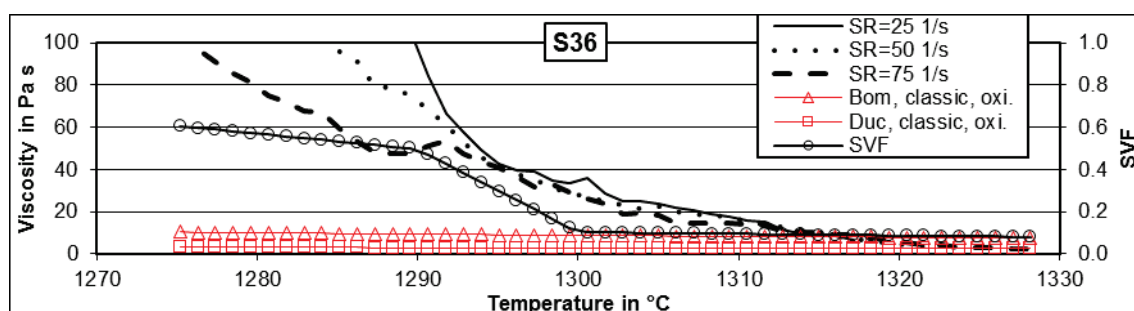


Figure 209: Slag S36, oxidizing atmosphere, classic modelling by best classic model (Bomkamp) and best advanced model (Duchesne).

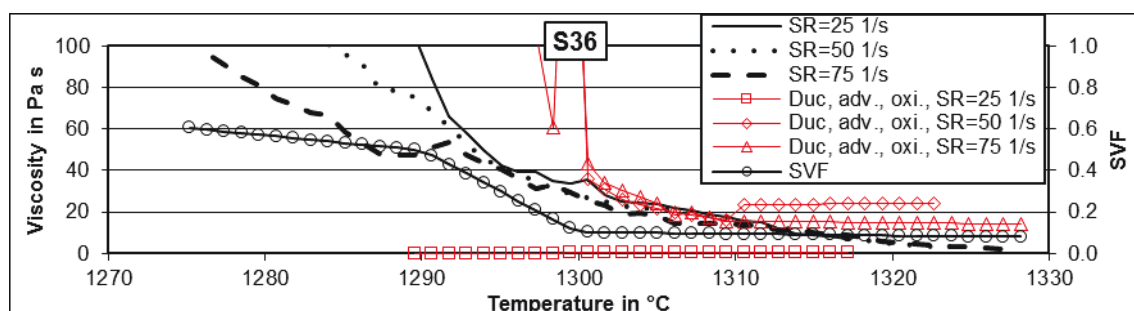


Figure 210: Slag S36, oxidizing atmosphere, advanced modelling by best advanced model.

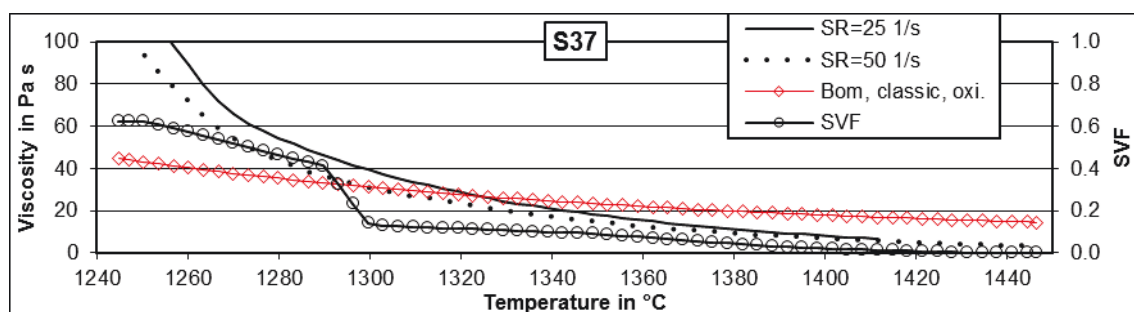


Figure 211: Slag S37, nitrogen atmosphere, classic modelling assuming oxidizing conditions.

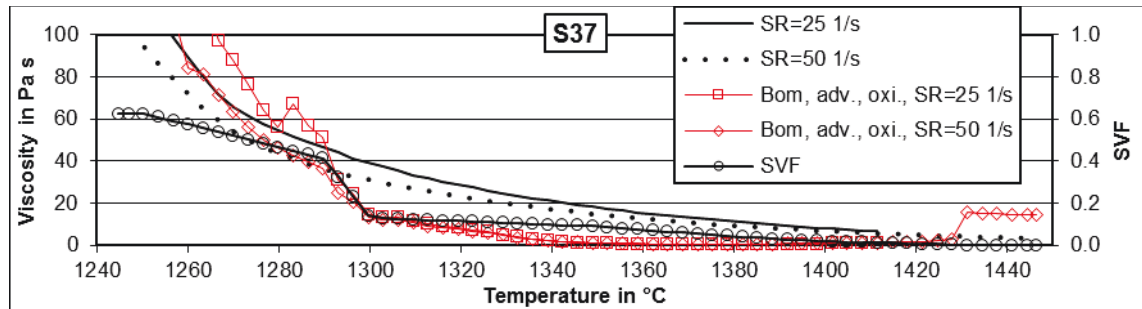


Figure 212: Slag S37, nitrogen atmosphere, advanced modelling assuming oxidizing conditions.

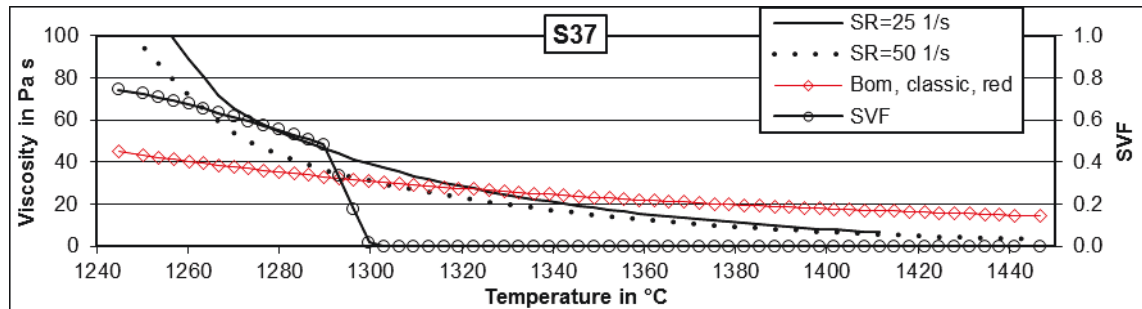


Figure 213: Slag S37, nitrogen atmosphere, classic modelling assuming reducing conditions.

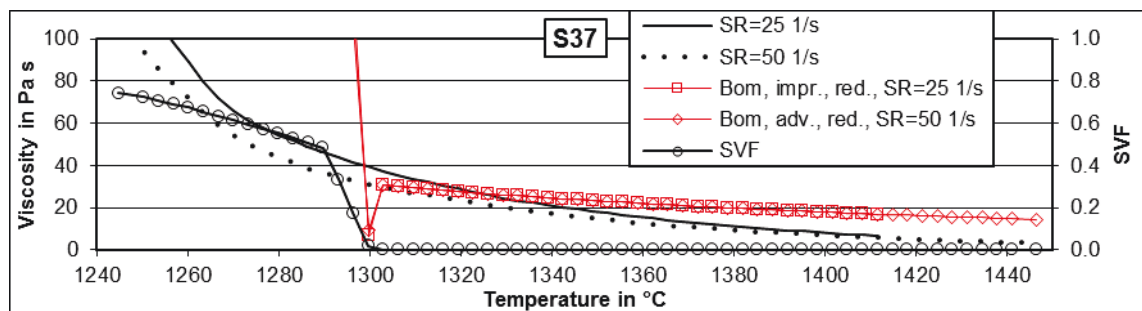
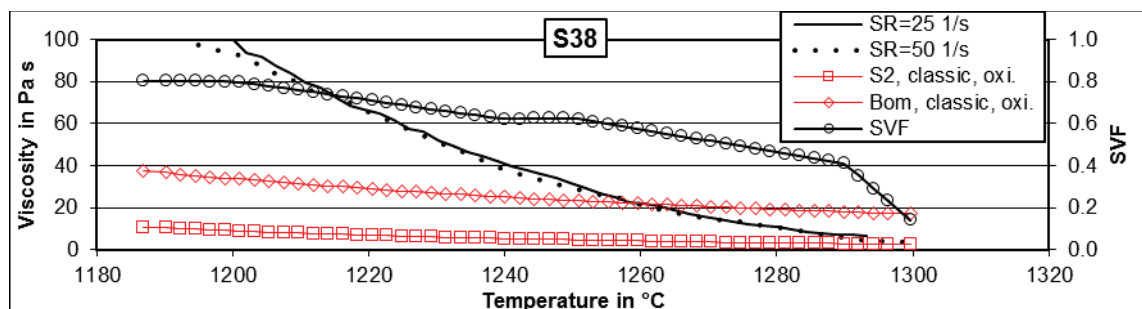
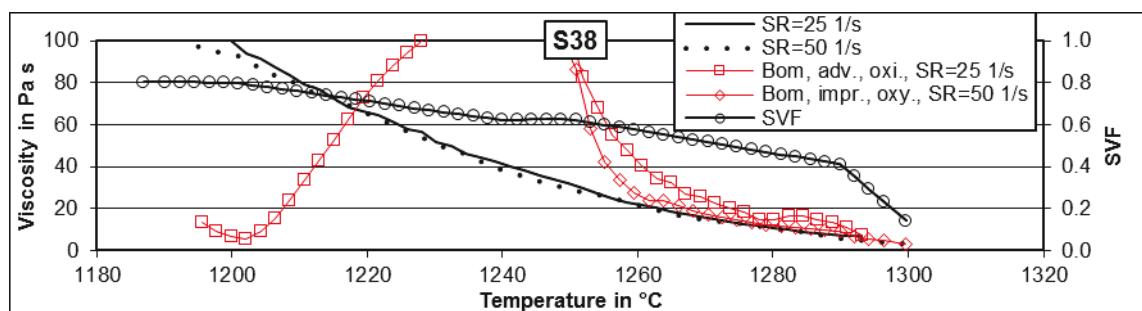


Figure 214: Slag S37, nitrogen atmosphere, advanced modelling assuming reducing conditions.

Figure 215: Slag S38, nitrogen atmosphere, classic modelling assuming oxidizing conditions, best model of AALE ≤ 25 Pa s (Bomkamp) and of AALE \leq Pa s (S2).Figure 216: Slag S38, nitrogen atmosphere, advanced modelling assuming oxidizing conditions, best model of AALE ≤ 25 Pa s.

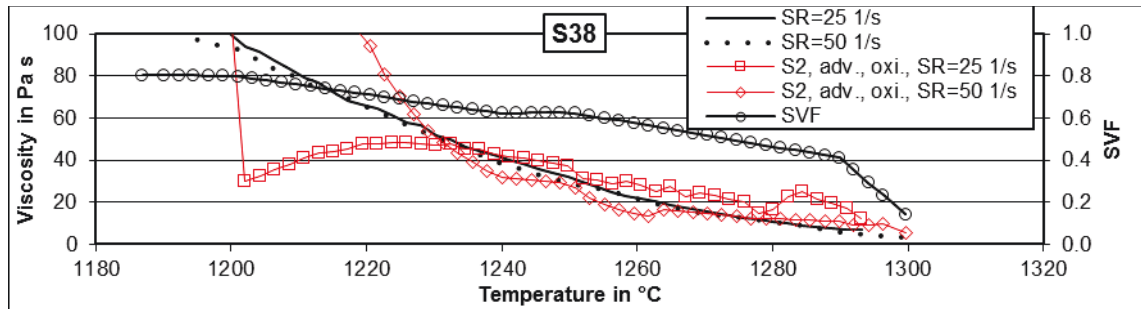


Figure 217: Slag S38, nitrogen atmosphere, advanced modelling assuming oxidizing conditions, best model of AALE ≤ 100 Pa s.

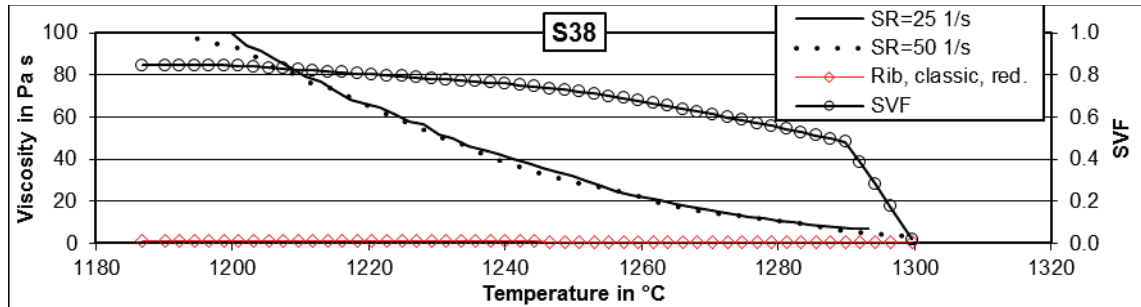


Figure 218: Slag S38, nitrogen atmosphere, classic modelling assuming reducing conditions, selected model is best for further advanced modelling.

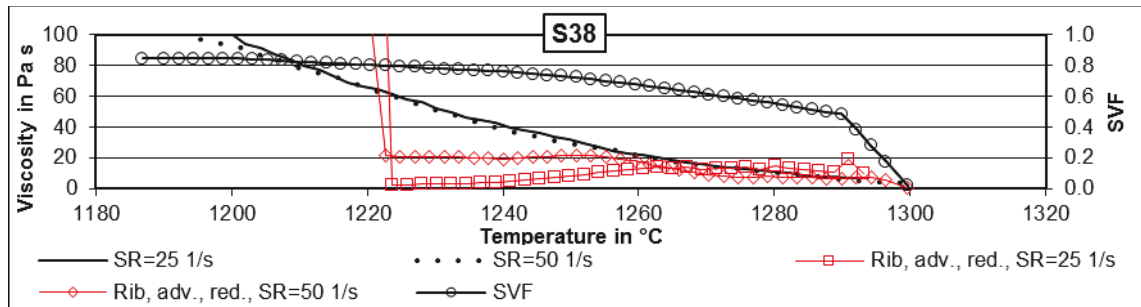


Figure 219: Slag S38, nitrogen atmosphere, advanced modelling assuming reducing conditions, selected model is best for advanced.

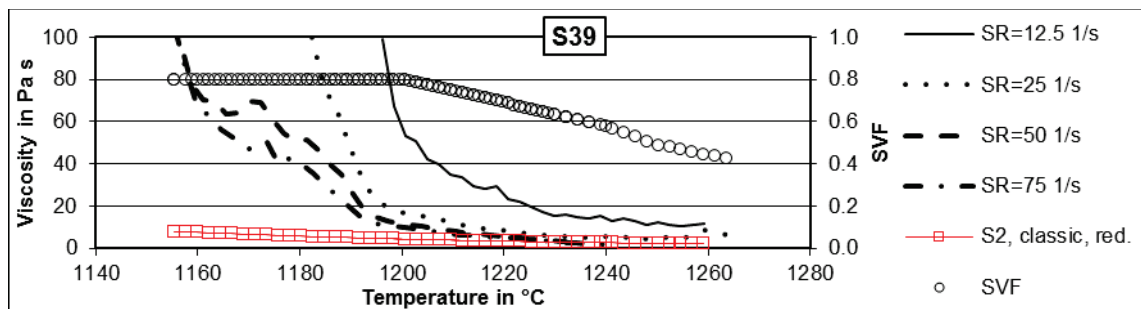


Figure 220: Slag S39, reducing atmosphere, classic modelling.

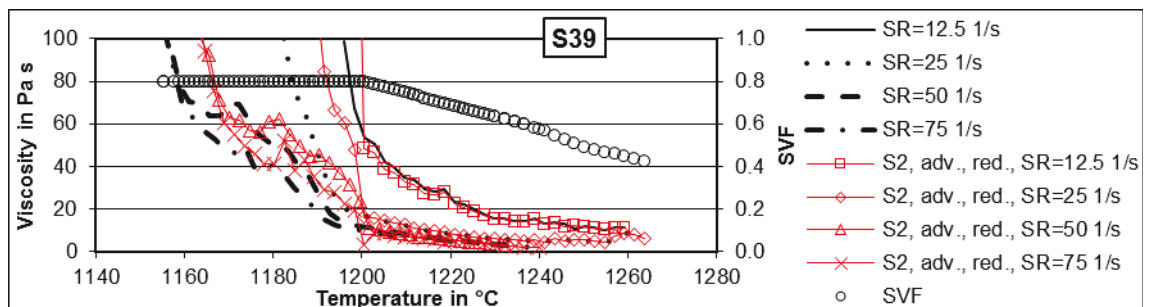


Figure 221: Slag S39, reducing atmosphere, advanced modelling.

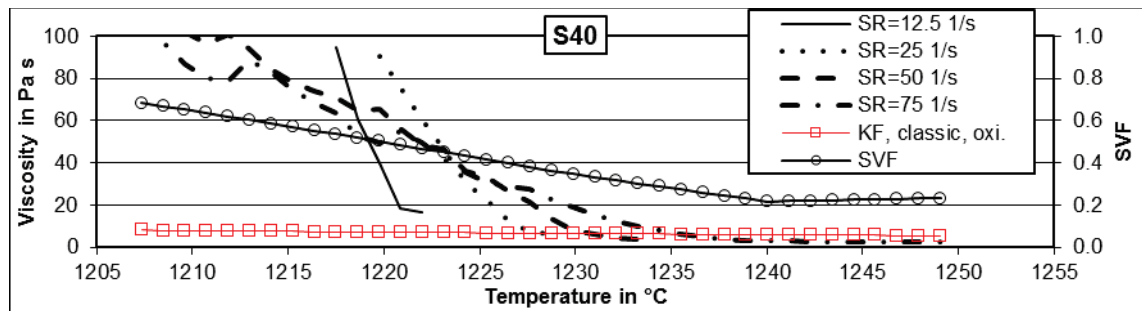


Figure 222: Slag S40, oxidizing atmosphere, classic modelling.

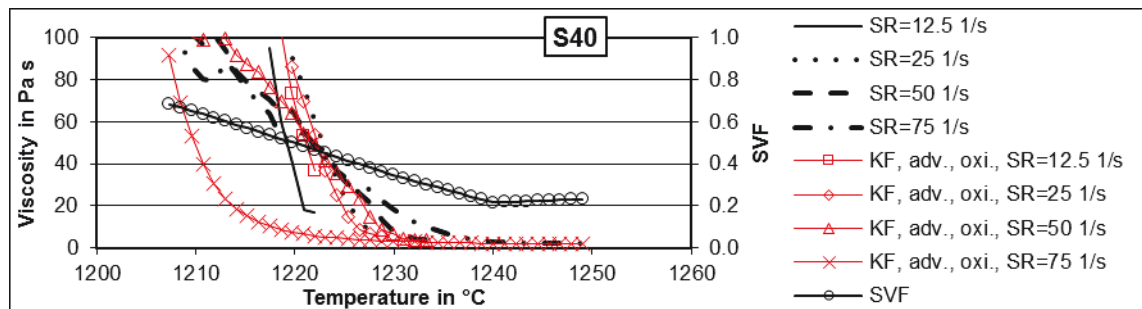


Figure 223: Slag S40, oxidizing atmosphere, advanced modelling.

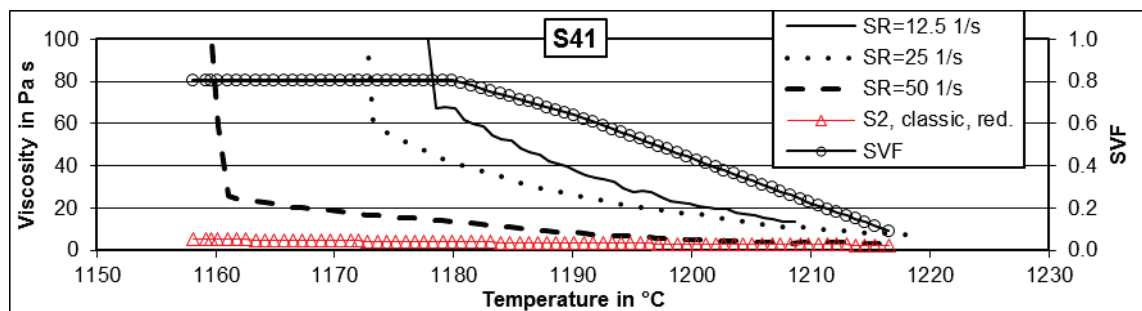


Figure 224: Slag S41, reducing atmosphere, classic modelling.

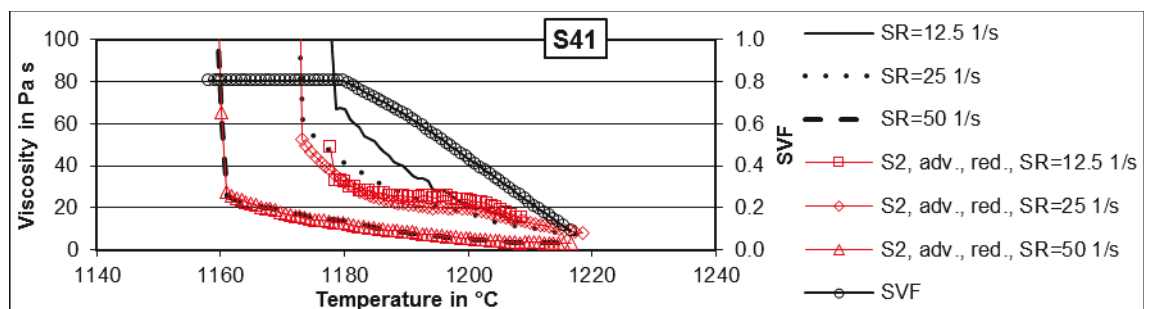


Figure 225: Slag S41, reducing atmosphere, advanced modelling.

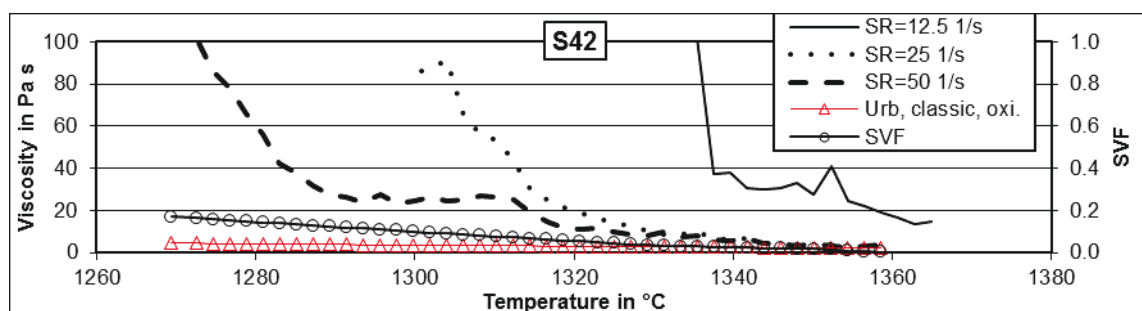


Figure 226: Slag S42, oxidizing atmosphere, classic modelling.

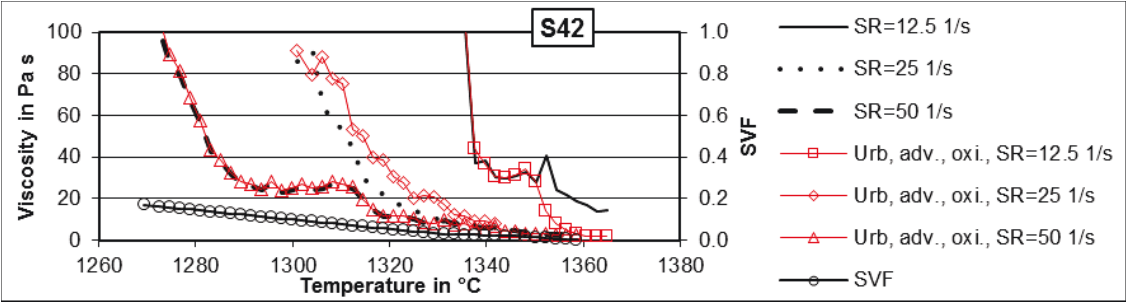


Figure 227: Slag S42, oxidizing atmosphere, advanced modelling.

References

- [1] Reid WT, Cohen P. The flow characteristics of coal-ash slags in the solidification range. *Trans. ASME* 1944;66:685–90.
- [2] Kestin J, Wakeham WA. The measurement of viscosity. *Transport properties of fluids, thermal conductivity, viscosity, and diffusion coefficient*, New York: Hemisphere 1988:73–147.
- [3] Newton I, Bernoulli D, MacLaurin C, Euler L. *Philosophiae naturalis principia mathematica*. excudit G. Brookman; impensis TT et J. Tegg, Londini; 1833.
- [4] Mezger TG. *The Rheology Handbook: For Users of Rotational and Oscillatory Rheometers*. 2nd ed. Hannover: Vincentz Network; 2006.
- [5] Ding J, Tracey P, Li W, Peng G, Whitten PG, Wallace GG. *Review on Shear Thickening Fluids and Applications*. Textiles and Light Industrial Science and Technology 2013.
- [6] Nikrityuk PA. *Computational Thermo-Fluid Dynamics: In Materials Science and Engineering*. John Wiley & Sons; 2011.
- [7] Tammann G. *Kristallisieren und Schmelzen*. Leipzig: Barth; 1903.
- [8] Tammann G. *Der Glaszustand*. Leipzig: Voss; 1933.
- [9] Tammann G. *Die Aggregatzustände*. 2nd ed. Leipzig: Voss; 1923.
- [10] Vogel W. *Glaschemie*. 3rd ed. Berlin: Springer; 1992.
- [11] Goldschmidt VM (ed.). *Geochemische Verteilungsgesetze der Elemente*. Oslo: Skrifter Norske Videnskaps Akademi; 1926.
- [12] Zachariasen WH. The atomic arrangement in glass. *J. Am. Chem. Soc* 1932;54(10):3841–51.
- [13] Warren B. E. X-Ray Diffraction of Vitreous Silica: *Zeitschrift für Kristallographie - Crystalline Materials* 1933;86(1):349.
- [14] Brill R, Hermann C, Peters C. Röntgenographische Fouriersynthese von Quarz. *Ann. Phys* 1942;433(3):233–44.
- [15] Poggemann J-F, Goß A, Heide G, Rädlein E, Frischat GH. Direct view of the structure of a silica glass fracture surface. *Journal of Non-Crystalline Solids* 2001;281(1–3):221–6.
- [16] Rao KJ. *Structural Chemistry of Glasses*. Kidlington, UK: Elsevier Science Ltd; 2002.
- [17] Sun K-H. Fundamental conditions of glass formations. *Journal of the American Ceramic Society* 1947;30(9):277–81.
- [18] Dietzel A. Die Kationenfeldstärken und ihre Beziehungen zu Entglasungsvorgängen, zur Verbindungsbildung und zu den Schmelzpunkten von Silicaten. *Zeitschrift für Elektrochemie und angewandte physikalische Chemie* 1942;48(1):9–23.
- [19] Lebedew AA. *Trudy Cossud. Opt. Inst* 1921;2:57.
- [20] Randall J. T, Rooksby H. P, Cooper B. S. 13. X-ray Diffraction and the Structure of Vitreous Solids — I: *Zeitschrift für Kristallographie - Crystalline Materials*;75:196; 2015. doi:10.1515/zkri-1930-0114; Available from:

- [//www.degruyter.com/view/j/zkri.1930.75.issue-1/zkri-1930-0114/zkri-1930-0114.xml](http://www.degruyter.com/view/j/zkri.1930.75.issue-1/zkri-1930-0114/zkri-1930-0114.xml).
- [21] Valenkov N, Poray-Koshitz E. X-ray Investigation of the Glassy State: *Zeitschrift für Kristallographie - Crystalline Materials*;95:195; 2015.
doi:10.1524/zkri.1936.95.1.195;
- [22] BERNAL JD. A Geometrical approach to the structure of liquids. *Nature* 1959;183(4655):141–7.
- [23] Smekal A. Über die Natur der glasbildenden Stoffe. *Glastechn. Ber* 1949;22:278–89.
- [24] Weyl WA. Atomistic interpretation of the melting of simple compounds. *J. Phys. Chem* 1955;59(2):147–51.
- [25] Weyl WA. *Silicates Ind.* 1959(24).
- [26] Stevels JM. *Progress in the theory of the physical properties of glass.* Elsevier Publishing Company; 1948.
- [27] Stevels JM. New light on the structure of glass. *Philips Technical Review* 1960;22:300–11.
- [28] Stevels JM. Networks in glass and other polymers. *Glass Ind* 1954;35:657–62.
- [29] Stevels JM. The Glass considered as a polymer. *Glass Ind* 1954;35(2):69–72.
- [30] Trapp HJ, Stevels JM. Physical properties of invert glasses. *Glastech Ber* 1959;32:32–52.
- [31] Huggins ML. The structure of glasses. *Journal of the American Ceramic Society* 1955;38(5):172–5.
- [32] Tilton LW. Noncrystal ionic model for silica glass. *Journal of Research of the National Bureau of Standards* 1957;59(2):193.
- [33] Mills KC, Hayashi M, Wang L, Watanabe T. Chapter 2.2 - The structure and properties of silicate slags. In: Seetharaman S, editor. *Treatise on Process Metallurgy*. Boston: Elsevier; 2014, p. 149–286.
- [34] Verein Deutscher Eisenhüttenleute (Allibert M, Gaye H, Janke D, Keene BJ, Kirner D et al. *Slag Atlas*. 2nd ed. Düsseldorf: Verlag Stahleisen GmbH; 1995.
- [35] Vargas S, Frandsen FJ, Dam-Johansen K. Rheological properties of high-temperature melts of coal ashes and other silicates. *Prog. Energy Combust. Sci.* 2001;27(3):237–429.
- [36] Scholze H. *Glas: Natur, Struktur und Eigenschaften*. Dritte, neubearbeitete Auflage. 3rd ed. Berlin, Heidelberg: Springer Berlin / Heidelberg; 1988.
- [37] Higman C, van der Burgt M. Gasification Processes. In: *Gasification (Second Edition)*. Burlington: Gulf Professional Publishing; 2008, p. 91–191.
- [38] Blum L. The composition of blast furnace slag (Zur Zusammensetzung der Hochofenschlacke). With analysis of various slags, and a discussion of the conditions of their formation, 2000 w. *Stahl und Eisen* 1901.
- [39] Lee YS, Min DJ, Jung SM, Yi SH. Influence of basicity and FeO content on viscosity of blast furnace type slags containing FeO. *ISIJ International* 2004;44(8):1283–90.
- [40] Winkler TB, Chipman J. An equilibrium study of the distribution of phosphorus between liquid iron and basic slags. *Trans. AIME* 1946;167:111–33.

- [41] Quon DHH, Wang SSB, Chen TT. Viscosity measurements of slags from Western Canadian coals. *Journal of Engineering for Gas Turbines and Power* 1985;107(3):803–6.
- [42] Nowok JW, Hurley JP, Stanley DC. Local structure of lignitic coal ash slag and its effect on viscosity. *Energy & Fuels* 1993;7:1135–40.
- [43] Folkedahl BC, Schobert HH. Effects of atmosphere on viscosity of selected Bituminous and Low-Rank Coal Ash Slags. *Energy & Fuels* 2005;19(1):208–15.
- [44] Roberts DG, Ilyushechkin AY, Harris DJ. Linking laboratory data with pilot scale entrained flow coal gasification performance. Part 1: Laboratory characterisation. *Fuel Process Technol* 2012;94(1):86–93.
- [45] Bottinga Y, Weill DF. The viscosity of magmatic silicate liquids; a model calculation. *Am J Sci* 1972;272(5):438–75.
- [46] Vogel W. *Chemistry of Glass*. Columbus, OH; 1985.
- [47] Lee SK, Stebbins JF. The degree of aluminum avoidance in aluminosilicate glasses. *Am. Mineral* 1999;84(5-6):937–45.
- [48] Henderson GS. The structure of silicate melts: A glass perspective. *The Canadian Mineralogist* 2005;43(6):1921–58.
- [49] Mysen BO, Virgo D, Scarfe CM, Cronin DJ. Viscosity and structure of iron- and aluminum-bearing calcium silicate melts at 1 atm. *American Mineralogist* 1985;70:487–98.
- [50] Riebling EF. Structure of Sodium Aluminosilicate Melts Containing at Least 50 mole % SiO₂ at 1500°C. *The Journal of Chemical Physics* 1966;44(8):2857–65.
- [51] Toplis MJ, Dingwell DB, Hess KU, Lenci T. Viscosity, fragility, and configurational entropy of melts along the join SiO₂-NaAlSiO₄. *American Mineralogist* 1997;82(9-10):979–90.
- [52] Urbain G, Bottinga Y, Richet P. Viscosity of liquid silica, silicates and aluminosilicates. *Geochimica et Cosmochimica Acta* 1982;46(6):1061–72.
- [53] Machin JS, Hanna DL. Viscosity studies of system CaO-MgO-Al₂O₃-SiO₂: I, 40% SiO₂*. *Journal of the American Ceramic Society* 1945;28(11):310–6.
- [54] Machin JS, Yee TB. Viscosity studies of system CaO-MgO-Al₂O₃-SiO₂: II, CaO-Al₂O₃-SiO₂*. *Journal of the American Ceramic Society* 1948;31(7):200–4.
- [55] Ohno A, Ross HU. Optimum Slag Composition for the blast-furnace smelting of Titaniferous Ores. *Canadian Metallurgical Quarterly* 1963;2:259–79.
- [56] Bockris JOLDC. Viscosity and the Structure of Molten Silicates. *Proceedings of the Royal Society of London. Series A. Mathematical and Physical Sciences* 1954;226(1167):423–35.
- [57] Shankar A, Görnerup M, Lahiri AK, Seetharaman S. Experimental investigation of the viscosities in CaO-SiO₂-MgO-Al₂O₃ and CaO-SiO₂-MgO-Al₂O₃-TiO₂ slags. *Metall and Materi Trans B* 2007;38(6):911–5.
- [58] Dingwell DB, Virgo D. The effect of oxidation state on the viscosity of melts in the system Na₂O-FeO-Fe₂O₃-SiO₂. *Geochimica et Cosmochimica Acta* 1987;51(2):195–205.
- [59] Nowok JW. Viscosity and structural state of iron in coal ash slags under gasification conditions. *Energy & Fuels* 1995;9:534–9.

- [60] Seki K, Oeters F. Viscosity measurements on liquid slags in the system CaO-FeO-Fe₂O₃-SiO₂. Transactions of the Iron and Steel Institute of Japan 1984;24(6):445–54.
- [61] Hurst HJ, Novak F, Patterson JH. Viscosity measurements and empirical predictions for some model gasifier slags. Fuel 1999;78(4):439–44.
- [62] Hurst HJ, Novak F, Patterson JH. Viscosity measurements and empirical predictions for fluxed Australian bituminous coal ashes. Fuel 1999;78(15):1831–40.
- [63] Hurst HJ, Patterson JH, Quintanar A. Viscosity measurements and empirical predictions for some model gasifier slags – II. Fuel 2000;79(14):1797–9.
- [64] Song W, Tang L, Zhu X, Wu Y, Rong Y, Zhu Z et al. Fusibility and flow properties of coal ash and slag. Fuel 2009;88(2):297–304.
- [65] Nowok JW, Benson SA, Steadman EN, Brekke DW. The effect of surface tension/viscosity ratio of melts on the sintering propensity of amorphous coal ash slags. Fuel 1993;72(7):1055–61.
- [66] Ammar MM, Gharib S, Halawa MM, El Badry K, Ghoneim NA, El Batal HA. Thermal conductivity of some silicate glasses in relation to composition and structure. Journal of Non-Crystalline Solids 1982;53(1–2):165–72.
- [67] Bodnar L, Cempta S, Tomasek K, Bobok L. Chem. Zvesti 1978;32:798–809.
- [68] Lakatos T, Johansson L, Simmingsköld B. Viscosity temperature relations in the glass system SiO₂-Al₂O₃-Na₂O-K₂O-CaO-MgO in the composition range of technical glasses. Glass Technology - European Journal of Glass Science and Technology 1972;13(3):88–95.
- [69] Bockris J. Viscous flow in silica and binary liquid silicates. Transactions of the Faraday Society 1955;51:1734–48.
- [70] Saito N, Hori N, Nakashima K, Mori K. Viscosity of Blast Furnace Type Slags. Metallurgical and Materials Transactions B: Process Metallurgy and Materials Processing Science 2003;34(5):509–16.
- [71] Dingwell DB. Shear viscosities of ferrosilicate liquids. American Mineralogist 1989;74(9-10):1038–44.
- [72] Stein DJ, Spera FJ. Experimental rheometry of melts and supercooled liquids in the system NaAlSiO₄-SiO₂: implications for structure and dynamics. American Mineralogist 1993;78(7-8):710–23.
- [73] Liska M, Klyuev VP, Antalík J, Stubna I. Physics and Chemistry of Glasses 1997;128:6–10.
- [74] Illig H-J. ABC Glas. 1st ed. Leipzig: VEB Deutscher Verlag für Grundstoffindustrie; 1983.
- [75] Kozakevitch P, Repetylo O, Thibault J. Revue de Métallurgie 1965(625):291–8.
- [76] Callis CF, van Wazer JR, Metcalf JS. Structure and Properties of the Condensed Phosphates. IX. Viscosity of Molten Sodium Phosphates. J. Am. Chem. Soc 1955;77(6):1471–3.
- [77] Kutchko BG, Kim AG. Fly ash characterization by SEM-EDS. Fuel 2006;85(17–18):2537–44.
- [78] Goodarzi F. Characteristics and composition of fly ash from Canadian coal-fired power plants. Fuel 2006;85(10–11):1418–27.
- [79] Gräbner M (ed.). Industrial coal gasification technologies covering baseline and high-ash coal. Wiley-VCH Verlag GmbH & Co. KGaA; 2014.

- [80] Elliott MA. Chemistry of coal utilization. Second supplementary volume 1981.
- [81] Ward RG. An introduction to the physical chemistry of iron & steel making. Edward Arnold; 1962.
- [82] Wallace P, Carmichael ISE. Sulfur in basaltic magmas. *Geochimica et Cosmochimica Acta* 1992;56(5):1863–74.
- [83] Duchesne MA, Bronsch AM, Hughes RW, Masset PJ. Slag viscosity modeling toolbox. *Fuel, Advances in Coal Science and Technology, ICCS&T* 2011 2013;114(0):38–43.
- [84] Bale CW, Pelton AD, Thompson WT, Eriksson G, Hack K, Chartrand P et al. FactSage 6.4. Thermfact and GTT-Technologies 2013.
- [85] Adam G, Gibbs Julian H. On the temperature dependence of cooperative relaxation properties in glass-forming liquids. *The Journal of Chemical Physics* 1965;43(1):139–46.
- [86] Cohen MH, Grest GS. Liquid-glass transition, a free-volume approach. *Physical Review B* 1979;20(3):1077–98.
- [87] Avramov I, Milchev A. Effect of disorder on diffusion and viscosity in condensed systems. *Journal of Non-Crystalline Solids* 1988;104(2–3):253–60.
- [88] Avramov I. Influence of disorder on viscosity of undercooled melts. *J. Chem. Phys* 1991;95(6):4439–43.
- [89] Zhang L, Jahanshahi S, Sun S, Chen C, Bourke B, Wright S et al. CSIRO's multiphase reaction models and their industrial applications. *JOM* 2002;54(11):51–6.
- [90] Shaw HR. Viscosities of magmatic silicate liquids; an empirical method of prediction. *Am J Sci* 1972;272(9):870–93.
- [91] Urbain G, Cambier F, Deletter M, Anseau MR. Viscosity of silicate melts. *Transactions & Journal of the British Ceramic Society* 1981;80:139–41.
- [92] Browning GJ, Bryant GW, Hurst HJ, Lucas JA, Wall TF. An empirical method for the prediction of coal ash slag viscosity. *Energy & Fuels* 2003;17(3):731–7.
- [93] Duchesne MA, Macchi A, Lu DY, Hughes RW, McCalden D, Anthony EJ. Artificial neural network model to predict slag viscosity over a broad range of temperatures and slag compositions: Gasification: Fundamentals and application. *Fuel Processing Technology* 2010;91(8):831–6.
- [94] Hoy HR, Roberts AG, Wilkins DM. Behavior of mineral matter in slagging gasification processes. Institute of Gas Engineers (London), Publication 1964;672.
- [95] Streeter RC, Diehl EK, Schobert HH. Measurement and Prediction of Low-Rank Coal Slag Viscosity. In: *The chemistry of low-rank coals*. American Chemical Society; 1984, p. 195–209.
- [96] Institute of Gas Technology. Energy and development administration report: Preparation of a coal conversion systems technical Data Book(FE-1730-21); 1976.
- [97] Bomkamp D. National Bureau of Standards Report: E(49-18)-1230; 1976.
- [98] Jung B, Schobert HH. Improved prediction of coal ash slag viscosity by thermodynamic modeling of liquid-phase composition. *Energy Fuels* 1992;6(4):387–98.
- [99] Urbain G. Viscosité et structure de silicoalumineux liquides. *Rev. Int. Hautes Temp. Réfract* 1974;11:133–45.

- [100] Urbain G. Viscosity Estimation of slags. *steel research international* 1987;58(3):111–6.
- [101] Mills KC. Viscosities of molten slags; 1992.
- [102] Mills KC, Broadbent CP. Evaluation of slag program for the prediction of physical properties of coal gasification slags. In: *Impact ash deposition coal fired plants*; 1993, p. 513–525.
- [103] Senior CL, Srinivasachar S. Viscosity of ash particles in combustion systems for prediction of particle sticking. *Energy & Fuels* 1995;9(2):277–83.
- [104] Vargas S, Frandsen F, Dam-Johansen K. ELSAM - Idemetsi Kosan cooperative research project: performance of viscosity models for high-temperature coal ashes. Lyngby; 1997.
- [105] Riboud PV, Roux Y, Lucas L-D, Gaye H. Improvement of continuous casting powders. *Fachberichte Hüttenpraxis Metallweiterverarbeitung* 1981;19(10):859–69.
- [106] Gronhovd GH. Slagging fixed-bed gasification of North Dakota lignite at pressures to 400 psig. US Dept. of the Interior, Bureau of Mines; 1970.
- [107] Roach PD, Raptis AC. Acoustic char flow monitor for the BI-GAS pilot plant; 1979.
- [108] Kalmanovitch DP, Frank M (eds.). *An effective model of viscosity for ash deposition phenomena*; 1988.
- [109] Machin JS, Yee TB, Hanna DL. Viscosity studies of system $\text{CaO-MgO-Al}_2\text{O}_3\text{-SiO}_2$: III, 35, 45, and 50 SiO_2 . *Journal of the American Ceramic Society* 1952;35(12):322–5.
- [110] Duchesne MA, Bronsch AM, Hughes RW, Masset PJ. Slag viscosity modeling toolbox. *Fuel* 2012:1–6.
- [111] Shiraishi Y, Ikeda K, Tamura A, Saito T. On the viscosity of molten FeO-SiO_2 systems. *Transactions of the Japan Institute of Metals* 1978;19(5):264–74.
- [112] Song W, Sun Y, Wu Y, Zhu Z, Koyama S. Measurement and simulation of flow properties of coal ash slag in coal gasification. *AIChE J* 2011;57(3):801–18.
- [113] Kashiwaya Y, Cicutti CE, Cramb AW, Ishii K. Development of double and single hot thermocouple technique for in situ observation and measurement of mold slag crystallization. *ISIJ International* 1998;38(4):348–56.
- [114] Kelton KF. Crystal nucleation in liquids and glasses. In: Henry Ehrenreich and David Turnbull, editor. *Solid State Physics*. Academic Press; 1991, p. 75–177.
- [115] Turnbull D. Kinetics of heterogeneous nucleation. *The Journal of Chemical Physics* 1950;18(2):198–203.
- [116] Rüssel C, Ehrt D. Neue Entwicklungen in der Glaschemie. *Chemie in unserer Zeit* 1998;32(3):126–35.
- [117] Birnie DP, Kingery WD. Quenching of solid samples for high temperature equilibrium measurement. *Journal of Materials Science* 1985;20(6):2193–8.
- [118] Wen G-H, Liu H, Tang P. CCT and TTT Diagrams to characterize crystallization behavior of mold fluxes. *Journal of Iron and Steel Research, International* 2008;15(4):32–7.
- [119] TNO. II. 3 High temperature glass melt properties.

- [120] Mills KC, Rhine JM. The measurement and estimation of the physical properties of slags formed during coal gasification: 1. Properties relevant to fluid flow. *Fuel* 1989;68(2):193–200.
- [121] Lange RA, Carmichael ISE. Densities of Na_2O - K_2O - MgO - MgO - FeO - Fe_2O_3 - Al_2O_3 - TiO_2 - SiO_2 liquids: New measurements and derived partial molar properties. *Geochimica et Cosmochimica Acta* 1987;51(11):2931–46.
- [122] Lange RA. A revised model for the density and thermal expansivity of K_2O - Na_2O - CaO - MgO - Al_2O_3 - SiO_2 liquids from 700 to 1900 K: extension to crustal magmatic temperatures. *Contributions to Mineralogy and Petrology* 1997;130(1):1–11.
- [123] Schwitalla DH. Density of slags obtained by MBP method. E-Mail. Institut für Energieverfahrenstechnik und Chemieingenieurwesen, TU Bergakademie Freiberg, Freiberg, Germany; 2015.
- [124] Wright S, Zhang L, Sun S, Jahanshahi S. Viscosity of a CaO - MgO - Al_2O_3 - SiO_2 melt containing spinel particles at 1646K. *Metallurgical and Materials Transactions B* 2000;31(1):97–104.
- [125] Kondratiev A, Jak E. Predicting coal ash slag flow characteristics (viscosity model for the Al_2O_3 - CaO - FeO - SiO_2 system). *Fuel* 2001;80(14):1989–2000.
- [126] Wright S, Zhang L, Sun S, Jahanshahi S. Viscosities of calcium ferrite slags and calcium alumino-silicate slags containing spinel particles: 6th Int. Conf. on Molten Slags, Fluxes and Salts. *Journal of Non-Crystalline Solids* 2001;282(1):15–23.
- [127] Hough DC, Sanyal A, Gruninger JH, Stewart GW, Annen KD. Development of an improved coal ash viscosity/temperature relationship for the assessment of slagging property in coal-fired boilers. *Journal of the Institute of Energy* 1986;59(439):77–81.
- [128] Rehage G, Schäfer EE. F. R. Eirich, Herausgeber: *Rheology, Theory and Applications*, Band IV. Academic Press, New York-London 1967. 522 Seiten mit zahlreichen Abbildungen. Preis: \$ 24,—. *Berichte der Bunsengesellschaft für physikalische Chemie* 1968;72(5):660–1.
- [129] Vand V. Viscosity of solutions and suspensions. I. Theory. *The Journal of Physical and Colloid Chemistry* 1948;52(2):277–99.
- [130] Quemada D. Rheology of concentrated disperse systems II. A model for non-newtonian shear viscosity in steady flows. *Rheologica Acta* 1978;17(6):632–42.
- [131] Murase T, McBirney AR. Properties of some common igneous rocks and their melts at high temperatures. *Geological Society of America Bulletin* 1973;84(11):3563–92.
- [132] Einstein A. Eine neue Bestimmung der Moleküldimensionen. *Annalen der Physik* 1906;324(2):289–306.
- [133] Einstein A. Berichtigung zu meiner Arbeit: „Eine neue Bestimmung der Moleküldimensionen“. *Annalen der Physik* 1911;339(3):591–2.
- [134] Roscoe R. The viscosity of suspensions of rigid spheres. *British Journal of Applied Physics* 1952;3(8):267–9.
- [135] Eilers H. The viscosity of the emulsion of highly viscous substances as function of concentration. *Kolloid-Zeitschrift* 1941;97(3):313–21.
- [136] Ward SG, Whitmore RL. Studies of the viscosity and sedimentation of suspensions Part 1.-The viscosity of suspension of spherical particles. *British Journal of Applied Physics* 1950;1(11):286.

- [137] Bronsch AM, Guhl S (eds.). Comparison of calculated and measured thermophysical slag properties: Viscosity and solid phases. Pennsylvania State University, Pennsylvania, USA: EMS Energy Institute; 2013.
- [138] Schobert HH, Streeter RC, Diehl EK. Flow properties of low-rank coal ash slags: Implications for slagging gasification. *Fuel* 1985;64(11):1611–7.
- [139] Bronsch AM. Abschlussbericht Versuchsanlage zur Schlackebadvergasung schwieriger Brennstoffe: Komplex 2: Druckschlackeerzeugung; 2015.
- [140] Zdaniewski W. DTA and X-Ray analysis study of nucleation and crystallization of $\text{MgO-Al}_2\text{O}_3\text{-SiO}_2$ glasses containing ZrO_2 , TiO_2 , and CeO_2 . *Journal of the American Ceramic Society* 1975;58(5-6):163–9.
- [141] Fredericci C, Zanotto ED, Ziemath EC. Crystallization mechanism and properties of a blast furnace slag glass. *Journal of Non-Crystalline Solids* 2000;273(1–3):64–75.
- [142] Francis AA. Non-isothermal crystallization kinetics of a blast furnace slag glass. *Journal of the American Ceramic Society* 2005;88(7):1859–63.
- [143] Öveçoğlu ML. Microstructural characterization and physical properties of a slag-based glass-ceramic crystallized at 950 and 1100 °C. *Journal of the European Ceramic Society* 1998;18(2):161–8.
- [144] Khater GA. The use of Saudi slag for the production of glass-ceramic materials. *Ceramics International* 2002;28(1):59–67.
- [145] Nowok JW. Viscosity and phase transformation in coal ash slags near and below the temperature of critical viscosity. *Energy Fuels* 1994;8(6):1324–36.
- [146] Nakada H, Nagata K. Crystallization of $\text{CaO-SiO}_2\text{-TiO}_2$ slag as a candidate for fluorine free mold flux. *ISIJ International* 2006;46(3):441–9.
- [147] Gan L, Zhang C, Zhou J, Shangguan F. Continuous cooling crystallization kinetics of a molten blast furnace slag. *Journal of Non-Crystalline Solids* 2012;358(1):20–4.
- [148] Meng Y, Thomas BG, Polycarpou AA, Prasad A, Henein H. Mould Slag Property Measurements to Characterize CC Mould – Shell Gap phenomena. *Canadian Metallurgical Quarterly* 2006;45(1):79–94.
- [149] Bronsch AM, Schwitalla DH, Guhl S. Results on experimental investigation and modelling of slag viscosities with consideration of partial crystallization. In: *Proceedings of the Thirty-First Annual International Pittsburgh Coal Conference*.
- [150] Park H, Park J-Y, Kim GH, Sohn I. Effect of TiO_2 on the viscosity and slag structure in blast furnace type slags. *steel research int* 2012;83(2):150–6.
- [151] Dingwell DB, Hess KU. Melt viscosities in the system Na-Fe-Si-OF-Cl : Contrasting effects of F and Cl in alkaline melts. *American Mineralogist* 1998;83:1016–21.
- [152] Kuo Y-M, Huang K-L, Wang C-T, Wang J-W. Effect of Al_2O_3 mole fraction and cooling method on vitrification of an artificial hazardous material. Part 1: Variation of crystalline phases and slag structures. *Journal of Hazardous Materials* 2009;169(1–3):626–34.
- [153] Duchesne MA, Ilyushechkin AY, Hughes RW, Lu DY, McCalden DJ, Macchi A et al. Flow behaviour of slags from coal and petroleum coke blends. *Fuel* 2012;97(0):321–8.
- [154] Allmann R. Röntgenpulverdiffraktometrie. Rechnergestützte Auswertung, Phasenanalyse und Strukturbestimmung; 39 Tabellen. 2nd ed. Berlin: Springer; 2003.

- [155] Döbelin N. Lesson 3: Sample Preparation & Problems. Lecture Handout. Uppsala, Sweden; 2013.
- [156] Etchepare J, Merian M, Kaplan P. Vibrational normal modes of SiO₂. II. Cristobalite and tridymite. *The Journal of Chemical Physics* 1978;68(4):1531–7.
- [157] Liu X, Ding C. Phase compositions and microstructure of plasma sprayed wollastonite coating. *Surface and Coatings Technology* 2001;141(2–3):269–74.
- [158] Van't Hoff JH, Dunsch L. *Etudes de dynamique chimique*, 1884. Akademische Verlagsgesellschaft; 1985.
- [159] Arrhenius S. On the reaction rate of the inversion of non-refined sugar upon souring. *Z Phys Chem* 1889;4:226–48.
- [160] Arrhenius S. *Kemien och det moderna livet*. H. Gebers; 1919.
- [161] Weymann HD. On the hole theory of viscosity, compressibility, and expansivity of liquids. *Kolloid-Zeitschrift & Zeitschrift für Polymere* 1962;181(2):131–7.
- [162] Weymann H. Theoretische und experimentelle Untersuchungen zur Platzwechseltheorie des viskosen Fließens. *Kolloid-Zeitschrift* 1954;138(1):41–56.
- [163] Meireles MRG, Almeida PEM, Simoes MG. A comprehensive review for industrial applicability of artificial neural networks: *Industrial Electronics, IEEE Transactions on*. *Industrial Electronics, IEEE Transactions on* DOI - 10.1109/TIE.2003.812470 2003;50(3):585–601.
- [164] Jain AK, Mao J, Mohiuddin KM. Artificial neural networks: A tutorial. *Computer* 1996;29(3):31–44.
- [165] Watt JD, Fereday F. Flow Properties of Slags formed from ashes of British coals: Part 1. Viscosity of homogeneous liquid slags in relation to slag composition. *Inst Fuel-J* 1969;42(338):99–103.
- [166] Hoy HR, Roberts AG, Wilkins DM. Behavior of mineral matter in slagging gasification processes. *J. Inst. Gas Engrs* 1965;5:444–69.
- [167] Quon DHH, Wang SSB, Chen TT. Viscosity measurements of slags from pulverized western Canadian coals in a pilot-scale research boiler. *Fuel* 1984;63(7):939–42.
- [168] Urbain G, Boiret M. Viscosities of liquid silicates. *Ironmaking and Steelmaking* 1990;17(4):255–60.
- [169] Urbain G, Carron JP, Calas G. Estimation de la Viscosité de Certains Aluminosilicates d'Intérêt Géologique. *Tables rondes du CNRS, Toulouse* 1978.
- [170] MATLAB. *The MathWorks*; 2008.
- [171] Ermolaeva. Relationship between surface tension, viscosity, and density of some ternary melts of refractory oxides. *Ogneupory* 1955;5:221.
- [172] Gorelkin O, Mikhailiov S, Popova E, Lazareva, E. Improving the effectiveness of direct alloying of steels with vanadium. *Akademiia Nauk SSSR, Izvestiia, Metally* 1976:16–21.
- [173] Musikhin VI, Lepinskikh BM, Chernyaev VG, Ishchuk NY, Klibus AV. Effect of iron, chromium, and vanadium oxides on the surface tension and density of calcium oxide-silicon dioxide-aluminium oxide-magnesium oxide melts. *Trudy Inst Met Sverdlovsk* 1969;20:75–81.
- [174] Popel SI, Sokolov VI, Korpachev VG. Influence of magnesium oxide on the physico-chemical properties of iron-silicate melts and foam stability (in Russian). *Tr. Uralsk. Politekh. Inst.* 1963;126:24–33.

- [175] Salautin VA, Evseev PP, Ratner BY, Gnuchev SM, Ponomarev BI. Changes in the composition and properties of electric-furnace slags used in the processing of transformer steel. *IZV AKAD NAUK SSSR, METALLY* 1968(5):3–10.
- [176] Toropov NA, Bryantsev BA. Physical–chemical properties and crystallization of melts of system MnO–FeO–SiO₂ (in Russian). *Strukturnye Prevrashcheniya v Steklakh pri Povyshennykh Temperaturakh* 1968:2156–9.
- [177] Am Yakushev, Romashin VM, Amfiteatrov VA. Viscosity of CaO based slags with variable Al₂O₃, SiO₂, and MgO Contents [J]. *Izvestiya Vysshikh Uchebnykh Zavedenij. Chernaya Metallurgiya* 1977;11:55–88.
- [178] Wu C, Chang J. A Novel Akermanite Bioceramic: Preparation and characteristics. *Journal of Biomaterials Applications* 2006;21(2):119–29.
- [179] Anthony J. Handbook of MINERALOGY: Volume II - Elements, Silica, Silicates. Tucson, Ariz.: Mineral Data Publishing.
- [180] Robbins M. The collector's book of fluorescent minerals. Springer Science & Business Media; 1983.
- [181] Roberts WL. Encyclopedia of minerals. 2nd ed. New York: Van Nostrand Reinhold; 1990.
- [182] Villars P. Material Phases Data System (MPDS), CH-6354 Vitznau, Switzerland; Springer Materials; sd_1622044: Springer-Verlag GmbH, Heidelberg; 2014.
- [183] Kamigaito O. Density of Compound Oxides. *Journal of the Ceramic Society of Japan* 2000;108(1262):944–7.
- [184] Reddy RG, Yen JY. Effect of solid particles on the viscosity of slags. *Extractive Metallurgy of Copper, Nickel and Cobalt* 1993;1:309–23.
- [185] Lejeune A-M, Richet P. Rheology of crystal-bearing silicate melts: An experimental study at high viscosities. *J. Geophys. Res* 1995;100(B3):4215–29.
- [186] Forsbacka L, Holappa L, Iida T, Kita Y, Toda Y. Experimental study of viscosities of selected CaO–MgO–Al₂O₃–SiO₂ slags and application of the Iida model. *Scandinavian Journal of Metallurgy* 2003;32(5):273–80.
- [187] Cukierman M, Uhlmann DR. Viscosity of liquid anorthite. *J. Geophys. Res.* 1973;78(23):4920–3.
- [188] Seggiani M. Modelling and simulation of time varying slag flow in a PreNFLO entrained-flow gasifier. *Fuel* 1998;77(14):1611–21.
- [189] Hüttentechnische Vereinigung der Deutschen Glasindustrie (HVG). Offenbach, Germany.
- [190] Nentwig T. Experimentelle Bestimmung und numerische Simulation von Viskositäten in Schlackesystemen unter Vergasungsbedingungen [Dissertation]. Aachen: Rheinisch-Westfälische Technische Hochschule Aachen; 2011.
- [191] Handfield G, Charette GG. Viscosity and structure of industrial high TiO₂ slags. *Canadian Metallurgical Quarterly* 1971;10(3):235–43.
- [192] Song W, Tang L, Zhu X, Wu Y, Zhu Z, Koyama S. Flow properties and rheology of slag from coal gasification. 17th International Symposium on Alcohol Fuels 2010;89(7):1709–15.
- [193] DIN Deutsches Institut für Normung e.V. Thermoelemente - Teil 1: Thermospannungen und Grenzabweichungen (IEC 60584-1:2013); Deutsche Fassung EN 60584-1:2013(DIN EN 60584-1): Deutsches Institut für Normung; 2013.

- [194] Deutsche Glastechnische Gesellschaft DGG. Viskositäts-Temperatur-Verhalten des Standardglases I der DGG; 2010.
- [195] Choudhary M, Szekely J, Medovar B, Emelyanenko YU. The velocity field in the molten slag region of ESR systems: A comparison of measurements in a model system with theoretical predictions. *Metallurgical and Materials Transactions B* 1982;13(1):35-43-43.
- [196] Xiangfa L, Zuogui Z, Zhen G, Xiufang B. The influence of electromagnetic stirring on Al-Ti-B master alloys. *JOM Journal of the Minerals, Metals and Materials Society* 2000;52(5):47-48-48.
- [197] Brückmann G, Sick G, Schwerdtfeger K. Slag movement in ESR of steel. *Metallurgical and Materials Transactions B* 1983;14(4):761-764-764.
- [198] Rückert A, Pfeifer H (eds.). Numerical modelling of the electroslag remelting process; 2007.
- [199] Li X, Wang T, Jiang X, Zhu B. Effect of electromagnetic field on melting slag resistance of MgO-C refractories. *Kuei Suan Jen Hsueh Pao* 2011;39(3):452–7.
- [200] Sato Y, Kameda Y, Nagasawa T, Sakamoto T, Moriguchi S, Yamamura T et al. Viscosity of molten silicon and the factors affecting measurement. *Journal of Crystal Growth* 2003;249(3-4):404–15.
- [201] EPRI. Slag Viscosity Measurements. Palo Alto, CA; 2001.
- [202] Becker F-M. Formeln und Tabellen für die Sekundarstufen I und II. 8th ed. Berlin: Paetec Ges. für Bildung und Technik; 2000.
- [203] Bryant GW, Browning GJ, Gupta SK, Lucas JA, Gupta RP, Wall TF. Thermomechanical analysis of coal ash: The influence of the material for the sample assembly. *Energy & Fuels* 2000;14(2):326–35.
- [204] Lide DR (ed.). CRC handbook of chemistry and physics: A ready-reference book of chemical and physical data. 90th ed. Boca Raton, FL: CRC Press; 2009.
- [205] Barin I. Thermochemical Data of Pure Substances, Thermochemical Data of Pure Substances. Wiley-VCH; 1997.